

Internal Report  
DESY F31-91-03  
July 1991

Measurement of the Decay of the  $\Upsilon(1S)$  and  $\Upsilon(2S)$   
Resonances to Muon Pairs  
and  
Determination of the Strong Coupling Constant  
Using the Crystal Ball Detector

by

Michael Kobel

Eigentum der	<b>DESY</b>	Bibliothek
Property of		library
Zugang:	26. NOV. 1991	
Accessions:		
Leihfrist:	7	Tage
Loan period:		days

**DESY behält sich alle Rechte für den Fall der Schutzrechtserteilung und für die wirtschaftliche Verwertung der in diesem Bericht enthaltenen Informationen vor.**

**DESY reserves all rights for commercial use of information included in this report, especially in case of filing application for or grant of patents.**

**“Die Verantwortung für den Inhalt dieses Internen Berichtes liegt ausschließlich beim Verfasser“**

**Measurement of the Decay of the  $\Upsilon(1S)$  and  $\Upsilon(2S)$   
Resonances to Muon Pairs  
and  
Determination of the Strong Coupling Constant  
using the Crystal Ball Detector**

Den Naturwissenschaftlichen Fakultäten  
der Friedrich-Alexander-Universität Erlangen-Nürnberg  
zur  
Erlangung des Doktorgrades

vorgelegt von

Michael Kobel

aus Bayreuth

Als Dissertation genehmigt von den Naturwissenschaftlichen  
Fakultäten der Universität Erlangen-Nürnberg

Tag der mündlichen Prüfung:

Vorsitzender der Promotionskommission:	Professor Dr. E. Kessler
Erstberichterstatter:	Professor Dr. H. Wegener
Zweitberichterstatter:	Professor Dr. K.R. Schubert
Drittberichterstatter:	Professor Dr. F. Lenz



*Siehst Du den Mond dort stehen?  
Er ist nur halb zu sehen,  
Und ist doch rund und schön.  
So ist's mit manchen Sachen,  
Die wir getrost belachen,  
Weil uns're Augen sie nicht seh'n.*

Für

Gaby

und

Pascal

# Zusammenfassung

Mit dem Crystal Ball Detektor wurde am  $e^+e^-$  Speicherring DORIS II das Verzweigungsverhältnis  $B_{\mu\mu}$  für den Zerfall der  $\Upsilon(1S)$  und  $\Upsilon(2S)$  Resonanzen in Myon-Paare sowie zum ersten Mal das Produkt aus ihrer myonischen Breite  $\Gamma_{\mu\mu}$  und ihrem Verzweigungsverhältnis in Elektron-Paare,  $B_{ee}$ , gemessen. Es ergaben sich Werte von

$$\begin{aligned} B_{\mu\mu}(1S) &= (2.31 \pm 0.12 \pm 0.10) \% \\ \Gamma_{\mu\mu}(1S) \cdot B_{ee}(1S) &= (31.2 \pm 1.6 \pm 1.7) \text{ eV} \end{aligned}$$

und

$$\begin{aligned} B_{\mu\mu}(2S) &= (1.22 \pm 0.28 \pm 0.19) \% \\ \Gamma_{\mu\mu}(2S) \cdot B_{ee}(2S) &= (6.5 \pm 1.5 \pm 1.0) \text{ eV}, \end{aligned}$$

wobei die beiden Fehler jeweils die statistische und die systematische Unsicherheit der Messung angeben. Unter Benützung des derzeitigen Weltmittelwertes von  $B_{ee}(1S) = (2.52 \pm 0.17) \%$  konnte zum ersten Mal die myonische Partialbreite

$$\Gamma_{\mu\mu}(1S) = (1.24 \pm 0.06 \pm 0.11) \text{ keV}$$

gemessen werden. Darüberhinaus konnte in der Abhängigkeit des Wirkungsquerschnittes von der  $e^+e^-$  Schwerpunktsenergie erstmals die erwartete Interferenz zwischen Myon-Paar Erzeugung im Kontinuum und in Resonanzzerfällen beobachtet werden.

Aus dem Ergebnis für  $B_{\mu\mu}(1S)$  erhält man den Skalenparameter  $\Lambda$  der Starken Wechselwirkung, indem man für das  $\Upsilon(1S)$  das Verhältnis von  $B_{\mu\mu}$  und der Zerfallsrate  $B_{ggg}$  in drei Gluonen auswertet. Renormiert man die Quanten-Chromo-Dynamik mit Hilfe des  $\overline{\text{MS}}$  Schemas für vier "flavors", so findet man

$$\Lambda_4^{\overline{\text{MS}}} = (210 \pm 25_{-50}^{+120}) \text{ MeV}.$$

Diese Zahl entspricht einer Starken Kopplungskonstanten von

$$\alpha_s^{\overline{\text{MS}}}(\mu=5 \text{ GeV}) = 0.184 \pm 0.006_{-0.013}^{+0.027}.$$

Die ersten Fehler an diesen Resultaten geben die jeweiligen experimentellen, und die zweiten Fehler die theoretischen Unsicherheiten an. Da letztere beim derzeitigen Stand der Theorie eigentlich prinzipiell nicht bestimmbar sind, sollten sie nur als ungefähre Schätzungen betrachtet werden.

# Abstract

Using the Crystal Ball detector at the  $e^+e^-$  storage ring DORIS II we have measured the branching fraction  $B_{\mu\mu}$  to muon pairs of the  $\Upsilon(1S)$  and  $\Upsilon(2S)$  resonances and for the first time the product of the muonic partial width  $\Gamma_{\mu\mu}$  and the branching fraction  $B_{ee}$  to electrons for both resonances. We obtain

$$\begin{aligned} B_{\mu\mu}(1S) &= (2.31 \pm 0.12 \pm 0.10) \% \\ \Gamma_{\mu\mu}(1S) \cdot B_{ee}(1S) &= (31.2 \pm 1.6 \pm 1.7) \text{ eV} \end{aligned}$$

and

$$\begin{aligned} B_{\mu\mu}(2S) &= (1.22 \pm 0.28 \pm 0.19) \% \\ \Gamma_{\mu\mu}(2S) \cdot B_{ee}(2S) &= (6.5 \pm 1.5 \pm 1.0) \text{ eV}, \end{aligned}$$

where the errors given are the statistical and systematic uncertainties, respectively. Inserting the present world average value of  $B_{ee}(1S) = (2.52 \pm 0.17) \%$  we measure for the first time the muonic partial width

$$\Gamma_{\mu\mu}(1S) = (1.24 \pm 0.06 \pm 0.11) \text{ keV}.$$

In addition we present the first evidence for the expected interference between  $\mu$ -pair production in the continuum and in  $\Upsilon(1S)$  decays.

Using our result on  $B_{\mu\mu}(1S)$  we derive a value for the scale parameter  $\Lambda$  of the strong interaction from exploiting the ratio of  $B_{\mu\mu}$  to the branching fraction  $B_{ggg}$  of the  $\Upsilon(1S)$  to three gluons. In the  $\overline{\text{MS}}$  renormalization scheme for the theory of Quantum Chromo Dynamics (QCD) we find for four flavors

$$\Lambda_4^{\overline{\text{MS}}} = (210 \pm 25_{-50}^{+120}) \text{ MeV}.$$

We convert this number into a measurement of the strong coupling constant

$$\alpha_s^{\overline{\text{MS}}}(\mu=5 \text{ GeV}) = 0.184 \pm 0.006_{-0.013}^{+0.027}.$$

In both results the experimental and the theoretical errors are listed, respectively. The values for the theoretical uncertainties should be taken as an educated guess. Given today's state of the art in QCD, they are in principle unknown.

# Contents

<b>Widmung</b>	<b>i</b>
<b>Zusammenfassung</b>	<b>ii</b>
<b>Abstract</b>	<b>iii</b>
<b>Contents</b>	<b>iv</b>
<b>1 Introduction</b>	<b>1</b>
<b>2 Theoretical Fundamentals</b>	<b>6</b>
2.1 The Standard Model of Elementary Particle Physics . . . . .	6
2.1.1 The Building Blocks of Matter . . . . .	6
2.1.2 The Forces . . . . .	7
2.1.3 The $SU(2)\times U(1)\times SU(3)$ Structure of Fermions . . . . .	8
2.1.4 The Masses . . . . .	9
2.1.5 Open Questions . . . . .	9
2.2 Renormalization of Gauge Theories . . . . .	11
2.2.1 Renormalization in QED . . . . .	11
2.2.2 Renormalization in QCD . . . . .	17
2.2.3 Renormalization Scheme Dependence of QCD Predictions . . . . .	20
2.3 The Process $e^+e^- \rightarrow \mu^+\mu^-$ at $\sqrt{s} \approx 10$ GeV . . . . .	27
2.3.1 First Order Corrections . . . . .	27
2.3.2 Higher Order Bremsstrahlung and Exponentiation . . . . .	39
2.3.3 MC Methods for Generating Radiative $\mu$ -Pair Events . . . . .	42
2.3.4 The DYMU2 Generator . . . . .	44
2.3.5 Effects of Bremsstrahlung and C.M. Energy Spread on Resonance Production . . . . .	47
2.4 The Process $e^+e^- \rightarrow e^+e^-$ . . . . .	49
<b>3 The Experimental Setup and its Simulation</b>	<b>53</b>
3.1 The Crystal Ball Detector . . . . .	53
3.2 The Triggers . . . . .	57
3.3 Calibration and Data Reconstruction . . . . .	58
3.4 Further Treatment of the Reconstructed Data . . . . .	58
3.5 Monte Carlo Event Simulation . . . . .	60
<b>4 Beam Energy, Luminosity, and Data Selection</b>	<b>63</b>
4.1 The Selection of Multihadronic Events . . . . .	64
4.2 Center of Mass Energy Determination . . . . .	65

4.3	The Selection of Bhabha Events . . . . .	67
4.4	Luminosity Determination . . . . .	68
4.5	The Selection of $\mu$ -Pair Events . . . . .	68
4.5.1	Possible Background Processes . . . . .	69
4.5.2	The Selection Criteria . . . . .	79
<b>5</b>	<b>Background Determination</b> . . . . .	<b>82</b>
5.1	Backgrounds other than $e^+e^-$ Interactions . . . . .	83
5.1.1	Cosmic Ray Events . . . . .	83
5.1.2	eN Events . . . . .	84
5.2	Continuum Backgrounds from $e^+e^-$ Interactions . . . . .	85
5.2.1	The Continuum Process $e^+e^- \rightarrow \mu^+\mu^-$ . . . . .	86
5.2.2	The Two-Photon Process $e^+e^- \rightarrow e^+e^-\mu^+\mu^-$ . . . . .	87
5.2.3	The Two-Photon Process $e^+e^- \rightarrow e^+e^-\pi^+\pi^-$ . . . . .	87
5.2.4	The Two-Photon Process $e^+e^- \rightarrow e^+e^-e^+e^-$ . . . . .	87
5.2.5	The Continuum Process $e^+e^- \rightarrow \tau^+\tau^-$ . . . . .	88
5.3	Continuum Background Subtraction . . . . .	88
5.3.1	The Scaling Factor $C$ . . . . .	90
5.3.2	The Systematic Error on the Luminosity Ratio . . . . .	92
5.3.3	The Systematic Error on the Background Ratio . . . . .	94
5.4	Resonant Background from $\Upsilon \rightarrow \mu^+\mu^-X$ . . . . .	101
5.4.1	The Process $\Upsilon \rightarrow \tau^+\tau^-$ . . . . .	102
5.4.2	The Process $\Upsilon(2S) \rightarrow \Upsilon(1S)X$ . . . . .	102
<b>6</b>	<b>Results for the Decay <math>\Upsilon \rightarrow \mu^+\mu^-</math></b> . . . . .	<b>103</b>
6.1	The Selection Efficiency for $\Upsilon \rightarrow \mu^+\mu^-$ . . . . .	104
6.1.1	The Efficiency Dependence on the C.M. Energy . . . . .	104
6.1.2	The Systematic error on the Efficiency . . . . .	105
6.2	The Determination of $B_{\mu\mu}$ . . . . .	106
6.2.1	The Number of $\Upsilon$ Resonances . . . . .	106
6.2.2	The Number of Resonant $\mu$ -Pairs . . . . .	111
6.3	The Determination of $\Gamma_{\mu\mu}B_{ee}$ . . . . .	113
6.3.1	The Fit to the Muonic Cross-Section . . . . .	113
6.3.2	Evidence for Interference . . . . .	114
<b>7</b>	<b>Discussion of the Results</b> . . . . .	<b>116</b>
7.1	The Leptonic Branching Ratios of $\Upsilon(1S)$ and $\Upsilon(2S)$ . . . . .	116
7.1.1	The New World Averages . . . . .	116
7.1.2	Consistency of $B_{\mu\mu}$ Values of Different Resonances . . . . .	118
7.2	The Leptonic Widths of $\Upsilon(1S)$ and $\Upsilon(2S)$ . . . . .	119
7.2.1	Measurement of $\Gamma_{\mu\mu}(1S)$ . . . . .	119
7.2.2	The New World Averages of $\Gamma_{\mu\mu}$ . . . . .	120
7.3	The Total Widths of $\Upsilon(1S)$ and $\Upsilon(2S)$ . . . . .	121
7.4	The Determination of $\alpha_s$ and $\Lambda$ . . . . .	121
7.4.1	Study of the Renormalization Scheme Dependence . . . . .	122
7.4.2	Comparison to Results for $\Lambda$ from Other Methods . . . . .	127
<b>8</b>	<b>Summary</b> . . . . .	<b>129</b>

<b>A</b>	<b>A Verified Upgrade of GHEISHA</b>	<b>131</b>
A.1	Changes in the $\delta$ -Ray and Energy Loss Simulation . . . . .	131
A.2	Verification with Crystal Ball Data . . . . .	136
A.2.1	The Lateral Energy Pattern . . . . .	137
A.2.2	The Energy Loss Distribution . . . . .	137
<b>B</b>	<b>The Erlangen Tube Chamber MC</b>	<b>144</b>
B.1	The Pulse Height Distributions . . . . .	145
B.2	The $z$ -Resolution . . . . .	148
B.3	The Hit Efficiencies . . . . .	160
B.4	Short Summary . . . . .	162
B.5	Systematic Errors . . . . .	163
B.5.1	Efficiencies . . . . .	164
B.5.2	Precision of Direction Measurements . . . . .	166
B.5.3	Photon Conversion Probability . . . . .	166
B.5.4	Time Dependence of Chamber Measurements . . . . .	168
<b>C</b>	<b>The Determination of the Beam Energy</b>	<b>169</b>
C.1	The Method . . . . .	169
C.2	Application to the $\Upsilon(2S)$ Data . . . . .	170
C.3	Application to the $\Upsilon(1S)$ Data . . . . .	171
C.4	Systematic Errors . . . . .	174
C.5	Combining the Data Points . . . . .	174
<b>D</b>	<b>The Efficiency Corrected Cross-Section</b>	<b>175</b>
	<b>Acknowledgements</b>	<b>176</b>
	<b>The Crystal Ball Collaboration</b>	<b>177</b>
	<b>Bibliography</b>	<b>178</b>
	<b>Lebenslauf</b>	<b>185</b>

# Chapter 1

## Introduction

In the past 35 years substantial progress has been achieved in understanding strongly interacting matter. Milestones in the experimental findings were the discovery that the proton is not point-like [1], the observation of structure inside the nucleon [2], the discovery of quarks with the new flavors charm [3] and beauty [4], and the proof of the existence of gluons [5]. The possible mass range for the presumably last missing element in the zoo of strongly interacting elementary particles, the top quark, has by now been considerably narrowed by indirect methods [6], indicating its possible detection in the near future.

Parallel to the experimental progress the theoretical development led from the concept of quarks [7] and partons [8] to a field theory of strong interaction, the Quantum Chromodynamics (QCD) [9]. Its basic approach of an underlying local gauge symmetry was taken from the successful “theory of light and matter”, the Quantum Electrodynamics (QED) [10], and its later unification with the theory of weak interactions to the Electroweak Theory [11]. The proof of their renormalizability [12] ensured that predictions for physical processes could be obtained from these theories with the help of perturbation expansions. However, two facts render perturbative calculations in QCD much harder and less accurate than in QED. In the GeV energy range the strong coupling constant  $\alpha_s$  is more than 20 times larger than the electromagnetic coupling  $\alpha_{em}$ , and there is a self-interaction between the mediating bosons, the gluons, which is absent in the case of photons.

The cleanest way to study strong interactions is the investigation of two-quark systems. Among these the spectroscopy of quarkonia yields the richest harvest of information. Quarkonia are bound states of a quark and its antiquark and their energy level schemes are similar to the positronium levels in QED. In Figure 1.1 we have plotted the level schemes for the heavy quarkonia bottomonium ( $b\bar{b}$ ) and charmonium ( $c\bar{c}$ ). A similar level scheme can be plotted for the lighter strangeonium ( $s\bar{s}$ ). Its lowest lying states are the  $^1S_0$   $\eta'(958)$ , the  $^3S_1$   $\phi(1020)$ , the  $^1P_1$   $h'_1(1380)$ , and the  $^3P_J$  states  $f'_0(\sim 1525)$ ,  $f'_1(1510)$ ,  $f'_2(1525)$ . However, all these states are more or less influenced by  $SU(3)_f$  mixing with  $u\bar{u}+d\bar{d}$  and are therefore no pure  $s\bar{s}$  states. The absence of  $SU(3)_f$  mixing effects for the heavy quarkonia facilitates the understanding of level spacings, and the occurrence of states below the respective open meson ( $D\bar{D}$ ,  $B\bar{B}$ ) threshold opens the possibility to study a variety of decay channels and various transitions within the quarkonia systems. Relativistic effects and non-perturbative QCD effects, which are still large for charmonium, decrease with increasing quark masses. This would suggest ideal conditions for the bound top-quark system. However, given a top-quark mass of more than 89 GeV [14], the top-quark decays on-shell into a W-Boson and a b-quark. Thus the weak decay of the toponium  $\Theta(t\bar{t}) \rightarrow W^+W^-B\bar{B}$  dominates and strong decay channels or cascade decays will hardly be observed. In addition, the  $\Theta$  widths may even be larger than the distance between successive toponium states [15]. Therefore the  $t\bar{t}$  spectroscopy does not

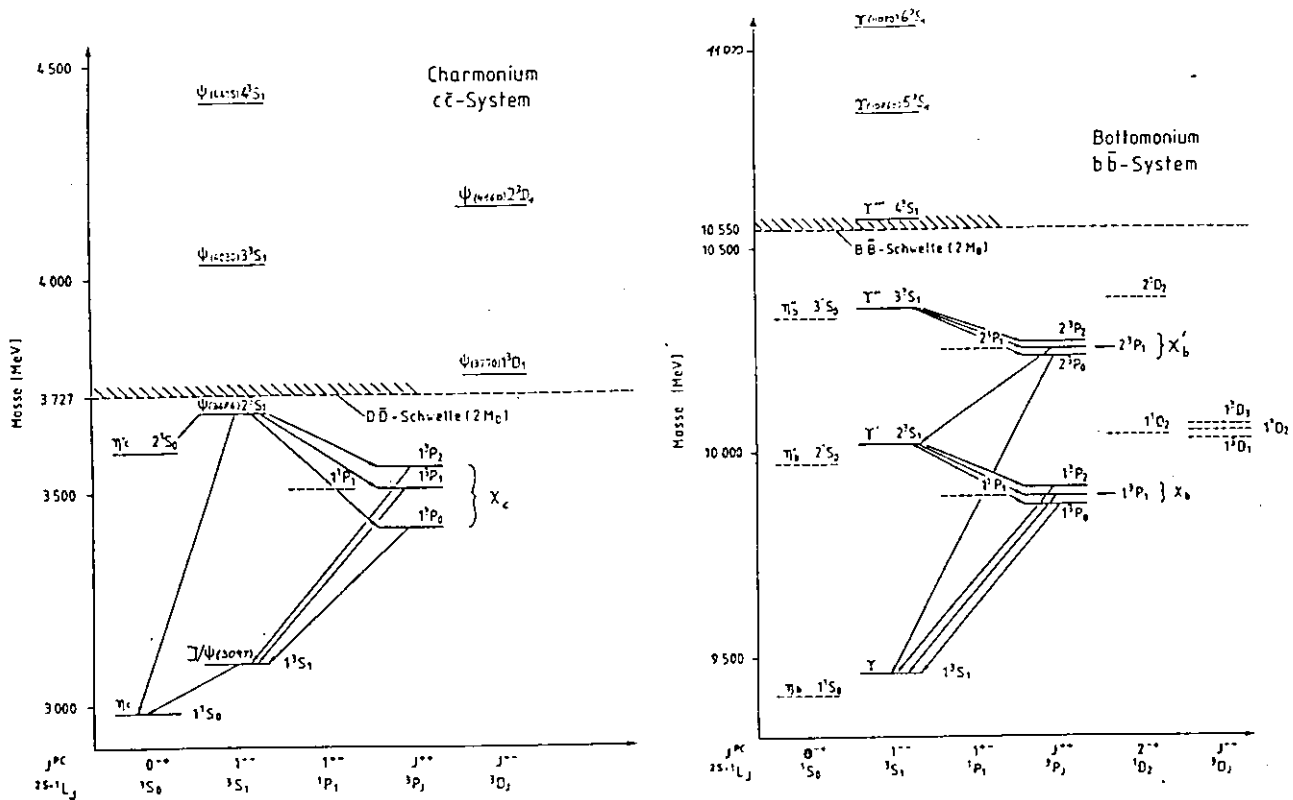


Figure 1.1: Energy level schemes for charmonium, and bottomonium [13]. States with dashed lines have not yet been observed. The arrows indicate measured radiative transitions. The numbers in parentheses give the mass in MeV. The spectroscopic notation  $n^{2s+1}L_J$  lists the radial quantum number  $n$ , the spin multiplet  $2s + 1$ , the angular momentum  $L$ , and the total spin  $J$ . Above the open meson threshold considerable mixing between  $^3S_1$  and  $^3D_1$  states may occur via coupled channel effects.

look very promising, and the  $b\bar{b}$  system appears to be the “Hydrogen atom of QCD”, where the strong interaction can be studied with the least distortions.

The  $b\bar{b}$  states with the quantum numbers of the photon,  $J^{PC} = 1^{--}$ , are called  $\Upsilon$  resonances, and can be directly produced in  $e^+e^-$ -annihilation into one virtual photon (Fig. 1.2).

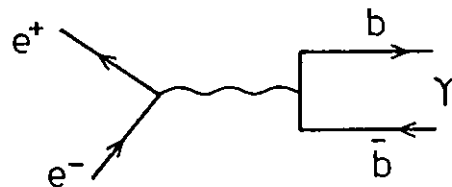


Figure 1.2: The production of  $\Upsilon$ -resonances in  $e^+e^-$ -annihilation.

Figure 1.3 shows the total cross section of  $e^+e^- \rightarrow$  hadrons in the center-of-mass (c.m.) energy region around 10 GeV. The data was taken by the CLEO detector at the CESR  $e^+e^-$  storage ring in Cornell (USA) [16]. The production of the  $\Upsilon(1S)$  to  $\Upsilon(6S)$  states shows up as resonances in the  $e^+e^-$  cross section.

The apparent widths of the  $\Upsilon(1S)$  to  $\Upsilon(3S)$  resonances in Figure 1.3 are governed by the



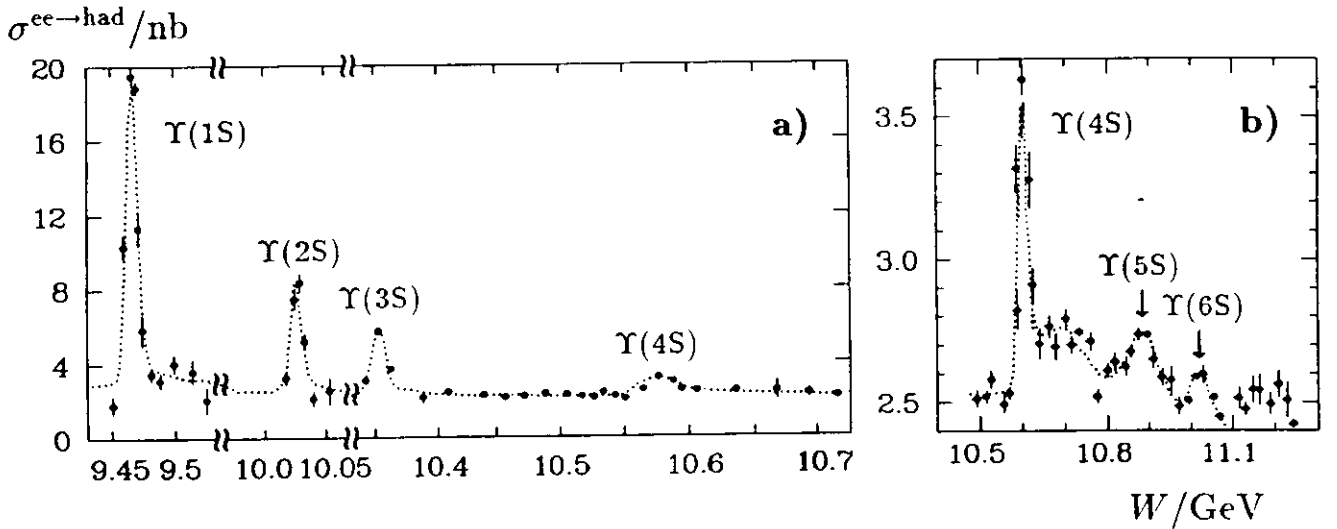


Figure 1.3: Total observed cross section of  $e^+e^- \rightarrow \text{hadrons}$  versus the  $e^+e^-$  center-of-mass energy as measured at CESR.

c.m. energy resolution of CESR, being about 4 MeV. Their true widths are only a few 10 keV. On the other hand, the  $\Upsilon(4S)$  to  $\Upsilon(6S)$  resonances are much broader than the storage ring resolution. Their widths range from 24 MeV to 110 MeV, since their masses lie above the energy threshold for open bottom production (Fig. 1.4a). This is an example for the Okubo-Zweig-Iizuka (OZI) rule [17], claiming that decays without  $q\bar{q}$  annihilation are largely preferred.<sup>1</sup> The main decay modes of the  $\Upsilon$ -resonances are listed below, roughly ordered according to their partial decay widths.

- Decay to two B-mesons above the threshold for open bottom production (Fig. 1.4a).
- Hadronic or electromagnetic transitions to lower lying  $\Upsilon$ -states (Fig. 1.4b and c)
- Annihilation to 3 gluons or 2 gluons plus a photon (Fig. 1.4d and e)
- Annihilation to 1 virtual photon (Fig. 1.4f and g)

Decays to one gluon are forbidden by color conservation since a single gluon is not a color singlet. A two-gluon or two-photon final state is not possible due to the Landau-Yang theorem [18]. The decay into three photons is negligibly small, as it is proportional to  $\alpha_{em}^3$ .

Those decay modes, which involve quark-antiquark annihilation to gluons, can in principle be calculated in QCD and compared to the experimental values. However, the mean binding radius of the quarks is still too large to neglect confinement, and thus non-perturbative effects. These effects are usually factorized into the wave function leaving a perturbatively calculable part. Predictions for partial decay widths thus depend on model calculations for the wave functions (e.g. non-relativistic potential models), and on the validity of perturbative QCD.

In ratios of two partial widths of the same resonance the dependence on the wave function cancels, and the ratio can be expressed in a power series of the strong coupling constant  $\alpha_s$ . Such a ratio is formed by the expressions for the 3-gluon width  $\Gamma_{ggg}$  of the  $\Upsilon$ -states and their leptonic width  $\Gamma_{ll}$ , which can be measured as the ratio of the corresponding branching fractions  $B_{ggg}$  and  $B_{ll}$ . Since the 3 gluon decay leads to a large variety of final states, the corresponding branching fraction can only be measured by subtracting the sum of all

<sup>1</sup>The OZI rule is meanwhile understood as originating from the running of the strong coupling constant  $\alpha_s$ , since diagrams without quark annihilation involve only soft gluons.

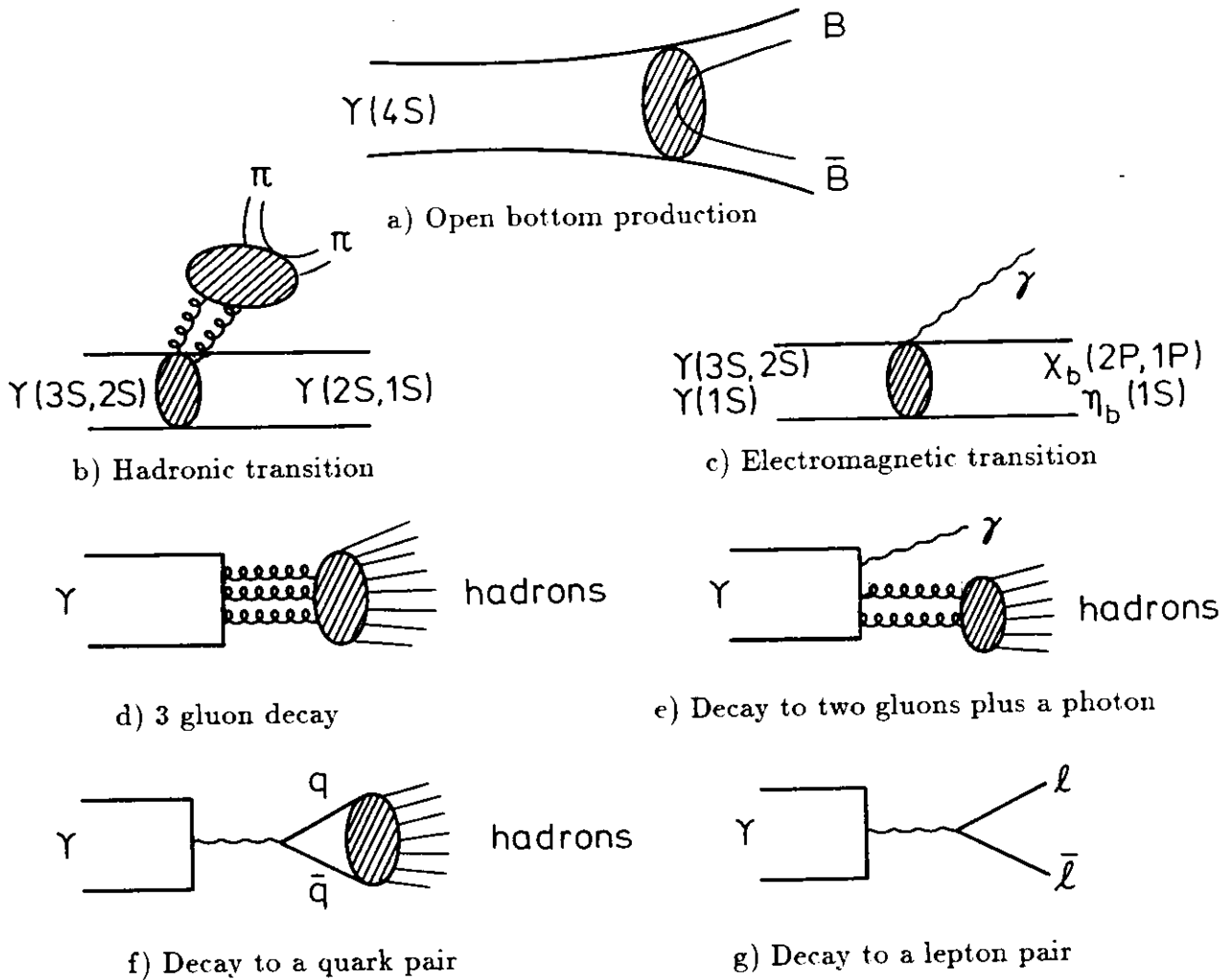


Figure 1.4: Possible  $\Upsilon$  decay modes. The hatched regions indicate fragmentation or soft gluon exchange.

other branching fractions from unity. The calculation of this latter sum also relies on the knowledge of  $B_u$ . The measurement of the electromagnetic decay  $\Upsilon \rightarrow \ell\bar{\ell}$  thus leads to an experimental result, which can be compared to perturbative QCD predictions. If the perturbative expansion is well behaved, the strong coupling constant  $\alpha_s$  can be extracted from this measurement. Apart from the strong coupling constant, fundamental parameters of the  $\Upsilon$ -resonances, namely their total widths and some branching ratios for cascade decays, are determined with the help of the  $\Upsilon$  decay to lepton pairs.

Since the total widths of the three lowest  $\Upsilon(nS)$  states,  $n=1,2,3$ , are about two orders of magnitude smaller than the energy resolution of today's  $e^+e^-$ -colliders, these total widths can only be obtained from the ratio of a partial decay width to the corresponding branching fraction. The only channel where both partial width and branching fraction can be measured, is the leptonic decay. The knowledge of the total width is in turn mandatory to convert theoretical predictions for partial widths into values for measurable branching fractions.

Furthermore, a precise knowledge of the leptonic branching ratio is needed to determine branching ratios for cascade decays between the  $\Upsilon$ -resonances, since such decays are usually measured in exclusive final states, where the lower lying resonance decays to a lepton pair.

In this work we present a measurement of the decay to muon pairs for the  $\Upsilon(1S)$  and the  $\Upsilon(2S)$ . The data was collected from the  $e^+e^-$  storage ring DORIS II at DESY during the years 1983 through 1986 using the Crystal Ball detector.

We measure the branching fraction to muons by analyzing the excess of  $\mu$ -pairs on resonance compared to the continuum  $\mu$ -pair production. A value for the product of the muonic width and the branching fraction to electrons is obtained by fitting the observed  $\mu$ -pair cross-section as a function of the c.m. energy in the region of the respective resonance.

The outline of this thesis is as follows. In Chapter 2 we review the underlying theory. Section 2.1 presents the basic ideas of today's "Standard Model" of elementary particle physics. The problem of renormalization is addressed for QED and QCD in Section 2.2. As an example for renormalization scheme dependence of QCD predictions the above mentioned ratio of  $\Gamma_{ggg}/\Gamma_{\mu\mu}$  of the  $\Upsilon$  states will be discussed. Section 2.3 deals with the process  $ee \rightarrow \mu\mu$ . We study radiative corrections to this process as well as interference effects between the resonance production and the continuum process. In addition we discuss their modeling by Monte Carlo event generators and describe special modifications of the event generator used in our analysis. Finally, Section 2.4 treats the process  $e^+e^- \rightarrow e^+e^-$ , which is used for the luminosity measurement.

Chapter 3 describes the experimental setup and its simulation by Monte Carlo (MC) techniques. Details of the MC simulation, however, which we have developed to precisely model the response of the tracking chamber and the calorimeter, are presented in the appendix.

Chapter 4 treats the data selection, the luminosity measurement, and the beam energy determination. It is shown, why the interference between continuum and resonance requires a precise knowledge of the c.m. energy. Details of the determination of this energy scale with the help of the multihadronic cross-section are again given in the appendix. We describe the selection of luminosity events, multihadronic events, and  $\mu$ -pair events.

The continuum background in our  $\mu$ -pair sample is studied and subtracted in Chapter 5 to obtain the observed cross-section for resonance decays to muons. We thoroughly investigate a bunch of systematic error sources connected with this subtraction, since the analysis heavily relies on a correct reproduction of acceptance changes between on- and off-resonance data.

The method of extracting  $B_{\mu\mu}$  and  $\Gamma_{\mu\mu}B_{e\epsilon}$  from the measured event numbers and cross-sections is explained in Chapter 6 and the results are given. It is studied, whether we need the interference term in the cross-section to describe the measured data.

Finally, Chapter 7 contains the discussion of our results and compares them to those of other experiments. We check whether the  $B_{\mu\mu}$  value for the  $\Upsilon(1S)$  is consistent with that of the  $\Upsilon(2S)$  and whether it can be scaled to the  $J/\psi$ . A value for the muonic width of the  $\Upsilon(1S)$  is obtained and compared to the electronic width. The total widths of the  $\Upsilon(1S)$  and  $\Upsilon(2S)$  resonances are determined. At the end of this chapter we derive values for the QCD scale parameter  $\Lambda$  and the strong coupling constant  $\alpha_s$  from our result on  $B_{\mu\mu}$  of the  $\Upsilon(1S)$ . The dependence of these numbers on the renormalization scheme is discussed.

In Chapter 8 the results are summarized and conclusions are presented.

# Chapter 2

## Theoretical Fundamentals

### 2.1 The Standard Model of Elementary Particle Physics

*“So when some fool physicist gives a lecture at UCLA in 1983 and says ‘This is the way it works, and look how wonderfully similar the theories are’, it’s not because Nature is really similar; it’s because the physicists have only been able to think of the same damn thing, over and over again.”*

R.P. Feynman [19](page 149) giving one possible reason why the theories of different forces are similar.

A comprehensive picture of elementary particle physics has emerged from the experimental and theoretical work of the 60’s, 70’s, and 80’s. It is widely accepted and thoroughly tested and therefore called the “Standard Model” (SM). We will outline its basic ideas below<sup>1</sup>.

#### 2.1.1 The Building Blocks of Matter

Table 2.1: Periodic system of the building blocks of matter.

Particles ( $m/\text{GeV}$ )	Generations			$Q$ ( $Q_{em}/e$ )	Forces			
	I	II	III		Grav.	Weak	Emag.	Strong
Leptons	$\nu_e$ ( $< 10^{-8}$ )	$\nu_\mu$ ( $< 2.5 \times 10^{-4}$ )	$\nu_\tau$ ( $< 0.03$ )	0	x	x		
	$e$ ( $5 \times 10^{-4}$ )	$\mu$ (0.1)	$\tau$ (1.8)	-1	x	x	x	
Quarks	$u$ ( $5 \times 10^{-3}$ )	$c$ (1.3)	$t$ (140)	2/3	x	x	x	x
	$d$ ( $9 \times 10^{-3}$ )	$s$ (0.2)	$b$ (5)	-1/3	x	x	x	x

The building blocks of matter are spin-1/2 fermions which are point-like down to a scale of  $10^{-18}\text{m}$ . They can be ordered in a “periodic system”, horizontally in groups of equal electromagnetic charge  $Q_{em} = Q \cdot e$ , and vertically in generations (Table 2.1). The higher generations essentially iterate the properties of the first generation at higher particle masses. The number of generations is not predicted in the SM. It has been shown recently [21] that the number of light neutrino generations ( $m_\nu < 45 \text{ GeV}$ ) is exactly three.

Neutrinos are the particles of lowest mass in each generation, and it is still an open question, if they are in fact massless. The properties of the  $\tau$ -neutrino are inferred from  $\tau$

<sup>1</sup>Section 2.1 follows, in parts, the synopsis given by W. Majerotto [20].

decays. Up to the present no reaction induced by a  $\nu_\tau$  has been observed. Together with the three charged particles  $e$ ,  $\mu$ , and  $\tau$  the neutrinos build up the family of leptons, which does not participate in the strong interaction.

The family of quarks consists of the 6 flavors up, down, strange, charm, bottom, and top. There exists only indirect evidence for the top quark constraining its mass with a precision of about 35 GeV [6]. The symmetry between quarks and leptons, and the mass pattern, also shown in Table 2.1, cannot be explained in the framework of the SM.

### 2.1.2 The Forces

As indicated in Table 2.1, four types of forces act between the fundamental particles: gravitation, the weak, the electromagnetic, and the strong interaction. The gravitation cannot yet be included in the SM, since a consistent quantum theory of gravitation is missing. Unified models including gravitation, like Supergravity or Superstring Theories, are beyond the scope of present experiments.

Formally, the remaining three forces arise from requiring local gauge symmetry of the underlying Lagrangian, namely the symmetry under the gauge group  $SU(3)_C \times SU(2)_L \times U(1)_Y$  (see Table 2.2). The local gauge invariance of the Lagrangian is achieved by adding a “minimal substitution” term in the covariant derivative, which consists of a product of coupling strength, group generators, and gauge fields.

Table 2.2: Gauge symmetry structure of the forces.

The left-right arrow indicates the mixing in the GSW-Model. The term in square brackets is valid for the  $Z^0$ , only.

Local Gauge Symmetry	Minimal Subst.	Coupling Constant	Vector Bosons	Force	
GSW-Model	$\left\{ \begin{array}{l} SU(2)_L \\ U(1)_Y \end{array} \right.$	$\left. \begin{array}{l} \alpha_w = (g^2[+g'^2])/4\pi \\ \alpha_{em} = e^2/4\pi \\ \alpha_s = g_s^2/4\pi \end{array} \right\} \xleftrightarrow{\theta_W} \left\{ \begin{array}{l} \alpha_w = (g^2[+g'^2])/4\pi \\ \alpha_{em} = e^2/4\pi \\ \alpha_s = g_s^2/4\pi \end{array} \right.$	$W^+W^-Z^0$	weak	
QCD	$SU(3)_C$		$\frac{g}{2}\vec{\tau}\vec{W}^\mu$	$\gamma$	elmag.
			$\frac{g}{2}YB^\mu$	$g_1, \dots, g_8$	strong

The symmetry group  $SU(2)_L \times U(1)_Y$  describes the electroweak interaction (Glashow-Salam-Weinberg (GSW) Model). The group  $SU(2)_L$  denotes transformations in the space of the weak isospin  $I^w$  of lefthanded ( $L$ ) fermion doublets and has three generators, e.g. the Pauli matrices  $\tau_i$ ,  $i=1,2,3$ . The corresponding quanta of the gauge fields introduced by requiring local gauge invariance of the Lagrangian are the three vector bosons  $W^+$ ,  $W^-$ , and  $W^0$ . The  $U(1)_Y$  group describes phase transformations with the weak hypercharge,  $Y^w = 2(Q - I_3^w)$ , acting as a generator. This implies one gauge boson  $B$ . The  $SU(2)_L$  bosons  $W$  only couple to left-handed fermions, whereas the  $B$  boson couples to the weak hypercharge, i.e. all fermions (except hypothetical right-handed neutrinos). The observed neutral vector bosons, the photon  $\gamma$  and the neutral weak boson  $Z^0$ , are linear combinations of  $B$  and  $W^0$ , such that the photon does not couple to neutrinos. The mixing angle is called Weinberg angle  $\theta_W$ . It relates the coupling strengths  $g$  and  $g'$  and thereby defines the electromagnetic coupling  $e$  via

$$e \equiv g \sin \theta_W = g' \cos \theta_W. \quad (2.1)$$

Its value is  $\sin^2 \theta_W = 0.226 \pm 0.005$  [22]. Due to this mixing, only the charged weak currents ( $W^+, W^-$ ) maintain the V-A coupling, i.e. the coupling to left-handed fermions, only. The coupling of the neutral weak current ( $Z^0$ ) depends on the charge and weak isospin of the fermions.

The group  $SU(3)_C$  is the symmetry of Quantum Chromo Dynamics (QCD) describing the strong interaction. It has 8 generators, e.g. the Gell-Mann matrices  $\lambda_i$ ,  $i=1, \dots, 8$  and is embedded in the space of the three quark colors ( $C$ ): red ( $r$ ), blue ( $b$ ), and green ( $g$ ). Again, the quest for local gauge invariance gives rise to 8 gauge bosons, the gluons.

The algebras  $SU(2)$  and  $SU(3)$  are non-abelian. To maintain gauge invariance, the field strength tensor must include terms which lead to a self-coupling among 3 or 4 gauge bosons. Thus, the gauge bosons themselves carry the charge of the corresponding interaction. The  $U(1)$  group is abelian, and therefore the photon does not couple to itself. Since both, the photon and the  $Z^0$ , have  $Y^w = I_3^w = 0$ , neither  $\gamma-Z^0$ , nor  $Z^0-Z^0$  couplings exist.

The range  $r$  of the forces is related to the mass  $m$  of the mediating bosons via  $r \sim 1/m$  ( $\hbar=c=1$ ). Therefore the weak interaction with  $m \sim 100$  GeV has a very short range of less than  $10^{-2}$  fm, whereas the electromagnetic force ( $m=0$ ) is of infinite range. In principle, also the strong force should have infinite range because the gluons are massless. However, all free particles are  $SU(3)_C$  singlets due to the confinement mechanism (see below). Since the gluons are  $SU(3)_C$  octet bosons, they do not couple to  $SU(3)_C$  singlet states. Thus, the range of the strong force is restricted to the dimensions of strongly bound systems, which is typically 1 fm.

### 2.1.3 The $SU(2) \times U(1) \times SU(3)$ Structure of Fermions

Table 2.3: Multiplet structure and charges with respect to the gauge group  $SU(2)_L \times U(1)_Y \times SU(3)_C$  for the first family of fermions.

The square brackets indicate, that right-handed neutrinos may not exist.

Multiplets	$SU(3)_C$ Singl.	$SU(3)_C$ Triplets			$I_3^w$	$Y_{Singlet}^w$	$Y_{Triplet}^w$
$SU(2)_L$ Doublets	$\begin{pmatrix} \nu_e \\ e \end{pmatrix}_L$	$\begin{pmatrix} u \\ d' \end{pmatrix}_L^r$	$\begin{pmatrix} u \\ d' \end{pmatrix}_L^b$	$\begin{pmatrix} u \\ d' \end{pmatrix}_L^g$	+1/2 -1/2	-1	+1/3
$SU(2)_L$ Singlets	$[\nu_{eR}]$	$u_R^r$	$u_R^b$	$u_R^g$	0	[0]	+4/3
$SU(2)_L$ Singlets	$e_R$	$d_R^r$	$d_R^b$	$d_R^g$	0	-2	-2/3

Each fermion generation has the same multiplet structure with respect to the gauge groups. The properties of the first generation are shown in Table 2.3. the subscripts  $L$  and  $R$  denote the left- and right-handed component of the fermion spinors  $\psi = \psi_L + \psi_R$ , where  $\psi_L = (1 - \gamma_5)\psi/2$  and  $\psi_R = (1 + \gamma_5)\psi/2$ . Right-handed neutrinos would only exist if neutrinos are massive. Grouping left-handed fermions to doublets creates the V-A ( $\sim \gamma_\mu(1 - \gamma_5)$ ) structure of the charged weak current and implies the parity violation of the weak interaction.

The left-handed weak isospin doublets define the weak eigenstates  $d'$ ,  $s'$ , and  $b'$ . The observed mass eigenstates  $d$ ,  $s$ , and  $b$  from Table 2.1 are superpositions of these states. Their relation is given by an unitary matrix, the Cabibbo-Kobayashi-Maskawa matrix  $M_{CKM}$  [23]

$$\begin{pmatrix} d' \\ s' \\ b' \end{pmatrix} = M_{CKM} \begin{pmatrix} d \\ s \\ b \end{pmatrix}. \quad (2.2)$$

This matrix can be parametrized with the help of three angles  $\cos \theta_{ij}$ , describing the mixing of the  $i^{th}$  with the  $j^{th}$  generation, and one phase  $\delta_{CP}$ , which is (if a non-integer multiple of  $\pi$ ) responsible for CP-violation. If the weak and the mass eigenstates were identical, no transitions between different quark flavors would be possible.

### 2.1.4 The Masses

Exact local gauge invariance would require all gauge bosons to be massless. Additionally, exact  $SU(2)_L$  symmetry is only possible for massless fermions. On the other hand, for the  $SU(3)_C$  symmetry of the strong interaction the fermion masses do not cause problems. Thus, the fermion and weak gauge boson masses have to be accommodated within the electroweak  $SU(2)_L \times U(1)_Y$  theory. The standard way is to introduce a spontaneous symmetry breaking of the ground state (vacuum), termed Higgs-mechanism [24], in a formalism extended to non-abelian groups by Kibble [25]. The minimal Higgs model introduces one complex isospin doublet of scalar Higgs fields. Three of its components create mass terms for the  $W^+$ ,  $W^-$ , and  $Z^0$ , whereas the 4<sup>th</sup> component shows up as a massive scalar, the Higgs particle. It has not yet been found, and its mass is highly uncertain. Recent work [26,6] has managed to constrain its mass to  $44 \text{ GeV} < m_H < 1000 \text{ GeV}$ .

The fermion masses arise from their Yukawa couplings to the Higgs field. Since this coupling has to be proportional to the fermion mass, there are as many coupling constants as different quark and lepton masses exist.

### 2.1.5 Open Questions

*“What is the connection between physics and life?”*

Most urgent question in physics, as felt by approximately every fifth student, but by not a single one of about 200 “grown-up” theorists and experimentalists, in a survey at CERN [27].

In the SM, there is no relationship between the  $SU(3)_C$  symmetry and the  $SU(2)_L \times U(1)_Y$  symmetry, between their gauge bosons, or between their coupling constants, i.e. there is yet no “unification” of these forces. In addition, the weak and electromagnetic forces are only partially unified. There are still two separate interactions, expressed in two coupling constants. They are related to each other via the Weinberg angle (cf. Eq. 2.1), whose value is not predicted by the SM. Thus, a real unification of the forces (even without gravitation) is still a pending problem.

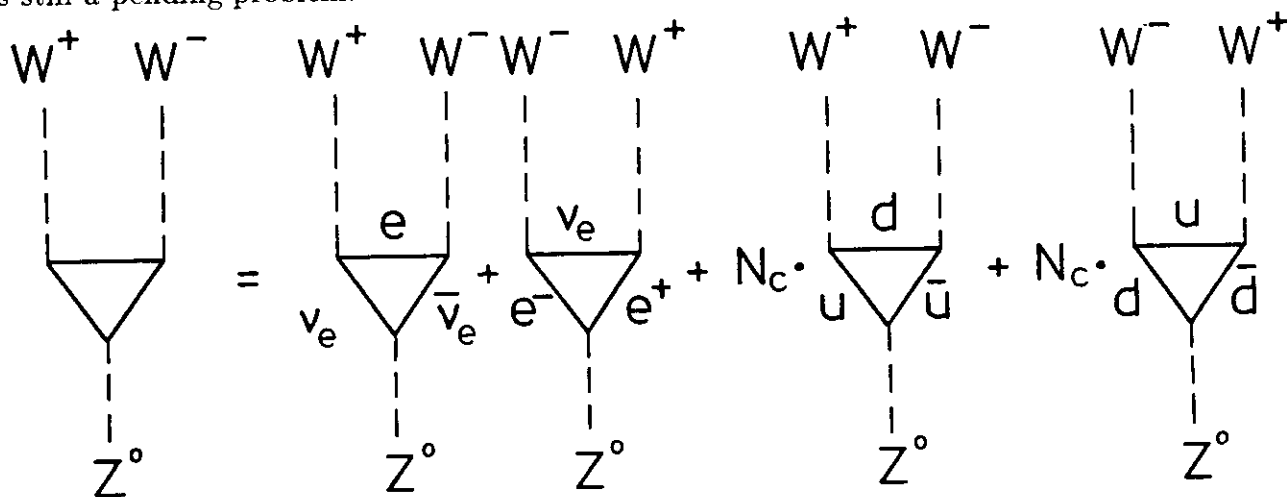


Figure 2.1: Triangle graphs in the GSW-Model.

It can be inferred from renormalization arguments, that there may be links between QCD and the GSW-Model, respectively between quarks and leptons. Triangle graphs like those in



Figure 2.1 would lead to non-renormalizable divergencies unless  $\sum_{\text{quarks, leptons}} Q = 0$ . Given identical numbers of lepton and quark generations, this leads to  $N_C(Q_u + Q_d) = -Q_e$ , i.e.  $N_C = 3$ . Thus, electric quark charge and the number of colors  $N_C$  may be linked through a yet undiscovered symmetry. On the other hand, given 3 colors, the above equation requires identical numbers of quark and lepton families, which may also be a hint to new symmetries.

A unified theory should also reduce the large number of free parameters in the SM. Whereas the  $SU(3)_C$  part has only one free parameter, namely the coupling constant  $\alpha_s$ , the electroweak part has 2 coupling constants, 2 free parameters in a minimal Higgs sector, 6 corresponding Yukawa couplings of the quarks to the Higgs field (the quark masses), and 4 CKM mixing parameters. If neutrinos have a Dirac mass, analogously 6 lepton Yukawa couplings and 4 lepton mixing parameters will enter the theory. For massless neutrinos, as assumed in the minimal standard model, no neutrino mixing is possible, and the Yukawa couplings of the 3 charged leptons are left. Thus there are at least 18 free parameters in the SM, which are listed in Table 2.4.

Table 2.4: *The 18 free parameters of the minimal standard model. The quarks masses and the value of  $\delta_{CP}$  are typical numbers given in the literature. All other parameters have been taken from Ref. [22].*

$\alpha_s$ ( $ q  = 5 \text{ GeV}$ )	$\alpha_{em}^{-1}$ ( $ q  = 0$ )	$G_F$ ( $\text{TeV}^{-2}$ )	$m_Z$ ( $\text{GeV}$ )	$m_H$ ( $\text{GeV}$ )	$\sin \theta_{12}$	$\sin \theta_{23}$	$\sin \theta_{13}$	$\delta_{CP}$
0.19 $\pm 0.03$	137.035990 $\pm 0.000006$	11.6637 $\pm 0.0002$	91.16 $\pm 0.03$	$> 44$ $< 1000$	0.220 $\pm 0.003$	0.046 $\pm 0.016$	0.004 $\pm 0.003$	$90^\circ$ $\pm 40^\circ$
$m_e$ ( $\text{keV}$ )	$m_\mu$ ( $\text{MeV}$ )	$m_\tau$ ( $\text{GeV}$ )	$m_d$ ( $\text{MeV}$ )	$m_u$ ( $\text{MeV}$ )	$m_s$ ( $\text{GeV}$ )	$m_c$ ( $\text{GeV}$ )	$m_b$ ( $\text{GeV}$ )	$m_t$ ( $\text{TeV}$ )
510.9991 $\pm 0.0002$	105.65839 $\pm 0.00003$	1.784 $\pm 0.003$	9 $\pm 2$	5 $\pm 1$	0.19 $\pm 0.02$	1.3 $\pm 0.1$	4.8 $\pm 0.3$	0.14 $\pm 0.04$

Due to relations between  $\alpha_{em}, g, g', G_F$  (the Fermi constant),  $\theta_W, m_Z, m_W$ , and  $\langle \Phi \rangle_{vac}$  (the Higgs field vacuum expectation value) there is some freedom to chose 3 of these parameters, besides the Higgs mass  $m_H$ , in order to cover the electroweak coupling constants and the Higgs sector. We list that set of parameters, which has been most precisely measured, namely  $\alpha_{em}, G_F$ , and  $M_Z$ . It is (on tree level) connected to the more fundamental set  $g, g'$ , and  $\langle \Phi \rangle_{vac}$  via

$$\begin{aligned}
 \alpha_{em} &= \frac{1}{4\pi} \frac{g^2 g'^2}{g^2 + g'^2} \\
 G_F^{-1} &= \sqrt{8} \langle \Phi \rangle_{vac}^2 \\
 m_Z &= \sqrt{\frac{g^2 + g'^2}{2}} \langle \Phi \rangle_{vac}.
 \end{aligned} \tag{2.3}$$

The values of the 18 parameters cannot be derived from the SM. Especially the wide spread of the mass values covering 6 orders of magnitude (even more than 11 orders, if neutrinos are massive) is not understood. The iteration of leptons and quarks in 3 generations remains a mystery.

Thus, in spite of its tremendous success, the SM leaves some important questions open. Today's high energy physics research has two goals. First to further test the SM and pin down its parameters more precisely (especially  $\alpha_s, m_t, m_H, \sin \theta_{ij}$ , and  $\delta_{CP}$ ), and second, to search for physics beyond the SM to obtain a deeper insight into its origin. In this thesis we can make a small contribution to the first item, namely the measurement of  $\alpha_s$ .



## 2.2 Renormalization of Gauge Theories

*“The shell game that we play to find  $m_0$  and  $e_0$  is technically called ‘renormalization’. But no matter how clever the word, it is what I would call a dippy process!”*

R.P. Feynman [19] (page 128).

A crucial feature of any gauge theory is its renormalizability. The absorption of divergencies occurring in the calculation of physical processes is mandatory for perturbative expansions. The other mandatory condition is the smallness of the expansion parameter to guarantee convergence. After Feynman, Tomonaga, and Schwinger [28] the calculations in modern gauge theories are expansions in terms of the coupling constant. Each subprocess of a given coupling constant power can be illustrated as a Feynman diagram, which is evaluated following certain rules.

The basic idea of renormalization is the interpretation of mass, couplings, and fields in the Lagrangian as to be “bare” quantities. These bare quantities are not measurable and can be infinite. They are hidden through higher order processes resulting in effective masses and couplings, which are the physically measurable quantities. A renormalization procedure defines, how to modify the Lagrangian through local counterterms to obtain finite values for certain divergent Feynman diagrams. After the renormalization, the remaining diagrams are free from serious divergencies order by order in perturbation theory. To maintain the predictive power of the theory, the renormalization scheme must be a “systematic and unambiguously fixed algorithm” [29], which satisfies the fundamental properties of locality, causality, and unitarity.

In the following we will discuss the renormalization of the coupling constants in QED and QCD.

### 2.2.1 Renormalization in QED

In the following we will discuss the renormalization of the electromagnetic photon-electron coupling, which is shown in Figure 2.2 together with its one-loop corrections.

The Feynman rules demand to integrate each loop over the inner 4-momentum vector  $k$ ,

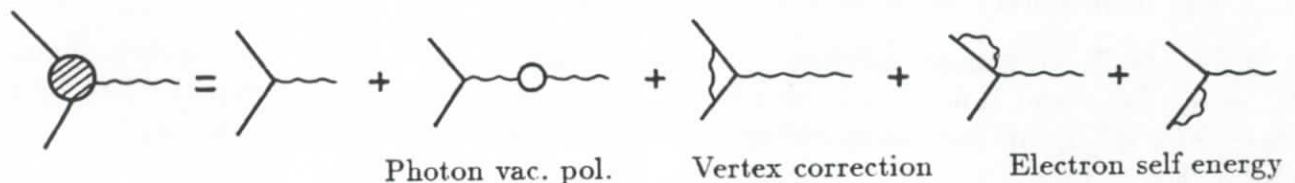


Figure 2.2: The photon-electron coupling and its 1-loop corrections. Loop contributions to external particles on their mass shell receive an extra factor  $1/2$  in the summation, which is not explicitly listed here.

which is not fixed by momentum conservation (see Fig. 2.3). These integrals are logarithmically divergent for  $|k| \rightarrow \infty$  (UV divergence), and have to be renormalized. The vertex correction and the electron self energy in addition diverge for  $k_0 \rightarrow 0$  (IR divergence). If all external particles are on their mass shell, both divergencies from the vertex correction and the electron self energy cancel due to the QED Ward identities [30]. In this case we are left

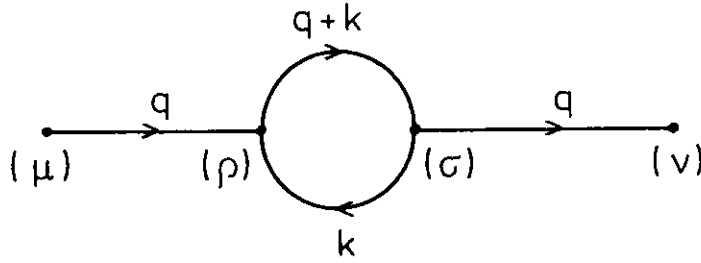


Figure 2.3: The flow of 4-momenta in a loop diagram.

with the divergence of the photon vacuum polarization diagram. The amplitude  $\mathcal{M}_{\mu\nu}$  for this diagram can be evaluated from the Feynman rules as [31]

$$\mathcal{M}_{\mu\nu} = \text{---}\gamma\text{---} \begin{array}{c} \uparrow \\ \text{f} \\ \circ \\ \downarrow \\ \bar{\text{f}} \end{array} \text{---}\gamma\text{---} = D_{\mu\rho}^{(0)}(-i\Sigma^{\rho\sigma})D_{\sigma\nu}^{(0)}, \quad (2.4)$$

where the tree level photon propagator  $D_{\alpha\beta}^{(0)}$  is defined in the Feynman gauge (omitting the usual  $+i\delta$  term in the denominator) as

$$D_{\alpha\beta}^{(0)} = -\frac{ig_{\alpha\beta}}{q^2}, \quad (2.5)$$

with  $g_{\alpha\beta}$  being the metric tensor. The tensor integral  $\Sigma^{\rho\sigma}$  is given by

$$-i\Sigma^{\rho\sigma} = (-1)\text{Tr} \int \frac{d^4k}{(2\pi)^4} \frac{i}{\not{k} + \not{q} - m_f} iQ_f e\gamma^\rho \frac{i}{\not{k} - m_f} iQ_f e\gamma^\sigma, \quad (2.6)$$

where  $m_f$  is the mass of the fermion inside the loop, and  $Q_f$  its electric charge in units of  $e$ .

The renormalization procedure now comprises three steps.

1. The *regularization*, i.e. the redefinition of the integrals, such that they become mathematically well defined objects.
2. The renormalization *prescription*, i.e. a strategy, how to remove the now well-defined divergencies.
3. The momentum *scale*, at which the renormalization is performed.

A choice of a Renormalization Scheme (RS) is defined by a choice for each of the three items. Following Duke and Roberts [32] we will call a Renormalization Convention (RC) to be a choice of a RS up to, but not including a choice of scale. Hence, a RS is made up by a RC plus a choice of scale.

## Regularization

The most widely used regularization procedure is that of dimensional regularization [33]. The Feynman integrals are evaluated in a space-time dimension  $D = 4 - \epsilon$  slightly less than 4. To keep the multiplying (bare) coupling constant dimensionless, an arbitrary (positive) scale parameter  $\mu$  has to be introduced via

$$\int \frac{d^4k}{(2\pi)^4} \longrightarrow \mu^\epsilon \int \frac{d^{4-\epsilon}k}{(2\pi)^{4-\epsilon}}.$$

At the end of the calculation, the limit  $\epsilon \rightarrow 0$  is performed.

Applying dimensional regularization, the tensor integral  $\Sigma^{\rho\sigma}$  from Eq. (2.6) can be decomposed [31] into a scalar integral  $\Sigma$  and a Lorentz tensor part  $\propto \Sigma_L$  according to

$$\Sigma^{\rho\sigma} = g^{\rho\sigma}\Sigma + q^\rho q^\sigma \Sigma_L. \quad (2.7)$$

Since the latter term is  $\propto q^\rho q^\sigma$ , it does not contribute to physical matrix elements due to current conservation, and the photon propagator on the one-loop level can be written as

$$D_{\mu\nu}^{(1)} = \text{---} + \text{---} \bigcirc \text{---} = -ig_{\mu\nu} \left( \frac{1}{q^2} - \frac{1}{q^2} \Sigma(q^2) \frac{1}{q^2} \right) \quad (2.8)$$

$$\equiv D_{\mu\nu}^{(0)}(1 + \Pi_0(q^2)).$$

The quantity  $\Pi_0(q^2) \equiv -\Sigma(q^2)/q^2$  is called unrenormalized photon vacuum polarization. In the two physically most important limits it can be written as

$$\Pi_0(q^2) = \frac{Q_f^2 \epsilon^2}{12\pi^2} \left( -\frac{2}{\epsilon} + \gamma_E - \ln 4\pi + \ln \frac{m_f^2}{\mu^2} \left\{ \begin{array}{l} -\frac{q^2}{5m_f^2} \quad \text{for } |q^2| \ll m_f^2 \\ +\ln \frac{|q^2|}{m_f^2} - \frac{5}{3} - i\pi\theta(q^2) \quad \text{for } |q^2| \gg m_f^2 \end{array} \right\} \right). \quad (2.9)$$

Here  $\gamma_E$  is the Euler constant and  $\theta$  is the Heaviside function. The expression for  $\Pi_0(q^2)$  diverges for  $\epsilon \rightarrow 0$ , and depends on the arbitrary parameter  $\mu$ .

### Renormalization Prescriptions

All renormalization prescriptions interpret  $\epsilon$  in the Lagrange density as a bare charge  $\epsilon_0$ . This bare charge is defined such that in the sum of all diagrams up to a given loop level the divergencies are cancelled through an (infinite) counterterm  $\delta\epsilon$ , i.e.

$$\epsilon_0 = \epsilon + \delta\epsilon. \quad (2.10)$$

E.g. the divergence of Eq. (2.9) is cancelled in a 1-loop renormalization of the photon propagator by those terms in the tree level amplitude, which contain the counterterm  $\delta\epsilon$ . It is the definition of this counterterm, where the various renormalization prescriptions differ.

**Minimal Subtraction** The Minimal Subtraction (MS) prescription [33] defines the counterterm  $\delta\epsilon$  such that only the  $2/\epsilon$  pole in Eq. (2.9) is removed after renormalization.

**Modified Minimal Subtraction** In principle, any other finite terms can be subtracted in addition to the  $2/\epsilon$  pole. Thus, there are an infinite number of modified minimal subtraction prescriptions. The most widely used, the so called  $\overline{\text{MS}}$ -prescription [34], subtracts in addition the quantity  $\gamma_E - \ln 4\pi$ , which is an artefact of dimensional regularization. This term arises from the analytic continuation of the 4-dimensional integral to  $4 - \epsilon$  dimensions with the help of  $\Gamma$ -functions. The  $\overline{\text{MS}}$  prescription generally leads to perturbation expansions which behave better for physical processes than the MS-prescription.

**Momentum Subtraction** Momentum-space subtraction (MOM prescription) [35] absorbs a complete set of radiative corrections to a given vertex at a typical 4-momentum  $q_0^2$  into the definition of the counterterms. The choice of the type of vertex and of the 4-momentum depends on the process under study.

The standard renormalization prescription applied in QED is the MOM mass-shell subtraction. Here, the radiative corrections to the electron-photon vertex are required to vanish for particles on their mass shell. In this prescription, the low-energy limit of Thomson scattering is equal to the Born term through all orders of perturbation theory, and its coupling constant is given by<sup>2</sup>  $\alpha = e^2/4\pi = (137.035990(6))^{-1}$ .

In the following we denote a RS by the superscript “RC, scale”, e.g. the MOM-subtraction as “MOM, $q_0^2$ ”. The 1-loop counterterm for the renormalization of the photon vacuum polarization reads in the MOM mass-shell subtraction ( $q_0^2 = 0$ )

$$\delta e^{\text{MOM},0} = -\frac{1}{2}e\Pi_0(0). \quad (2.11)$$

This can, for example, be verified for the renormalized amplitude for the annihilation process of two charged leptons

$$\begin{aligned} \mathcal{M} &= \begin{array}{c} \ell_i^+(p_2) \\ \ell_i^-(p_1) \end{array} \begin{array}{c} \diagup \\ \diagdown \end{array} \begin{array}{c} \diagdown \\ \diagup \end{array} \begin{array}{c} \ell_f^+(p_4) \\ \ell_f^-(p_3) \end{array} + \begin{array}{c} \diagup \\ \diagdown \end{array} \begin{array}{c} \diagdown \\ \diagup \end{array} \begin{array}{c} \diagdown \\ \diagup \end{array} \begin{array}{c} \diagup \\ \diagdown \end{array} \\ &= \bar{v}_{\ell_i^+}(p_2) i e_0 \gamma^\mu u_{\ell_i^-}(p_1) D_{\mu\nu}^{(1)}(q^2) \bar{u}_{\ell_f^-}(p_3) i e_0 \gamma^\nu v_{\ell_f^+}(p_4), \end{aligned} \quad (2.12)$$

where  $q = p_1 + p_2 = p_3 + p_4$  and  $u, v$  and  $\bar{u}, \bar{v}$  are the fermion spinors and their adjoints, respectively. Inserting Eq. (2.9) for the photon propagator yields a factor  $e_0^2(1 + \Pi_0(q^2))$  in the resulting amplitude. The recipe is, to formally perform a perturbative expansion also in  $\delta e$  or equivalently in  $\Pi_0$ , yielding with Eqs. (2.10) and (2.11)

$$\begin{aligned} \mathcal{M} \propto e_0^2(1 + \Pi_0(q^2)) &= e^2(1 - \frac{1}{2}\Pi_0(0))^2(1 + \Pi_0(q^2)) \\ &= e^2(1 + \Pi_0(q^2) - \Pi_0(0) + \dots) \\ &\equiv e^2(1 + \Pi^{\text{MOM},0}(q^2)). \end{aligned} \quad (2.13)$$

The quantity

$$\Pi^{\text{MOM},q_0^2}(q^2) \equiv \Pi_0(q^2) - \Pi_0(q_0^2) \quad (2.14)$$

is called renormalized photon vacuum polarization. As can be seen from Eq. (2.9) it is now finite and for  $q_0^2 = 0$  given by<sup>3</sup>

$$\Pi^{\text{MOM},0}(q^2) = Q_f^2 \frac{\alpha}{3\pi} \cdot \begin{cases} (-\frac{q^2}{5m_f^2}) & \text{for } |q^2| \ll m_f^2 \\ \ln \frac{|q^2|}{m_f^2} - \frac{5}{3} - i\pi\theta(q^2) & \text{for } |q^2| \gg m_f^2 \end{cases}. \quad (2.15)$$

By construction,  $\Pi^{\text{MOM},0}(0) = 0$ , i.e. it vanishes for real photons. For light fermions ( $m_f^2 \ll |q^2|$ ) inside the loop it logarithmically increases with  $q^2$ . Heavy fermions are suppressed by  $q^2/m_f^2$ . At a given  $q^2$ , the complete vacuum polarization contribution at the 1-loop level is to a good approximation obtained by summing over all fermions with  $m_f^2 \ll |q^2|$ .

$$\Pi_\gamma^{\text{MOM},0}(q^2) = \sum_{m_f^2 \ll |q^2|} Q_f^2 \frac{\alpha}{3\pi} \left( \ln \frac{|q^2|}{m_f^2} - \frac{5}{3} - i\pi\theta(q^2) \right). \quad (2.16)$$

<sup>2</sup>Throughout the theory chapter we use the natural units  $\epsilon_0 = \hbar = c = 1$ .

<sup>3</sup>The complete formula for all values of  $q^2$  can e.g. be found in Ref. [36].

Usually, the leading logarithmic terms to all orders of  $\alpha$  are included in the renormalization, corresponding to the summation

$$\begin{aligned}
 D_{\mu\nu} &= \text{---} + \text{---} \circ \text{---} + \text{---} \circ \text{---} \circ \text{---} + \text{---} \circ \text{---} \circ \text{---} \circ \text{---} + \dots \\
 &= D_{\mu\nu}^{(0)} \cdot (1 + \Pi_\gamma(q^2) + \Pi_\gamma^2(q^2) + \Pi_\gamma^3(q^2) + \dots) \quad (2.17) \\
 &= D_{\mu\nu}^{(0)} / (1 - \Pi_\gamma(q^2)).
 \end{aligned}$$

The vacuum polarization can either be considered as a correction to the photon propagator (Eq. (2.17)) or to the electric charge. The latter point of view involves the concept of a “running coupling constant”

$$\begin{aligned}
 \alpha_{em}^{\text{MOM}}(q^2) &= \frac{\alpha_{em}^{\text{MOM}}(0)}{(1 - \text{Re}\Pi_\gamma^{\text{MOM},0}(q^2))} \\
 &= \frac{\alpha}{\left(1 - \sum Q_f^2 \frac{\alpha}{3\pi} \left(\ln \frac{|q^2|}{m_f^2} - \frac{5}{3}\right)\right)}, \quad (2.18)
 \end{aligned}$$

i.e. the charge, respectively the coupling constant, increases with rising  $q^2$ . The running coupling constant  $\alpha_{em}^{\text{MOM}}(q^2)$  is related by this formula to  $\alpha_{em}^{\text{MOM}}$  at the renormalization scale  $q_0^2 = 0$ . This reference value  $\alpha_{em}^{\text{MOM}}(0)$  is used as the expansion parameter, although a given process may involve vertices of large  $q^2$ . The Thomson limit mentioned above infers  $\alpha_{em}^{\text{MOM}}(0) = \alpha$ .

The behaviour of  $\alpha_{em}(q^2)$  can be understood from the idea of a cloud of virtual fermion pairs surrounding a charged particle. These pairs are polarized in the electric field and thus screen its bare charge (Fig. 2.4). If the test charge is far away ( $q^2 = 0$ , Thomson limit), we will measure  $\alpha_{em} = \alpha$ . At closer distances, i.e. higher  $q^2$ , the test charge penetrates a part of the cloud and feels a larger charge. The infinite bare charge is not measurable at finite  $q^2$ .

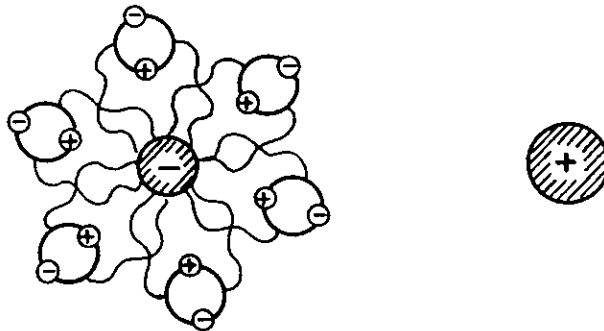


Figure 2.4: The screening of the bare charge.

### Renormalization Scale

Equation (2.9) for the unrenormalized vacuum polarization  $\Pi_0(q^2)$  contains the arbitrary scale parameter  $\mu$ , which was introduced to keep the coupling dimensionless. The “art of choosing  $\mu$ ” is another delicate task in the renormalization procedure. Since the number of higher order processes rapidly increases, theoretical calculations of Feynman amplitudes can cover merely a few low orders completely. However, only if the renormalization procedure is carried out to all orders, the answer of different RS’s to a given problem will be identical. At any finite order of perturbation theory different RS’s will yield different results. The “art of

choosing  $\mu''$  is, to keep the (unknown) higher order corrections small, so that the finite order result only weakly depends on the RS.

In the MOM prescription the ambiguity of  $\mu$  is transferred to the freedom of choosing a physical  $q_0^2$ , where the higher order corrections (calculated up to a finite order) are absorbed e.g. into a reference value of the coupling constant. In QED there is a salient 4-momentum transfer  $q_0^2 = 0$ , the Thomson limit, which is used as a reference scale, and where the coupling constant is finite and precisely measurable. We will see, however, that this is not the case in QCD. In the MS and  $\overline{\text{MS}}$  prescriptions the scale parameter  $\mu$  is basically arbitrary, but generally chosen to be equal to a typical (large) momentum in the process under study. The MS and  $\overline{\text{MS}}$  conventions can thus be more easily transferred to QCD.

Process independent arguments in favor or against various RS's have been extensively discussed in literature [37]. A disadvantage of the MS prescriptions is e.g., that they are bound to dimensional regularization, which is not fully consistent<sup>4</sup>. Also, there is no physical meaning of the scale parameter  $\mu$ , in contrast to  $q_0^2$  being the square of a physical 4-momentum. On the other hand, the MOM prescription can be used with any regularization procedure, but is generally more difficult to handle. Not only  $q_0^2$  but also the vertex, for which the higher order corrections are removed by renormalization, is not fixed. Frequent choices in QCD are e.g. the quark-gluon vertex or alternatively the triple-gluon vertex. MOM off-shell subtraction in addition does not preserve the Ward identities and leads to gauge dependent coupling constants. We will not discuss all these subtleties, but simply summarize, that there is nothing like a correct RS. There may be, however, a RS best suited for a given process. This question will be further addressed in the case of QCD renormalization.

As we will see below, the scales  $\mu^2$  for RC=MS, $\overline{\text{MS}}$  and  $q_0^2$  for RC=MOM enter the running of  $\alpha_{em}^{\text{RC}}(q^2)$  exactly in the same way. We thus use in the following  $\mu^2$  for both scale variables  $\mu^2$  and  $q_0^2$ , keeping in mind, however, the difference in their physical meaning. Having chosen a scale  $\mu^2$  (or  $q_0^2$ ), the coupling constant  $\alpha_{em}^{\text{RC}}(\mu^2)$  serves as expansion parameter and thus as a reference value for the running coupling constant  $\alpha_{em}^{\text{RC}}(q^2)$  according to

$$\alpha_{em}^{\text{RC}}(q^2) = \frac{\alpha_{em}^{\text{RC}}(\mu^2)}{1 - [\Pi_{\gamma}^{\text{RC},\mu^2}(q^2) - \Pi_{\gamma}^{\text{RC},\mu^2}(\mu^2)]} \quad (2.19)$$

$$\equiv \frac{\alpha_{em}^{\text{RC}}(\mu^2)}{1 - \tilde{\Pi}_{\gamma}^{\mu^2}(q^2)}. \quad (2.20)$$

(Setting in Eq. (2.19) RC=MOM and  $\mu^2=q_0^2=0$  recovers Eq. (2.18) for the case of MOM mass-shell subtraction, since Eq. (2.14) implies  $\Pi^{\text{MOM},q_0^2}(q_0^2) = 0$ .)

The 1-loop scaling function for the running coupling constant

$$\tilde{\Pi}_{\gamma}^{\mu^2}(q^2) \equiv \Pi_{\gamma}^{\text{RC},\mu^2}(q^2) - \Pi_{\gamma}^{\text{RC},\mu^2}(\mu^2) \quad (2.21)$$

does, in leading order of  $\alpha_{em}$ , not depend on the RC. For the simple case, where only electron loops contribute to the photon propagator, the identity  $\Pi^{\text{MOM},q_0^2}(q^2) - \Pi^{\text{MOM},q_0^2}(q_0^2) = \Pi^{\overline{\text{MS}},\mu^2}(q^2) - \Pi^{\overline{\text{MS}},\mu^2}(\mu^2)$  for  $q_0^2 = \mu^2$  can be verified with the help of Eqs. (2.14), (2.9), and Eq. (2.22) below. It illustrates the above mentioned equivalence of  $\mu^2$  and  $q_0^2$  for the definition of the running coupling constant.

Another interesting equivalence is the coincidence of next-to-leading-order expansion coefficients of  $\alpha_{em}^{\text{RC}}(\mu^2)$  for different RC's at a suitable choice of scale. For the process of Eq. (2.12), the expansion coefficients of the Feynman amplitude  $\mathcal{M}$  (Eq. (2.13)) in terms of  $\alpha_{em}^{\text{RC}}(\mu^2)$  are

<sup>4</sup>Since  $\gamma_5$  cannot be analytically continued into  $4 - \epsilon$  dimensions, problems with chirality arise in dimensional regularization.

determined by  $\Pi^{\text{RC},\mu^2}(q^2)$ . Comparing the electron-loop contribution to the photon vacuum polarization renormalized in the  $\overline{\text{MS}}$  scheme

$$\Pi^{\overline{\text{MS}},\mu^2}(q^2) = Q_f^2 \frac{\alpha_{em}^{\overline{\text{MS}}}(\mu^2)}{3\pi} \cdot \begin{cases} \ln \frac{m_e^2}{\mu^2} - \frac{q^2}{5m_e^2} & \text{for } |q^2| \ll m_e^2 \\ \ln \frac{|q^2|}{\mu^2} - \frac{5}{3} - i\pi\theta(q^2) & \text{for } |q^2| \gg m_e^2 \end{cases} \quad (2.22)$$

to the corresponding expressions for MOM mass-shell renormalization (Eq. (2.15)), and to the analog  $\overline{\text{MS}}$  expression (not listed explicitly), we find the identity

$$\Pi^{\text{MOM},0}(q^2) = \Pi^{\overline{\text{MS}},m_e^2}(q^2) = \Pi^{\text{MS},m_e^2 \exp(\gamma_E)/4\pi}(q^2). \quad (2.23)$$

This shows, that the next-to-leading-order coefficients are identical in different RC's for all values of  $q^2$ , if the respective renormalization is performed at a suitable scale. Having the same coefficients for an expansion in the parameter  $\alpha_{em}^{\text{RC}}(\mu^2)$  leads to the same results for the coupling constant, i.e.

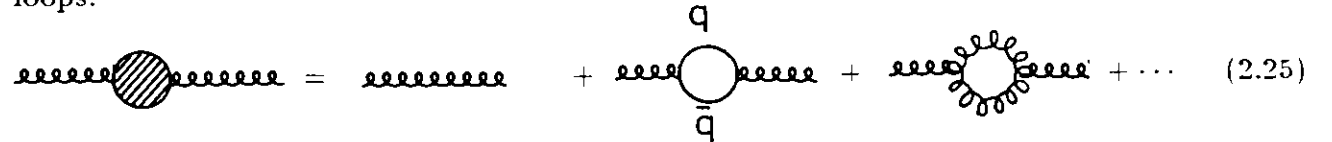
$$\alpha_{em}^{\text{MOM}}(0) = \alpha_{em}^{\overline{\text{MS}}}(m_e^2) = \alpha_{em}^{\text{MS}}(m_e^2 \exp(\gamma_E)/4\pi), \quad (2.24)$$

however, at different scales  $q^2 = \mu^2$ . In spite of different values of  $\alpha_{em}^{\text{RC}}(q^2)$  in different RC's (cf. Eq. (2.20)) we thus obtain identical predictions for a given process, if we chose the renormalization scale according to Eq. (2.23). All the above mentioned facts will become more transparent with the explicit QCD examples in the next section.

In the MOM mass-shell renormalization, generally applied in QED, all expansions are performed in terms of  $\alpha = \alpha_{em}^{\text{MOM}}(0)$ , i.e. at the same scale  $\mu^2=0$  for all processes. The running of  $\alpha$  is hidden in the expansion coefficients, and the same coupling constant  $\alpha$  is measured in all processes, regardless of their  $q^2$ . If each process on the other hand is renormalized at its own  $\mu^2$ , as in QCD, the running of the coupling constant  $\alpha_s(\mu^2)$  can be explicitly measured.

### 2.2.2 Renormalization in QCD

The 1-loop renormalization of the gluon propagator in QCD works similar to the 1-loop renormalization of the photon propagator in QED. The only difference are additional gluon loops.



$$\text{gluon line with blob} = \text{gluon line} + \text{gluon loop} + \text{ghost loop} + \dots \quad (2.25)$$

The renormalization of the gluon vacuum polarization leads to a 1-loop scaling function for the running of  $\alpha_s$ , (cf. Eq. (2.21))

$$\tilde{\Pi}_g^{\mu^2}(q^2) = \frac{2}{3} n_F \frac{\alpha_s^{\text{RC}}(\mu^2)}{4\pi} \ln \frac{|q^2|}{\mu^2} - 11 \frac{\alpha_s^{\text{RC}}(\mu^2)}{4\pi} \ln \frac{|q^2|}{\mu^2},$$

where the first term comes from the quark loops and the second one arises from the gluon loops,  $n_F$  denotes the number of quark flavors with  $m_q < \mu$  (by convention not  $2m_q < \mu$ !), and  $\mu$  is the arbitrary renormalization scale. The quark loop term leads to a color charge screening just like the fermion loops in QED leads to a screening of the electromagnetic charge. The gluon loop contribution, however, has the opposite sign, indicating, that a given color charge is increased by the color field of the virtual gluon loops. Analogously to QED (Eq. (2.20))

the strong coupling constant  $\alpha_s^{\text{RC}}(q^2)$  can now be expressed in 1-loop renormalization with respect to a reference scale  $\mu^2$

$$\begin{aligned}\alpha_s^{\text{RC}}(q^2) &= \frac{\alpha_s^{\text{RC}}(\mu^2)}{1 - \bar{\Pi}_g^2(q^2)} \\ &= \frac{\alpha_s^{\text{RC}}(\mu^2)}{1 + \beta_0 \frac{\alpha_s^{\text{RC}}(\mu^2)}{4\pi} \ln \frac{|q^2|}{\mu^2}},\end{aligned}\quad (2.26)$$

where  $\beta_0 \equiv 11 - \frac{2}{3}n_F$ . Equation (2.26) only holds, if no flavor threshold is opened between  $\mu^2$  and  $q^2$ , that means for constant  $n_F$ . If  $\beta_0 > 0$ , i.e.  $n_F < 16.5$ , the gluon loops dominate over the quark loops. Assuming the number of quark generations to be three (as indicated by the number of light neutrino generations), we have  $n_F \leq 6$  for all  $q^2$ . Thus, in contrast to QED, the QCD coupling constant increases with decreasing  $q^2$ , i.e. increasing distances. For small  $q^2$  approaching a value  $\Lambda^2$  given by

$$\Lambda^{\text{RC}2} = \mu^2 \exp\left(-\frac{4\pi}{\beta_0 \alpha_s^{\text{RC}}(\mu^2)}\right), \quad (2.27)$$

Eq. (2.26) even leads to a infinite value of  $\alpha_s$ . On the other hand,  $\alpha_s$  decreases logarithmically at small distances, i.e.  $\alpha_s(q^2 \rightarrow \infty) = 0$ . Thus, quarks and gluons can move essentially freely within a bound state of small enough radius (asymptotic freedom), but they cannot be separated from each other and observed as single free particles (confinement). At very low  $q^2$  a perturbative approach to QCD is not possible, since the coupling constant diverges. This renders the choice of the renormalization scale  $\mu^2$  much more ambiguous than in QED, since a mass-shell renormalization for gluons is not applicable. The MOM renormalization has to be performed at some arbitrary off-shell 4-momentum  $\mu^2 = q_0^2$ , which must be chosen such, that (again unknown) higher order contributions are kept small. Likewise, there is no natural scale  $\mu^2 = \mu_0^2$ , which can act as a reference scale in Eq. (2.26), and which may be used as renormalization scale in the MS and  $\overline{\text{MS}}$  prescriptions.

Due to this ambiguity, any RC and any scale  $\mu^2 = \mu_0^2$  can be used to define the one fundamental parameter of QCD. This parameter  $\alpha_s^{\text{RC}}(\mu_0^2)$  can then be used in Eq. (2.26) to calculate the running of  $\alpha_s^{\text{RC}}(q^2)$ . Instead of relating  $\alpha_s^{\text{RC}}(q^2)$  to an arbitrary reference point  $\mu_0^2$ , the running of  $\alpha_s$  can alternatively expressed by rewriting Eq. (2.27) as

$$\alpha_s^{\text{RC}}(\mu^2) = \frac{4\pi}{\beta_0 \ln \frac{\mu^2}{\Lambda^{\text{RC}2}}}. \quad (2.28)$$

$\Lambda^{\text{RC}}$  then acts as the one fundamental parameter of QCD, replacing  $\alpha_s^{\text{RC}}(\mu_0^2)$ . Again,  $\Lambda^{\text{RC}}$  depends on the RC, but not on the renormalization scale.

Additional complications arise from the dependence of  $\beta_0$  on the number  $n_F$  of quark flavors with  $\mu > m_i$ , ( $i=1, \dots, n_F$ ), where  $m_i$  is the mass of the quark with the  $i^{\text{th}}$  flavor. To retain  $\alpha_s(\mu^2)$  as a smooth function, threshold terms [38] must be added in Eq. (2.26), which again depend on  $\mu^2$ . Alternatively, distinct parameters  $\Lambda_{n_F}^{\text{RC}}$  for each  $n_F$  can be introduced in Eq. (2.28), so that at a flavor threshold

$$\beta_0(n_F=i) \ln \frac{m_{i+1}^2}{\Lambda_i^{\text{RC}2}} = \beta_0(n_F=i+1) \ln \frac{m_{i+1}^2}{\Lambda_{i+1}^{\text{RC}2}}, \quad (2.29)$$

holds. Thus, there is also no unique QCD scale parameter  $\Lambda^{\text{RC}}$  even for a given RC. Since all  $\Lambda_{n_F}^{\text{RC}}$  are related to each other, only one of them has to be given. The standard one is  $\Lambda_4^{\overline{\text{MS}}}$ , because it is currently best determined.



Both 1-loop parametrizations of the running coupling constant  $\alpha_s^{\text{RC}}$ , that from Eq. (2.26) extended by additional threshold terms, and that from Eq. (2.28) with distinct parameters  $\Lambda_{n_F}^{\text{RC}}$ , are equivalent. However, the consistency of measurements of  $\alpha_s^{\text{RC}}$  at different  $q^2 = \mu^2$  can be more conveniently checked by comparing their corresponding  $\Lambda$  parameters. Thus, the determination of this QCD scale parameter has become a standard, although  $\Lambda$  has no physical meaning and could be completely omitted in QCD.

The running of  $\alpha_s$  is still perceptibly modified by corrections beyond 1-loop order, e.g. by graphs like

$$(2.30)$$

In order to compare results on  $\Lambda$  obtained from  $\alpha_s$  measurements at different  $\mu^2$ , the functional dependence  $\alpha_s(\mu^2)$  must be evaluated at least at the 2-loop level.

This is done by exploiting the fact, that the value of an observable  $P(q^2, \alpha_s(\mu^2), \mu^2)$  must not depend on the arbitrary renormalization scale  $\mu^2$ , i.e.

$$\frac{dP}{d\mu^2} = \frac{\partial P}{\partial \mu^2} + \frac{\partial \alpha_s}{\partial \mu^2} \frac{\partial P}{\partial \alpha_s} = 0. \quad (2.31)$$

The partial derivative  $\partial \alpha_s / \partial \mu^2$  defines the renormalization  $\beta$ -function via the Renormalization Group Equation

$$\frac{\partial \alpha_s}{\partial \mu^2} \equiv -\frac{\alpha_s}{\mu^2} \beta(\alpha_s). \quad (2.32)$$

$\beta(\alpha_s)$  can be expanded in a power series of  $\alpha_s^i$ , where  $i + 1$  corresponds to the loop-level of renormalization, according to

$$\beta(\alpha_s) = \frac{\alpha_s}{4\pi} \sum_{i=0}^{\infty} \beta_i \left( \frac{\alpha_s}{4\pi} \right)^i. \quad (2.33)$$

The coefficients  $\beta_i$  are obtained by renormalization group techniques [39] as

$$\begin{aligned} \beta_0 &= 11 - \frac{2}{3} n_F \\ \beta_1 &= 102 - \frac{38}{3} n_F \\ \beta_2^{\overline{\text{MS}}} &= \frac{2857}{2} - \frac{5033}{18} n_F + \frac{325}{54} n_F^2. \end{aligned} \quad (2.34)$$

$\beta_0$  and  $\beta_1$  are independent of the RC, whereas  $\beta_2$  was calculated in the  $\overline{\text{MS}}$  prescription.  $\alpha_s(\mu^2)$  is evaluated from integrating the Renormalization Group Equation (2.32)

$$-\int_{\mu_0^2}^{\mu^2} \frac{d\mu^2}{\mu^2} = \int_{\alpha_s(\mu_0^2)}^{\alpha_s(\mu^2)} \frac{d\alpha_s}{\alpha_s \beta(\alpha_s)}. \quad (2.35)$$

The freedom in choosing the lower integration limit represents the freedom in defining the one fundamental QCD parameter. Selecting a certain  $\mu_0^2$  on the left-hand side of Eq. (2.35) would cause  $\alpha_s(\mu_0^2)$  to become this fundamental parameter. Again, the role of  $\alpha_s(\mu_0^2)$  is generally transferred to  $\Lambda$  by choosing  $\mu_0^2$  such that  $\alpha_s(\mu_0^2 = \Lambda^2) = \infty$  (cf. the discussion above). Solving the integral with the latter choice leads at the 1-loop level ( $\beta(\alpha_s) = \beta_0 \alpha_s / 4\pi$ ) to Eq. (2.28). The result of the 2-loop level is

$$\ln \frac{\mu^2}{\Lambda^2} = \frac{4\pi}{\beta_0 \alpha_s} - \frac{\beta_1}{\beta_0^2} \ln \left( 1 + \frac{\beta_0}{\beta_1} \frac{4\pi}{\alpha_s} \right). \quad (2.36)$$

For  $\alpha_s = 0.2$  and  $n_F = 4$  the 2-loop correction to  $\ln(\mu^2/\Lambda^2)$  due to the second term on the right-hand side of Eq. (2.36) is 24%, and thus  $\Lambda$  itself changes by a factor of  $\exp(0.24 \cdot 2\pi/\beta_0\alpha_s) = 2.5$  !

Rewriting Eq. (2.36) as

$$\alpha_s = \frac{4\pi}{\beta_0 \ln \frac{\mu^2}{\Lambda^2}} \left[ 1 - \frac{\beta_1 \alpha_s}{\beta_0 4\pi} \ln \left( 1 + \frac{\beta_0 4\pi}{\beta_1 \alpha_s} \right) \right] \quad (2.37)$$

and expanding in terms of  $\ln(\ln(\mu^2/\Lambda^2))/\ln(\mu^2/\Lambda^2)$  for  $\mu^2 \gg \Lambda^2$  leads to a functional form for  $\alpha_s$  [22,40]

$$\alpha_s(\mu^2) = \frac{4\pi}{\beta_0 \ln \frac{\mu^2}{\Lambda^2}} \left[ 1 - \frac{\beta_1}{\beta_0^2} \frac{\ln(\ln \frac{\mu^2}{\Lambda^2})}{\ln \frac{\mu^2}{\Lambda^2}} \right]. \quad (2.38)$$

Results for  $\alpha_s$  and  $\Lambda$  obtained from this formula deviate from those of Eq. (2.36) typically by only 1–2% and 3–6%, respectively. A formula for  $\alpha_s$  on the 3-loop level can be found in Ref. [38].

### 2.2.3 Renormalization Scheme Dependence of QCD Predictions

In the following we discuss, how the perturbative calculation of an observable  $P$  in QCD depends on the RS. Perturbative corrections to processes of leading order  $p$  are expressed in a power series of the form

$$P = \left( \frac{\alpha_s}{\pi} \right)^p \left[ 1 + B_1 \frac{\alpha_s}{\pi} + B_2 \left( \frac{\alpha_s}{\pi} \right)^2 + \dots \right]. \quad (2.39)$$

As already discussed in Section 2.2.1, various ultraviolet divergencies in calculating  $B_i$  have to be removed with the help of a RS, i.e. the choice of a RC and a scale  $\mu$ . The application of the renormalization procedure changes the infinite bare coupling constant to a renormalized value  $\alpha_s^{\text{RC}}(\mu)$ , which is then taken as expansion parameter<sup>5</sup>

$$P = \left( \frac{\alpha_s^{\text{RC}}(\mu)}{\pi} \right)^p \left[ 1 + B_1^{\text{RC}}(\mu) \frac{\alpha_s^{\text{RC}}(\mu)}{\pi} + B_2^{\text{RC}}(\mu) \left( \frac{\alpha_s^{\text{RC}}(\mu)}{\pi} \right)^2 + \dots \right]. \quad (2.40)$$

Thus, the expansion coefficients as well as the expansion parameter, the coupling constant, depend on the choice of RS. The renormalizability of QCD [12] ensures that the prediction for  $P$  does not depend on the RS chosen, if the calculation is carried out to all orders in the perturbation series. As all calculations, however, have to stop at finite order  $r$ , the quantity

$$P_r^{\text{RS}} = \left( \frac{\alpha_s^{\text{RC}}(\mu)}{\pi} \right)^p \left[ 1 + \sum_{i=1}^r B_i^{\text{RC}}(\mu) \left( \frac{\alpha_s^{\text{RC}}(\mu)}{\pi} \right)^i \right]. \quad (2.41)$$

will explicitly depend on the RS.

In practical calculations it is obvious to chose that RS, in which the calculations can be most easily performed, which is in QCD the  $\overline{\text{MS}}$  prescription together with an appropriate choice of scale. However, as soon as theoretical calculations  $P_r^{\text{RS}}$  are to be compared to experimental results  $P^{\text{meas}}$ , which intrinsically contain all higher order corrections, one would like to find a best renormalization scheme  $\text{RS}_{\text{opt}}$ , where

$$P_r^{\text{RS}_{\text{opt}}} \approx P^{\text{meas}}, \quad (2.42)$$

<sup>5</sup>In the following we write all equations in terms of  $\mu$  rather than of  $\mu^2$  in order to keep them readable.

i.e. where the sum of all corrections of order larger than  $r$  vanishes, or is at least smaller than the experimental error on  $P$ . Since the higher order corrections are not known, any strategy to find  $RS_{opt}$  involves some guesswork.

In order to discuss some of these “guessworks”, we first study, how  $P$ , changes, if we change the RS. Since most of the available QCD predictions are calculated at the 1-loop level, and the following can be generalized easily to higher orders [32], we will restrict ourselves to  $r = 1$ . We start from a quantity  $P$  of leading order  $p$  in  $\alpha_s$ , which has been calculated in a prescription RC as

$$P_1^{RC,\mu} = \left( \frac{\alpha_s^{RC}(\mu)}{\pi} \right)^p \left[ 1 + B_1^{RC}(\mu) \frac{\alpha_s^{RC}(\mu)}{\pi} \right], \quad (2.43)$$

If we change the RS by keeping RC, but changing the scale to  $\mu'$ , we find from the running of  $\alpha_s$  according to Eq. (2.26)

$$\frac{\alpha_s^{RC}(\mu)}{\pi} = \frac{\alpha_s^{RC}(\mu')}{\pi} \left[ 1 + \frac{\alpha_s^{RC}(\mu')}{\pi} \frac{\beta_0}{2} \ln \frac{\mu}{\mu'} \right]^{-1} \quad (2.44)$$

$$= \frac{\alpha_s^{RC}(\mu')}{\pi} \left[ 1 - \frac{\alpha_s^{RC}(\mu')}{\pi} \frac{\beta_0}{2} \ln \frac{\mu}{\mu'} + \mathcal{O} \left\{ \left( \frac{\alpha_s^{RC}(\mu')}{\pi} \right)^2 \right\} \right]. \quad (2.45)$$

Inserting Eq. (2.45) into Eq. (2.43) yields in next-to-leading order

$$P_1^{RC,\mu'} = \left( \frac{\alpha_s^{RC}(\mu')}{\pi} \right)^p \left[ 1 + \left( B_1^{RC}(\mu) - \frac{p\beta_0}{2} \ln \frac{\mu}{\mu'} \right) \frac{\alpha_s^{RC}(\mu')}{\pi} \right], \quad (2.46)$$

and thus

$$B_1^{RC}(\mu') = B_1^{RC}(\mu) - \frac{p\beta_0}{2} \ln \frac{\mu}{\mu'}. \quad (2.47)$$

Note, that  $B_1^{RC}(\mu') = B_1^{RC}(\mu)$  for  $p = 0$ . This is a special case of the rule, that all RS's have the same coefficient in leading order of  $\alpha_s$ . (Comparing leading-order predictions with experimental results thus yields a value for  $\alpha_s$ , which does not run with the chosen scale  $\mu$ .)

If the RS is changed by going from one RC to another convention RC', while keeping the scale  $\mu$  unchanged, a relation between  $\alpha_s^{RC}(\mu)$  and  $\alpha_s^{RC'}(\mu)$  has to be determined. It can be written as

$$\frac{\alpha_s^{RC}(\mu)}{\pi} = \frac{\alpha_s^{RC'}(\mu)}{\pi} \left[ 1 + v_1^{RC \rightarrow RC'} \frac{\alpha_s^{RC'}(\mu)}{\pi} + v_2^{RC \rightarrow RC'} \left( \frac{\alpha_s^{RC'}(\mu)}{\pi} \right)^2 + \dots \right], \quad (2.48)$$

where the  $v_i$  do *not* depend on  $\mu$ . The first order coefficients  $v_1$  read [41]

$$\begin{aligned} v_1^{\overline{MS} \rightarrow \overline{MS}} &= \frac{\beta_0}{4} (\ln 4\pi - \gamma_E) = 5.373 - 0.3256 n_F \\ v_1^{\overline{MS} \rightarrow \text{MOM}(qqg)} &= \frac{85}{144} J - \frac{47}{48} - \frac{5}{12} \beta_0 = -4.179 + 0.2778 n_F \\ v_1^{\overline{MS} \rightarrow \text{MOM}(3g)} &= \frac{51}{16} J - \left( \frac{1}{2} + \frac{1}{3} J \right) \beta_0 = -6.623 + 0.8542 n_F \\ v_1^{\text{RC} \rightarrow \text{RC}'} &= -v_1^{\text{RC}' \rightarrow \text{RC}}, \end{aligned} \quad (2.49)$$

where  $J$  is defined as

$$J = \frac{4}{\sqrt{3}} \sum_{n=1}^{\infty} \frac{\sin(n\frac{\pi}{3})}{n^2} = 2.344.$$

and MOM(qqg) and MOM(3g) denotes MOM subtraction for the quark-gluon vertex and the 3-gluon vertex<sup>6</sup>, respectively, both performed in Landau gauge. (The expressions for other gauges can be found in Ref. [41].)

By inserting Eq. (2.48) into Eq. (2.43) we obtain

$$B_1^{\text{RC}'(\mu)} = B_1^{\text{RC}(\mu)} + pv_1^{\text{RC} \rightarrow \text{RC}'}. \quad (2.50)$$

Combining both Eqs. (2.47) and (2.50) the relation between the first order coefficients becomes for a change of RC as well as a change of scale

$$B_1^{\text{RC}'(\mu')} = B_1^{\text{RC}(\mu)} + pv_1^{\text{RC} \rightarrow \text{RC}'} - \frac{p\beta_0}{2} \ln \frac{\mu}{\mu'}. \quad (2.51)$$

This transformation has still the form of Eq. (2.47). Thus, a change of RS from  $(\text{RC}, \mu)$  to any  $(\text{RC}', \mu')$  is equivalent to keeping RC and changing only the scale from  $\mu$  to  $\bar{\mu}$ , given by

$$\ln \frac{\bar{\mu}}{\mu'} = \frac{2}{\beta_0} v_1^{\text{RC} \rightarrow \text{RC}'}. \quad (2.52)$$

“Equivalent” means in this context that all numbers in the perturbative expansion of Eq. (2.43) are equal, namely

$$B_1^{\text{RC}'(\mu')} = B_1^{\text{RC}(\bar{\mu})} \quad \text{and} \quad (2.53)$$

$$\alpha_s^{\text{RC}'(\mu')} = \alpha_s^{\text{RC}(\bar{\mu})}. \quad (2.54)$$

Since  $\mu' \neq \bar{\mu}$ , the latter equality again shows, that different RC's lead to different running coupling constants  $\alpha_s^{\text{RC}}$ , i.e. to different QCD scale parameters  $\Lambda^{\text{RC}}$ . As can be seen from Eqs. (2.28) and (2.52), the latter are related to each other by the Celmaster-Gonsalves relation

$$\Lambda_{n_F}^{\text{RC}'} = \Lambda_{n_F}^{\text{RC}} \exp \left( -\frac{2}{\beta_0} v_1^{\text{RC} \rightarrow \text{RC}'} \right). \quad (2.55)$$

Note, that this 1-loop relation is exact to all orders of perturbation theory [41], i.e. it has no higher order corrections depending on  $v_i$ ,  $i > 1$ . Special cases of Eq. (2.55) are

$$\Lambda_4^{\text{MOM}(3g)} = 2.16 \Lambda_4^{\overline{\text{MS}}} \quad (2.56)$$

$$\Lambda_4^{\text{MOM}(qqg)} = 2.66 \Lambda_4^{\overline{\text{MS}}}. \quad (2.57)$$

We now return to our problem, of how to compare a measured quantity  $P^{\text{meas}}$  to its perturbative QCD prediction  $P_1^{\text{RC}, \mu}$ . The usual way is to calculate values for  $\alpha_s^{\text{RC}}(\mu)$  and/or  $\Lambda^{\text{RC}}$  from setting

$$P^{\text{meas}} \stackrel{!}{=} P_1^{\text{RC}, \mu}.$$

If QCD is the correct theory of strong interactions, all measurements, whose predictions are calculable by perturbative QCD, have to lead to consistent values of  $\alpha_s^{\text{RC}}(\mu)$  and  $\Lambda^{\text{RC}}$ , respectively. For each process, an optimal RS has to be found in order to limit the higher order corrections  $\sim [\alpha_s^{\text{RC}}(\mu)(\ln \frac{q^2}{\mu^2} + \dots)]^i$ , where  $q$  is the typical 4-momentum transfer of the process under study. As discussed above, the RS ambiguity can be reduced to the ambiguity of the scale  $\mu$  for any given RC (cf. also the discussion in Section 2.2.1). An optimum scale

<sup>6</sup>To be precise, the symmetric point 3-gluon vertex, where all gluons have the same  $q^2$ .

$\mu_{\text{opt}}$  limits the higher order corrections and thus has to limit  $\alpha_s^{\text{RC}}(\mu)$  as well as  $\ln(q^2/\mu^2)$ . This leads to the conditions

$$\mu_{\text{opt}} \gg \Lambda^{\text{RC}} \quad \text{and} \quad (2.58)$$

$$\mu_{\text{opt}} \sim |q|. \quad (2.59)$$

However, the choice of  $\mu = |q|/5$  may be as appropriate as, say,  $\mu = 2|q|$ . Many refined procedures have been invented in order to shed more light on the question, how to “guess”  $\mu_{\text{opt}}$ . We will outline below the basic ideas of some procedures, which are most widely applied.

**1) Natural scale (NAT)** Choosing the “natural scale” means choosing  $\mu^2 = q^2$  for the renormalization scale, where  $q$  is the typical 4-momentum of the process under study. This choice is widely used in the MOM prescriptions, where higher order corrections to a basic vertex are absorbed in the renormalization at  $q_0^2 = \mu^2$ . Choosing  $q_0^2 = q^2$  should lower the higher order corrections to the calculations [42]. In the MS prescriptions the renormalization scale is less directly related to physical momenta.

**2) Grunberg’s method of Fastest Apparent Convergence (FAC)** Formally, the value of  $\alpha_s$  can cover the full range from  $\alpha_s(\infty) = 0$  to  $\alpha_s(\Lambda) = \infty$ . Thus, it is possible to find a scale  $\mu_{\text{eff}}$  for any observable  $P$ , so that

$$P_{\infty}^{\text{RC}, \mu_{\text{eff}}^{\text{RC}}} = \left( \frac{\alpha_s^{\text{RC}}(\mu_{\text{eff}}^{\text{RC}})}{\pi} \right)^p, \quad (2.60)$$

i.e. the sum of all higher order corrections vanishes (“effective charge”). Again, the value for  $\mu_{\text{eff}}$  can only be obtained from calculating to  $r = \infty$ . If  $P$  is calculated to finite order  $r$ , the Grunberg’s method of Fastest Apparent Convergence [43] uses the equality

$$P_r^{\text{RC}, \mu_{\text{FAC}}^{\text{RC}}} = \left( \frac{\alpha_s^{\text{RC}}(\mu_{\text{FAC}}^{\text{RC}})}{\pi} \right)^p, \quad \text{i.e.} \quad (2.61)$$

$$\sum_{i=1}^r B_i^{\text{RC}}(\mu_{\text{FAC}}^{\text{RC}}) \left( \frac{\alpha_s^{\text{RC}}(\mu_{\text{FAC}}^{\text{RC}})}{\pi} \right)^i = 0, \quad (2.62)$$

to calculate  $\mu_{\text{FAC}}^{\text{RC}}$  as an  $r^{\text{th}}$  order approximation to  $\mu_{\text{eff}}$ . Equation (2.62) does not necessarily imply that the corrections of orders larger than  $r$  are small, and that  $\mu_{\text{FAC}}^{\text{RC}}$  is a good approximation of  $\mu_{\text{eff}}$ .

**3) Stevenson’s Principle of Minimal Sensitivity (PMS)** The calculation of a quantity  $P$  to all orders does not depend on the RS. Stevenson’s Principle of Minimal Sensitivity [44] imposes this condition on the calculation to finite order

$$\frac{\partial P_r^{\text{RS}}}{\partial RS} = 0, \quad (2.63)$$

i.e., it mimics a feature of the full result already at finite order  $r$ . For  $r = 1$  it yields approximately (for  $\alpha_s \ll 4\pi\beta_0/\beta_1 \approx 2$ , which is always fulfilled in perturbative QCD)

$$P_1^{\text{RC}, \mu_{\text{PMS}}^{\text{RC}}} = \left( \frac{\alpha_s^{\text{RC}}(\mu_{\text{PMS}}^{\text{RC}})}{\pi} \right)^p \left( 1 - \frac{p}{p+1} \frac{\beta_1}{4\beta_0} \frac{\alpha_s^{\text{RC}}(\mu_{\text{PMS}}^{\text{RC}})}{\pi} \right). \quad (2.64)$$

The first order coefficient  $B_1^{\text{RC}}(\mu_{\text{PMS}}^{\text{RC}})$  varies between  $-0.5$  and  $-2$  depending on  $n_F$  and  $p$ . Thus, the PMS choice of scale is not too different from the FAC choice, where  $B_1^{\text{RC}}(\mu_{\text{FAC}}^{\text{RC}}) = 0$ . This is true also at higher orders [32]. Note, that in the PMS method the coefficient  $B_1$  is independent from the RC, and moreover identical for all processes of given  $n_F$  and  $p$ .

#### 4) Brodsky, Lepage, and Mackenzie's Absorption of Vacuum Polarization (AVP)

Brodsky, Lepage, and Mackenzie [45] have proposed to absorb all vacuum polarization corrections into the running coupling constant, as it is done in the case of QED. In QCD, the fermion vacuum polarization corrections manifest themselves as a dependence of the perturbation expansion coefficients on  $n_F$ . For the 1-loop coefficient

$$B_1^{\text{RC}}(\mu) = b_1^{\text{RC}} + a_1^{\text{RC}}(\mu)\beta_0 \quad (2.65)$$

the  $n_F$  dependence is contained in  $\beta_0$ , which also includes the gluon loops. The vacuum polarization corrections are absorbed on the 1-loop level by defining the scale  $\mu_{\text{AVP}}^{\text{RC}}$  such, that

$$a_1^{\text{RC}}(\mu_{\text{AVP}}^{\text{RC}}) = 0. \quad (2.66)$$

In the AVP method the difference between the 1-loop coefficients in different RC's is the same for all processes of identical lowest order  $p$ , and is given by the  $\beta_0$  independent part of  $pv_1^{\text{RC} \rightarrow \text{RC}'}$  (cf. Eqs. (2.49) and (2.50)). An especially large difference is obtained between the AVP method applied in the  $\overline{\text{MS}}$  and in the MOM(3g) prescription

$$B_1^{\text{MOM}(3g)}(\mu_{\text{AVP}}^{\text{MOM}(3g)}) = B_1^{\overline{\text{MS}}}(\mu_{\text{AVP}}^{\overline{\text{MS}}}) + p \frac{51}{16} J,$$

yielding e.g. for  $p = 3$  a difference of 22.4 ! The 3-gluon vertex, however, has a different structure of fermion loop corrections, which are partially process-dependent and should thus not be completely absorbed. The applicability of the AVP method is thus restricted to those perturbation expansions, which do not contain higher order corrections to gluon-gluon vertices. This excludes 1-loop AVP renormalization for the MOM(3g) convention, and for processes with gluon-gluon vertices in lowest order. Since gluon-gluon vertices appear on 1-loop level at the latest, the AVP method cannot be applied beyond the 1-loop level.

The above considerations will be illustrated in the following with the help of the ratio of leptonic and gluonic width of the  $\Upsilon$  resonance. The leptonic width  $\Gamma_{ll}$  of the  $\Upsilon$  states is given by the Van-Royen-Weisskopf formula [46], corrected to first order QCD [47] as

$$\Gamma_{ll} = 16\pi Q_b^2 \alpha_{em}^2(m_\Upsilon) \frac{|\psi(0)|^2}{m_\Upsilon^2} \left( 1 - \frac{16}{3} \frac{\alpha_s(\mu)}{\pi} \right), \quad (2.67)$$

where  $Q_b = -1/3$  is the charge of the b-quark in units of  $e$ ,  $\psi(0)$  is its wave function at the origin, and  $\alpha_{em}$  is the electromagnetic coupling constant, which has to be evaluated at  $m_\Upsilon$  to absorb the QED vacuum polarization corrections<sup>7</sup>. The first order QCD correction to the lowest order diagram in Figure 2.5(a) corresponds to the 1-gluon exchange diagram, shown in Figure 2.5(b).

The calculation of the 3-gluon width  $\Gamma_{ggg}(\Upsilon)$  has been performed in the  $\overline{\text{MS}}$  renormalization prescription at  $\mu = m_\Upsilon$  and yields the result [48]

$$\Gamma_{ggg} = \frac{160}{81} (\pi^2 - 9) [\alpha_s^{\overline{\text{MS}}}(m_\Upsilon)]^3 \frac{|\psi(0)|^2}{m_\Upsilon^2} \left[ 1 + \frac{\alpha_s^{\overline{\text{MS}}}(m_\Upsilon)}{\pi} (2.78\beta_0 - 19.4\{\pm 0.5\}) \right]. \quad (2.68)$$

<sup>7</sup>We chose this form in order to disentangle the QED from the QCD corrections. If other QED corrections, such as final state Bremsstrahlung, are to be included, we would have to return to the standard QED expansion in terms of  $\alpha = \alpha_{em}(0)$ .



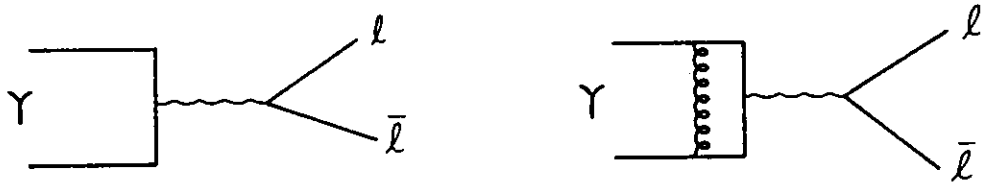


Figure 2.5: a) lowest order diagram for  $\Upsilon \rightarrow \ell\bar{\ell}$ . b) first order QCD correction.

This first order QCD correction sums the contribution of 315 Feynman diagrams in 14 different classes. The error given corresponds to the 2-sigma error of the numerical integration.

As can be seen, both partial widths (2.67) and (2.68) can be factorized into a (non-perturbative and non-relativistic) wave function and a perturbation series in  $\alpha_s$ . This factorization is feasible, because the annihilation of the heavy quarks is only possible at distances of  $\mathcal{O}(1/m_b) \cong 0.04$  fm, much less than the radius of the  $\Upsilon$ , which is  $\sim 0.2$  fm for the  $\Upsilon(1S)$ , and  $\sim 0.5$  fm for the  $\Upsilon(2S)$  [49]. Thus, the non-perturbative long-distance structure of the  $\Upsilon$  enters only in the wave function  $\psi(0)$ . Forming the ratio of  $\Gamma_{ggg}/\Gamma_{\ell\ell}$  the wave function drops out, and the quantity

$$P(\Upsilon \rightarrow \ell\bar{\ell}) \equiv \frac{9\alpha_{em}^2(m_\Upsilon)}{10\pi^2(\pi^2-9)} \frac{\Gamma_{ggg}}{\Gamma_{\ell\ell}} = 6 \times 10^{-6} \frac{\Gamma_{ggg}}{\Gamma_{\ell\ell}} \quad (2.69)$$

has the standard form of a perturbative expansion, namely

$$P_1^{\overline{\text{MS}},\mu}(\Upsilon \rightarrow \ell\bar{\ell}) = \left( \frac{\alpha_s^{\overline{\text{MS}}}(\mu)}{\pi} \right)^3 \left[ 1 + \frac{\alpha_s^{\overline{\text{MS}}}(\mu)}{\pi} \left( (2.78 - \frac{3}{2} \ln \frac{m_\Upsilon}{\mu}) \beta_0 - 14.1 \right) \right]. \quad (2.70)$$

We will now study the scheme dependence of the above expansion by keeping (for simplicity) the  $\overline{\text{MS}}$  prescription as a basis and varying the scale  $\mu$ . The appropriate scales  $\mu$ , as recommended by the methods discussed above, and the resulting expansion parameters  $B_1^{\overline{\text{MS}}}(\mu)$  are collected in Table 2.5.

Table 2.5: The 1-loop expansion parameter  $B_1^{\overline{\text{MS}}}$  for  $P(\Upsilon \rightarrow \ell\bar{\ell})$  as function of different RS's. The RS ambiguity has been converted to the choice of scale  $\bar{\mu}^{\overline{\text{MS}}}$  in the  $\overline{\text{MS}}$  prescription.

RC	$\overline{\text{MS}}$	$\overline{\text{MS}}$	MOM(3g)	$\overline{\text{MS}}$	$\overline{\text{MS}}$	$\overline{\text{MS}}$	MOM(3g)
$\mu$	$\mu_{\text{NAT}}^{\ell}$	$\mu_{\text{FAC}}^{\overline{\text{MS}}}$	$\mu_{\text{NAT}}^{\ell}$	$\mu_{\text{PMS}}^{\overline{\text{MS}}}$	$\mu_{\text{NAT}}^{3g}$	$\mu_{\text{AVP}}^{\overline{\text{MS}}}$	$\mu_{\text{NAT}}^{3g}$
$\bar{\mu}^{\overline{\text{MS}}}/m_\Upsilon$	1	0.48	0.46	0.44	0.333	0.157	0.154
$B_1^{\overline{\text{MS}}}(\bar{\mu}^{\overline{\text{MS}}})$	+9.1	0.0	-0.6	-1.2	-4.7	-14.1	-14.3

In fact, there are two “natural scales” involved in this ratio. The appropriate scale for the 3-gluon decay is probably something like the average gluon energy,  $\mu_{\text{NAT}}^{3g} = m_\Upsilon/3$ . On the other side, the perturbative correction of the leptonic width (Fig. 2.5(b)) arises from hard gluon momenta, suggesting  $\mu_{\text{NAT}}^{3g} = m_\Upsilon$ . (The effect of soft gluons is a Coulomb-like attraction, which is already contained in the potential and thus in the wave function  $\psi(0)$ .) Since the 1-loop  $\alpha_s$  correction for  $\Gamma_{\ell\ell}$  is the leading order in  $\alpha_s$ , i.e.  $p=0$ , its first

order coefficient does not depend on  $\mu$  (cf. Eq. (2.47)). Nevertheless we list both choices of  $\mu_{\text{NAT}}$  for the  $\overline{\text{MS}}$  prescription and for the MOM(3g) prescription, which was again calculated in the Landau gauge. The corresponding MOM-scale  $\mu^{\text{MOM}(3g)}$  is converted to a  $\overline{\mu}^{\overline{\text{MS}}}$  by  $\overline{\mu}^{\overline{\text{MS}}} = \mu^{\text{MOM}(3g)}/2.16$  as inferred from Eq. (2.52). The scales of FAC, PMS, and AVP are calculated following Eqs. (2.62), (2.64), and (2.66), respectively. It may be interesting to note, that different RS's can lead to similar results, e.g.  $(\overline{\text{MS}}, \text{FAC}) \approx (\text{MOM}(3g), \text{NAT}(\ell\ell)) \approx (\overline{\text{MS}}, \text{PMS})$ , and  $(\overline{\text{MS}}, \text{AVP}) \approx (\text{MOM}(3g), \text{NAT}(3g))$ . Not all of these coincidences occur by mere accident, as already indicated above in the discussion of the PMS and FAC scales.

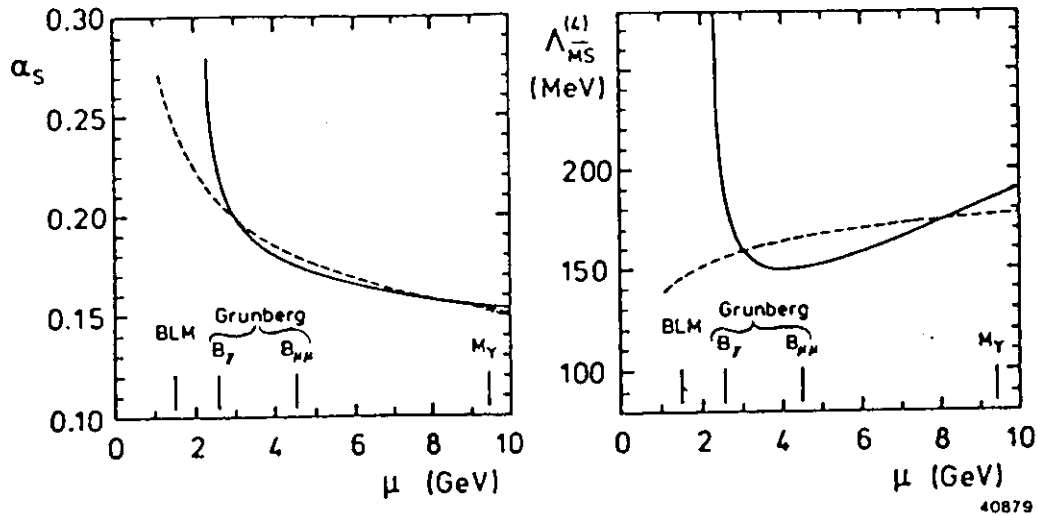


Figure 26: a)  $\alpha_s$  vs. the scale  $\mu$  at which it is evaluated. b) The same for  $\Lambda_{\overline{\text{MS}}}^{(4)}$ . The solid curves are from an evaluation of the  $\Upsilon(1S)$  leptonic branching ratio, the dashed curves are from  $B_\gamma$ , the decay of the  $\Upsilon(1S)$  into a photon plus hadrons. Also indicated are the specific scales discussed in the text.

The main point of Table 2.5, however, is that the first order coefficient depends very strongly on  $\mu$ , i.e. on the RS. The variation of  $B_1(\mu)$  is in fact not consistent with the running of  $\alpha_s(\mu)$ . This can be seen from Figs. 2.6(a) and (b) [50], where the solutions for  $\alpha_s^{\overline{\text{MS}}}$  and  $\Lambda_4^{\overline{\text{MS}}}$  are plotted versus the scale  $\mu^{\overline{\text{MS}}}$ . The solid curves were derived from

$$P_1^{\text{RS}}(\Upsilon(1S) \rightarrow \ell\bar{\ell}) \stackrel{!}{=} P^{\text{mcas}}(\Upsilon(1S) \rightarrow \ell\bar{\ell}) = (1.87 \pm 0.12) \times 10^{-4} \quad (2.71)$$

by inserting Eqs. (2.70) and (2.38). There is no solution for  $\Lambda_4^{\overline{\text{MS}}}$  (and for  $\alpha_s^{\overline{\text{MS}}}$ ) if the scale  $\mu$  is chosen to  $\mu \approx 0.16m_\Upsilon$ , as recommended by the schemes  $(\overline{\text{MS}}, \text{AVP})$  and  $(\text{MOM}(3g), \text{NAT}(3g))$ . The reason for this divergence is, that for a typical value of  $\alpha_s^{\overline{\text{MS}}}(0.16m_\Upsilon) \approx 0.25$  the term  $(1 - 14\alpha_s^{\overline{\text{MS}}}(\mu)/\pi)$  becomes negative. Since the RS's  $(\overline{\text{MS}}, \text{AVP})$  and  $(\text{MOM}(3g), \text{NAT}(3g))$  both have some physical motivation (at least, there are no physical arguments against them), this failure and the (too) strong scale dependence has cast doubt on the reliability of extracting  $\alpha_s$  from  $\Gamma_{\text{ggg}}/\Gamma_\ell$  in the  $\Upsilon$  system, and has even called in question the possibility of a perturbative analysis for this ratio [45,32].

We postpone the discussion, whether such a conclusion can really be drawn, to Section 7.4.1. First we want to present our measurement of  $B_{\ell\ell}$ , which will update the value of  $P^{\text{mcas}}(\Upsilon \rightarrow \ell\bar{\ell})$ . We therefore continue with a discussion of the theoretical fundamentals for this measurement.



## 2.3 The Process $e^+e^- \rightarrow \mu^+\mu^-$ at $\sqrt{s} \approx 10$ GeV

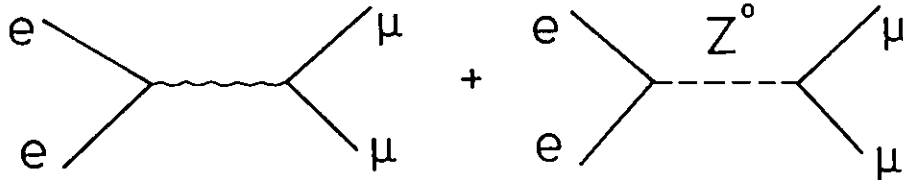


Figure 2.7: Lowest order elektroweak diagrams for  $e^+e^- \rightarrow \mu^+\mu^-$ .

The lowest order electroweak Feynman diagrams describe the process  $e^+e^- \rightarrow \mu^+\mu^-$  by annihilation in a virtual photon or a  $Z^0$  (Fig. 2.7). At c.m. energies  $\sqrt{s}$  around 10 GeV the phase space suppression of muons is negligible, and the differential continuum cross-section (i.e. without  $\Upsilon$ -production) is given to lowest order by [51,52]

$$\frac{d\sigma_{\text{Born}}}{d\Omega} = \frac{\alpha^2}{4s} \left( (1 + Z_1(s))(1 + \cos^2 \theta) + Z_2(s) \cos \theta \right), \quad (2.72)$$

where  $\cos \theta$  is the angle of the outgoing  $\mu^+$  with respect to the incoming  $e^+$  direction ( $\equiv +z$ -direction). The influence of the  $Z$ -propagator is included by the terms  $Z_1(s)$  and  $Z_2(s)$ , which both are composed from a  $\gamma$ - $Z^0$  interference term and a  $Z^0$  resonance term. They read for  $s \ll m_Z^2$

$$\begin{aligned} Z_1(s) &= -2v_\ell^2 \frac{s}{m_Z^2} + (a_\ell^2 + v_\ell^2) \frac{s^2}{m_Z^4} \\ Z_2(s) &= -4a_\ell^2 \frac{s}{m_Z^2} + 8a_\ell^2 v_\ell^2 \frac{s^2}{m_Z^4}. \end{aligned} \quad (2.73)$$

The axial and vector couplings of the  $Z$  to charged leptons are  $a_\ell = -(2 \sin 2\theta_W)^{-1} = -0.598 \pm 0.004$  and  $v_\ell = a_\ell(4 \sin^2 \theta_W - 1) = 0.058 \pm 0.012$ , where the errors come from the uncertainty of  $\sin^2 \theta_W$ . At  $\sqrt{s} \approx 10$  GeV the  $\gamma$ - $Z$  interference terms  $\propto s/m_Z^2$  dominate. At these c.m. energies the  $Z$ -contribution to the  $\theta$ -symmetric part of the cross-section is negligible, since  $Z_1 = (0.7 \pm 0.4) \times 10^{-4}$ , whereas  $Z_2 = -2 \times 10^{-2}$  is the source of a small forward-backward asymmetry in  $\cos \theta$ . This asymmetry, however, does not contribute to the total cross-section. If one does not discriminate between  $\mu^+$  and  $\mu^-$  in the final state, it will not even alter the differential cross-section. Thus, we will neglect both,  $Z_1$  and  $Z_2$ , in the following discussion and regard the Born cross-section as coming exclusively from one-photon annihilation yielding a total cross-section of

$$\sigma_{\text{Born}}(s) = \int \frac{d\sigma_{\text{Born}}}{d\Omega} d\Omega = \frac{4\pi}{3} \frac{\alpha^2}{s} = \frac{86.85 \text{ nb}}{s/\text{GeV}^2}. \quad (2.74)$$

### 2.3.1 First Order Corrections

In the following we will discuss corrections to the process  $e^+e^- \rightarrow \mu^+\mu^-$  from resonance production and from  $\alpha^3$  terms, which arise from the interference of the Born diagram with 1-loop diagrams of identical initial and final state. Other  $\mathcal{O}(\alpha^3)$  corrections are the Bremsstrahlung diagrams, which have one additional photon in the final state. The contributing diagrams can be grouped in 6 classes as shown in Figure 2.8. We will assume standard QED on-shell MOM renormalization of the lepton-photon vertex for on-shell leptons and  $q^2=0$ . The corrections to the photon propagator, i.e. Diagrams (a)–(c) in Fig. 2.8 will be treated first.

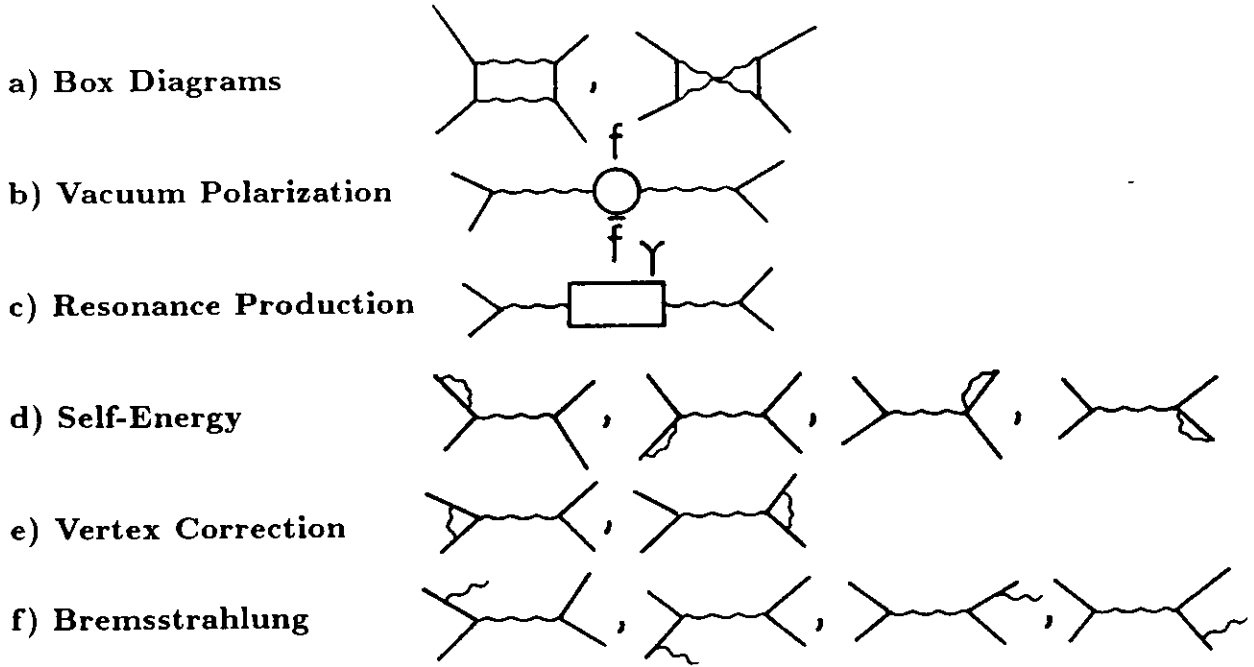


Figure 2.8: Diagrams (a), (b), (d), and (e) lead to first order corrections for  $e^+e^- \rightarrow \mu^+\mu^-$  through their interference with the Born diagram, Diagram (c) shows resonance production in lowest order, whereas Diagrams (f) are the lowest order radiative processes  $e^+e^- \rightarrow \mu^+\mu^-\gamma$ .

### The Box Diagrams

The contribution of the box diagrams with two photons (Fig. 2.8(a)) to the total cross-section is zero [52]. They merely cause an additional forward-backward asymmetry, which suppresses the asymmetry effect of the weak interactions. We neglect them in the following.

### Vacuum Polarization

As already deduced in Section 2.2.1, the amplitude  $\mathcal{M}_{\text{Born}}$  for the lowest order diagram is changed by adding the chain sum over the vacuum polarizations to

$$\begin{aligned}
 \mathcal{M}_0^{\text{VP}} &= \text{Born} + \text{Born} \cdot \text{loop} + \text{Born} \cdot \text{loop} \cdot \text{loop} + \dots \\
 &= \mathcal{M}_{\text{Born}} \cdot \left( 1 + \Pi_\gamma(q^2) + \Pi_\gamma^2(q^2) + \dots \right) \\
 &= \mathcal{M}_{\text{Born}} \cdot \left( \frac{1}{1 - \Pi_\gamma(q^2)} \right). \tag{2.75}
 \end{aligned}$$

$\Pi_\gamma$  contains all fermion loop contributions far away from hadronic resonances and can be obtained from Eq. (2.16) for  $s = q^2 \gg m_\tau^2$  as

$$\Pi_\gamma(s) = \Pi_e + \Pi_\mu + \Pi_\tau + \Pi_{\text{had}} + i \frac{\alpha}{3} \sum_{m_j^2 \ll s} Q_j^2, \tag{2.76}$$

where  $\Pi_\ell$ ,  $\ell = e, \mu, \tau$  is the real part of the lepton vacuum polarization, given by

$$\Pi_\ell = \frac{\alpha}{3\pi} \left( \ln \frac{s}{m_\ell^2} - \frac{5}{3} \right). \tag{2.77}$$

The real part  $\Pi_{had}$  of the hadronic vacuum polarization could in principle be obtained analogously from

$$\Pi_{had} = \frac{\alpha}{3\pi} \sum_{q=u,d,s,c} \left( \ln \frac{s}{m_q^2} - \frac{5}{3} \right). \quad (2.78)$$

However, due to the uncertainty in the quark masses and the presence of hadronic resonances, the hadronic contribution can be more accurately determined from the visible hadronic cross-section. The imaginary part of  $\Pi_\gamma$  is connected with the total cross-section  $\sigma^{e^+e^- \rightarrow f\bar{f}}$  for the production of fermion-antifermion pairs via

$$\Im \Pi_\gamma(s) = \frac{s}{4\pi\alpha} \sum_{f\bar{f}} \sigma^{e^+e^- \rightarrow f\bar{f}}(s) = \frac{\alpha}{3} \sum_{m_f^2 \ll s} Q_f^2. \quad (2.79)$$

From this follows a dispersion relation for the real part of  $\Pi_\gamma$  [53], which reads for  $\Pi_{had}$

$$\Pi_{had}(s) = \frac{s}{4\pi^2\alpha} \Re e \int_{4m_z^2}^{\infty} \frac{\sigma^{e^+e^- \rightarrow had}(s')}{s - s' - i\epsilon} ds'. \quad (2.80)$$

Table 2.6: Vacuum polarization corrections in the energy region of the  $\Upsilon$  resonances. All numbers for  $\Pi$  are given in percent.

$\sqrt{s}/\text{GeV}$	$\Pi_e$	$\Pi_\mu$	$\Pi_\tau$ <sup>8</sup>	$\Pi_{had}$ [54]	$\Re \Pi_\gamma$	$\Im \Pi_\gamma$	$\alpha_{em}^{-1}(s)$
9.46	1.39	0.57	0.11	$1.52 \pm 0.07$	$3.59 \pm 0.07$	1.54	$132.1 \pm 0.1$
10.58	1.41	0.58	0.13	$1.58 \pm 0.07$	$3.70 \pm 0.07$	1.62	$131.9 \pm 0.1$

From Eqs. (2.76), (2.77), and (2.80) we find at  $s \approx (10 \text{ GeV})^2$  the values listed in Table 2.6. Replacing in the Born cross-section (Eq. (2.74))  $\alpha = \alpha_{em}(0) = 1/137$  by  $\alpha_{em}(10 \text{ GeV}) = 1/132$  (cf. Eq. (2.20)) would be the simplest way to account for the photon vacuum polarization. However, since other corrections, like Bremsstrahlung, couple due to on-shell renormalization with  $\alpha_{em}(0) = \alpha$  exactly, it is more convenient to write

$$\sigma_0^{VP} = \frac{\sigma_{Born}}{|1 - \Pi_\gamma|^2} \quad (2.81)$$

in order to avoid the use of  $\alpha_{em}$  at different  $q^2$  in one and the same formula. From Table 2.6 we find corrections to the Born cross-section ranging from  $1/(1 - \Re \Pi_\gamma)^2 = 1/0.929$  at  $\sqrt{s} = 9.46 \text{ GeV}$  to  $1/0.927$  at  $\sqrt{s} = 10.58 \text{ GeV}$ . The influence of  $\Im \Pi_\gamma$  is negligible.

Note, that  $\Pi_{had}$  only contains the effects of hadronic resonances with mass  $M^2 \ll s$ , but no contributions from the  $\Upsilon$  resonances. These are discussed in the following.

### Resonance Production

A special case of vacuum polarization occurs, when the c.m. energy is near the mass of a narrow hadronic resonance. Since the photon is a vector particle, only resonances with  $J^{PC} = 1^{--}$  can be produced in  $e^+e^-$  annihilation to one virtual photon. At  $s = (10 \text{ GeV})^2$ , resonances with  $M^2 \ll s$ , i.e. narrow resonances below and including the  $\psi$ -family, are already contained in the hadronic vacuum polarization  $\Pi_{had}$ . The effect of the  $\Upsilon$ -family has to be treated separately, since it may alter the cross-section  $\sigma^{e^+e^- \rightarrow \mu\mu}(s)$  by orders of magnitude. The

<sup>8</sup>These values have been obtained from the exact formula of Ref. [36]. The application of Eq. (2.77), valid in the limit  $m_f^2 \ll s$ , would enlarge the results only by 0.02.

Feynman diagrams for the production of a resonance with mass  $M$  and total width  $\Gamma$  lead to the amplitude

$$\begin{aligned} \mathcal{M}_0^{\text{Res}} &= \text{diagram 1} + \text{diagram B} \\ &= \mathcal{M}_{\text{Born}} \cdot (1 + B), \end{aligned} \quad (2.82)$$

where the resonance amplitude  $B(s)$  is given in units of the Born amplitude  $\mathcal{M}_{\text{Born}}$  by the relativistic Breit-Wigner [55]

$$B(s) = \frac{\sqrt{9\Gamma_{\mu\mu}\Gamma_{ee}}}{\alpha M} \frac{s}{s - M^2 + iM\Gamma}. \quad (2.83)$$

Note that, in this case, a chain sum  $B + B^2 + B^3 \dots$  must not be formed. The ‘‘coupling constant’’  $\sqrt{9\Gamma_{\mu\mu}\Gamma_{ee}}/\alpha M$  in front of the Breit-Wigner, which replaces the electromagnetic coupling  $\alpha$ , already includes implicitly all chain terms, since  $\Gamma_{\ell}$  ( $\ell=e,\mu$ ) is a measured quantity and thus contains all higher order corrections.

The cross-section of  $e^+e^- \rightarrow \mu^+\mu^-$  including a resonance is thus given by  $\sigma_0^{\text{Res}} = \mathcal{M}_0^{\text{Res}} \mathcal{M}_0^{\text{Res}*}$ , yielding

$$\sigma_0^{\text{Res}} = \sigma_{\text{Born}}(1 + 2\Re B(s) + |B(s)|^2) \quad (2.84)$$

$$= \frac{4\pi\alpha^2}{3s} \left( 1 + 2 \frac{\sqrt{9\Gamma_{\mu\mu}\Gamma_{ee}}}{\alpha M} \frac{s(s - M^2)}{(s - M^2)^2 + M^2\Gamma^2} + \frac{9\Gamma_{\mu\mu}\Gamma_{ee}}{\alpha^2 M^2} \frac{s^2}{(s - M^2)^2 + M^2\Gamma^2} \right) \quad (2.85)$$

$$\equiv \sigma^C + \sigma^I + \sigma^R. \quad (2.86)$$

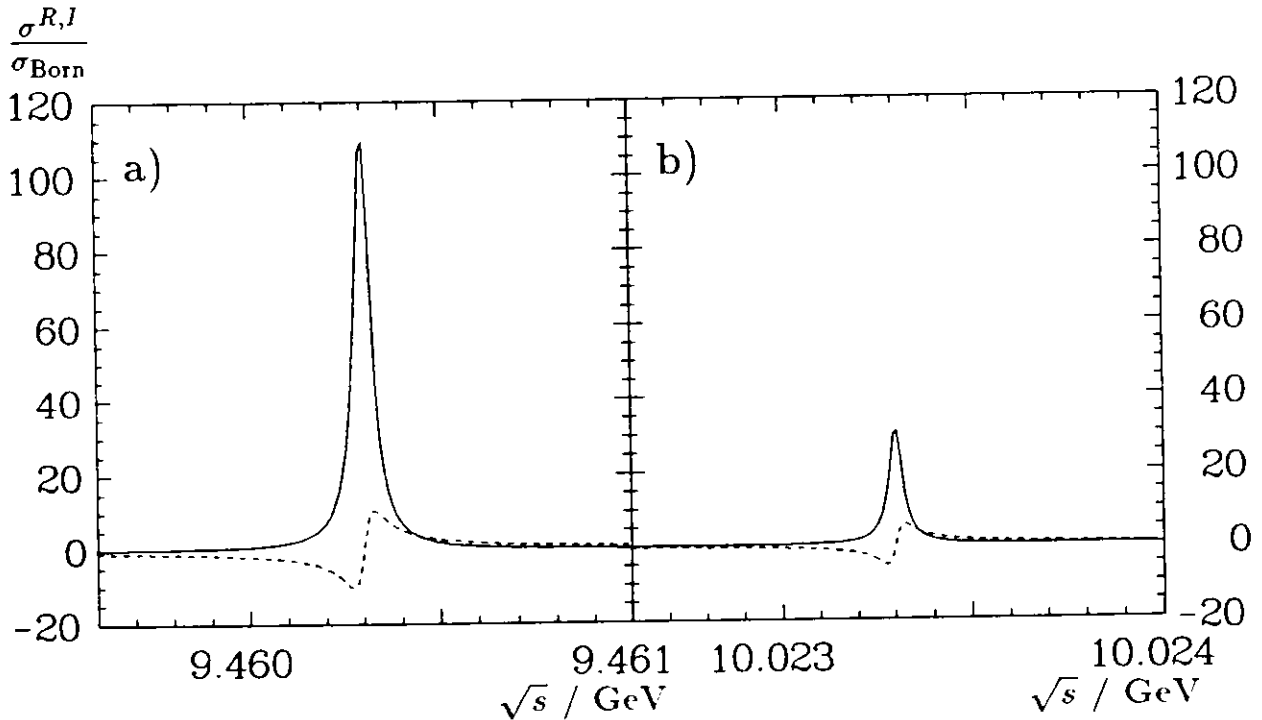


Figure 2.9: Resonance term  $\sigma^R$  (solid line) and interference term  $\sigma^I$  (dashed line) for the  $Y(1S)$  (a) and the  $Y(2S)$  (b) in units of the Born cross-section for  $e^+e^- \rightarrow \mu^+\mu^-$ .

The first term in the parentheses denotes the continuum cross-section (C), the last term is the interference (I) between the resonant  $\mu$ -pair production (R), and the second term is the interference (I) between

both. The energy dependence of  $|B(s)|^2 = \sigma^R/\sigma_{\text{Born}}$  and  $2\Re B(s) = \sigma^I/\sigma_{\text{Born}}$  is plotted in Figs. 2.9(a) and (b) for the  $\Upsilon(1S)$  and the  $\Upsilon(2S)$  resonance, respectively. The PDG values [22] for the  $\Upsilon$  resonance parameters were used for these plots. The interference term has maximum values of

$$I_0 = \sigma^I(M(M \pm \Gamma)) = \pm \frac{4\pi\alpha}{M^2} \sqrt{B_{\mu\mu}B_{ee}}, \quad (2.87)$$

whereas the peak value of the resonance term is

$$R_0 = \sigma^R(M^2) = \frac{12\pi}{M^2} B_{\mu\mu}B_{ee}. \quad (2.88)$$

The ratio of these two maxima is thus  $|I_0/R_0| = \alpha/\sqrt{9B_{\mu\mu}B_{ee}}$ , yielding about 1/10 for the  $\Upsilon(1S)$  and about 1/5 for the  $\Upsilon(2S)$ , as can be seen from Figs. 2.9(a) and (b). The values of both maxima are much larger than the Born cross-section.

Plotting in Fig. 2.10 the complete cross-section of Eq. (2.85), we find a modification of the Born cross-section by up to a factor  $\sim 100$  due to the presence of the narrow  $\Upsilon$  resonances and their interference with the continuum. However, this large effect will be considerably reduced by corrections due to initial state photon radiation and due to the c.m. energy spread at  $e^+e^-$  colliders (see Section 2.3.5).

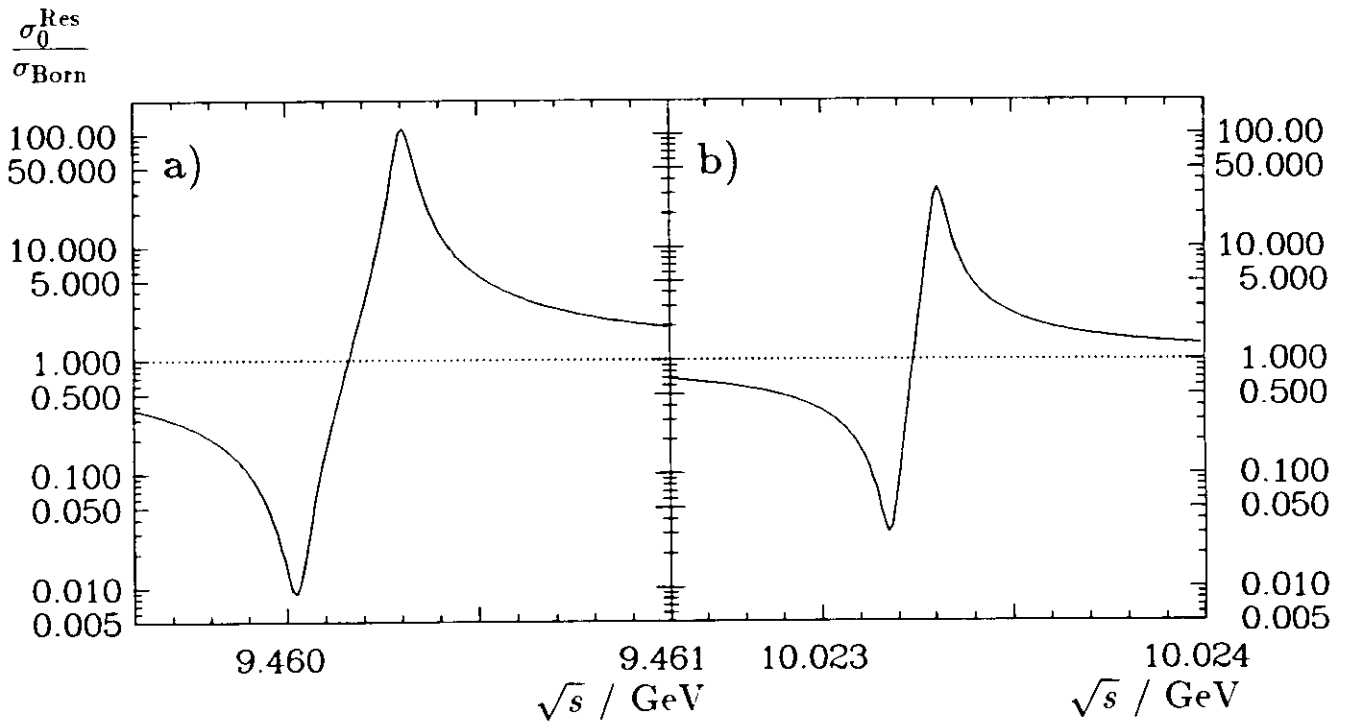


Figure 2.10: The Born cross-section for  $e^+e^- \rightarrow \mu^+\mu^-$  (dotted line) is strongly modified (solid line) by including the resonance terms of the  $\Upsilon(1S)$  (a) and the  $\Upsilon(2S)$  (b) and their interference with the continuum.

For broad resonances, like the  $\Upsilon(4S)$ , the situation changes. Since  $\Gamma(4S) = 23.8$  MeV  $\gg \Gamma_{\ell\ell}(4S) = 0.24$  keV, the leptonic branching ratio  $B_{\ell\ell}(4S) = 10^{-5}$  and thus the ratio of the maxima of interference and resonance is about 250. Hence, the interference term is the dominant term, but its maximum amounts to only 0.4% of the Born cross-section (Fig. 2.11). Being smaller than the width of the  $\Upsilon(4S)$ , the c.m. energy spread does not strongly alter its resonance and interference terms.

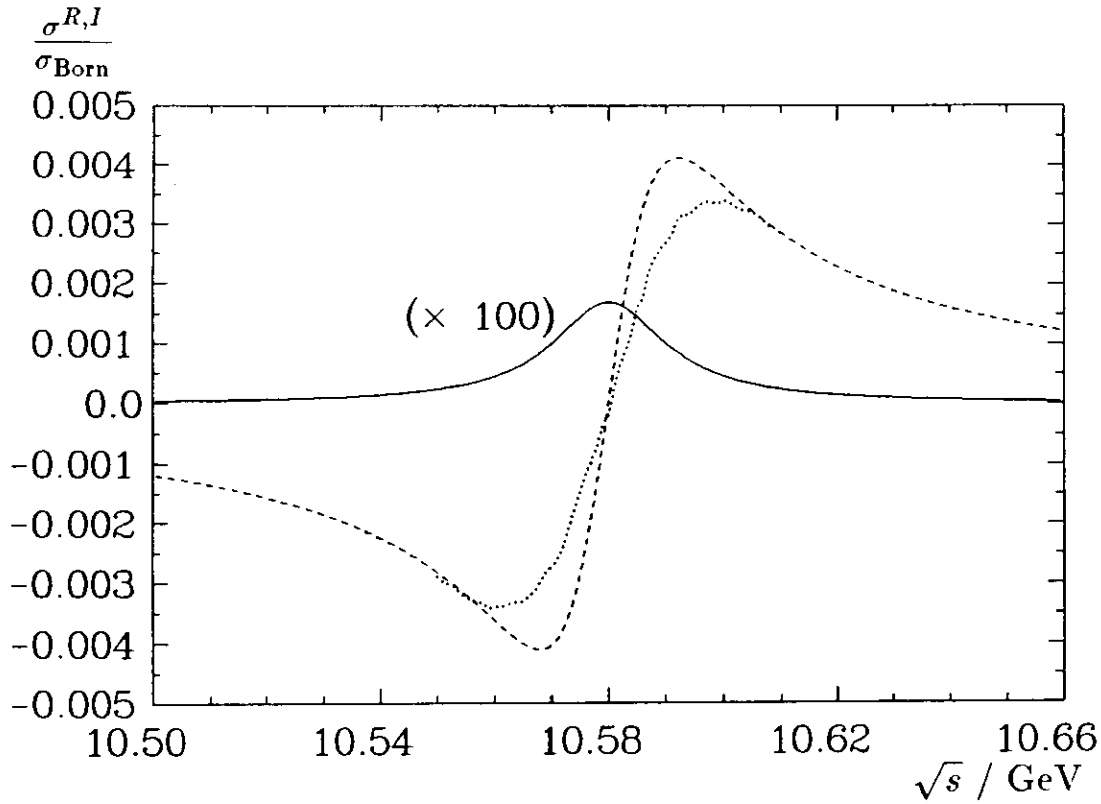


Figure 2.11: Resonance term (solid line) and interference term (dashed line) for the  $\Upsilon(4S)$  resonance in units of the Born cross-section for  $e^+e^- \rightarrow \mu^+\mu^-$ . The resonance has been blown up by a factor of 100. The dotted line shows the result of a convolution of the interference term with a c.m. energy spread of 8.5 MeV.

### The Total Correction to the Photon Propagator

The amplitude for  $e^+e^- \rightarrow \mu^+\mu^-$  including the summed corrections of the vacuum polarization and all  $\Upsilon$  resonances to the photon propagator is derived from combining Eqs. (2.75) and (2.82) to

$$\mathcal{M}_0 = \mathcal{M}_{\text{Born}} \left( \frac{1}{1 - \Pi_\gamma} + \sum_{n=1}^6 B_n \right), \quad (2.89)$$

where  $B_n$  denotes the Breit-Wigner amplitudes from Eq. (2.83) for the  $\Upsilon(nS)$  resonances. Evaluating  $\sigma_0 = \mathcal{M}_0 \mathcal{M}_0^*$  and neglecting the interference terms  $2\Re\{B_i B_j^*\}$  between different  $\Upsilon$  states, since their mass differences are much larger than their widths, we find

$$\sigma_0 = \sigma_{\text{Born}} \left( \frac{1 + 2(1 - \Re\Pi_\gamma) \sum \Re B_n + 2\Im\Pi_\gamma \sum \Im B_n}{1 - 2\Re\Pi_\gamma + |\Pi_\gamma|^2} + \sum |B_n|^2 \right). \quad (2.90)$$

Neglecting  $(\Im\Pi_\gamma)^2$  in the denominator of the above equation, we find the form

$$\sigma_0 \approx \sigma_{\text{Born}} \left( \frac{1}{(1 - \Re\Pi_\gamma)^2} + \frac{2 \sum \Re B_n}{1 - \Re\Pi_\gamma} + \left[ \frac{2\Im\Pi_\gamma \sum \Im B_n}{(1 - \Re\Pi_\gamma)^2} + \sum |B_n|^2 \right] \right) \quad (2.91)$$

with somewhat simpler terms for continuum, interference and resonance. By comparing Eq. (2.91) to Eq. (2.84) we see, that the continuum term acquires its usual vacuum polarization correction  $1/(1 - \Re\Pi_\gamma)^2$ , the interference terms are corrected by  $1/(1 - \Re\Pi_\gamma)$ , and the resonance terms are increased by an additive correction  $\sim \Im\Pi_\gamma \Im B$ . The latter two corrections arise from the interference between vacuum polarization and resonance production.

Compared to  $|B|^2$  the term  $\Im m \Pi_\gamma \Im m B$  is suppressed by  $\sim \alpha^2/B_u$ . Thus, for the  $\Upsilon(1S)$  through  $\Upsilon(3S)$  resonances having  $B_u = \mathcal{O}(10^{-2})$  it only introduces a marginal correction to  $|B|^2$ , even though its maximum value is  $\mathcal{O}(0.1)$ . For the  $\Upsilon(4S)$  and higher  $\Upsilon$  states with  $B_u = \mathcal{O}(10^{-5})$  on the other hand, it exceeds the resonance proper  $|B|^2$  by a factor of more than 10, but its maximum value is only  $\mathcal{O}(10^{-4})$ .

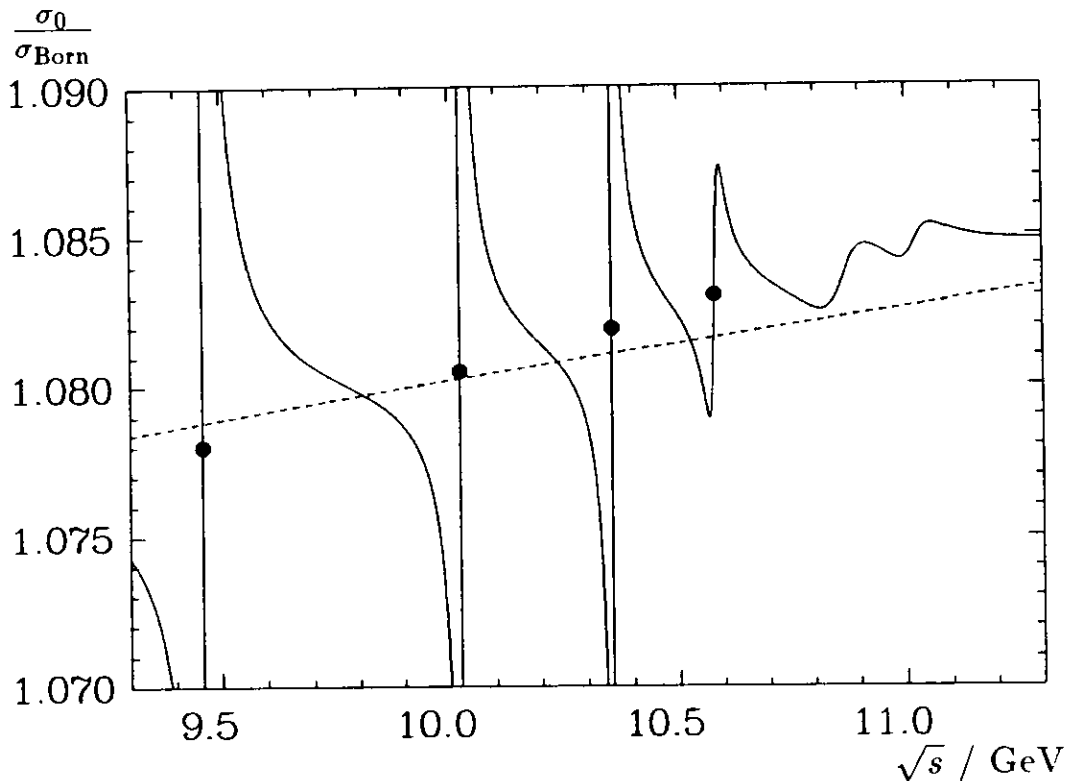
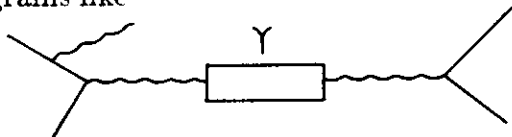


Figure 2.12: Modification of the vacuum polarization correction  $\sigma_0/\sigma_{\text{Born}}$  by the  $\Upsilon$  resonances. The dashed line shows the logarithmic increase of  $(1 - \Pi_\gamma(s))^{-2}$ . The solid line contains in addition the  $\Upsilon$  Breit-Wigners and their interference terms. The dots are explained in the text.

The dependence of  $\sigma_0/\sigma_{\text{Born}}$  on  $\sqrt{s}$  is plotted in Fig. 2.12. The maxima of the interference and resonance terms in the vicinity of the narrow  $\Upsilon$  resonances are far outside this plot, as can be seen from Figs. 2.9 and 2.10. However, even between the  $\Upsilon$ -resonances a distinct modification of the smooth increase of  $(1 - \Pi_\gamma)^{-2}$  (dashed line) is observed. It is mainly caused by their interference terms with the continuum, since the purely resonant terms are negligibly small between the  $\Upsilon$ -resonances.

A precise knowledge of  $\sigma_0/\sigma_{\text{Born}}$  is important, when data taken at different beam energies are subtracted from each other. If we e.g. want to subtract the continuum contribution measured off-resonance from data taken on-resonance, we have to know the ratio of the respective continuum cross-sections. The continuum cross-section under a given resonance  $\Upsilon(nS)$  including the modifications of  $\sigma_0$  induced by all other  $\Upsilon$  resonances, can be obtained by omitting the  $B_n$  term of this resonance in Eq. (2.90). In Fig. 2.12 we have indicated these continuum cross-sections by dots. The variation of the dots with the radial quantum number  $n$  describes the deviation of the continuum cross-section at  $\sqrt{s} = m_{\Upsilon(nS)}$  from an  $1/s$  behaviour. From the  $\Upsilon(1S)$  at 9.46 GeV to the  $\Upsilon(4S)$  at 10.58 GeV this deviation is 0.5%. It has about equal contributions from the photon vacuum polarization  $(1 - \Pi_\gamma)^{-2}$  and from the summed effect of the interference terms of all  $\Upsilon$ -resonances other than  $\Upsilon(nS)$ , i.e.  $\sum_{n=1,2,3,5,6} 2\Re B_n(10.58 \text{ GeV}) - \sum_{n=2,3,4,5,6} 2\Re B_n(9.46 \text{ GeV})$ .

The cross-section  $\sigma_0$  from Eq. (2.90) contains all next-to-leading order corrections to the photon propagator as well as the leading logarithms of higher order corrections, and the  $\Upsilon$  resonance terms. By adding corrections to the external lepton lines, the photon propagator is generally not influenced. We thus adopt  $\sigma_0$  as the new basic cross-section to which corrections from the lepton lines are applied. As we will see, the only exception is Bremsstrahlung down to a resonance, i.e. diagrams like



where the value of  $\sigma_0$  strongly depends on the emitted photon energy. Thus, the formulae in the next paragraphs are not valid at c.m. energies close to a resonance. Our final result in Section 2.3.2, however, will not have such a restriction on its validity.

### Electron and Muon Self-Energy

Due to on-shell renormalization the contributions of the diagrams in Fig. 2.8(d) vanish, since the initial and final state particles are on their mass shell.

### Vertex Correction

For a vertex with  $q^2=0$  the diagrams in Fig. 2.8(e) would vanish, likewise, after on-shell renormalization. For  $q^2 \neq 0$  their UV divergencies still cancel with those of the electron and muon self-energy due to the Ward identities. However, an infrared divergence remains. The interference of the Born diagram with each of the vertex correction diagrams results in an  $\mathcal{O}(\alpha)$  correction  $\delta^{\text{VC}}$  which modifies our reference cross-section  $\sigma_0$  to  $\sigma^{\text{VC}}$  given by

$$\sigma^{\text{VC}} = \sigma_0(1 + \delta_e^{\text{VC}} + \delta_\mu^{\text{VC}}), \quad (2.92)$$

where  $\delta_e^{\text{VC}}$  refers to the left-hand diagram, and  $\delta_\mu^{\text{VC}}$  to the right-hand diagram in Fig. 2.8(e). The infrared divergence of  $\delta^{\text{VC}}$  is regularized with the help of a fictitious small photon mass  $\lambda$ . The result reads [51]

$$\delta_\ell^{\text{VC}} = \frac{2\alpha}{\pi} \left[ -1 + \frac{\pi^2}{3} + \frac{3}{4} \ln \frac{s}{m_\ell^2} - \frac{1}{4} \ln^2 \frac{s}{m_\ell^2} - \left( \ln \frac{s}{m_\ell^2} - 1 \right) \ln \frac{m_\ell}{\lambda} \right], \quad (2.93)$$

where  $\ell = e, \mu$ . In the limit  $\lambda \rightarrow 0$  the terms  $\delta^{\text{VC}}$  make the cross-section  $\sigma^{\text{VC}}$  negative<sup>9</sup> and divergent to  $-\infty$ . This divergence is a standard phenomenon in QED and can in principle be remedied by calculating to all orders of  $\alpha$ .

However, if this were possible, one would find that the cross-section

$$\sigma^{ee \rightarrow \mu\mu} = \left| \begin{array}{l} \text{Born diagram} \\ + \text{vertex corrections} \\ + \text{self-energy corrections} \\ + \dots \end{array} \right|^2$$

identically vanishes. This — on the first view — surprising result comes from the Bloch-Nordsieck Theorem discussed below.

<sup>9</sup>This is possible, since we truncated the expansion of the cross-section at  $\mathcal{O}(\alpha^3)$ , i.e. at the level of interference between vertex correction and Born diagram. This truncation differs from taking an absolute square of the sum of the corresponding Feynman amplitudes, which would guarantee for positiveness.



### The Bloch-Nordsieck and the Kinoshita-Lee-Nauenberg theorems

The essential work for the understanding of the infrared divergence problem was done in 1937 by Bloch and Nordsieck [56]. The Bloch-Nordsieck Theorem says, that the probability to emit zero or any finite number of photons from the scattering of charged particles is precisely zero. Each process involving charged particles is accompanied by the emission of an infinite number of photons with arbitrary small energies. In the language of Feynman diagrams, their theorem relates the process  $e^+e^- \rightarrow \mu^+\mu^-$  without photon emission (Fig. 2.8(a)) to the process  $e^+e^- \rightarrow \mu^+\mu^- + m\gamma$  (Fig. 2.8(f) for  $m=1$ ), which has a different final state. The Bloch-Nordsieck Theorem claims, that not only  $\sigma^{ee \rightarrow \mu\mu} = 0$ , but also  $\sigma^{ee \rightarrow \mu\mu + m\gamma} = 0$  for any finite number  $m$ . The only process occurring in nature is  $e^+e^- \rightarrow \mu^+\mu^- + \infty\gamma$ .

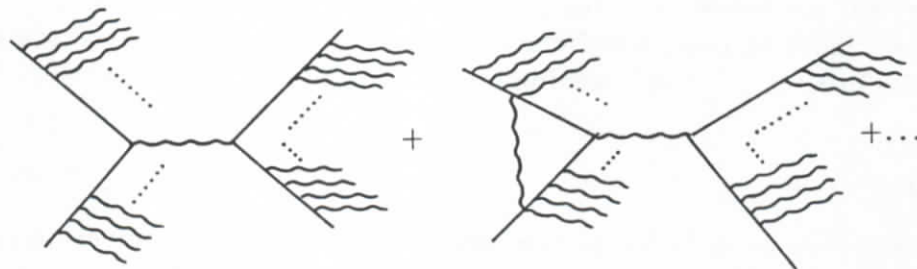


Figure 2.13: The process  $e^+e^- \rightarrow \mu^+\mu^-$  is always accompanied by an infinite number of radiated photons.

Thus, we would have to calculate the type of Feynman diagrams in Fig. 2.13, which cannot even be drawn in a finite amount of time. However, Bloch and Nordsieck already showed, that generally the observed cross-section measured in a given detector is very close to the cross-section that would have been obtained, if all radiative corrections are ignored.

The basic proof for this, which restores the ability to calculate  $e^+e^- \rightarrow \mu^+\mu^-$  and any other QED process in a perturbation series in  $\alpha^n$ , is the theorem of Kinoshita, Lee, and Nauenberg [57]. They showed, that a cancellation of mass singularities occurs in all orders of the perturbation expansion, if one sums over all states of the same energy. Mass singularities are logarithmic terms containing the photon mass  $\lambda$  or any other particle mass  $m$ , which diverge for  $\lambda, m \rightarrow 0$ . In our case the infrared (IR) divergences from the virtual photons in the vertex correction are cancelled in each order of  $\alpha$  by the infrared divergences from the real photons emitted in the Bremsstrahlung diagrams, if we sum over the degenerate states with  $\sum E_\mu + \sum E_\gamma = \sqrt{s}$ .

The usual illustration of this principle stresses the fact that any experiment can detect photons only up to a minimum energy  $E_\gamma = E_0$ . The IR divergencies from the emission of virtual (vertex correction) and real (Bremsstrahlung) photons, which occur in any calculation to finite order in  $\alpha$ , are restricted to the range  $E_\gamma < E_0$  for any finite  $E_0$ . Thus, any experiment observes a finite cross-section with zero photons, i.e. with  $E_{\gamma_i} < E_0$  for all photons  $\gamma_i$ . In addition, it finds a finite cross-section of events, where photons from Bremsstrahlung with  $E_{\gamma_i} > E_0$  are detected. Hence, the infrared divergence is absent in experimental measurements.

This argument, however, neglects the fact that events with Bremsstrahlung below  $E_0$  and events without Bremsstrahlung could *in principle* be distinguished. If the threshold  $E_0$  for an experiment is low enough, the calculations to any finite order of perturbation theory can no longer describe the observed cross-sections, as we will show below (Section 2.3.2). Thus physically there is no escape from calculating to all orders in  $\alpha$ . The cancellation of IR diver-

gencies to finite order in  $\alpha$  does not occur in a quantum mechanical sense by the cancellation of *amplitudes*. It emerges from a mathematical relation such that in a perturbation expansion for processes with *different* final states the respective IR divergencies of *cross-sections* “happen to” cancel in each order of perturbation theory. Without the knowledge of this cancellation, expressed in the Kinoshita-Lee-Nauenberg Theorem, the summation of divergent cross-sections for processes with different final states would be physically not meaningful.

When the Kinoshita-Lee-Nauenberg Theorem is fully applicable, all terms  $\propto \ln(s/m^2)$  or  $\propto \ln(\sqrt{s}/\lambda)$  vanish in the (unrenormalized)<sup>10</sup> total cross-section. Then the higher order corrections of a perturbative series are really  $\mathcal{O}((\alpha/\pi)^n)$  and do not contain large logarithms. In those cases the Born cross-section (corrected for vacuum polarization) is a very good approximation to the exact cross-section, even if the Born process itself does not at all occur in nature. As we will see below, the final state radiation in the process  $e^+e^- \rightarrow \mu^+\mu^-$  is an example for the Kinoshita-Lee-Nauenberg Theorem, whereas in the initial state radiative corrections only the  $\ln \lambda$  terms cancel, leaving large corrections  $\sim \alpha \ln(s/m_e^2) \ln(s/m_\mu^2)$ .

### Bremsstrahlung

The differential cross-section for initial or final state photon radiation is given to order  $\alpha$ , i.e. for the emission of one photon according to Diagrams 2.8(f) by [51,52]

$$\frac{d\sigma_{1,\ell}}{dx} = \sigma_0(s_\ell) \beta_\ell \frac{1}{x} \left[ \frac{1 + (1-x)^2}{2} \right], \quad (2.94)$$

where  $\ell = e, \mu$  again denotes initial and final state radiation, respectively. The radiation spectrum, valid for any electromagnetic scattering process, is expressed in terms of the photon energy fraction  $x \equiv k^0/E$ , where  $k^0$  is the photon energy and  $E$  denotes the electron beam energy. The difference between the initial and final state radiation comes from the values of  $s_\ell$  and  $\beta_\ell$ . The effective c.m. energy  $s_\ell$  is the squared 4-momentum transfer  $q^2$  of the virtual annihilation photon, which is given for one-photon Bremsstrahlung diagrams as<sup>11</sup>

$$s_\mu = s \quad (2.95)$$

$$s_e = s(1-x). \quad (2.96)$$

The final state radiation does not change the squared c.m. energy  $s$ , whereas initial photon radiation reduces  $s$  by a factor  $(1-x)$ .

The factors  $\beta_\ell$  are the “effective radiator thicknesses”

$$\beta_\ell = \frac{2\alpha}{\pi} \left( \ln \frac{s}{m_\ell^2} - 1 \right) \quad (2.97)$$

and act as an effective coupling constant for Bremsstrahlung. Around  $\sqrt{s} \approx 10$  GeV this effective coupling constants are much larger than  $\alpha$  due to the large logarithms  $\ln((10 \text{ GeV})^2/m_e^2) = 19.8$  and  $\ln((10 \text{ GeV})^2/m_\mu^2) = 9.1$ . We find  $\beta_e = 0.087$  and  $\beta_\mu = 0.038$  at  $s = (10 \text{ GeV})^2$ .

<sup>10</sup>The renormalization of the charge re-introduces large, but not divergent terms  $\propto \ln(s/m^2)$  for the vacuum polarization, as we have seen in Section 2.2.

<sup>11</sup>For multi-photon radiation  $s_e$  would read  $s_e = s(1-x) + m_\gamma^2 = s(1-x + \sum_{i>j} x_i x_j (1 - \cos \theta_{ij})/2)$ , where now  $x = \sum x_i/E$  is the sum of all radiated photon energy fractions and  $m_\gamma^2$  is the invariant mass of the radiated photons.

To get a qualitative impression of the initial and final state photon spectra we approximate  $\sigma_0 \approx \sigma_{\text{Born}}$  in Eq. (2.94) and use the relation  $\sigma_{\text{Born}}(s(1-x)) = \sigma_{\text{Born}}(s)/(1-x)$  yielding

$$\frac{d\sigma_{1,e}}{dx} = \sigma_{\text{Born}}(s)\beta_e \left[ \frac{1}{x} - \frac{1}{2} + \frac{1}{2(1-x)} \right] \quad (2.98)$$

$$\frac{d\sigma_{1,\mu}}{dx} = \sigma_{\text{Born}}(s)\beta_\mu \left[ \frac{1}{x} - 1 + \frac{x}{2} \right]. \quad (2.99)$$

Both differential cross-sections are divergent for  $x \rightarrow 0$ . For  $x \ll 1$  their ratio is given by  $\beta_e/\beta_\mu$ . E.g., for  $\sqrt{s} \approx 10$  GeV the probability for emission of low-energy photons from the initial state is (only)  $0.087/0.038 = 2.3$  times larger than for final state radiation (see Fig. 2.14). For high-energy photons, however, the initial state radiation largely dominates.

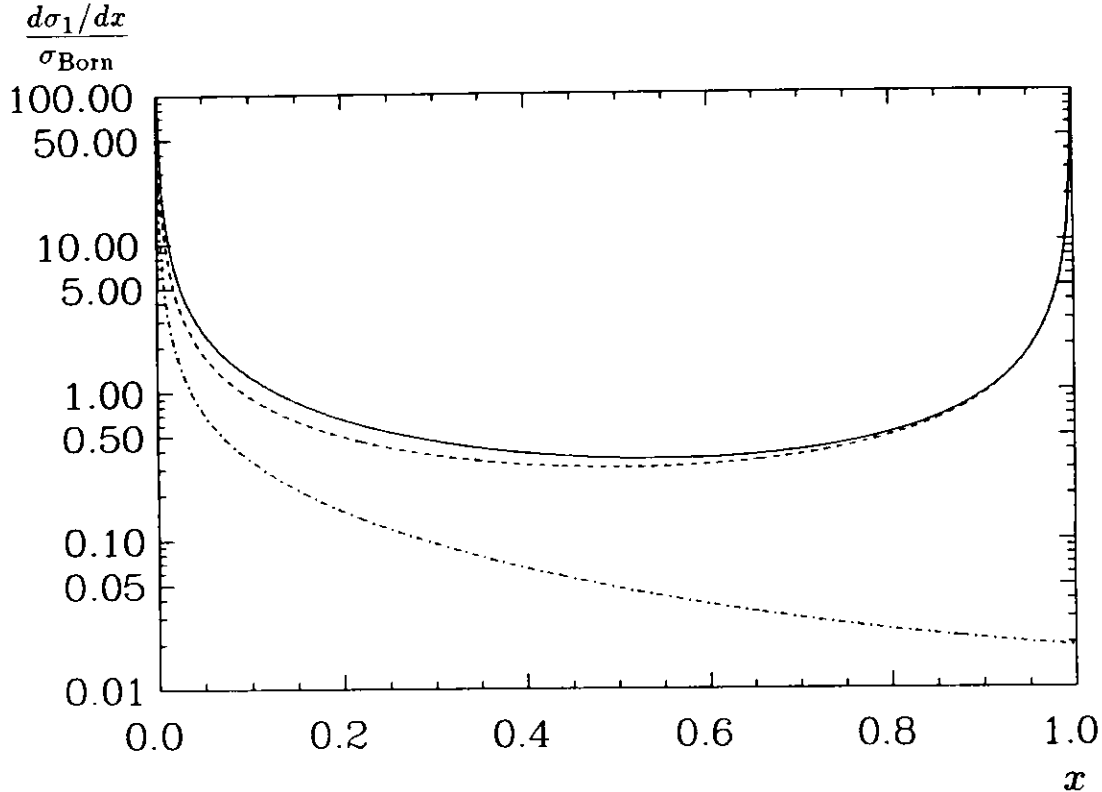


Figure 2.14: First order radiation spectra from initial (dashed) and final (dashed-dotted) state radiation and their sum (solid line).

This is due to the additional factor  $1/(1-x)$ , introduced by the scaling of the Born cross-section. In fact, there would be a divergence for  $x \rightarrow 1$ , if the energy of the initial state radiation were not limited by  $x_{\text{max}} = 1 - 4m_\mu^2/s$ , since  $s_{e,\text{min}} = s(1-x_{\text{max}}) = 4m_\mu^2$ .

In order to regularize the divergence for  $x \rightarrow 0$ , again a small photon mass  $\lambda$  is introduced. The soft photon spectrum is then integrated up to an arbitrary hard-soft limit  $x_0$ , yielding the total cross-section for the diagrams with one-photon Bremsstrahlung as

$$\begin{aligned} \sigma^{\text{BS}} &= \int_0^{x_0} \left( \frac{d\sigma_{1,e}}{dx} + \frac{d\sigma_{1,\mu}}{dx} \right) dx + \int_{x_0}^{x_{\text{max}}} \left( \frac{d\sigma_{1,e}}{dx} + \frac{d\sigma_{1,\mu}}{dx} \right) dx \\ &= \sigma_0(s)(1 + \delta_e^{\text{Soft}} + \delta_\mu^{\text{Soft}}) + \int_{x_0}^{x_{\text{max}}} \left( \frac{d\sigma_{1,e}}{dx} + \frac{d\sigma_{1,\mu}}{dx} \right) dx, \end{aligned} \quad (2.100)$$

where with  $\ell = e, \mu$  [51]

$$\delta_\ell^{\text{Soft}} = \frac{2\alpha}{\pi} \left[ -\frac{\pi^2}{6} + \frac{1}{2} \ln \frac{s}{m_\ell^2} - \frac{1}{4} \ln^2 \frac{s}{m_\ell^2} + \left( \ln \frac{s}{m_\ell^2} - 1 \right) \ln \frac{2x_0 E}{\lambda} \right]. \quad (2.101)$$

It is important to note, that this value of  $\delta^{\text{Soft}}$  has been calculated under the assumption, that the cross-section  $\sigma_0$  does not vary much in the range from  $s$  to  $s(1-x_0)$ . It is thus only valid far from resonances, which introduce large fluctuations for small changes of  $s$  (cf. Fig. 2.12).

Just like the  $\mathcal{O}(\alpha^3)$  cross-section  $\sigma^{\text{VC}}$  for  $e^+e^- \rightarrow \mu^+\mu^-$  without real photon radiation (Eq. (2.92)), the total  $\mathcal{O}(\alpha^3)$  cross-section  $\sigma^{\text{VC}}$  for  $e^+e^- \rightarrow \mu^+\mu^-\gamma$  is divergent. Comparing  $\delta_\ell^{\text{Soft}}$  (Eq. (2.101)) and  $\delta^{\text{VC}}$  (Eq. (2.93)) it is evident, that both divergencies cancel, resulting in a finite summed cross-section  $\sigma_1$  to order  $\alpha^3$

$$\begin{aligned}\sigma_1 &= \sigma^{\text{VC}} + \sigma^{\text{BS}} \\ &= \sigma_0(s)(1 + \delta_{1,e} + \beta_e \ln x_0 + \delta_{1,\mu} + \beta_\mu \ln x_0) + \int_{x_0}^{x_{\text{max}}} \left( \frac{d\sigma_{1,e}}{dx} + \frac{d\sigma_{1,\mu}}{dx} \right) dx \quad (2.102) \\ &\equiv \sigma_1^{\text{Soft}} + \sigma_1^{\text{Hard}},\end{aligned}$$

where the residual correction  $\delta_{1,\ell}$  is given from Eqs. (2.93) and (2.101) as

$$\begin{aligned}\delta_{1,\ell} &\equiv \delta_\ell^{\text{VC}} + \delta_\ell^{\text{Soft}} - \beta_\ell \ln x_0 \\ &= \frac{3}{4}\beta_\ell + \frac{2\alpha}{\pi} \left( \frac{\pi^2}{6} - \frac{1}{4} \right).\end{aligned}\quad (2.103)$$

The philosophy of the summation of divergent cross-sections  $\sigma^{\text{VC}}$  and  $\sigma^{\text{BS}}$ , belonging to different final states, has already been discussed in the previous paragraph.

To estimate, how much the cross-section is changed through the inclusion of vertex correction and Bremsstrahlung, we rewrite Eq. (2.102) as

$$\sigma_1 \equiv \sigma_{\text{Born}} + \Delta\sigma_{1,e} + \Delta\sigma_{1,\mu}. \quad (2.104)$$

If we again use for a moment the approximation  $\sigma_0 \approx \sigma_{\text{Born}}$ , we find the respective corrections

$$\frac{\Delta\sigma_{1,\ell}}{\sigma_{\text{Born}}} = \delta_{1,\ell} + \beta_\ell \ln x_0 + \frac{1}{\sigma_{\text{Born}}} \int_{x_0}^{x_{\text{max}}} \frac{d\sigma_{1,\ell}}{dx} dx \quad \ell = e, \mu. \quad (2.105)$$

Inserting the approximated final state spectrum from Eq. (2.99) and evaluating the integral yields

$$\begin{aligned}\frac{\Delta\sigma_{1,\mu}}{\sigma_{\text{Born}}} &= \delta_{1,\mu} + \beta_\mu \ln x_0 + \beta_\mu \int_{x_0 \approx 0}^{x_{\text{max}} \approx 1} \left( \frac{1}{x} - 1 + \frac{x}{2} \right) dx \\ &\approx \delta_{1,\mu} + \beta_\mu \ln x_0 - \beta_\mu \ln x_0 - \frac{3}{4}\beta_\mu \\ &= \frac{2\alpha}{\pi} \left( \frac{\pi^2}{6} - \frac{1}{4} \right).\end{aligned}\quad (2.106)$$

This is a very small correction of  $\mathcal{O}(\alpha/\pi)$ , as expected from the Kinoshita-Lee-Nauenberg Theorem. All logarithmic mass terms contained in  $\beta_\mu$  have cancelled<sup>12</sup>. On the other hand, the initial state correction is given from Eqs. (2.98) and (2.105) approximately as

$$\begin{aligned}\frac{\Delta\sigma_{1,e}}{\sigma_{\text{Born}}} &= \delta_{1,e} + \beta_e \ln x_0 + \beta_e \int_{x_0 \approx 0}^{x_{\text{max}} = 1 - 4m_\mu^2/s} \left( \frac{1}{x} - \frac{1}{2} + \frac{1}{2(1-x)} \right) dx \\ &\approx \delta_{1,e} + \beta_e \ln x_0 - \beta_e \ln x_0 - \frac{1}{2}\beta_e - \frac{1}{2}\beta_e \ln \frac{4m_\mu^2}{s} \\ &\approx \frac{1}{2}\beta_e \left( \ln \frac{s}{4m_\mu^2} + \frac{1}{2} \right) = 0.36 \quad \text{for } s = (10 \text{ GeV})^2.\end{aligned}\quad (2.107)$$

<sup>12</sup>The exact result of this correction is the famous value  $3\alpha/4\pi = 0.0017$ .



This large correction arises from the product of large logarithmic mass terms  $\sim \ln(s/m_e^2) \times \ln(s/m_\mu^2)$ , which are not cancelled here, since the initial state radiation spectrum acquires a singularity  $\propto 1/(1-x)$  in contrast to the final state spectrum. The correction comes from events with initial state photons of high energy, which change the invariant mass of the virtual annihilation photon to  $s_e = (1-x)s$ . Thereby the annihilation cross-section is increased  $\propto 1/s_e$ . In the language of the Kinoshita-Lee-Nauenberg Theorem we do not expect a cancellation of the lepton mass terms, because we are not summing over all degenerate initial states. The machine preselects the electron and the positron to have energy  $E$  each and no other degenerate states participate in the interaction. In contrast to the lepton mass terms, the photon mass terms cancel for both, the initial and the final state radiation. This ensures the total cross-section to  $\mathcal{O}(\alpha^3)$  to be finite.

Altogether, we find from the non-resonant Diagrams 2.8(a), (b), and (d-f) corrections to the Born cross-section, which are at  $\sqrt{s}=10$  GeV about 7.8% from the vacuum polarization (Eq. (2.81)), about 36% from the initial state radiation (Eq. (2.107)), and about 0.2% from the final state radiation (Eq. (2.106)). The total non-resonant  $\mathcal{O}(\alpha^3)$  correction is thus 44%. From these numbers one may conclude, that corrections due to initial state radiation are large, whereas that of final state radiation are small. However, this is only true, if the *total* cross-section for  $e^+e^- \rightarrow \mu^+\mu^-$  is calculated. Performing a measurement of this process, the prediction for the *observed* cross-section obtained with a given detector and set of selection cuts is relevant. The effect of Bremsstrahlung is twofold. First, there are additional photons in the event, and second, the acollinearity of the final state muons differs from  $180^\circ$ . Thus, typical selection cuts will reject most of the events containing high-energy photons. This will reduce the large correction from initial state radiation. In the low-energy photon region initial state radiation at  $\sqrt{s}=10$  GeV is only a factor of 2.3 more frequent than final state radiation. Moreover, it is very much peaked in beam direction where the photons remain unobserved. The final state radiation, on the contrary, prefers the direction of the outgoing muons. When both muons are observed, then also the final state photons enter the detector. If a detector is sensitive to low-energetic photons, this may further enhance the the influence of final state radiation. Compared to the pure Born prediction, the inclusion of final state radiation will always lower the observed  $\mu$ -pair cross-section. The sign of the initial state correction depends on the selection cuts applied. Typically, both initial and final state corrections to the predictions for the observed cross-section amount up to  $\sim 10\%$ , in contrast to the corresponding corrections on the total cross-section derived above.

How a realistic simulation of Bremsstrahlung can be achieved with the help of Monte Carlo event generators will be discussed in Section 2.3.3. It is already clear from the above discussion, that both, initial and final state radiation, have to be implemented as completely as possible to supply a precise prediction for the observed cross-section for the process  $e^+e^- \rightarrow \mu^+\mu^-$ . We will thus first discuss the effects of higher order Bremsstrahlung corrections.

### 2.3.2 Higher Order Bremsstrahlung and Exponentiation

The separation of the total cross-section  $\sigma_1$  for  $e^+e^- \rightarrow \mu^+\mu^-(\gamma)$  into a soft and a hard photon part (see Eq. (2.102)) leads to the introduction of an arbitrary hard-soft limit  $x_0$ . The corrections  $\Delta\sigma_{1,t}/\sigma_{\text{Born}}$  (Eq. (2.105)), and thus the analytic calculation of the *total* cross-section  $\sigma_1$ , do not depend on  $x_0$ , as long as  $x_0 \leq 10^{-2}$ . Then the approximations in the derivation of Eqs. (2.106) and (2.107) are justified.

Any Monte Carlo (MC) simulation, based on Eq. (2.102), on the other hand, follows the differential cross-section  $d\sigma_1/dx$  (Eq. (2.94)) to generate radiative events  $e^+e^- \rightarrow \mu^+\mu^-\gamma$  in the hard photon region. In the soft photon region a MC produces non-radiative Born-

like events. However, the soft photon cross-section  $\sigma_1^{\text{Soft}}$  in Eq. (2.102) is positive only for<sup>13</sup>  $x_0 \geq 10^{-4}$  at  $\sqrt{s} \approx 10$  GeV, and for  $x_0 \geq 10^{-3}$  at  $\sqrt{s} \approx 100$  GeV. A MC simulation down to arbitrary low photon energies is thus not possible with Eq. (2.102), since the hard photon cross-section above  $x_0$  is obviously too large. Precision measurements, however, require a correct simulation of the photon spectra at least down to  $x_0 = 10^{-3}$ . It is therefore necessary to incorporate higher order Bremsstrahlung corrections.

To investigate the behaviour of those higher order corrections, it is sufficient to restrict ourselves to initial state radiation. Calculating the real Bremsstrahlung and virtual vertex corrections up to  $\mathcal{O}(\alpha^2)$  yields for  $x_0 \ll 1$  [52,58]

$$\sigma_2 = \sigma_0(s) \left( 1 + \delta_{1,e} + \delta_{2,e} + (1 + \delta_{1,e})\beta_e \ln x_0 + \frac{1}{2}\beta_e^2 \ln^2 x_0 \right) + \int_{x_0}^{x_{\text{max}}} \frac{d\sigma_{2,e}}{dx} dx, \quad (2.108)$$

where

$$\frac{d\sigma_{2,e}}{dx} = \sigma_0(s_e) \left[ \beta_e \frac{1}{x} \left( \frac{1 + (1-x)^2}{2} \right) (1 + \delta_{1,e} + \beta_e \ln x) + \mathcal{O} \left( \frac{\alpha^2}{\pi^2} \right) \right], \quad (2.109)$$

and  $\delta_{2,e} = 0.0035$  at  $\sqrt{s} = 10$  GeV emerges analogously to  $\delta_{1,e}$  as residual term from the cancellation of the infrared divergencies for real and virtual photons. Its value is slightly dependent on the treatment of real and virtual pair production (cf. footnote 12 in Ref. [52]). The photon energy variable  $x$  is now denoting the total energy radiated by both photons.

We see, however, that the  $x_0$  problem has not vanished. Only its sign has changed. For  $x_0 \rightarrow 0$  the soft photon cross-section now diverges to  $+\infty$ , whereas the hard photon cross-section, given by the integral in Eq. (2.108), diverges to  $-\infty$ . The sum of both, i.e.  $\sigma_2$ , is again finite. If we add the corresponding terms for final state radiation ( $e \rightarrow \mu$ ), we even notice, that unphysical negative cross-sections occur below precisely the same lower limit of  $x_0$  as they did in the first order radiative cross-section of Eq. (2.102). The  $x_0$  problem actually cannot be overcome by going to any finite higher order. The only way out is the so-called exponentiation procedure going to fully infinite order in  $\alpha$ . For that Eq. (2.108) is rewritten as

$$\sigma_2 = \sigma_0(s)(1 + \delta_{1,e} + \delta_{2,e})(1 + \beta_e \ln x_0 + \frac{1}{2}\beta_e^2 \ln^2 x_0) + \int_{x_0}^{x_{\text{max}}} \frac{d\sigma_{2,e}}{dx} dx, \quad (2.110)$$

with

$$\frac{d\sigma_{2,e}}{dx} = \sigma_0(s_e) \left[ \beta_e \frac{1}{x} \left( \frac{1 + (1-x)^2}{2} \right) (1 + \delta_{1,e})(1 + \beta_e \ln x) + \mathcal{O} \left( \frac{\alpha^2}{\pi^2} \right) \right], \quad (2.111)$$

which is identical to Eqs. (2.108) and (2.109) up to second order radiative corrections. We recognize the expansion of an exponential

$$x^{\beta_e} = \exp(\beta_e \ln x) = \sum_{m=0}^{\infty} \frac{1}{m!} (\beta_e \ln x)^m \quad (2.112)$$

in the soft photon cross-section as well as in the hard photon spectrum. That all terms of this expansion are realized as leading logarithms in the perturbation series has been proven in the classic paper by Yennie, Frautschi, and Suura [59].

<sup>13</sup>Actually, through the interference between initial and final state radiation, which we have neglected, the soft photon cross-section depends on the muon angle  $\theta$ . Requiring  $d\sigma_1^{\text{Soft}}(\theta)/d\Omega > 0$  for all  $\theta$  further increases the lower bounds of the allowed region for the hard-soft limit by a factor of 10.

The exponentiated cross-section, exact to second order, then reads

$$\sigma_2^{\text{exp}} = \sigma_0(s)(1 + \delta_{1,e} + \delta_{2,e})x_0^{\beta_e} + \int_{x_0}^{x_{\text{max}}} \frac{d\sigma_{2,e}^{\text{exp}}}{dx} dx, \quad (2.113)$$

with<sup>14</sup>

$$\frac{d\sigma_{2,e}^{\text{exp}}}{dx} = \sigma_0(s_e) \left[ \beta_e \frac{1}{x^{1-\beta_e}} \left( \frac{1 + (1-x)^2}{2} \right) (1 + \delta_{1,e} + \delta_{2,e}) + \mathcal{O}\left(\frac{\alpha^2}{\pi^2}\right) \right], \quad (2.114)$$

where the  $\delta_2$  term is usually added in  $d\sigma_{2,e}^{\text{exp}}/dx$  to ensure

$$\begin{aligned} \sigma_2^{\text{Soft}} &= \int_0^{x_0} \frac{d\sigma_{2,e}^{\text{exp}}}{dx} dx \approx \sigma_0(s) \int_0^{x_0} \beta_e \frac{1}{x^{1-\beta_e}} (1 + \delta_{1,e} + \delta_{2,e}) dx \quad \text{for } x_0 \ll 1 \\ &= \sigma_0(s)(1 + \delta_{1,e} + \delta_{2,e})x_0^{\beta_e}. \end{aligned} \quad (2.115)$$

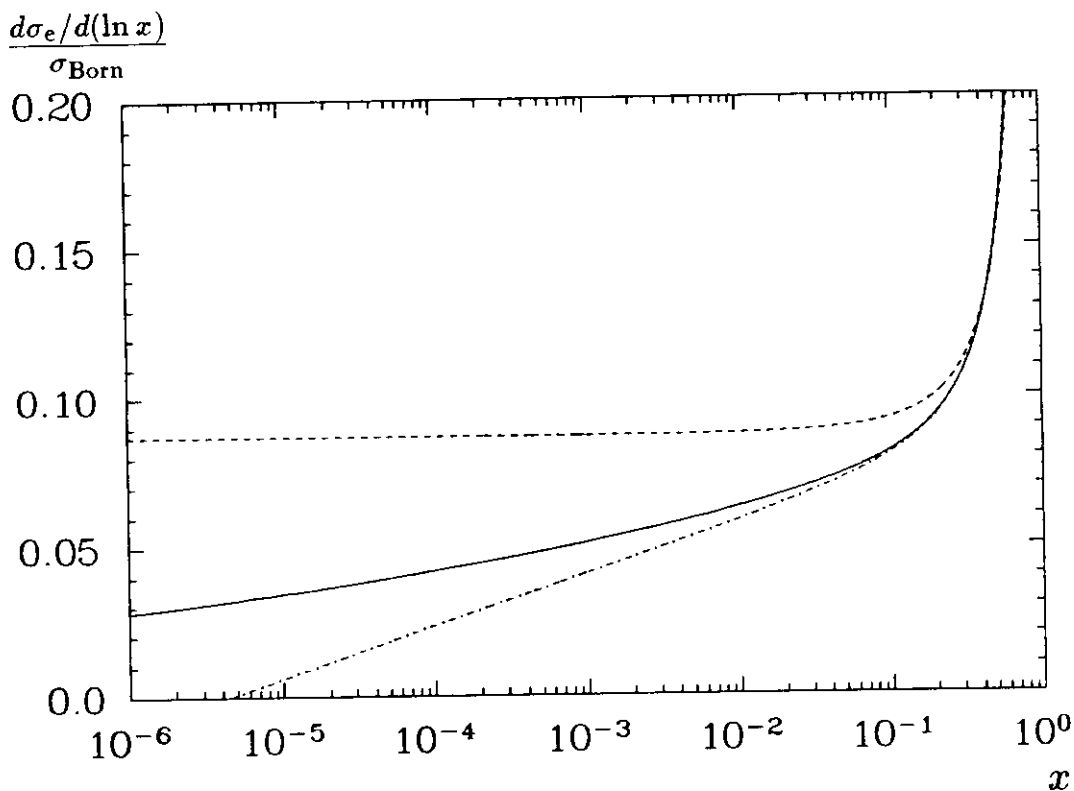


Figure 2.15: Initial state radiation spectra. The dashed line is the first order Eq. (2.98), the dashed-dotted line the second order Eq. (2.109), and the solid line describes the exponentiated spectrum of Eq. (2.114). Note, that the dashed line in this figure ( $d\sigma_{1,e}/d\ln x$ ) describes the same spectrum as the dashed line ( $d\sigma_{1,e}/dx$ ) in Fig. 2.14.

The soft photon cross-section in Eq. (2.115) is now positive for arbitrary low values of  $x_0$ . Moreover, comparing Eqs. (2.115) and (2.113) it is obvious, that the hard-soft limit  $x_0$  has become unnecessary, and the differential cross-section of Eq. (2.114) is valid over the full energy range, i.e.

$$\sigma_2^{\text{exp}} = \int_0^{x_{\text{max}}} \frac{d\sigma_{2,e}^{\text{exp}}}{dx} dx. \quad (2.116)$$

<sup>14</sup> Since exponentiation is only rigorous in the limit  $x \rightarrow 0$ , often only the soft photon part is exponentiated. The term  $1/x^{1-\beta_e}$  then appears not as a factor, but rather as the first term in a sum (cf. Eqs. (2.98) and (2.99)).

The main effect of exponentiation is the modification of the low-energy photon spectrum from  $1/x$  to  $1/x^{1-\beta_e}$ . Thereby the cross-section without photon emission is made to vanish exactly (Eq. (2.116)), as required by the Bloch-Nordsieck Theorem.

We have plotted the initial state spectra  $d\sigma_e/d\ln x = x \cdot d\sigma_e/dx$  for the first order (Eq. (2.98)), the second order (Eq. (2.109)), and the second order exponentiated spectrum (Eq. (2.114)) in Fig. 2.15 for  $\sqrt{s} \approx 10$  GeV. In the latter two spectra, the small terms denoted by  $\mathcal{O}(\alpha^2/\pi^2)$  have been omitted. The approximation  $\sigma_0(s_e) \approx \sigma_{\text{Born}}(s)/(1-x)$  has been applied for all spectra. For small  $x$  these spectra exhibit considerable differences. In applications, where a proper simulation of photons below  $x = 0.1$  is needed, the use of the exponentiated spectrum is mandatory (cf. Section 2.3.5).

Eq. (2.113) holds only far from resonances, where the cross-section  $\sigma_0(s_e)$  is approximately constant for  $s_e$  in the range between  $s$  and  $s(1-x_0)$ . In contrast to that, Eq. (2.116) is even valid near narrow resonances. It does no longer contain a term, derived from integrating the soft photon cross section under the assumption of a constant  $\sigma_0(s_e)$ . The differential spectrum of Eq. (2.114) properly accounts for resonances in  $\sigma_0(s_e)$ , accessible by photon radiation. Combining Eqs. (2.116), (2.114), and (2.90) we have a complete treatment of the process  $e^+e^- \rightarrow \mu^+\mu^-$  in the 10 GeV range. It covers exponentiated initial state radiation exact to second order, and includes all diagrams depicted in Fig. 2.8(a-e). The final state Bremsstrahlung can be exponentiated and included analogously.

### 2.3.3 MC Methods for Generating Radiative $\mu$ -Pair Events

As already discussed in Section 2.3.1, the prediction for the *observed* cross-section of the process  $e^+e^- \rightarrow \mu^+\mu^-$  for a given detector and data selection is the essential quantity for experimental measurements. These predictions can only be obtained by means of MC event generation and simulation of the detector response. There are basically three methods of generating radiative  $\mu$ -pair events, which can be distinguished e.g. by the number of generated photons. A more detailed discussion of methods and generators can be found in Ref. [60].

**The classic one-photon approach** is applied in the generators BKMUON [61], MMG1 [51], and MUSTRAAL [62] written by Berends, Kleiss, and Jadach. It creates events with zero or one photon, basically following the cross-section  $\sigma_1$  from Eq. (2.102). In the soft photon region, non-radiative Born-like events are produced, whereas events with one photon are generated for photon energy fractions above the hard-soft limit  $x_0$ . The photon is attributed to initial or final state Bremsstrahlung according to their respective differential cross-sections. These differential cross-sections may be exponentiated (as in BKMUON) or not (as in MMG1 and MUSTRAAL). Even if the spectra are exponentiated, the hard-soft limit can not be pushed to arbitrary low values. Since only one photon is emitted, the initial state radiation would fill for  $x_0 = 0$  the complete cross-section, leaving no room for final state radiation (and vice versa).

**The exclusive exponentiation** is the rigorous exponentiation procedure for the multibody Lorentz-invariant phase space, as derived in the classic work of Yennie, Frautschi, and Suura [59]. It is utilized in the YFS2 Monte Carlo [63] by Jadach and Ward. In the usual *inclusive* (“ad hoc”) exponentiation, discussed in Section 2.3.2, the continuation of the soft photon exponentiation into the hard photon region is somewhat ambiguous (see footnote 14 on page 41). The deeper reason for that is, that the higher order corrections correspond to the emission of many photons, but are exponentiated into a energy spectrum of a single photon. In the *exclusive* exponentiation, on the other hand, there is no need for inventing an interpolation between a soft and a hard photon



region [64]. Instead, an arbitrary large number of photons is explicitly generated over the entire phase space. An energy cutoff  $x_0$  limits this number in practical applications, but can in principle be set arbitrarily low.

The explicit generation of many photons has two additional advantages. First, the prediction for the *observed* cross-section improves, since the photons may be seen in the detector. Second, the initial state photons may require a non-zero invariant mass (see footnote 11 on page 36), and can thus model muon kinematics, which are not accessible by one photon, only.

The YFS2 generator is based on the exclusive exponentiation of the initial state radiation spectrum, exact to  $\mathcal{O}(\alpha^2)$ . Alas, it generates no final state radiation. This weak point is overcome in the KORALZ generator [65], based on the YFS2 program. A disadvantage of both programs is the length and complexity of their codes, rendering extensions or modifications very difficult for the user.

**The structure function approach** is a sort of compromise between the one-photon approach and the exclusive Yennie-Frautschi-Suura (YFS) exponentiation. Based on a resummation technique of Gribov and Lipatov [66], Kuraiev and Fadin [67] have calculated the probability distribution (structure function)  $D_e(z_{+/-}, s)$  for the electron (-) or positron (+) to emit an arbitrary number of photons with an energy sum  $x_{+/-} = \sum k_i^0/E$  in an interaction with c.m. energy  $\sqrt{s} = 2E$ . The electron and the positron are then left at the interaction vertex with a fraction  $z_{+/-} = 1 - x_{+/-}$  of their initial energy. (An analogous structure function, the evolution of the quark distribution in the proton with  $\ln q^2$  [68], has been used already for a long time to describe QCD Drell-Yan processes [69].)

The structure functions  $D_e$  (and  $D_\mu$ ) for initial (and final) state radiation are normally exploited to generate one photon per particle, i.e. at most 4 photons for the process  $e^+e^- \rightarrow \mu^+\mu^-$ . Then, however, the information about the emission angle is lost, since each generated photon carries the summed energy of all photons emitted from the respective lepton line. Without a reinstatement of a photon angular distribution, a structure function MC is little useful for experiments with photon detection. However, as soon as an angular distribution for photon radiation is attached, it clearly improves over the one-photon approach by two reasons. First, including exponentiation and generating more than one photon in a single event opens the possibility to set the  $x_0$  parameter arbitrarily low. Second, the two initial state photons acquire an invariant mass-distribution which is very close to that from the rigorous YFS exponentiation.

In fact, the structure function approach has even one advantage compared to the YFS exponentiation. The radiative corrections are explicitly decoupled from the annihilation process, so that the functional dependences of the annihilation cross-section  $\sigma_0(s_e)$  can be easily modified. An introduction of a finite c.m. energy spread  $w$  creates no severe problems, likewise. For this reasons we have chosen the structure function generator DYMU2 [70] as the basis for our simulation of  $e^+e^- \rightarrow \mu^+\mu^-$  events. This generator, our changes, and the application of our modified generator are described below.

### 2.3.4 The DYMU2 Generator

In their DYMU2 generator, Campagne and Zitoun apply the structure function approach to generate two initial state photons and one final state photon according to a differential cross-section of

$$\frac{d\sigma}{dx_+ dx_- dy} = (1 + K_1 + K_2) D_e(1 - x_+, s) D_e(1 - x_-, s) \sigma_0(s_e) D_\mu(1 - y, s_e), \quad (2.117)$$

where  $y \equiv 2k^0/\sqrt{s_e}$  denotes the final state photon energy fraction in the  $\gamma\mu\mu$  c.m. system. Initial state radiation is described by the exponentiated structure functions  $D_e$ , which are exact to order  $\alpha^2$ . Final state radiation is given by the exponentiated structure function  $D_\mu$ , which is exact only to order  $\alpha$  and thus attached to only one of the outgoing muons. The most important terms of  $D_e$  can be motivated from the squared bracket in Eq. (2.114) as follows.

First, the effective Bremsstrahlung coupling constant  $\beta_e$  has to be replaced by  $\beta_e/2$  to distribute the photons over two electrons. Second, only the terms  $\propto \beta_e^j$  are kept in  $\delta_{j,e} \equiv d_j \beta_e^j + K_j$ , where  $d_1 = 3/4$  and  $K_1 = 2\alpha/\pi(\pi^2/6 - 1/4)$  can be directly read off Eq. (2.103). (The terms  $K_j$  explicitly appear in a so-called K-factor in Eq. (2.117) to guarantee for the normalization of  $D_e$ ). Finally, the exponentiation is performed for the soft photon part  $\propto 1/x$  only, yielding

$$D_e(1 - x, s) = \frac{\beta_e}{2} \left[ \frac{1}{x^{1-\beta_e/2}} \left( 1 + d_1 \frac{\beta_e}{2} + d_2 \left( \frac{\beta_e}{2} \right)^2 \right) - 1 + \frac{x}{2} \right] + \mathcal{O} \left( \frac{\alpha^2}{\pi^2} \right). \quad (2.118)$$

The proper derivation of this expression for  $D_e$ , including the  $\mathcal{O}(\alpha^2/\pi^2)$  terms, has been performed in Ref. [67]. Campagne and Zitoun refined this structure function [71] such, that its double appearance in Eq. (2.117) leads to a total cross-section, which is precisely equal to the exact  $\mathcal{O}(\alpha^2)$  result of Ref. [72].

The final state structure function is given to  $\mathcal{O}(\alpha)$  as

$$D_\mu(1 - y, s_e) = \beta_\mu \left[ \frac{1}{y^{1-\beta_\mu}} (1 + d_1 \beta_\mu + K_1) - 1 + \frac{y}{2} \right], \quad (2.119)$$

which has to be compared to Eq. (2.99). The emission of photons under finite angles to the radiating particles has to be attached “by hand” to a structure function MC. In DYMU2 the first order distribution from Ref. [51] is used for emission of both, initial and final state photons.

All radiative corrections are decoupled from the annihilation cross-section  $\sigma_0$ , which has to be evaluated after initial state radiation at the c.m. energy  $s_e$  of the electrons, which is given by

$$s_e = s(1 - x_+ - x_- + x_+ x_- [1 - \cos \theta_{+-}]/2) \quad (2.120)$$

$$\equiv s(1 - v), \quad (2.121)$$

where  $\theta_{+-}$  is the angle between the two initial state photons. As the DYMU2 generator — like most of the other generators discussed above — was written for the  $Z^0$  peak, it uses the identity [73]

$$\alpha_{em}(m_Z) = \frac{\alpha}{|1 - \Pi_\gamma(m_Z)|} = \frac{\sqrt{2}}{\pi} G_F m_Z^2 \sin^2 \theta_W \cos^2 \theta_W \quad (2.122)$$

to include the vacuum polarization via [71]

$$\begin{aligned}\sigma_0(s) &= \frac{4\pi\alpha_{em}^2(m_Z)}{3s}(1 + Z(s)) \\ &= \frac{8}{3\pi s}G_F^2 m_Z^4 \sin^4\theta_W \cos^4\theta_W(1 + Z(s)),\end{aligned}\quad (2.123)$$

where  $Z(s)$  denotes the  $\gamma$ - $Z$  interference and pure  $Z$  terms in the cross-section (cf. Eq. (2.72)).

In this work we utilize the DYMU2 generator as a very efficient and flexible tool for generating  $e^+e^- \rightarrow \mu^+\mu^-$  events in the c.m. energy region of the  $\Upsilon$  resonances, as well as for obtaining predictions for cross-sections separately for resonance production, continuum, and for their interference. For this purpose we have introduced two modifications.

First, the scheme of Eq. (2.122) for covering the vacuum polarization at the  $Z^0$  resonance is not valid at  $\sqrt{s} \approx 10$  GeV. We replace the annihilation cross-section  $\sigma_0$  of Eq. (2.123) by Eq. (2.90), which covers explicitly the vacuum polarization  $\Pi_\gamma(s)$  as well as all  $\Upsilon$  resonances and their interference terms with the continuum<sup>15</sup>. The calculation of the leptonic part of the vacuum polarization is performed according to Eq. (2.77), whereas for the hadronic part we use the routine PIHINT [61,51,62], which interpolates the results of Ref. [74].

Second, to generate a correct prediction for shape and magnitude of the resonance cross-sections, we include the spread of the DORIS c.m. energy. It is Gaussian distributed around a mean energy  $W$  according to

$$G(\sqrt{s} - W) = \frac{1}{\sqrt{2\pi}w} \exp\left[-\frac{(\sqrt{s} - W)^2}{2w^2}\right],\quad (2.124)$$

At DORIS II, the width of this distribution is  $w = 7.9$  MeV and  $w = 8.2$  MeV for  $W$  in the region of the  $\Upsilon(1S)$  and  $\Upsilon(2S)$  resonances, respectively. (These values will be determined in Section 6.2.1.) We select a new c.m. energy for each event following the probability distribution of Eq. (2.124).

The total generated cross-section is thus simulated by the double convolution

$$\begin{aligned}\sigma^{ee \rightarrow \mu\mu}(W) &= (1 + K_1 + K_2) \int_0^\infty G(\sqrt{s} - W) \times \\ &\int_0^{v_1} \int_0^{y_{max}(v)} D_e(1 - x_+, s) D_e(1 - x_-, s) \sigma_0(s(1 - v)) D_\mu(1 - y, s(1 - v)) dy dv (x_+, x_-) d\sqrt{s},\end{aligned}\quad (2.125)$$

where  $v$  is defined in Eq. (2.121). Photons are explicitly generated above  $x_+, x_-, y > x_0$ . The limit  $x_0$  was chosen to  $x_0 = 10^{-5}$ , which is much less than  $w/E \approx 1.6 \times 10^{-3}$ , to obtain a precise prediction for the resonance shape (see below). The final state photons were generated up to their kinematic limit of  $y_{max} = 1 - 4m_\mu^2/s(1 - v)$ . The kinematic limit of  $v_{max} = 1 - 4m_\mu^2/s$  for initial state radiation, which ranges from 0.9995 at  $\sqrt{s} = 9.46$  GeV to 0.9996 at  $\sqrt{s} = 10.58$  GeV, cannot be reached with a reasonable amount of CPU time consumption. This restriction does not harm, since the acceptance of standard  $\mu$ -pair selections is negligibly small for  $v \rightarrow 1$ . We run the DYMU2 generator with an upper limit of  $v_1 = 0.99$ , i.e. with a minimum c.m. energy after initial state radiation of  $\sqrt{s_{e,min}} = \sqrt{s(1 - v_1)} = 0.1\sqrt{s}$ .

To give an impression about the abundance of radiated photons, we list in Table 2.7 the percentage of generated events with 0, 1, 2, or 3 photons above  $x_0 = 10^{-5}$  for c.m. energies in the continuum below the  $\Upsilon(1S)$ . We also give the corresponding numbers for subsequently imposing the conditions, that the photons are not collinear to the beams and not collinear

<sup>15</sup>Since for the  $\Upsilon$  resonances  $\Gamma/E \approx 10^{-5}$  is very small, it is essential to perform the computer calculations of  $s_e$  and  $\sigma_0(s_e)$  in double precision.

to the outgoing muons. (The cuts on the collinearity are chosen typical for the detection capabilities of the Crystal Ball detector, which is in principle sensitive to energy depositions down to  $x = 7 \times 10^{-5}$ .) From the decrease of the event fractions with increasing number of photons we deduce, that the restriction to at most three explicitly generated photons is well justified. Note, that also those photons, which are emitted collinear to the leptons, may perceptibly influence the event signature via the muon acollinearity (initial state photons) or the lateral spread of the muonic energy deposition in the detector (final state photons).

Table 2.7: The percentage of  $e^+e^- \rightarrow \mu^+\mu^-$  events from the DYMU2 generator with 0, 1, 2, or 3 photons fulfilling the listed conditions.

number of photons	0	1	2	3	sum
$x > 10^{-5}$	28.4	44.4	23.2	4.0	100
and not col. to beams within $21^\circ$	60.9	35.2	3.8	0.1	100
and not col. to muons within $14^\circ$	74.6	23.4	1.9	0.03	100

The modified DYMU2 generator is extensively used throughout this work for calculations of cross-sections and simulation of the detector acceptance for various “components” of the total cross-section  $\sigma^{e^+e^- \rightarrow \mu^+\mu^-}$ . The following components are modeled by optionally selecting or dropping certain terms in  $\sigma_0$  from Eq. (2.90).

- a) **Continuum Under a Given Resonance:** For simulating continuum events in the c.m. region of the  $\Upsilon(1S)$  and  $\Upsilon(2S)$  resonances, the corresponding resonance term and its interference with the continuum are removed from the cross-section. This is achieved by setting  $B_n \equiv 0$  for  $n = 1$  and  $n = 2$  in Eq. (2.90), respectively. The resulting event sample models the continuum cross-section below the given  $\Upsilon$  resonance. It includes all effects induced by the other  $\Upsilon$  resonances, e.g. their summed interference effects (cf. Fig. 2.12) and their radiative tails (not included in Fig. 2.12). Accounting for these effects is important, because they modify the  $1/s$  dependence of the continuum cross-section.
- b) **Pure Resonance Excitation:** By setting  $\sigma_0 = \sigma_{\text{Born}}|B_n|^2$  for  $n = 1, 2$  we simulate the pure resonance excitation  $e^+e^- \rightarrow (\gamma\gamma)\Upsilon \rightarrow (\gamma\gamma)\mu^+\mu^-(\gamma)$ . The generator then automatically creates initial state photon energies, which lead to a c.m. energy  $s_e \approx m_\Upsilon$ . Event samples generated in this mode at different mean c.m. energies  $W$  in the region of the  $\Upsilon$  resonances are the basis for calculating the  $\mu$ -pair selection efficiency for  $\Upsilon \rightarrow \mu^+\mu^-$  as a function of  $W$ .
- c) **Cross-section for  $\Upsilon \rightarrow \mu^+\mu^-$  as a function of  $W$ :** In addition to creating event samples for acceptance and efficiency calculations, as in (a) and (b), we use the DYMU2 generator as a tool to perform the convolution of non-radiative cross-section  $\sigma_0$ , radiation spectrum, and c.m. energy spread. In this mode of application we are not interested in the generated events, but only in the total cross-section. We run DYMU2 with the full expression for  $\sigma_0$  at different mean c.m. energies  $W$ , and subtract point by point the predicted continuum cross-section, obtained according to (a). The result, displayed as dots in Fig. 2.16, is the sum of the  $\Upsilon$  resonance excitation curve and its interference with the continuum, since both terms have been dropped in (a). Analogously we can obtain the  $\Upsilon$  excitation curve without interference (solid lines in Fig. 2.16) by starting with an expression for  $\sigma_0$ , where the interference terms are omitted. Finally, by subtracting the two curves from each other, we extract the interference contribution as a

function of  $W$  (dashed lines in Fig. 2.16). In our data analysis the latter curve is used to correct the measured  $\mu$ -pair cross-section for the interference effect (see Section 6.2). The  $W$ -dependence of the measured cross-section is fitted with the help of the former two curves (see Section 6.3).

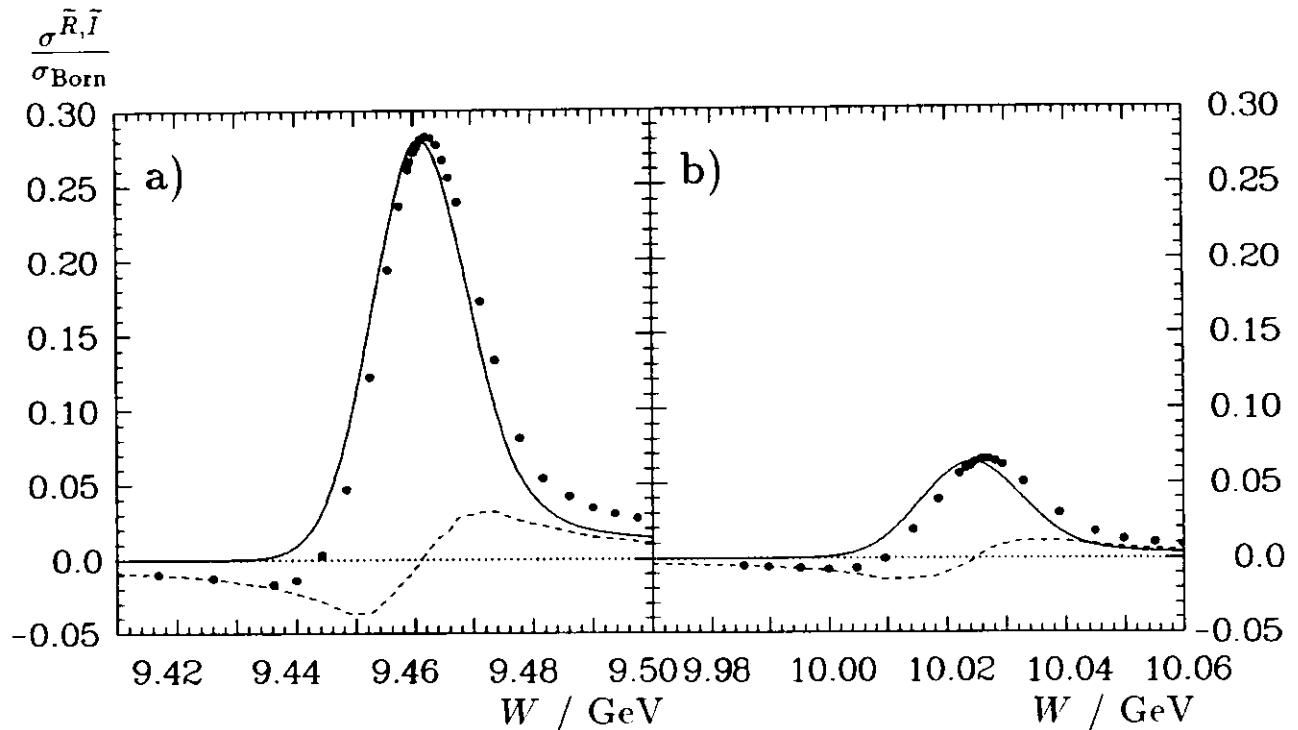


Figure 2.16: The resonance excitation curve  $\sigma^{\bar{R}}$  (solid line) its interference with the continuum  $\sigma^{\bar{I}}$  (dashed line), and the sum of both (dots) for the  $\Upsilon(1S)$  (a) and the  $\Upsilon(2S)$  (b) as predicted by the DYMU2 generator for the DORIS c.m. energy spread. All curves are plotted in units of the Born cross-section for the continuum process  $e^+e^- \rightarrow \mu^+\mu^-$ . We used the  $\Upsilon$  parameters from Ref. [22].

### 2.3.5 Effects of Bremsstrahlung and C.M. Energy Spread on Resonance Production

The double convolution with the DORIS c.m. energy spread and the spectrum for initial state radiation drastically changes the shape and magnitude of the  $\Upsilon$  resonance peaks. The peak cross-sections at  $\sqrt{s}=m_\Upsilon$ , originally amounting to  $R_0(1S)=111\sigma_{\text{Born}}$  and  $R_0(2S)=32\sigma_{\text{Born}}$  (cf. Fig. 2.9), are now reduced to  $\bar{R}(1S)=0.28\sigma_{\text{Born}}$  and  $\bar{R}(2S)=0.064\sigma_{\text{Born}}$  and slightly shifted to  $W_{\text{peak}} = m_\Upsilon + (1.0 \pm 0.1)$  MeV (solid lines in Fig. 2.16). This means, that only a relatively small excess of  $\mu$ -pairs from  $\Upsilon$  resonance decays can be observed above the continuum cross-section, in contrast to what might be expected from Fig. 2.9. In addition, the width of the peak is now of the order of the c.m. energy spread, exhibiting a distinct tail to higher c.m. energies.

An approximate analytical expression for the magnitude of the peak reduction can be obtained from estimating the effects of successively convoluting the non-radiative cross-section  $\sigma_0$  with  $G(\sqrt{s} - W)$  and the Bremsstrahlung spectrum. Convoluting first with the Gaussian distribution  $G(\sqrt{s} - W)$  of Eq. (2.124), the area  $A$  under the non-radiative Breit-Wigner will

not change. This area is given as

$$A = \frac{6\pi^2 \Gamma_{ee} \Gamma_{\mu\mu}}{M^2 \Gamma} = \frac{\pi}{2} \Gamma R_0, \quad (2.126)$$

where we have inserted the peak cross-section  $R_0$  from Eq. (2.88). Since  $\Gamma \ll w$  we can assume that the resonance shape is a Gaussian of width  $w$  after this convolution. This corresponds to an approximation of the resonance Breit-Wigner by a  $\delta$ -function. We then have

$$A = \sqrt{2\pi} w \tilde{R}_0, \quad (2.127)$$

where  $\tilde{R}_0$  denotes the peak cross-section after the convolution. From Eqs. (2.126) and (2.127) follows that

$$\tilde{R}_0 = \sqrt{\frac{\pi}{2}} \frac{\Gamma}{2w} R_0. \quad (2.128)$$

Inserting  $w(1S)=7.9$  MeV,  $w(2S)=8.2$  MeV, and  $\Gamma$  from Ref. [22], we find a reduction by factors of 240 and 300 for the  $\Upsilon(1S)$  and the  $\Upsilon(2S)$ , respectively.

The radiative corrections now modify the Gaussian resonance shape and further reduce the peak cross-section to a value  $\bar{R}$ . The amount of this reduction can be estimated as [75]

$$\bar{R} = \left(\frac{2w}{M}\right)^{\beta_e} \tilde{R}_0 = 0.57 \tilde{R}_0. \quad (2.129)$$

Thus, even after folding with the relatively large c.m. energy spread<sup>16</sup>, the initial state radiation reduces the peak cross-section by about 43%. This reduction is due to initial state photons of energy fractions  $x \gtrsim w/E$ , which reduce the c.m. energy to  $s_e = s(1-x) \lesssim (\sqrt{s}-w)^2$ . To obtain a precise prediction for shape and magnitude of the resonance curves, a correct modeling of the photon spectrum well below  $x = 10^{-3}$  is thus mandatory. Photon spectra to first or second order in  $\alpha$ , which are not exponentiated, do not meet this requirement, as can be concluded from Fig. 2.15.

The decrease of the peak cross-section from combining c.m. energy spread and Bremsstrahlung is given approximately from Eqs. (2.129) and (2.128) by

$$\bar{R} = \sqrt{\frac{\pi}{2}} \frac{\Gamma}{2w} \left(\frac{2w}{M}\right)^{\beta_e} R_0. \quad (2.130)$$

The values  $\bar{R}(1S)=0.26\sigma_{\text{Born}}$  and  $\bar{R}(2S)=0.060\sigma_{\text{Born}}$ , obtained by this analytical estimation, deviate by less than 10% from those of Fig. 2.16. Note, that Fig. 2.16 describes the *total* resonant cross-section  $\sigma^{\bar{R}}$  normalized to the Born cross-section  $\sigma_{\text{Born}}$ . The *observed* resonance enhancement normalized to the *observed* continuum cross-section, however, depends on the applied selection cuts, and may thus differ from the curves in Fig. 2.16 by some 10%.

The ratio  $|\bar{I}/\bar{R}|$  of the maxima of the interference and resonance cross-sections, which is  $\sim 1/10$  for the  $\Upsilon(1S)$  and  $\sim 1/5$  for the  $\Upsilon(2S)$ , is not affected by the selection cuts, because it refers to the same event topologies, and has thus identical selection efficiencies. We note, that this ratio has not changed much compared to the corresponding ratio  $|I_0/R_0|$  (Eqs. (2.87) and (2.88)), which does not include corrections from Bremsstrahlung and beam energy spread. Since  $\bar{R}/R_0 \propto \Gamma$  (Eq. (2.130)), this approximate invariance can only hold, if  $\bar{I}/I_0 \propto \Gamma$ , likewise.

<sup>16</sup>If the correction from initial state radiation is applied before including the c.m. energy spread we would have to replace  $2w$  by the total width  $\Gamma$  in Eq. (2.129). The reduction of the peak cross-section would then be 65%.

The latter relation is not obvious, but can be illustrated by the following arguments. For any  $X \gg \Gamma/2$  we can write the tails of the interference term  $\sigma^I$  in Eq. (2.86) as

$$\sigma^I(s = (M + X)^2) = \frac{4\pi\alpha^2}{3} \frac{\sqrt{9B_{ee}B_{\mu\mu}}}{\alpha M} \frac{\Gamma}{XM} = I_0 \frac{\Gamma}{X}, \quad (2.131)$$

where we have used  $|s - M^2| \approx 2XM \gg \Gamma M$  and inserted  $I_0$  from Eq. (2.87). After convoluting  $\sigma^I$  with the c.m. energy spread we find the extrema  $\bar{I}$  of the resulting cross-section  $\sigma^{\bar{I}}$  in Fig. 2.16 to be located at about  $W \approx M \pm 1.5w$ . At this value of  $W$ , the resulting cross-section  $\sigma^{\bar{I}}$  emerges from sampling the original cross-section  $\sigma^I$  along the tail and over the resonance region weighting with a Gaussian of width  $w$  centered at  $W$ . Since the interference term  $\sigma^I$  is asymmetric with respect to  $M$ , and the Gaussian weight does not change much across the narrow resonance region ( $\Gamma \ll w$ ), the net contribution from the resonance region will be negligible. The main contributions to  $\bar{I}$  will arise from the tail region, where  $\sigma^I$  is proportional to  $\Gamma$ , as shown in Eq. (2.131). We thus find from these qualitative arguments the extreme value of the convoluted interference cross-section  $\bar{I} \propto \Gamma I_0$  acquiring the same  $\Gamma$  dependence as  $\bar{R}$  (Eq. (2.130)). The additional convolution with the Bremsstrahlung spectrum has no influence on this reasoning. We conclude, that the ratio  $|\bar{I}/\bar{R}|$ , and thus the shape of the summed cross-section from resonance and interference, does not depend on  $\Gamma$  as long as  $\Gamma \ll w$ . A more quantitative analytic discussion of the interference term, similar to our discussion of the resonance term, is not possible, because here a zero-width approximation is not possible.

## 2.4 The Process $e^+e^- \rightarrow e^+e^-$

At the end of the theory chapter we deal with the Bhabha scattering process  $e^+e^- \rightarrow e^+e^-$ , which is the basis of the luminosity measurement of most experiments at  $e^+e^-$  colliders. It is well suited for this purpose, since energetic electron pairs are easily to detect without prominent background, and since its cross-section is large. The large cross-section arises from the existence of a  $t$ -channel scattering graph (Fig. 2.17(b)) in addition to the  $s$ -channel annihilation diagram analogously to  $e^+e^- \rightarrow \mu^+\mu^-$  (Fig. 2.17(a)).

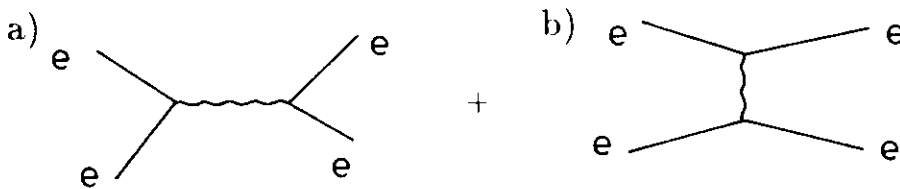


Figure 2.17: Diagrams for the Bhabha scattering process. a)  $s$ -channel annihilation b)  $t$ -channel scattering.

The Born-term differential cross-section is very much peaked in beam direction and reads [76]

$$\begin{aligned} \frac{d\sigma^{ee \rightarrow ee}}{d\Omega} &= \frac{\alpha^2}{4s} \left( \frac{3 + c^2}{1 - c} \right)^2 \\ &= \frac{d\sigma_t}{d\Omega} + \frac{d\sigma_{int}}{d\Omega} + \frac{d\sigma_s}{d\Omega}, \end{aligned} \quad (2.132)$$

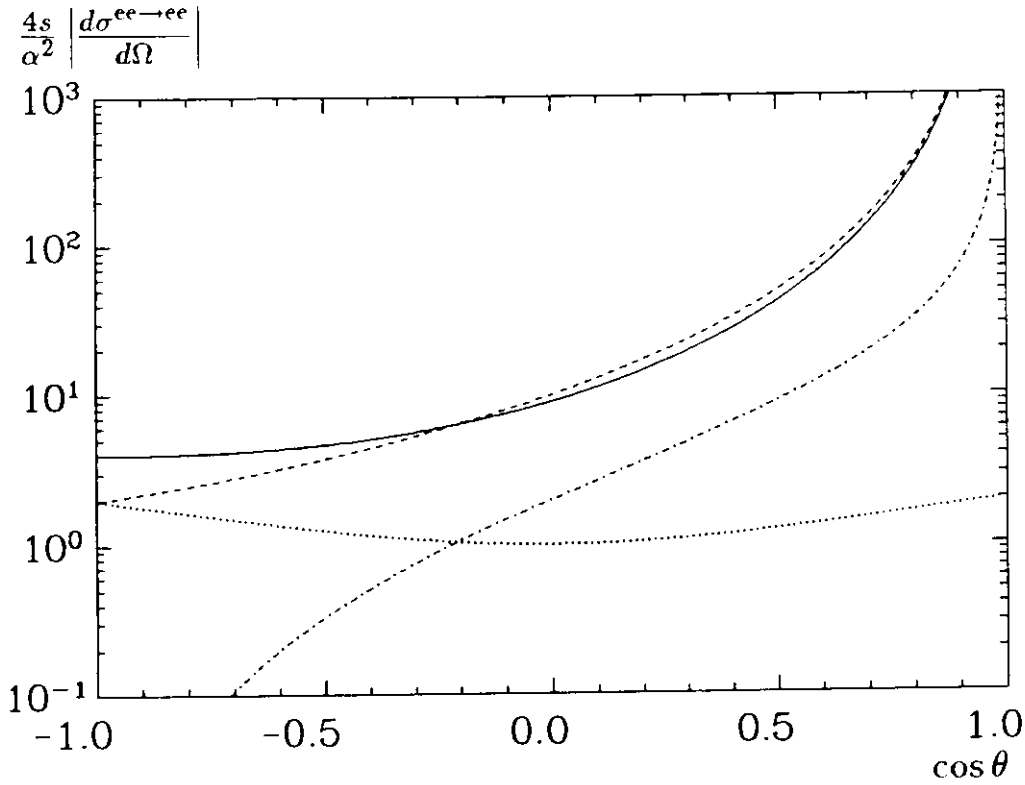


Figure 2.18: Contributions to the differential Bhabha cross-section (solid line). The dotted line describes the  $s$ -channel, the dashed line is the  $t$ -channel, and the dashed-dotted line shows their (negative) interference term.

where  $c \equiv \cos \theta$  is the cosine of the angle of the outgoing  $e^+$  with respect to the  $e^+$  beam direction. The differential cross-section can be split up in the contributions of the  $t$ -channel, the  $s$ -channel, and their interference according to

$$\begin{aligned} \frac{d\sigma_t}{d\Omega} &= \frac{\alpha^2}{4s} \frac{10 + 4c + 2c^2}{(1-c)^2} \\ \frac{d\sigma_{int}}{d\Omega} &= -\frac{\alpha^2}{4s} \frac{2(1+c)^2}{1-c} \\ \frac{d\sigma_s}{d\Omega} &= \frac{\alpha^2}{4s} (1+c^2). \end{aligned} \quad (2.133)$$

These angular distributions are plotted in Fig. 2.18.

In the energy region of the  $\Upsilon$  resonances, the cross-section for  $e^+e^- \rightarrow e^+e^-$  is modified by resonance contributions from the process  $e^+e^- \rightarrow \Upsilon \rightarrow e^+e^-$ . Before the observed number of  $e^+e^-$  events can be used for luminosity determination, these contributions have to be subtracted.

Adding the resonance amplitude of Fig. 2.19 to the two lowest order amplitudes of Fig. 2.17 yields [55]

$$\frac{d\sigma^{ee \rightarrow ee}}{d\Omega} = \frac{d\sigma_t}{d\Omega} + \frac{d\sigma_{int}}{d\Omega} (1 + \Re e B_e) + \frac{d\sigma_s}{d\Omega} (1 + 2\Re e B_e + |B_e|^2), \quad (2.134)$$

where the resonance Breit-Wigner  $B_e$  is given by Eq. (2.83), if  $\Gamma_{\mu\mu}$  is replaced by  $\Gamma_{ee}$  (which makes no difference if lepton universality is assumed).

In contrast to the process  $e^+e^- \rightarrow \mu^+\mu^-$ , we have in this case three different angular distributions, namely  $d\sigma_t/d\Omega$ ,  $d\sigma_{int}/d\Omega$ , and  $d\sigma_s/d\Omega$ . To each of these distributions the resonance term  $|B_e|^2$ , and the interference term  $\Re e B_e$  are attached with different coefficients. Their



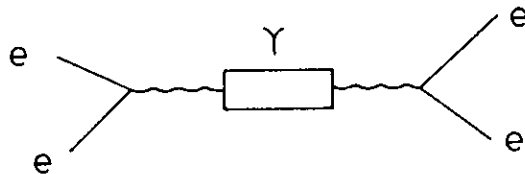


Figure 2.19: Resonance contribution to the process  $e^+e^- \rightarrow e^+e^-$ .

respective contribution to the total cross-section depends on the selection cut for Bhabha events at  $|c| < c_0$ . E.g., the  $s$ -channel contribution  $\int_{-c_0}^{c_0} (d\sigma_s/d\Omega)d\Omega / \int_{-c_0}^{c_0} (d\sigma^{ee \rightarrow ee}/d\Omega)d\Omega$  ranges from 2.1% for  $c_0 = 0.90$  to 8.7% for  $c_0 = 0.50$ . At  $c_0 = 0.75$ , which is applied in the Crystal Ball Bhabha selection, we find the lowest order cross-section to be composed of 5%  $s$ -channel, -19%  $s$ - $t$  interference, and 114%  $t$ -channel contributions. As estimated from Eq. (2.130), the resonance decays  $\Upsilon \rightarrow \ell\bar{\ell}$  amount after corrections for initial state radiation and the DORIS c.m. energy spread to a fraction of about 0.26 and 0.06 of the  $s$ -channel Born term for the  $\Upsilon(1S)$  and the  $\Upsilon(2S)$ , respectively. The total observed Bhabha cross-section is thus increased by about  $0.26 \times 5\% = 1.3\%$  and  $0.06 \times 5\% = 0.3\%$  due to  $\Upsilon(1S) \rightarrow e^+e^-$  and  $\Upsilon(2S) \rightarrow e^+e^-$ , respectively. The fractional error on this estimate is roughly (10–20)%. Its uncertainties arise from the precision of Eq. (2.130), from the errors on the  $\Upsilon$  resonance parameters, and from neglecting radiative corrections to the  $t$ -channel cross-section.

The interference between continuum and resonance enters the observed cross-section  $\int_{-c_0}^{c_0} d\Omega (d\sigma^{ee \rightarrow ee}/d\Omega)$  as  $\int_{-c_0}^{c_0} d\Omega (2\Re B_e [d\sigma_s/d\Omega + 0.5d\sigma_{int}/d\Omega])$ . These terms arise from the product of the resonance diagram with the  $s$ -channel and the  $t$ -channel diagram, respectively. The corresponding interference term in the muonic final state was simply  $2\Re\sigma_{Born}$  (cf. Eq. (2.84)). The presence of the  $t$ -channel diagram can thus be expressed by an additional factor  $(1 + \int d\Omega (d\sigma_{int}/d\Omega) / 2 \int d\Omega (d\sigma_s/d\Omega))$ . The value of this factor ranges from -1.8 at  $c_0 = 0.9$  to -0.3 for  $c_0 = 0.5$ . We see, that the negative sign of the  $t$ -channel interference dominates. For  $c_0 = 0.75$ , we find by inserting the above numbers a value of  $(1 + (-19\%) / 2 \times 5\%) = -0.9$ . Relative to the respective  $s$ -channel cross-sections, the magnitude of the interference between resonance decays to  $e^+e^-$  and  $e^+e^-$  continuum production for a cut at  $c_0 = 0.75$  is thus comparable to the effect in the  $\mu\mu$  final state. Its sign, however, is reverse.

Fig. 2.20 shows the behaviour of the Bhabha cross-section in the region of the  $\Upsilon(1S)$  and  $\Upsilon(2S)$  resonance, which enters our luminosity calculation (Section 4.4). Note, that the interference contribution is now positive below, and negative above the resonances.

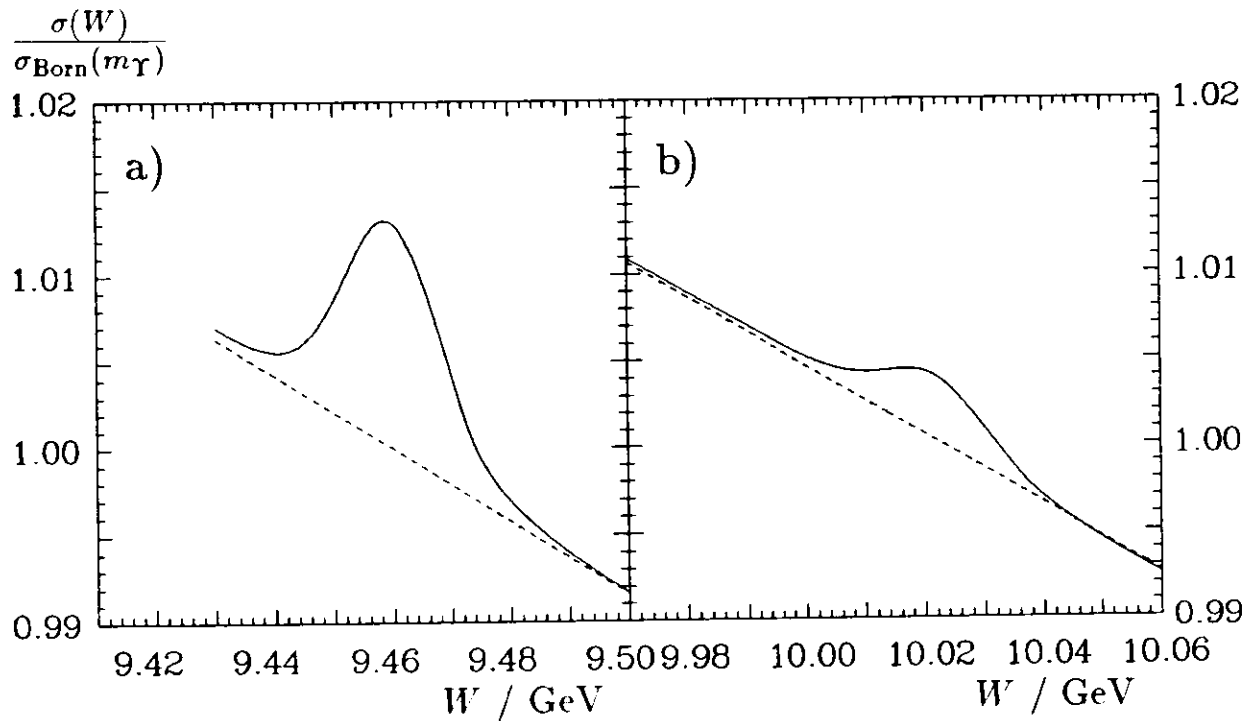


Figure 2.20: The contribution of (a) the  $\Upsilon(1S)$  and (b) the  $\Upsilon(2S)$  resonance (solid lines) to the continuum Bhabha cross-section (dashed lines). The cross-sections were normalized to  $\sigma(m_\Upsilon) = 1$ . As calculated for a cut at  $c_0 = 0.75$ , the resonance enhancements at  $m_\Upsilon$  are 1.3% and 0.35% for the  $\Upsilon(1S)$  and the  $\Upsilon(2S)$  respectively. The 2S enhancement is slightly larger than given in the text since it was calculated from an older value of  $B_{\mu\mu}$ .

## Chapter 3

# The Experimental Setup and its Simulation

*“The thing that is important  
is the thing that is not seen ...”*

A. de Saint-Exupéry, “The Little Prince”

### 3.1 The Crystal Ball Detector

The Crystal Ball detector was operated in the years 1982–1986 at the DORIS II  $e^+e^-$  storage ring in Hamburg at center of mass energies in the region of the  $\Upsilon$  resonances. Before that, it had been successfully employed for charmonium physics at the SPEAR  $e^+e^-$  storage ring in Stanford [77]. It is basically designed for precisely measuring the energies and directions of electromagnetically showering particles over a wide energy range. The energy or momenta of other particles cannot be measured, since there is no magnetic field in the detector. A limited particle identification is possible via the recognition of different types of interactions in the detector.

The experimental setup is shown in Fig. 3.1. It is described elsewhere [78], and its properties are only briefly summarized here. Its main part is a nonmagnetic calorimeter consisting of a spherical shell of 672 NaI(Tl) crystals covering 93% of  $4\pi$  sr. Each crystal is about 16 radiation lengths deep, corresponding to about one nuclear interaction length (Fig. 3.2). The arrangement is based on an icosahedron, in which each face, called “Major Triangle”, is subdivided into four smaller triangles, called “Minor Triangles”, which in turn are formed by the triangular surfaces of nine individual crystals. A complete sphere would contain 720 crystals. To allow entry and exit of the beams, 24 crystals are omitted on each side. The layers of 30 crystals nearest to the beam pipe on each side are called “Tunnel Regions”. The “Main Ball”, used in the trigger and data analysis, excludes the Tunnel Regions and covers 84% of the solid angle. The overall solid angle coverage is increased to 98% by NaI(Tl) “Endcap Crystals”.

The large number of crystals provides a fine segmentation of the ball with angles of  $\sim 7^\circ$  between the centers of adjacent crystals, corresponding to distances of 3 cm at the inner ball shell, and 8 cm at the outer shell. The minimum energy recorded per crystal is 0.35 MeV. This small threshold together with the fine detector segmentation provides an ideal basis for recognizing different types of interactions in the calorimeter by their lateral energy distributions (“patterns”).

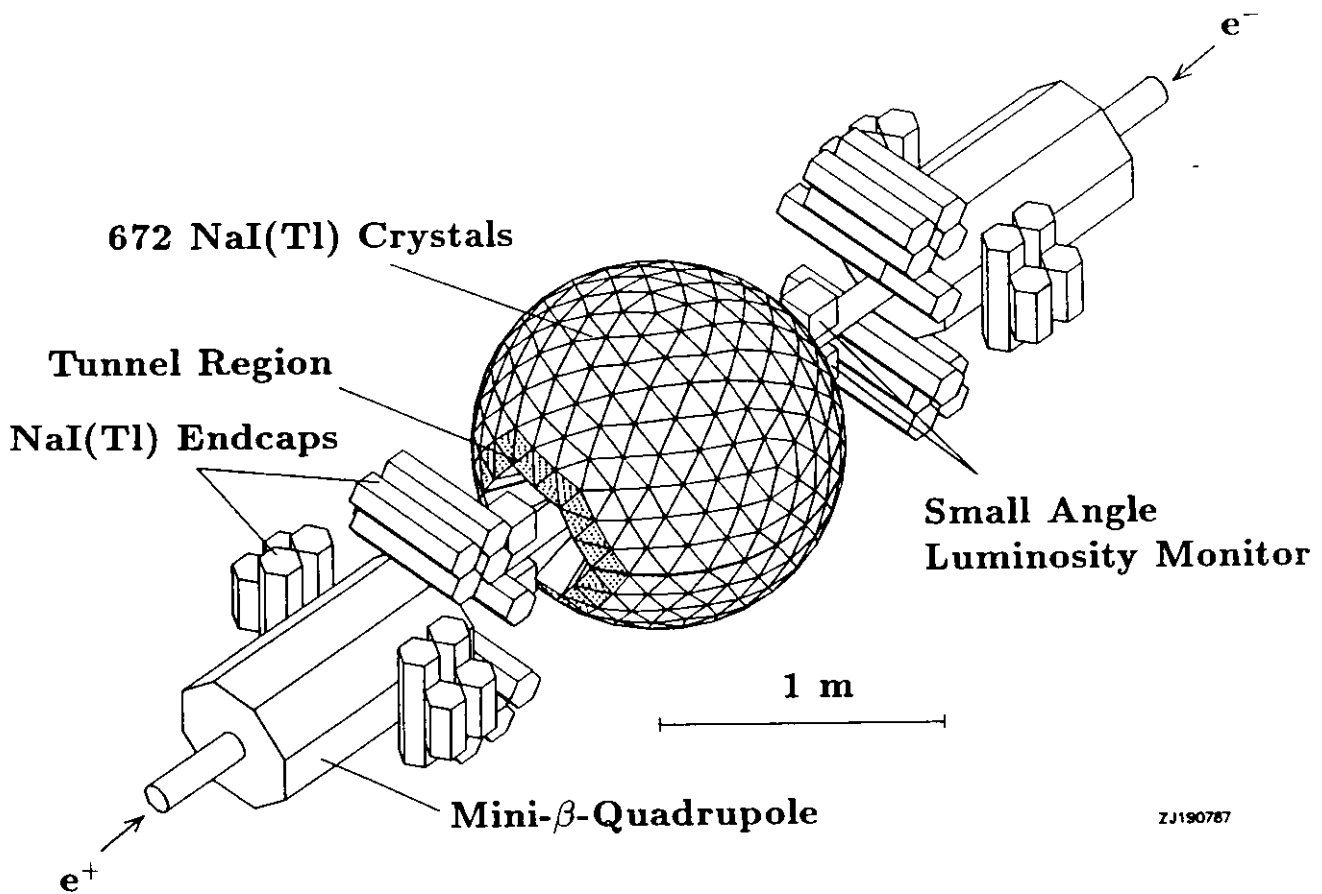


Figure 3.1: View of the Crystal Ball detector as installed at DORIS II.

Pure ionization and excitation can be distinguished from electromagnetic showers or high-energy nuclear interactions by the fact, that all but few percent of the energy deposition is contained in one or two crystals. The most probable energy loss in the crystals for minimum ionizing particles with  $\beta\gamma=4-5$  is 195-200 MeV, and increases to 217 MeV at  $\beta\gamma=45$  (see Section A.2.2 in the appendix). The width of the energy loss distribution is about 20 MeV, with some dependence on the particle momenta.

Approximately two thirds of the hadrons are expected to undergo nuclear interactions while traversing the calorimeter. The rest, if charged, loses energy by pure ionization and excitation. Nuclear interactions of high-energy hadrons result in very irregular patterns. Patterns from nuclear interactions of low-energy hadrons, on the other hand, can be less clearly distinguished from pure Coulomb interactions.

Electromagnetic showering particles, i.e. photons and electrons<sup>1</sup>, are leaving all their energy in a very symmetric pattern. About 98% of their deposited energy is distributed among a symmetric group of 13 crystals (cf. Fig. 3.5). The leaking out energy as well as geometric effects, depending on the position within one crystal where the particle enters, are taken into account by the application of small corrections [79,80]. Using this definition, the measured energy resolution for electromagnetically showering particles is  $\sigma_E/E = (2.7 \pm 0.2)\%/\sqrt{E/\text{GeV}}$ .

The central cavity of the detector is equipped with a set of tube chambers with charge

<sup>1</sup>Since the Crystal Ball cannot distinguish between positive and negative particles, we generally refer to both electrons and positrons as electrons.

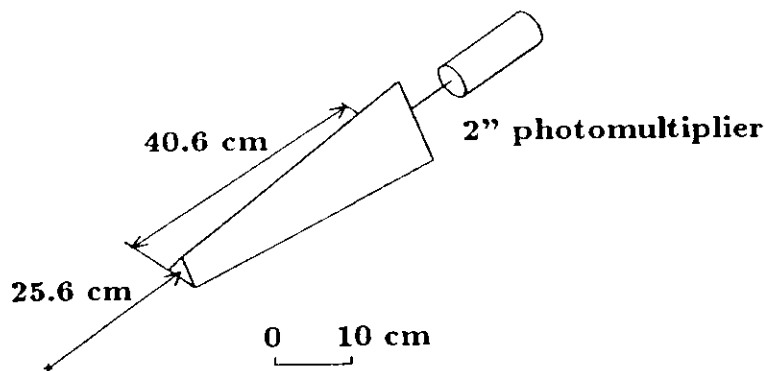


Figure 3.2: The size and shape of a single crystal. The interaction point is marked by a cross.

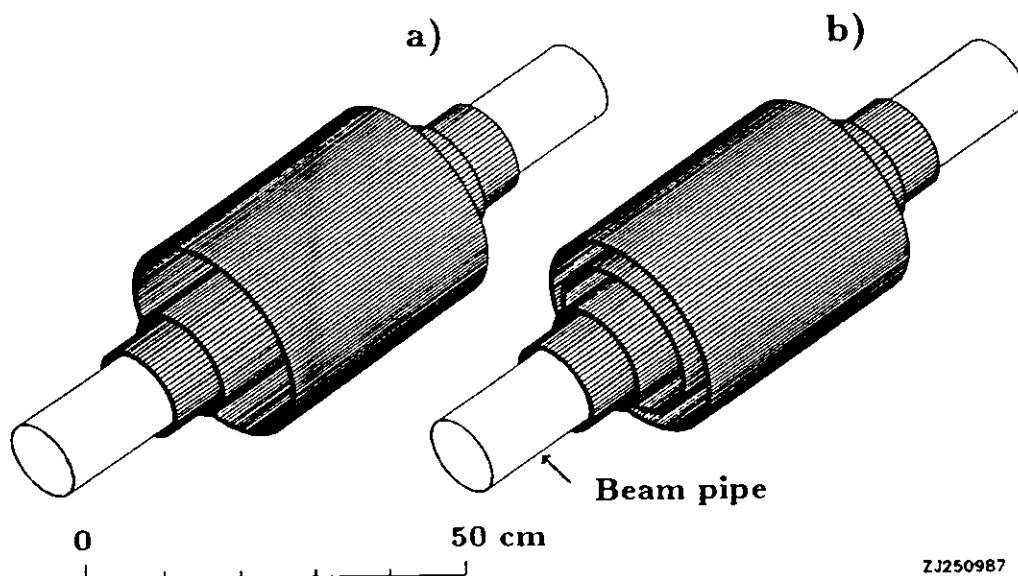


Figure 3.3: Tube chamber setups for the  $\Upsilon(2S)$  data (a) and for the  $\Upsilon(1S)$  and  $\Upsilon(4S)$  data (b).

division readout. The  $\Upsilon(2S)$  data used in this analysis were taken with a chamber setup with a total number of 600 tubes, consisting of two double layers of proportional tubes and one double layer of streamer tubes (Fig. 3.3(a)). The latter were a remnant of an older chamber setup exclusively operated in the limited streamer mode. They were filled with a mixture of  $\sim 76\%$  Ar, 20% Isobutane, 4% Methylal, and 0.25% Freon, called "Magic Gas". This mixture gives high pulse heights at the anodes, which are almost independent of the primary ionization. For the  $\Upsilon(1S)$  and  $\Upsilon(4S)$  data the streamer tubes have been replaced by two additional double layers of proportional tubes, resulting in a total number of 800 tubes grouped in four double layers. (Fig. 3.3(b)). The proportional tubes in both setups (filled with 79% Ar, 20%  $\text{CO}_2$ , and 1%  $\text{CH}_4$ ) record mean pulse heights for minimum ionizing particles, which are by a factor of  $\sim 20$  lower than those of the streamer tubes.

The reconstruction of the  $z$ -position of a hit along the wire has a typical resolution of about 4% of the wire's half length  $L$ , corresponding to 13 mm for the innermost double layer and 7 mm for the outermost double layer. The resolution depends on the particle momentum and the  $z$ -position and is not Gaussianly distributed (see Appendix B). The precision in the azimuthal angle  $\varphi$  for a hit is determined by the tube radius of 3 mm.

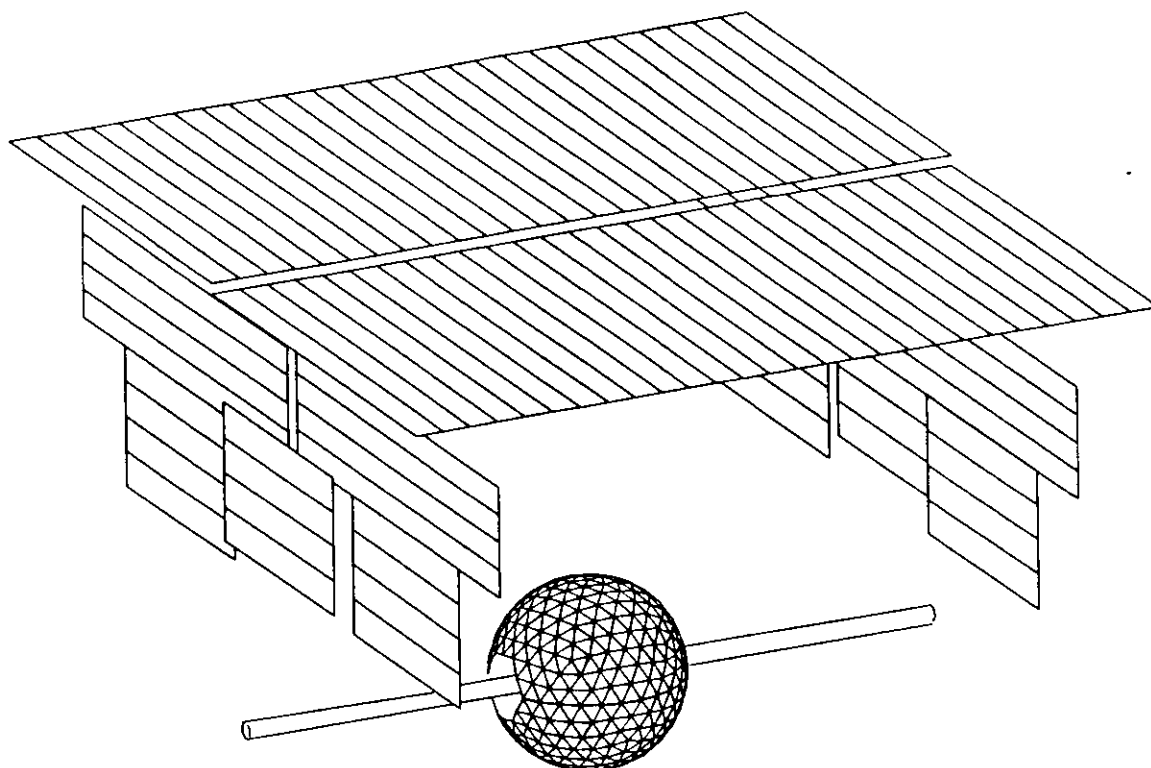


Figure 3.4: The Time of Flight is measured with the help of a “Ball-ToF” and a “Roof-ToF” system.

For proper chamber operation each double layer records at least one hit for a traversing charged particle with an ‘OR’-efficiency of larger than 95%. The performance of the chambers was very time dependent, however. E.g., a degradation of the streamer tubes with time reduced their ‘OR’ efficiencies to less than 50% for some data taking periods. Details of this time dependence and its simulation are discussed in Appendix B.

The Time of Flight (ToF) system of the Crystal Ball detector has two parts, the “Ball-ToF” and the “Roof-ToF” system, which are shown in Fig. 3.4.

The Ball-ToF system measures the timing of the calorimeter signals with the help of 20 Constant Fraction Discriminators and 20 TDCs, each processing the summed signals of one Major Triangle. Note, that these signals arise from energy depositions along a path of 40 cm, which is unusually large for a timing measurement. The 20 Major Triangle timings are backed up by timing measurements for the summed signals of the upper and the lower ball hemisphere, respectively, as well as by two timings for the full ball energy sum. The discriminator thresholds for the Major Triangle and hemisphere timings correspond to energy depositions of 90 MeV. The energy thresholds for the full ball timing measurements are higher and depend on the data taking period.

The Roof-ToF system is a set of 94 scintillation counters located on the roof and at the side walls of the detector hut. It covers 25% of the solid angle but provides timing information for about 80% of the triggered cosmic ray events. The position of the hit along the counter is measured in two independent ways from the pulse height ratio and from the timing difference at both ends with a precision of about 10 cm.

The Ball-ToF and Roof-ToF measurements are performed at mean distances to the interaction point of 0.45 m and 3.5 m, respectively. Both measurements have a resolution of 1.0 ns for high energy muons, improving to 0.4 ns for the Ball-ToF measurement of high en-

ergy showering particles. With the help of the timing difference between the two components, cosmic ray events can be separated by about 14 standard deviations from  $e^+e^-$  annihilation events. A more precise timing measurement, which would be feasible with the Roof-ToF, is thus not needed.

## 3.2 The Triggers

The Crystal Ball hardware triggers are designed to reduce the trigger rate for events which are not caused by  $e^+e^-$  interactions. Trigger decisions are commonly based on energy balance in the ball or on the total amount of deposited energy. The trigger criteria suppress cosmic ray events, and interactions of beam electrons with rest gas atoms or with the wall of the beam pipe. A varying set of about 20 different triggers was installed during Crystal Ball data taking at DORIS. The typical trigger rate was about 4 Hz, which has to be compared to a bunch crossing frequency of  $10^6$  Hz. Still, most of these trigger holds were not created by genuine  $e^+e^-$  interactions.

All triggers used in this analysis are entirely based on the calorimeter information. The fundamental quantities for the trigger decisions are the analog energy sum over 9 crystals in a Minor Triangle, the sum over the 36 crystals in a Major Triangle, and the total energy deposited in the Main Ball. The Tunnel Regions and Endcap Crystals are not included in any of this analog energy sums. The energy deposits in the Tunnel Regions are instead used to veto certain triggers. Thresholds, which are cited below for these analog energy sums, refer to efficiency levels of about 90% for setting a trigger bit, and of about 10% for setting a veto bit.

### The Triangle Triggers

Muon pair events are efficiently recorded by two triggers. One trigger requires two back-to-back Major Triangles, each having a deposited energy of more than 150 MeV; the other trigger requires at least 90 MeV in each of two back-to-back Minor Triangles, and a total energy of at least 220 MeV. Both triggers are vetoed by energy depositions of more than 35 MeV in either Tunnel Region. We will refer to them in the following as “Major Triangle Trigger” and “Minor Triangle Trigger”, respectively<sup>2</sup>.

### The Total Energy Trigger

The Total Energy Trigger requires at least 1.8 GeV of energy deposited in the Main Ball. Bhabha events and multi-hadron events, passing the respective Crystal Ball selection programs, deposit energies well above this threshold.

### The DBM Trigger

An important trigger for studying beam related background is the Doris Bunch Marker (DBM) trigger. It collects “Background Events” with a rate of 0.1 Hz by triggering on every  $10^7$ th bunch crossing with no other condition. These Background Events provide a

---

<sup>2</sup>In the Crystal Ball jargon the latter trigger was called “Quark Pair Trigger” and the former was the “TOPO 20V” trigger. Actually, the requirements of the TOPO 20V trigger were much more involved. They are, however, equivalent to the conditions listed, if there are exactly two energy depositions of more than 150 MeV in the Main Ball. An even more efficient trigger for  $\mu$ -pairs, called the “Mu Pair Trigger”, was not used, because its performance was unreliable.

valuable information about the distribution and the frequency of beam-related or spurious energy depositions and tube hits.

### 3.3 Calibration and Data Reconstruction

The NaI(Tl) energy scale is set for each  $\sim 5 \text{ pb}^{-1}$  of accumulated luminosity using radioactive sources [81], a van-de-Graaf generator [82], and large-angle Bhabha scattering events [79].

The  $z$ -information of the tube chamber hits is calibrated with the help of large-angle Bhabha events, likewise [83]. The  $\varphi$ -information of each hit is set equal to the  $\varphi$  position of the tube center. These  $\varphi$  values have been “calibrated” by comparing the hits from Bhabha electrons with the  $\varphi$  positions of their energy depositions in the calorimeter. The measured pulse heights of the hits are not subjected to a calibration.

Event samples of electron pairs, muon pairs, and cosmic rays provide the basis for the ToF calibration. For the Ball-ToF an optimum resolution is obtained by assigning and fitting delay constants for each crystal and cable involved in the analog summing of the Major Triangle energy [84,85]. It is further improved by correcting for time dependent drifts in each constant and for the overall dependence on the amount of deposited energy. After accomplishing the Ball-ToF calibration, the Roof-ToF is calibrated with the help of the timing difference of cosmic ray muons with respect to the Ball [86].

Data reconstruction is performed in several steps. First crystals are grouped into clusters, where a cluster is defined as a group of geometrically adjacent crystals, each having at least 10 MeV deposited energy. In a second step the local maximums inside the clusters are determined. They are called particle bumps. The next step correlates hits inside the chambers with the particle bumps in the ball. A straight line fit through the hits found in this procedure is used for the direction definition of charged particles. Finally the ToF information is evaluated and assigned to the energy depositions in the calorimeter.

### 3.4 Further Treatment of the Reconstructed Data

The output data format of the reconstruction procedure contains not only the results of the various assignments of direction, deposited energy, and timing for each particle bump. In addition, all detector information is kept, which was used in the reconstruction, e.g. the deposited energy in each crystal, pulse heights for each tube hit, and timing information for each component of the ToF system. It is thus easily possible to modify the definitions of the particle assignments with respect to the standard reconstruction procedure. This freedom is exploited in most Crystal Ball analyses in order to adjust the definitions of energy, direction, and timing to the actual needs. A special sort of Crystal Ball data tapes, the “PACK” tapes, even contain the “raw” signals from the chamber and ToF system in a compressed format. They can be retrieved if the tube hits or the timing are to be reproduced with different calibration constants.

In this work we have recovered some tube hits from the raw data by reducing the pulse height cut for about one third of the  $Y(4S)$  data<sup>3</sup>.

The tube chamber information is analyzed by the TAGTRK program [85], written for the tracking of two particles. An essential feature of this routine is its ability to detect vertices

<sup>3</sup>The cuts for the four double layers were reduced from (60,30,30,30) mV to (40,15,20,20) mV for the runs 16563 - 17667, since it turned out after data reconstruction, that the hit pulse heights were rather low in this period. The larger cuts, taken from the preceding period of data, would have led to considerable inefficiencies of the tubes.



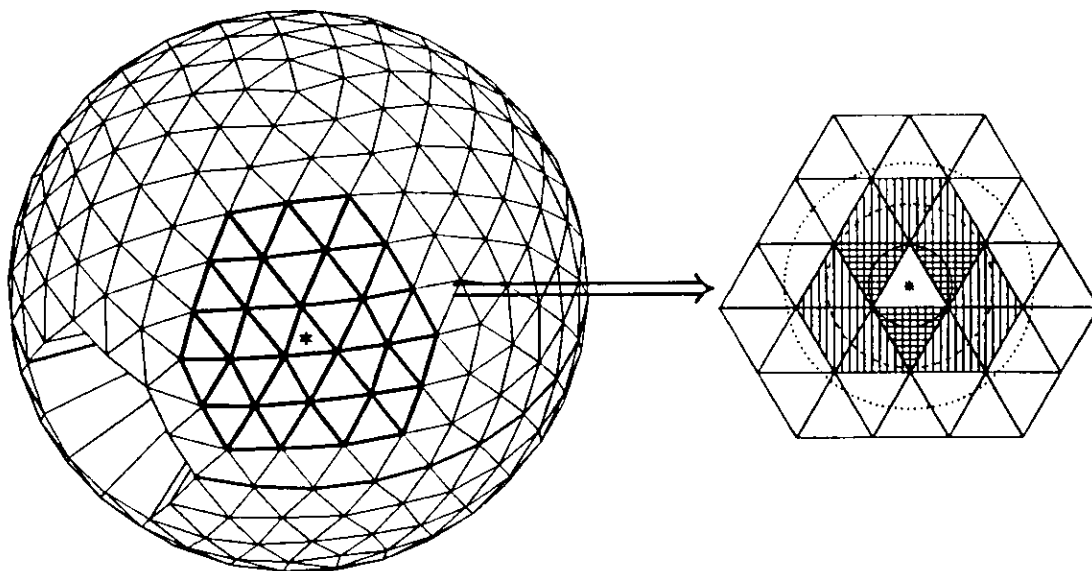


Figure 3.5: Definition of deposited energy  $E_{dep}$ . The shaded area is the group of thirteen crystals with the local energy maximum marked by an asterisk. The indicated circles correspond to one, two and three Molière radii for electromagnetic showering particles.

off beam axis, which is not possible with the standard Crystal Ball tracking package (cf. also Ref. [87]). The location of the event vertex is found by maximizing the number of tube hits traversed by the fitted tracks. An unmistakable assignment of off-axis vertices is achieved by imposing additional constraints on the number of traversed hits. One of them is a cut in the “on-axis significance”  $\kappa$ , describing the fractional excess of hits for the on-axis vertex assignment relative to the off-axis assignment.

The decision, whether a particle is called “charged” is based on the number of correlated tube hits. We set the TAGTRK parameters such, that particles originating from the beam-axis are called charged, if at least one (two) hit(s) in the chamber setup with 3 (4) double layers is (are) correlated in  $\varphi$  with their bumps in the ball. An additional hit is required, if the hit(s) is (are) found in the innermost double layer, which usually contains a lot of background hits. Applying this definition, charged particles originating from the interaction region are detected with an efficiency of more than 98% for both setups.

If at least two hits are found to be correlated with a particle bump in  $\varphi$  and  $z$ , the track direction is determined by fitting a straight line through the tube hits and the particle bump. The resulting accuracy of the direction measurement is about  $2\text{--}3^\circ$  in  $\theta$ , the polar angle with respect to the beam axis, and better than  $1^\circ$  in  $\varphi$ . The direction of a particle with less than two tube hits is determined from the location of its energy cluster in the ball with respect to the event vertex.

A particle’s deposited energy  $E_{dep}$  is defined as the sum of the energies over a symmetric group of 13 neighboring crystals including the particle bump at its center (see Fig. 3.5). The definition is motivated from the energy depositions of electromagnetic showers (cf. Section 3.1). The lateral pattern are described by the pattern fractions  $F_1$ ,  $F_2$ , and  $F_4$ . They represent the probability, that a given fraction of the deposited energy  $E_{dep}$  was distributed among 1, 2, or 4 crystals. For the  $F_1$  and  $F_2$  fractions the crystals with the highest energy deposits are used, whereas the 4 crystals include the one with the maximum energy deposit and its three nearest neighbor crystals.

The Ball-ToF measurement for each particle is taken from the corresponding Major Trian-

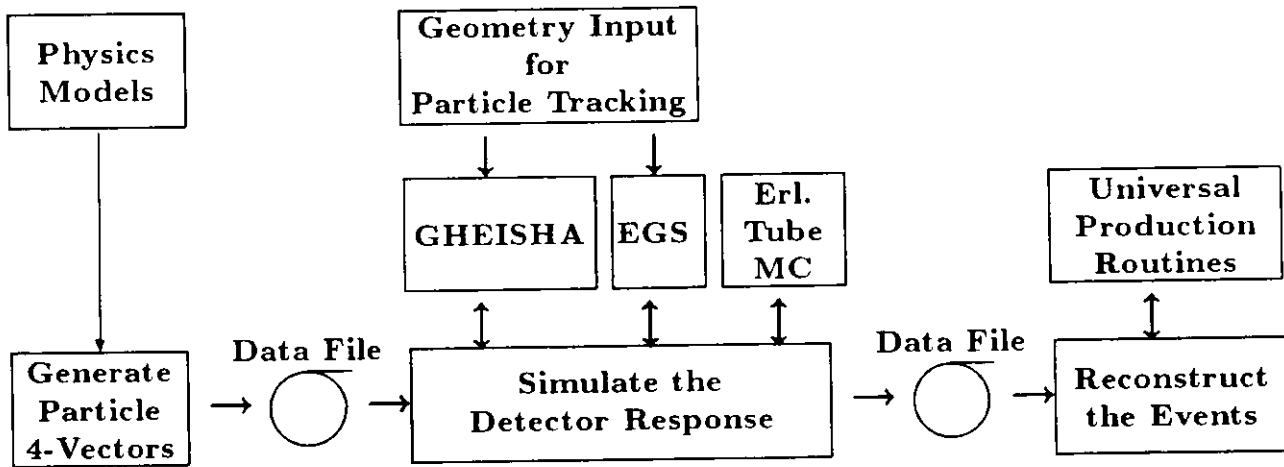


Figure 3.6: The organization chart of the Crystal Ball MC.

gle timing. For a few percent of the particles the Major Triangle timing was not available or unreliable due to bad hardware. In those cases we used the hemisphere and full ball timings as a backup. Events without any valid timing are encountered with a frequency of less than  $10^{-5}$ .

### 3.5 Monte Carlo Event Simulation

The organization of the Crystal Ball Monte Carlo is shown in Fig. 3.6. The process of the event generation is subdivided into two steps: generation of particle 4-vectors, and simulation of the detector response. The output of the detector simulation has the same format as real data and is reconstructed using the same “universal” production routines.

The detector response to electromagnetically showering particles is simulated by the EGS 3 code [88] while the interactions of all other particles including muons are simulated with an upgraded version [89] of the GHEISHA 6 program<sup>4</sup> [90]. Among other modifications, corrections in the modeling of energy loss and  $\delta$ -electrons have been applied. They have been proven to be important for a realistic simulation of particle interactions in the Crystal Ball, which is essential for our analysis. More details about our GHEISHA modifications are given in Appendix A. It is worthwhile to mention, that a common treatment of the Crystal Ball geometry was adopted for EGS and GHEISHA. Replacing the GHEISHA geometry handling by EGS-like geometry routines [91,92], both precision and speed of particle tracking have been improved.

The Crystal Ball geometry input does not only contain the positions and dimensions of the calorimeter crystals, but also those of the inner and outer ball shells, of the crystal wrapping foils, and of the endcap sheathing material. In this analysis we used a special geometry version, which also includes the beampipe and the material equivalent of the tube chamber walls and of their support structure [93].

The pulse height distributions of the tube chamber hits, their efficiency, and the smearing of the charge division (including their respective run-dependence) are modeled after corresponding data from Bhabha events by a separate tube chamber Monte Carlo program. This “Erlangen Tube chamber MC” (E.T.MC) is described in detail in Appendix B.

Since there is a very irregular agglomeration of material between the Ball and the Roof-ToF counters (phototubes, cables, electronics, superstructure, dryhouse), a realistic Roof-

<sup>4</sup>The version 6 of the GHEISHA package is essentially identical to the published version 7.

ToF simulation is not possible. The Ball-ToF has been simulated in this work by a Gaussian distribution with center and width determined from the data.

Extra energy in the crystals and additional hits in the tube chambers originating from beam-related background are taken into account by adding special Background Events to the Monte Carlo events. These Background Events are obtained with the DBM trigger described in Section 3.2 and reproduce the actual detector behaviour specific for a given period of data taking.

We have completed the run-dependence of the detector simulation by implementing variations in the mean position ( $\langle x \rangle, \langle y \rangle, \langle z \rangle$ ) and in the length  $l$  of the  $e^+e^-$  intersection region along the beam axis. (The Crystal Ball coordinate system is defined by the  $z$ -axis going in direction of flight of the positrons, the  $y$ -axis pointing upward and the  $x$ -axis pointing towards the middle of the DORIS II ring. The origin is set in the center of the ball calorimeter. In polar coordinates the azimuthal angle  $\varphi$  is measured starting from the  $x$ -axis. The polar angle  $\theta$  refers to the  $+z$  direction.) These beam spot parameters have been determined in Ref. [83] as the relative positions of event vertices and calorimeter<sup>5</sup>. We have averaged these results over appropriate periods as depicted in Figs. 3.7(a)–(d). Since our analysis is less sensitive to the beam spot position than to its width (cf. Section 5.3.3), we could afford not to follow each change in the  $\langle x \rangle$ -position of the vertex.

We have also modeled the systematic influence of a vertex position ( $\langle x \rangle, \langle y \rangle$ )  $\neq (0, 0)$  on the  $\varphi$  calibration of the tubes. This influence is rather involved and could thus be reproduced only qualitatively.

---

<sup>5</sup>Changes in these ( $\langle x \rangle, \langle y \rangle, \langle z \rangle$ ) positions of the vertex may either be due to beam shifts or to shifts of the ball calorimeter. From studies done with the tube chambers, which are mounted on fixed positions around the beam pipe, we find that the  $y$ -position of the beam was constant at about 0.10 cm above the center of the tube chamber system. The variations in Fig. 3.7(b) do thus reflect a sinking of the calorimeter. This relative shift of calorimeter and tubes was included in our MC simulation. The  $x$ -variations, on the contrary, are also observed with the tube chambers indicating underlying variations of the beam orbit.

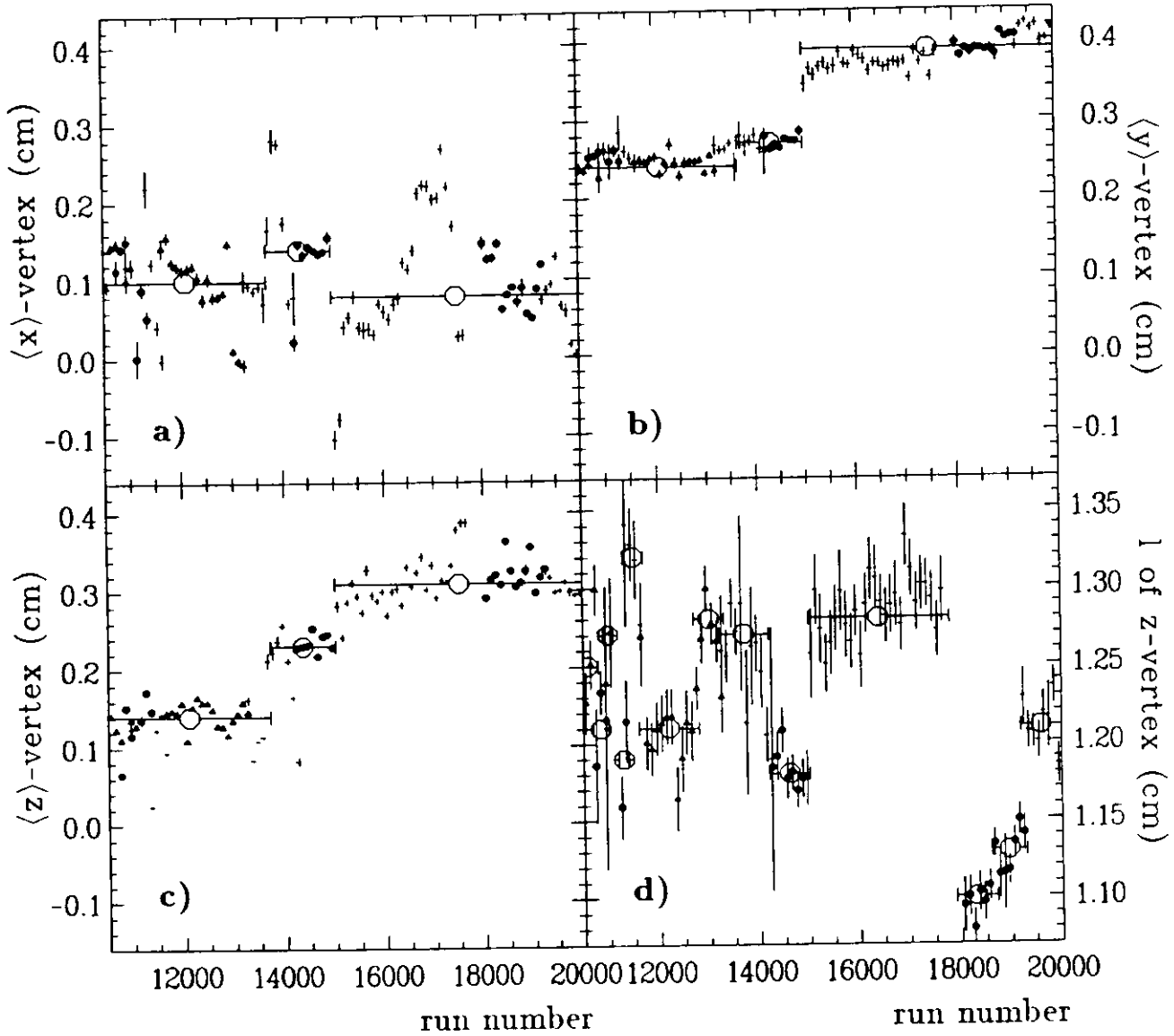


Figure 3.7: Mean position ( $\langle x \rangle$ ,  $\langle y \rangle$ ,  $\langle z \rangle$ ) and length  $l$  of the  $e^+e^-$  intersection region as a function of run number [83]. The full dots are  $\Upsilon(1S)$  data, the triangles are  $\Upsilon(2S)$  data, and the crosses are  $\Upsilon(4S)$  data. The big open circles with horizontal error bars show our average for the MC input and its range of validity. Not all runs shown in this plot were used in our analysis.

## Chapter 4

# Beam Energy, Luminosity, and Data Selection

*“The recitals of explorers are put down first in pencil. One waits until the explorer has furnished proofs, before putting them down in ink.”*

A. de Saint-Exupéry, “The Little Prince”

One of the aims of our measurement of the  $\Upsilon$  decay to  $\mu$ -pairs is to extract its branching ratio  $B_{\mu\mu} = \#(\Upsilon \rightarrow \mu\mu) / \#(\Upsilon)$ . The total number of resonant  $\mu$ -pairs  $\#(\Upsilon \rightarrow \mu\mu)$  is proportional to the observed number  $N^{\Upsilon \rightarrow \mu\mu}$  of resonance decays to muons, which is obtained from subtracting the expected continuum yield  $N^{e^+e^- \rightarrow \mu\mu}$  from the observed number  $N^{\mu\mu}$  of  $\mu$ -pairs in on-resonance running.

$$\begin{aligned} B_{\mu\mu} &\propto \frac{N^{\Upsilon \rightarrow \mu\mu}}{N^{\Upsilon \rightarrow \text{had}}} \\ &= \frac{N^{\mu\mu} - N^{e^+e^- \rightarrow \mu\mu}}{N^{\text{had}} - N^{e^+e^- \rightarrow \text{had}}}. \end{aligned} \quad (4.1)$$

The total number  $\#(\Upsilon)$  of produced  $\Upsilon$  resonances is determined from the observed number  $N^{\Upsilon \rightarrow \text{had}}$  of multihadronic decays, because they constitute the dominant decay mode with both, branching ratio and detection efficiency larger than 90%. The number  $N^{\Upsilon \rightarrow \text{had}}$  is in turn obtained from the number of observed multi-hadron events  $N^{\text{had}}$  in on-resonance running subtracting the continuum contribution  $N^{e^+e^- \rightarrow \text{had}}$ .

There are two major problems connected with this measurement, which have to be thoroughly studied. First, the resonance peaks of  $e^+e^- \rightarrow \Upsilon \rightarrow \mu^+\mu^-$  rise only marginally above the  $e^+e^- \rightarrow \mu^+\mu^-$  continuum background (see Section 2.3.5). By subtracting the continuum measured at a different c.m. energy and at a different time under different experimental conditions introduces large errors, unless we correct for all energy and time dependences (see Section 5.3).

Second, due to the interference between  $\mu$ -pairs from resonance decays and from continuum production, the result for  $B_{\mu\mu}$  depends on the c.m. energy, where the on-resonance data is taken (see Section 4.2). The data taking at DORIS, however, is not accompanied by a reliable online measurement of the beam energy. We thus exploit the observed hadronic cross-section together with measurements of the magnetic field in a storage ring bending magnet to determine the c.m. energy  $W$  a posteriori, as detailed in Appendix C. Besides reducing considerably the systematic error of the  $B_{\mu\mu}$  measurement (Section 6.2), the determination

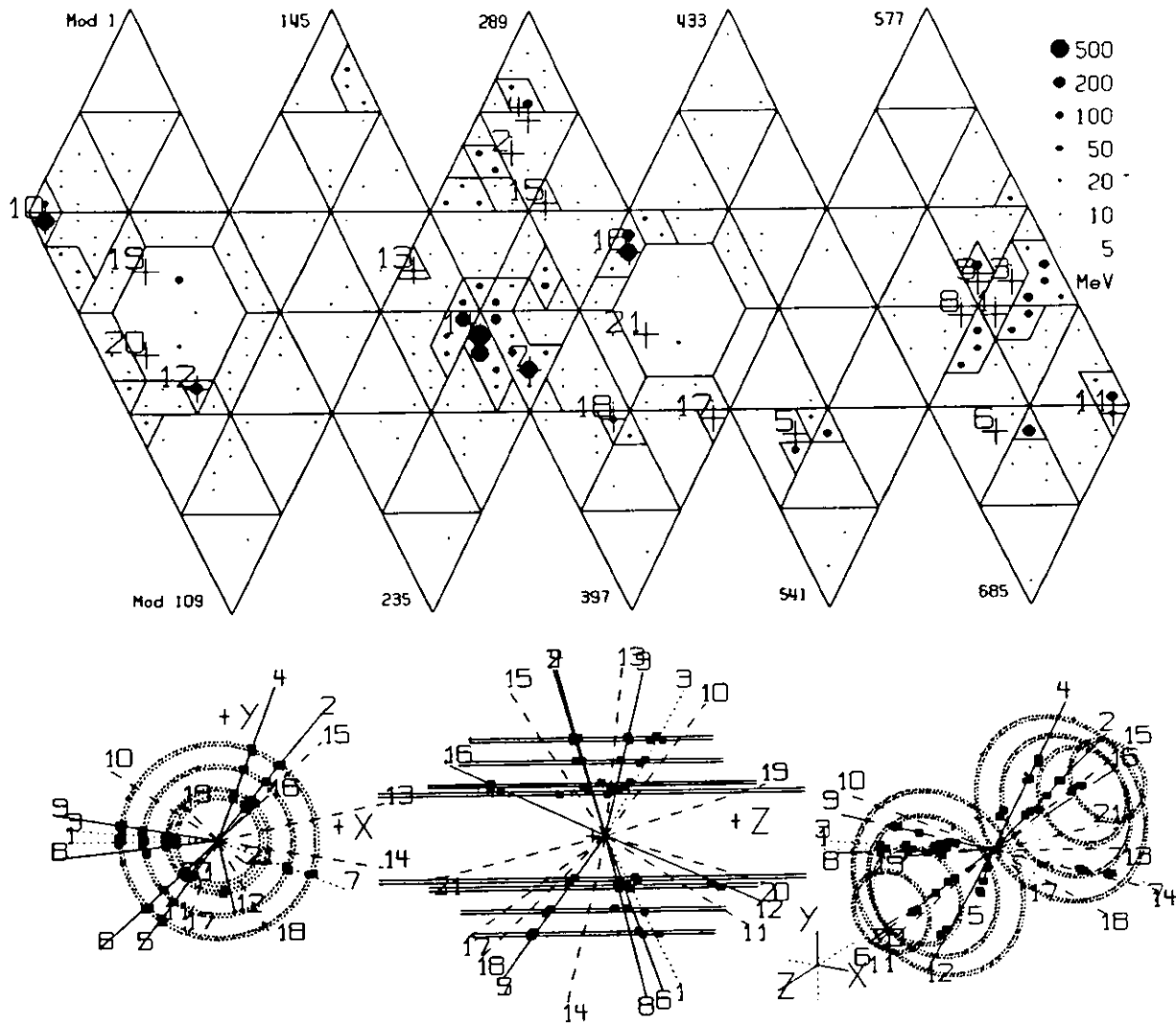


Figure 4.1: Typical example for a multi-hadron event in the Crystal Ball detector. The upper part of the event display is a mercator-like projection of the calorimeter where the Minor Triangles and the boundaries of the energy clusters are indicated. The sizes of the dots are a measure of the deposited energy in each crystal. The lower part shows three different views of the chambers ( $x$ - $y$ ,  $z$ - $R$ , 3- $D$ ). Hits used for track fitting are displayed as squares.

of  $W$  enables us to fit the muonic cross-section in the region of the resonance as a function of  $W$ . From this fit we derive results on the product of the branching ratio  $B_{e\bar{e}}$  to electrons and the muonic width  $\Gamma_{\mu\mu}$  of the  $\Upsilon$  resonances (Section 6.3).

Altogether three types of event samples enter the analysis, namely multihadronic events to derive the number of produced  $\Upsilon$  resonances and to determine the c.m. energy  $W$ , Bhabha events for the luminosity determination, and finally  $\mu$ -pair events. We describe the selection of these event samples and the determination of c.m. energy and luminosity in turn.

## 4.1 The Selection of Multihadronic Events

For the determination of the c.m. energy and for the calculation of the number of produced  $\Upsilon$  resonances we select multihadronic events with the standard Crystal Ball multi-hadron cuts [94]. The selection criteria are suited to suppress background from beam-gas and beam-

wall reactions, two-photon collisions, and QED processes like electron- and tau-pair production. The most important selection cuts exploit the fact, that the latter background has a small average multiplicity and that the former has a large total momentum along the beam axis.

The selection efficiencies for hadronic  $\Upsilon$  decays are high, e.g. about 94% for the 3-gluon decay, and about 81% for the qq decay. In terms of the observed continuum cross-section from  $ee \rightarrow qq$  the remaining background comprises about 3% from tau-pair events, and 0.5% each from (radiative) Bhabha events, from two-photon induced hadronic events, and from beam-gas/wall reactions [92].

The resulting samples comprise  $447 \times 10^3$  and  $253 \times 10^3$  multi-hadron events from the  $\Upsilon(1S)$  and the  $\Upsilon(2S)$  data, respectively. A typical multihadronic event is shown in Fig. 4.1.

## 4.2 Center of Mass Energy Determination

If the shape of the resonance excitation curves  $\sigma^{ee \rightarrow \Upsilon \rightarrow \mu\mu}(W)$  and  $\sigma^{ee \rightarrow \Upsilon \rightarrow \text{had}}(W)$  were identical, we would find the same value for  $B_{\mu\mu}$  from Eq. (4.1), regardless at which (on-resonance) c.m. energy  $W$  our data is taken. This would be the case if there was no interference between resonance decays and continuum, or if the hadronic and the muonic decay channel interfered in the very same way with the continuum. However, only  $\Upsilon$  decays to fermion pairs, namely  $\Upsilon \rightarrow qq$  and  $\Upsilon \rightarrow \ell\bar{\ell}$  interfere with their corresponding nonresonant continuum production according to Eq. (2.84), whereas for all other  $\Upsilon$  decays, like  $\Upsilon \rightarrow ggg$  or  $\Upsilon(2S) \rightarrow X + \Upsilon(1S) \rightarrow X + \text{hadrons}$ , there is no or negligible interference with the continuum. The maximum interference contribution for  $\Upsilon \rightarrow \ell\bar{\ell}$  is 10% and 20% of the resonance peak height for the  $\Upsilon(1S)$  and the  $\Upsilon(2S)$ , respectively (see Section 2.3.1 on page 31). In contrast to that it is only 1% for  $\Upsilon(1S,2S) \rightarrow \text{hadrons}$ , since the decay  $\Upsilon \rightarrow qq$  forms only a small fraction of the hadronic  $\Upsilon$  decay modes. We thus find the “true” value for  $B_{\mu\mu} = \#(\Upsilon \rightarrow \mu\mu) / \#(\Upsilon)$  only at  $W = W_0$ , where the interference contribution vanishes. From Fig. 2.16 we find for a c.m. energy spread of  $w \approx 8$  MeV

$$W_0 = m_\Upsilon + (1.3 \pm 0.2) \text{ MeV}, \quad (4.2)$$

which is very near the (radiatively corrected) peak of the non-interfering  $\Upsilon$  cross-section at

$$W_{\text{peak}} = m_\Upsilon + (1.0 \pm 0.1) \text{ MeV}. \quad (4.3)$$

Since the interference contribution to the hadronic cross-section is small,  $W_{\text{peak}}$  equals in good approximation the c.m. energy, where the maximum of the hadronic cross-section is observed.

Any strategy for on-resonance running tries to find this maximum hadronic cross-section by scanning over the resonance. All on-resonance data is then taken at  $W \approx W_{\text{peak}} \sim W_0$ , if the beam energy remains stable. The stability of the DORIS beam energy is monitored in two ways. First, the Crystal Ball experiment records the observed hadronic cross-section  $\sigma_{\text{online}}^{\text{had}}$  during data taking.

Second, the magnetic field at the beam position in a storage ring bending magnet is measured using the nuclear magnetic resonance (NMR) effect. This bending magnet is located outside of the storage ring, but connected in series with all storage ring magnets so that it has exactly the same current<sup>1</sup>. The magnetic field  $B$  of this magnet is thus — for a fixed orbit — proportional to  $\oint_{\text{orbit}} B(l)dl$  around the storage ring, which is directly related to  $W = 2E_{\text{beam}}$  via a constant  $c_{\text{orbit}}$

$$W = c_{\text{orbit}} B. \quad (4.4)$$

<sup>1</sup>For the first  $8 \text{ pb}^{-1}$  of our data sample the NMR reading did not yet exist.

The combination of both methods does still not guarantee, that  $W$  can be kept stable during data taking. The measurement of  $\sigma_{online}^{had}$  is uncertain due to statistics, and due to slightly varying acceptance and beam-gas/wall background for both the hadronic and luminosity events counted online. The varying acceptance is due to the lack of up-to-date detector calibration constants at the time of data taking. The varying beam-related background comes in due to a simplified online event selection with larger background than in our offline selection.

The NMR measurement suffers from changes in the beam orbit with respect to the scan period, where  $B_{peak} \equiv B(W_{peak})$  was determined. These changes may occur after any break in the storage ring operation when both beams have been lost completely (e.g. after failures in the  $e^+e^-$  supply from the LINACs or in the case of power failures). Changes in the orbit manifest themselves in a modification of  $c_{orbit}$ , so that running at  $B_{peak}$  will no longer mean running at  $W_{peak}$ . Changes of  $W$  by, say,  $w/3 \approx 2.7$  MeV, which reduce  $\sigma_{online}^{had}$  by only 4% on the  $\Upsilon(1S)$  and by 3% on the  $\Upsilon(2S)$ , may remain unnoticed during on-resonance data taking. However, such a change would affect the measurement of  $B_{\mu\mu}$ . From Fig. 2.16 we derive, that a shift in the c.m. energy away from  $W_0$  changes the measured value of  $B_{\mu\mu}$  (Eq. 4.1) approximately linearly to

$$B_{\mu\mu}(W) = B_{\mu\mu}(W_0) \left( 1 + a \frac{W - W_0}{w} \right), \quad (4.5)$$

if  $|W - W_0| \lesssim w$ . We find  $a(1S) = 15\%$  and  $a(2S) = 30\%$  resulting in errors of 5% for  $B_{\mu\mu}(1S)$  and 10% for  $B_{\mu\mu}(2S)$  for our example of a shift by  $w/3$ . The systematic error on  $B_{\mu\mu}$  from the uncertainty in  $W$  can only be reduced by precisely determining the c.m. energy for our on-resonance data. For that we have to find data taking periods with a constant beam orbit and measure their parameters  $c_{orbit}$ . Details of this procedure are given in Appendix C.

In principle we plot the observed hadronic cross-section as a function of the measured magnetic field  $B$  for short enough periods in time, so that the conversion factor  $c_{orbit}$  between  $B$  and  $W$  can be regarded as a constant within each period. In these plots we fit the  $B$ -position of the  $\Upsilon$  resonances above the hadronic continuum. Periods adjacent in time were combined if they could be consistently described by a common fit. The conversion factors for the combined periods are then determined by inserting the values of the  $\Upsilon$  masses from Ref. [22] for the corresponding positions of the  $\Upsilon$  resonances in  $B$ . The  $\Upsilon(2S)$  data can be consistently fitted with a single conversion factor, whereas we get a set of 5 different conversion factors for the  $\Upsilon(1S)$  data. They correspond to shifts ranging from 6.5 MeV to 44.2 MeV compared to those c.m. energy values, which would have been obtained by utilizing the  $\Upsilon(2S)$  conversion factor. From the errors of the fits and from the variation of the results within the sets of combined subperiods, we derive an error of  $\Delta W = 0.5$  MeV on our determination of  $W$ .

A subset of  $8 \text{ pb}^{-1}$  of the  $\Upsilon(2S)$  data was collected before a regular NMR reading existed at DORIS. Their c.m. energies were determined by exploiting resonance depolarization measurements [95.96] with a resulting precision  $\Delta W$  ranging from 0.5 MeV to 2.0 MeV.

A precise determination of  $W$  for the  $\Upsilon(4S)$  data is not necessary, since the interference with muons from  $\Upsilon(4S)$  decays changes the observed continuum cross-section by at most 0.30% (as obtained from correcting the dotted curve in Fig. 2.11 for initial state radiation). Compared to this, the interference term in the energy region of the  $\Upsilon(2S)$  and the  $\Upsilon(1S)$  is 4 and 9 times larger, respectively (cf. dashed lines in Fig. 2.16). The c.m. energy of the  $\Upsilon(4S)$  resonance data was instead set equal to the  $\Upsilon(4S)$  mass from Ref. [22], accounting for possible offsets by an error of  $\Delta W = 15$  MeV. The c.m. energies of the continuum data below the  $\Upsilon(4S)$  were calculated from their difference in the nominal beam energy to the  $\Upsilon(4S)$  resonance data, allowing for an error of  $\Delta W = 20$  MeV.



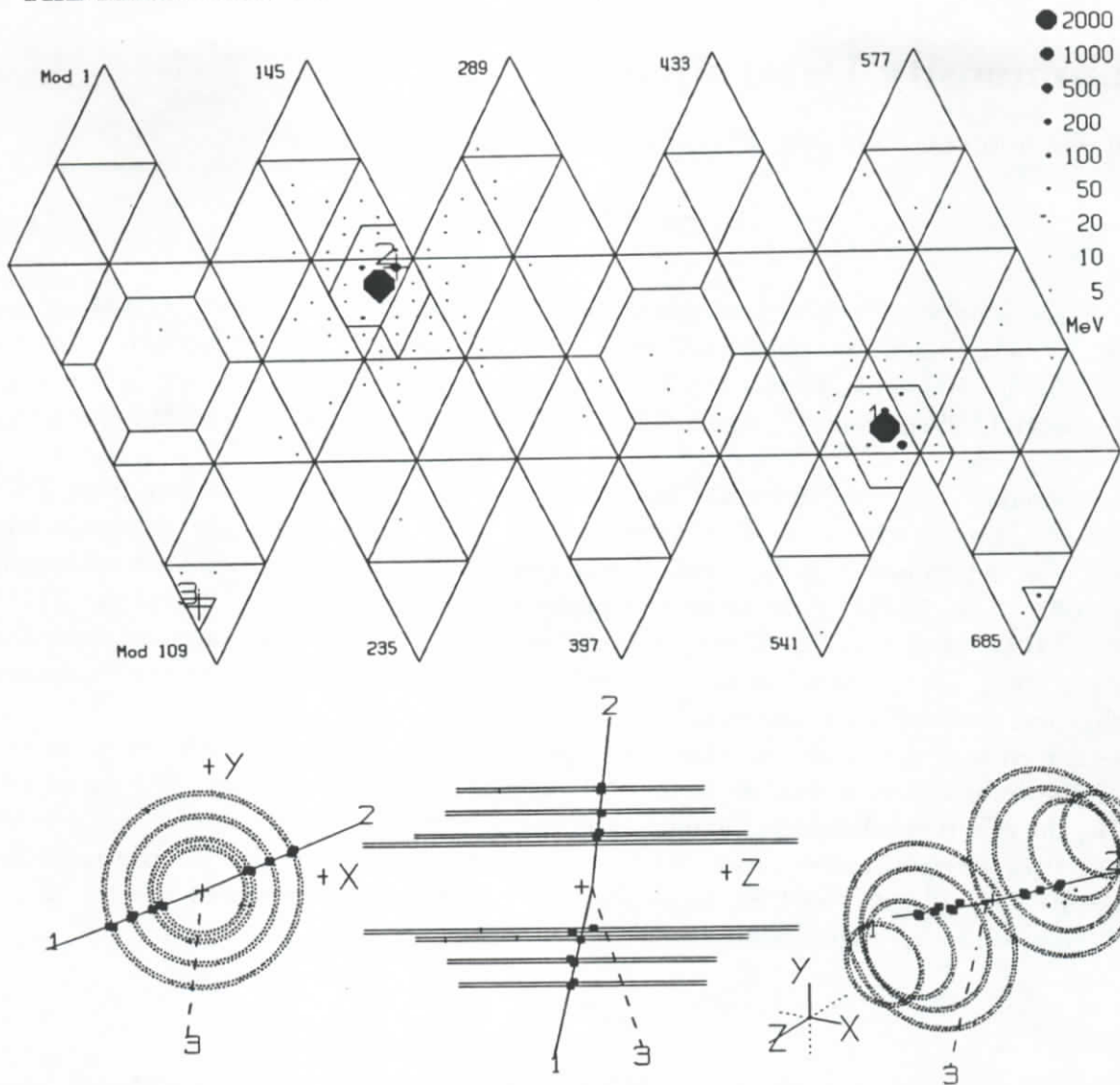


Figure 4.2: Typical example for a (radiative) Bhabha event in the Crystal Ball detector.

For the analysis we assemble data sets of constant c.m. energy  $W$  by collecting data with nearby values of  $W$  from all periods and assigning to each data set a luminosity weighted average c.m. energy  $W_i = \sqrt{\sum \mathcal{L} W^2 / \sum \mathcal{L}}$ . We end up with 28 data sets of different c.m. energies around the  $\Upsilon(1S)$ , 13 data sets around the  $\Upsilon(2S)$ , and 4 data sets on and below the  $\Upsilon(4S)$ .

### 4.3 The Selection of Bhabha Events

The standard reactions to measure the luminosity in the Crystal Ball detector are the processes  $e^+e^- \rightarrow e^+e^-$  and  $e^+e^- \rightarrow \gamma\gamma$ . Events from both processes are selected by requiring exactly two clusters in the calorimeter with a deposited energy of  $E_{dep} > 0.7E_{beam}$ . Both clusters have to lie within  $|\cos\theta| < 0.75$ , where the directions are determined not from the tracks in the chambers, but from the energy depositions in the ball with respect to the origin  $(0,0,0)$ . The selected luminosity events are composed of about 11%  $e^+e^- \rightarrow \gamma\gamma$  events and 89% Bhabha events. Background from sources like  $e^+e^- \rightarrow \tau^+\tau^-$  or  $ee \rightarrow qq$  is below 0.2%. More details can be found in Ref. [83]. A typical luminosity event is shown in Fig. 4.2.

## 4.4 Luminosity Determination

The integrated luminosity for each of our data sets is determined by [83]

$$\mathcal{L} = N_{\mathcal{L}} \frac{W^2}{c_{\mathcal{L}}}, \quad (4.6)$$

where  $N_{\mathcal{L}}$  is the number of selected luminosity events,  $c_{\mathcal{L}} = 1294.3 \text{ nb-GeV}^2$ , and  $W$  is the c.m. energy as determined in Appendix C and Section 4.2 above. The systematic error on  $c_{\mathcal{L}}$  is 2.5% [83,96]. It has its main contributions from a variation of selection cuts within reasonable limits (1.9%), from 4<sup>th</sup> order QED corrections (1.0%), and from MC statistics (1.0%).

For on-resonance data the luminosity has to be corrected for the contribution from  $\Upsilon \rightarrow e^+e^-$ . The variation of the  $\Upsilon \rightarrow e^+e^-$  contribution with the c.m. energy  $W$ , including interference effects between  $\Upsilon$  decays and Bhabha scattering, has been taken into account according to Fig. 2.20. Right on the resonance peaks we subtract  $(1.30 \pm 0.15)\%$  at the  $\Upsilon(1S)$  and  $(0.35 \pm 0.10)\%$  at the  $\Upsilon(2S)$ . The systematic errors on this subtraction arise from the uncertainty in the  $\Upsilon$  branching ratios to  $e^+e^-$ , and from radiative corrections to the resonance peak heights and to the  $e^+e^-$  continuum<sup>2</sup>.

We further correct the luminosity for the dependence of the selection efficiency on the length  $l$  of the intersection region of the  $e^+e^-$  beams along the beam axis. If  $l$  varies (cf. Fig. 3.7(d)), the effective solid angle changes, which is covered by the calorimeter coordinates of  $|\cos\theta| < 0.75$ . From studies on 4-vector level, based on the angular distributions for Bhabha events (Eq. (2.132)) and on those for  $e^+e^- \rightarrow \gamma\gamma$ , we determined the fractional change of the selection efficiency, which results in a change of

$$\frac{\Delta c_{\mathcal{L}}}{c_{\mathcal{L}}} = 0.47\% \frac{\Delta l}{\text{mm}}. \quad (4.7)$$

Here  $\Delta l$  is the deviation of the vertex spread from the value of 1.21 cm, which was used for the determination of  $c_{\mathcal{L}}$ . Depending on the run number we find from Fig. 3.7 luminosity corrections ranging from  $-0.52\%$  to  $+0.33\%$ .

## 4.5 The Selection of $\mu$ -Pair Events

The most prominent features of  $\mu$ -pair events are their acollinearity and their energy depositions in the calorimeter. If no high-energy photons are emitted from the initial or final state, the muons will go into opposite directions (“back-to-back”) and create exactly two energy clusters in the ball, facing each other. In the very most cases the clusters can be correlated with hits in the chambers. The path of 5 GeV muons in the calorimeter intersects typically only one or two crystals, since deviations from the exact radial direction due to multiple scattering ( $\sim 1^\circ$ ) and finite size of the  $e^+e^-$  intersection region ( $\sim 3^\circ$ ) are less than the angular distance between two crystals ( $\sim 7^\circ$ ). The energy loss of 5 GeV muons in the calorimeter peaks at about 217 MeV (see Appendix A) with a (Gaussian) width of about 22 MeV and a Landau tail towards higher energy losses. Energy depositions adjacent to the crystals

<sup>2</sup>Fig. 2.20 shows the fractional contribution to  $e^+e^- \rightarrow e^+e^-$ , only. We neglected the reduction due to the presence of  $e^+e^- \rightarrow \gamma\gamma$ , since it should be partially cancelled by radiative corrections to the t-channel Bhabha scattering, which were not included in the derivation of Fig. 2.20. After the completion of the analysis we have performed more precise estimates, which yield slightly smaller reductions, but remain within one standard deviation of the errors cited.

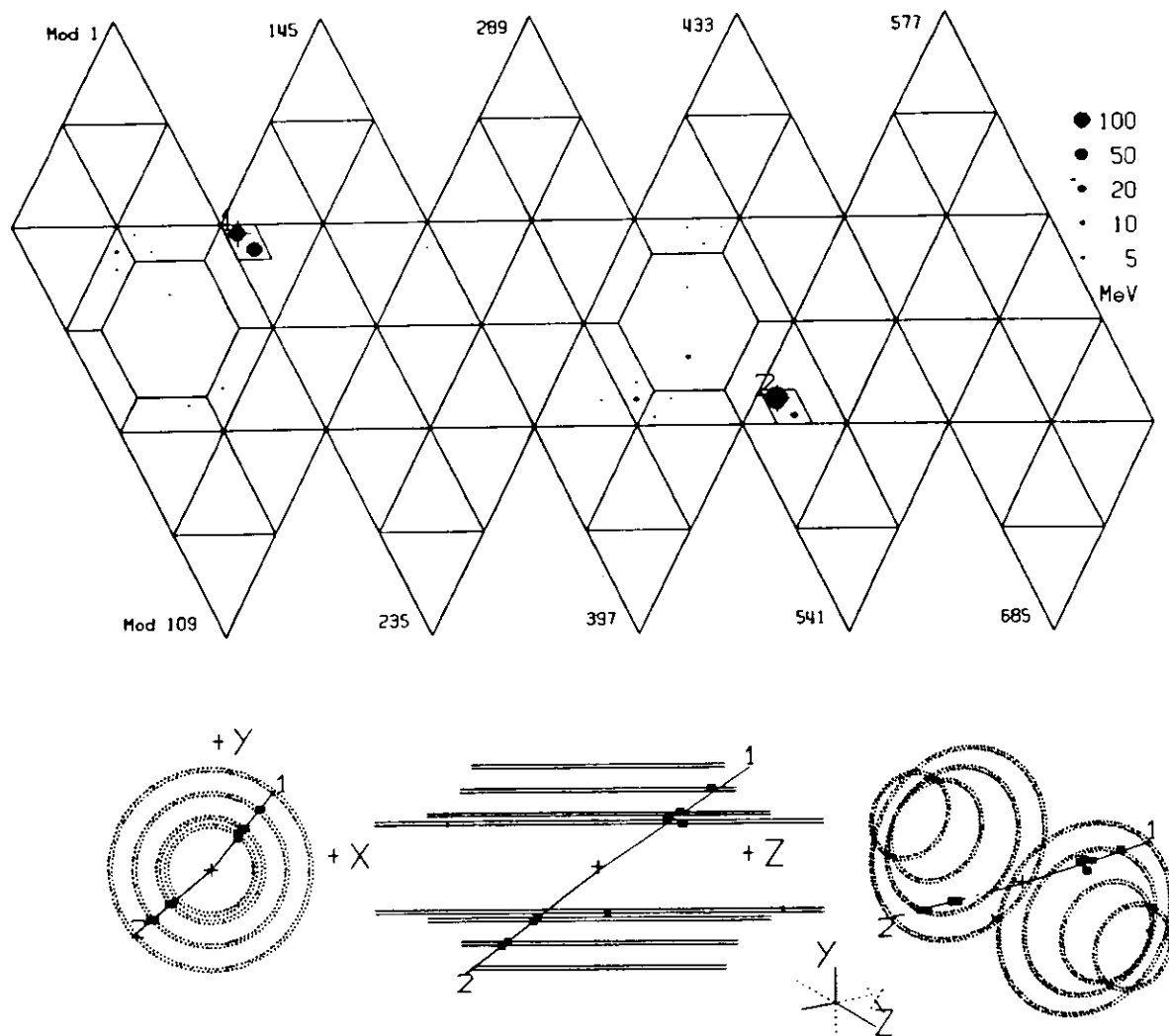


Figure 4.3: Typical example for a  $\mu$ -pair event in the Crystal Ball detector.

with the largest energy deposits, which are caused by  $\delta$ -electrons or by collinear final state photons, are in general smaller than 10 MeV. Energy depositions away from the two muon clusters arise from beam-related background and from initial or final state photons emitted under large angles with respect to the incoming and outgoing leptons. The distribution of this extra energy is peaked at values of  $\approx 5$  MeV, but reveals a long tail extending essentially up to the beam energy. A typical event is shown in Fig. 4.3.

#### 4.5.1 Possible Background Processes

As discussed in Section 2.3.5 the events from  $\Upsilon$  decays to  $\mu^+\mu^-$  sit on a large continuum background from  $e^+e^- \rightarrow \mu^+\mu^-$ . Events from both sources are identical, except the fact, that the energy of *initial* state photons from the resonance production is limited to  $E_\gamma \lesssim 10$  MeV by the c.m. energy spread. The background further contains contributions from two-photon reactions  $e^+e^- \rightarrow e^+e^-X$ , where  $X = \mu^+\mu^-$ ,  $\pi^+\pi^-$ , or  $e^+e^-$ , muonic decays of  $\tau$ -pairs from  $e^+e^- \rightarrow \tau^+\tau^-$ , cosmic ray events, and interactions of the beam electrons with the wall of the beam pipe. (The process  $e^+e^- \rightarrow \pi^+\pi^-$  is negligible [85].) We will sketch the main features of these backgrounds below.

## Two-Photon Events

The most prominent background to  $e^+e^- \rightarrow \Upsilon \rightarrow \mu^+\mu^-$  from sources other than the continuum background  $e^+e^- \rightarrow \mu^+\mu^-$  is the two-photon production of particle pairs according to Diagram 4.4. Since the incident electron pairs generally escape undetected under small angles with respect to the beam pipe, the resulting event looks like a single pair of particles. Lacking a magnetic field, the Crystal Ball detector cannot distinguish low-energy particles from two-photon interactions from 5 GeV muons on the basis of a momentum measurement.

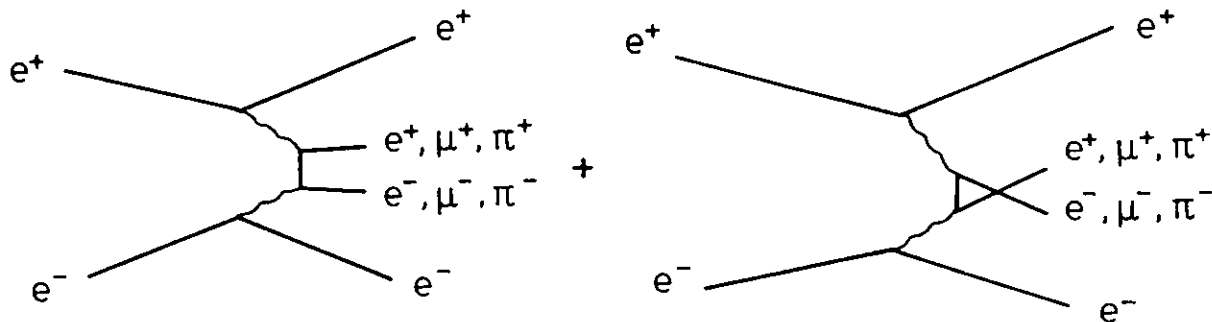


Figure 4.4: Two-photon production of particle pairs.

At  $\sqrt{s} \approx 10$  GeV the total cross-section for two-photon processes is huge with respect to the  $e^+e^- \rightarrow \mu^+\mu^-$  annihilation cross-section, namely about 400 nb for  $e^+e^- \rightarrow e^+e^-e^+e^-$ , 60 nb for  $e^+e^- \rightarrow e^+e^-\mu^+\mu^-$ , and 6 nb for  $e^+e^- \rightarrow e^+e^-\pi^+\pi^-$ , compared to 1 nb for  $e^+e^- \rightarrow \mu^+\mu^-$ . The naively expected suppression of two-photon processes by  $\alpha^2$  with respect to the one-photon annihilation is largely overcompensated by the two photons being emitted essentially on their mass shell, whereas the annihilation process is suppressed by the off-shell propagator of the virtual photon. (The two-photon cross-section increases with powers of  $\ln(s/m_e)$ , whereas the annihilation cross-section falls like  $1/s$ .) The two photons in the process  $\gamma\gamma \rightarrow X$  have in general different energies and their directions are strongly peaked along the beam axis. Due to the large total cross-sections, however, the part of the final state phase space, where the particles are emitted back-to-back with an opening angle of  $\zeta \approx 180$  degree, and under large enough angles  $|\cos\theta| < 0.84$  to the beam axis, is still appreciable. The corresponding distributions for the process  $e^+e^- \rightarrow e^+e^-\mu^+\mu^-$ , obtained from MC studies, are shown in Fig. 4.5.

Besides exploiting its angular distribution the two-photon background can be reduced by the energy depositions in the calorimeter. Since 5 GeV muons typically deposit energies in the range of 150 MeV to 400 MeV, all two-photon events with particles of kinetic energy  $T < 150$  MeV can be rejected. We can further exploit the distribution of the pattern fraction  $F_2$ , defined in Section 3.4, to distinguish electrons (Fig. 4.6) from muons (dashed line in Fig. 4.13(b)), since the lateral energy distributions of electromagnetic showers above 150 MeV is spread over more than two crystals.

Low energy muons and pions from two-photon processes can be less efficiently separated from 5 GeV muons by pattern recognition techniques. After all we showed in Appendix A that there is some noticeable difference in the  $F_2$  pattern fractions between low- and high-energy muons, which can be used to further reduce the two-photon muon background by  $\sim 30\%$ . The pattern fraction of charged pions at low energies are very similar to those of muons of the same energy, in contrast to what is written in Ref. [85]. The energy and range of hadronic reaction products from strongly interacting pions at low energies are too small to perceptibly change the pion's energy depositions or their lateral pattern.

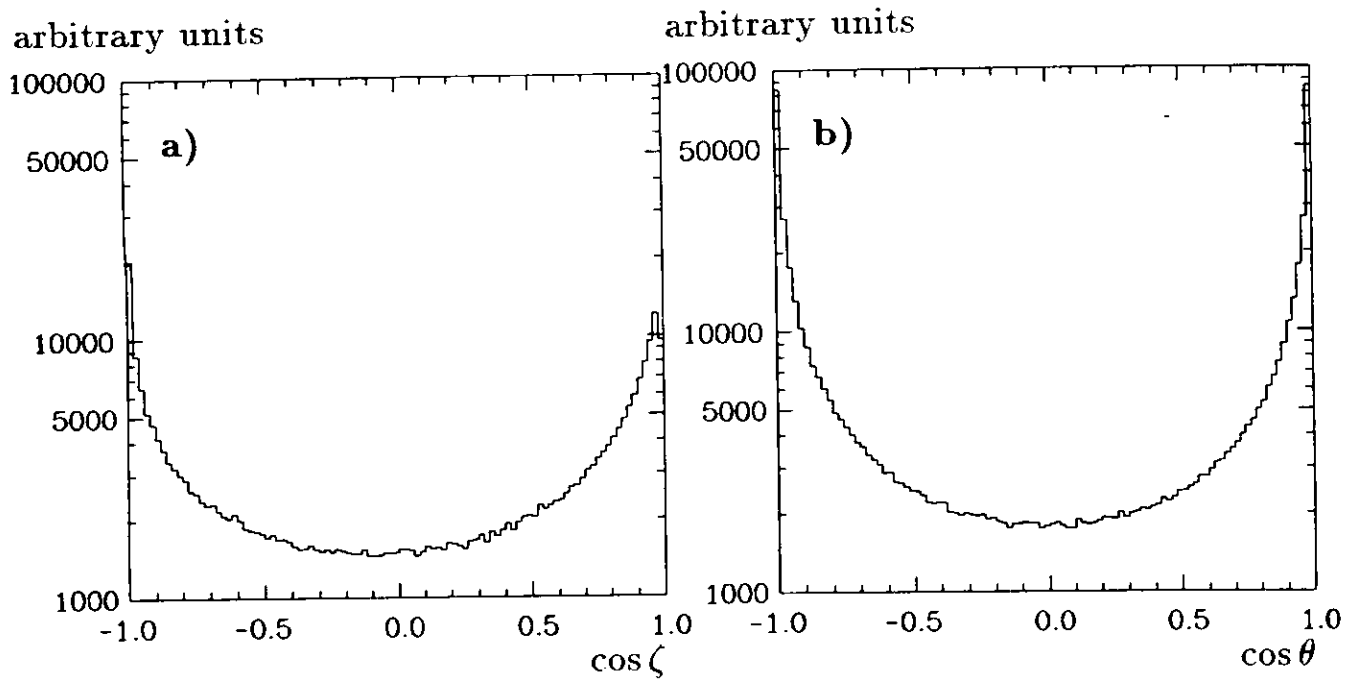


Figure 4.5: Monte Carlo prediction for acollinearity (a) and  $\cos \theta$  distribution (b) of muons from  $\gamma\gamma \rightarrow \mu^+\mu^-$ .

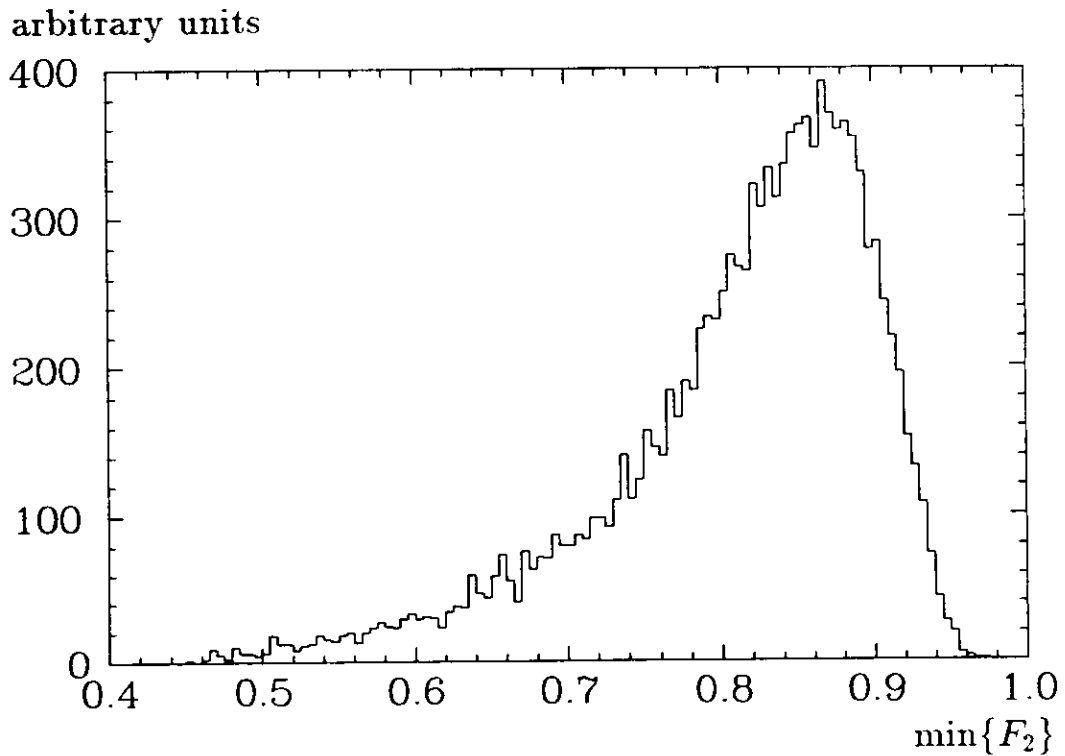


Figure 4.6: The minimum of the  $F_2$  pattern fraction for the two electrons from  $\gamma\gamma \rightarrow e^+e^-$ , where both have a kinetic energy  $T \gtrsim 150$  MeV.

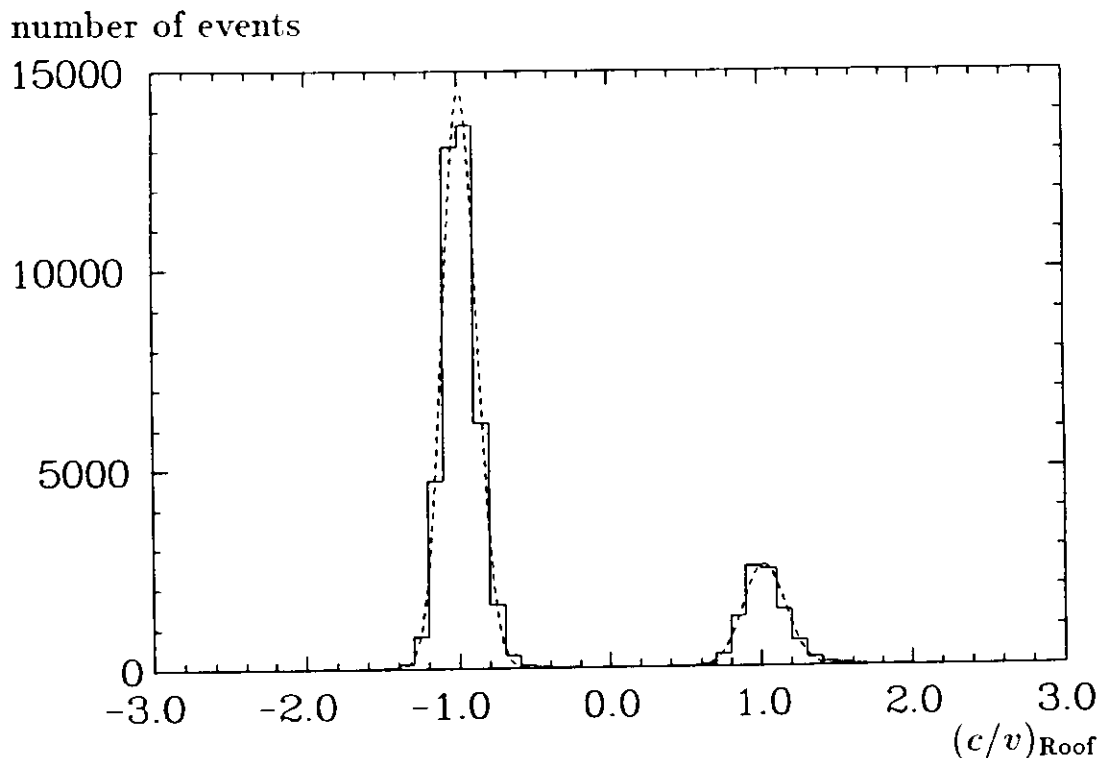


Figure 4.7: Cosmic ray events and annihilation events are clearly distinguished by the measurement of their inverse velocity with the help of the RooF-ToF.

### Tau Pair Events

The main background contribution from tau pair events comes from channels, where both taus decay to one charged particle plus neutrinos, e.g.  $\tau^- \rightarrow e^- \bar{\nu}_e \nu_\tau$ ,  $\tau^- \rightarrow \mu^- \bar{\nu}_\mu \nu_\tau$ , or  $\tau^- \rightarrow \pi^- \nu_\tau$ , which together have a branching ratio of 47% for each tau. Since the charged particle energies are typically  $\sim 2$  GeV, and thus much higher than in two-photon processes, the electrons and about two third of the pions, which interact hadronically, can be easily distinguished from muons by the amount and lateral spread of their energy depositions in the calorimeter. Cuts on acollinearity further reduce the  $\tau^+ \tau^-$  background, since the charged particles are in general not emitted back-to-back due to the presence of 2–4 neutrinos in  $\tau^+ \tau^-$  events.

### Cosmic Ray Background

A muon pair event can be faked by a single cosmic ray muon, which traverses the ball near its center. Such a cosmic ray will create two energy depositions, which are roughly facing each other and thus fulfill the requirements of our  $\mu$ -pair triggers (cf. Section 3.2). In fact, most of the trigger holds for the Major and Minor Triangle Trigger are caused by cosmic rays. Cosmic ray events can be separated from annihilation events with the help of timing and vertex information. Cosmic ray tracks in the chambers passing the beam line with an impact parameter larger than about 1 cm are efficiently rejected by the TAGTRK tracking algorithm [85].

The RooF-ToF counters are intersected for about 80% of the triggered cosmic ray events and (for unpolarized beams) for 50% of the annihilation  $\mu$ -pair events. For these events we

compute the inverse velocity of the particle which traverses the Roof-ToF counters by

$$\left(\frac{c}{v}\right)_{Roof} = c \frac{T_{Roof} - T_{up}}{|\vec{r}_{Roof} - \vec{r}_{Ball}|}, \quad (4.8)$$

where  $T_{Roof}$  is the time of flight measured at the roof counters, and  $T_{up}$  is the Ball-ToF measurement of the Major Triangle containing the energy cluster in the upper ball hemisphere. The distance is measured from  $|\vec{r}_{Ball}|$  half-way inside the crystals to the position  $\vec{r}_{Roof}$  of the Roof-ToF hit, which has a typical distance of 3.5 m from the ball center. For cosmic rays we find  $(c/v)_{Roof}$  centered at  $-1$ , whereas for annihilation  $\mu$ -pairs  $(c/v)_{Roof}$  is centered at  $+1$ , both measured with a resolution of 0.15 (see Fig. 4.7). The separation of the two peaks is hence about 14 standard deviations.

Half of the solid angle, accommodating  $\sim 20\%$  of the cosmic ray muons, is not covered by the Roof-ToF counters. There we have to put up with the Ball-ToF, only. In order to obtain a better resolution, we define a mean inverse velocity averaged over *both* particles as

$$\left(\frac{c}{v}\right)_{Ball} = c \frac{0.5(T_{up} + T_{down}) - T_{vtx}}{\langle |\vec{r}_{Ball} - \vec{r}_{vtx}| \rangle}, \quad (4.9)$$

where  $|\vec{r}_{Ball}| = 45$  cm is again given by the half-way ball radius.  $T_{vtx}$  is the time-zero of the beam crossing, defined in the ToF calibration as  $T_{vtx} = -1.5$  ns. Since all TDCs are started by the beam-crossing signal,  $(c/v)_{Ball}$  is the mean inverse particle velocity for beam-related particles, only. Cosmic rays are not correlated with the beam-crossing, and have a flat distribution of  $T_{up}$  and  $T_{down}$  ( $\approx T_{up} + 3$  ns) within the Crystal Ball trigger timing window of  $\pm 16$  ns around the bunch crossing-signal. Therefore their  $(c/v)_{Ball}$  is ill-defined and flatly distributed. In Fig. 4.8 we observe this flat background below the peak from beam-related events. As shown in Fig. 4.10(a) below, this peak is actually a superposition of two peaks. One of them is the  $(c/v)_{Ball}$  distribution of  $\mu$ -pairs from  $e^+e^-$  annihilation, centered at 1 with a resolution of 0.46. The other peak arises from eN events.

### Background from eN events

A very unwelcome background are eN events from interactions of the beam electrons with nuclei in the wall of the beam pipe (“beam-wall”) or with nuclei of rest gas atoms on the beam axis (“beam-gas”). The amount of eN background depends on the storage ring performance and is thus very time dependent and in addition hard to estimate. Evidence of beam-wall eN background faking  $\mu$ -pair events comes from the x-y vertex distribution of preselected  $\mu$ -pair events with off-axis vertices (Fig. 4.9), showing a clear image of the beam pipe at a radius of about 6 cm.

Cosmic ray events, which also have off-axis “vertices”<sup>3</sup> have been essentially completely removed from this sample by a cut of  $(c/v)_{Roof} > 0$ . For that purpose only those events were collected, where one of the muon candidates pointed to the Roof-ToF counters. The very most of the off-axis events do not record a Roof-ToF hit even though this could be expected from their track directions. This indicates that the particles are low energetic and are stopped in the calorimeter or on their way to the Roof-ToF counters. This is confirmed by their distribution of  $(c/v)_{Ball}$ , which is peaked at  $c/v = 2.4$  (solid line in Fig. 4.10(a)), i.e. at velocities clearly lower than  $c$ . (A small background in Fig. 4.10(a), flatly distributed in  $(c/v)_{Ball}$ , comes from cosmic ray events, which could not be rejected due to inefficiencies in the Roof-ToF counters.) For a comparison, the on-axis events with a Roof-ToF hit, which are dominantly genuine  $e^+e^- \rightarrow \mu^+\mu^-$  events with  $c/v \approx 1$ , are also shown as dashed line in Fig. 4.10(a).

<sup>3</sup>The vertex of a cosmic ray track is defined as the point of closest distance to the beam axis.

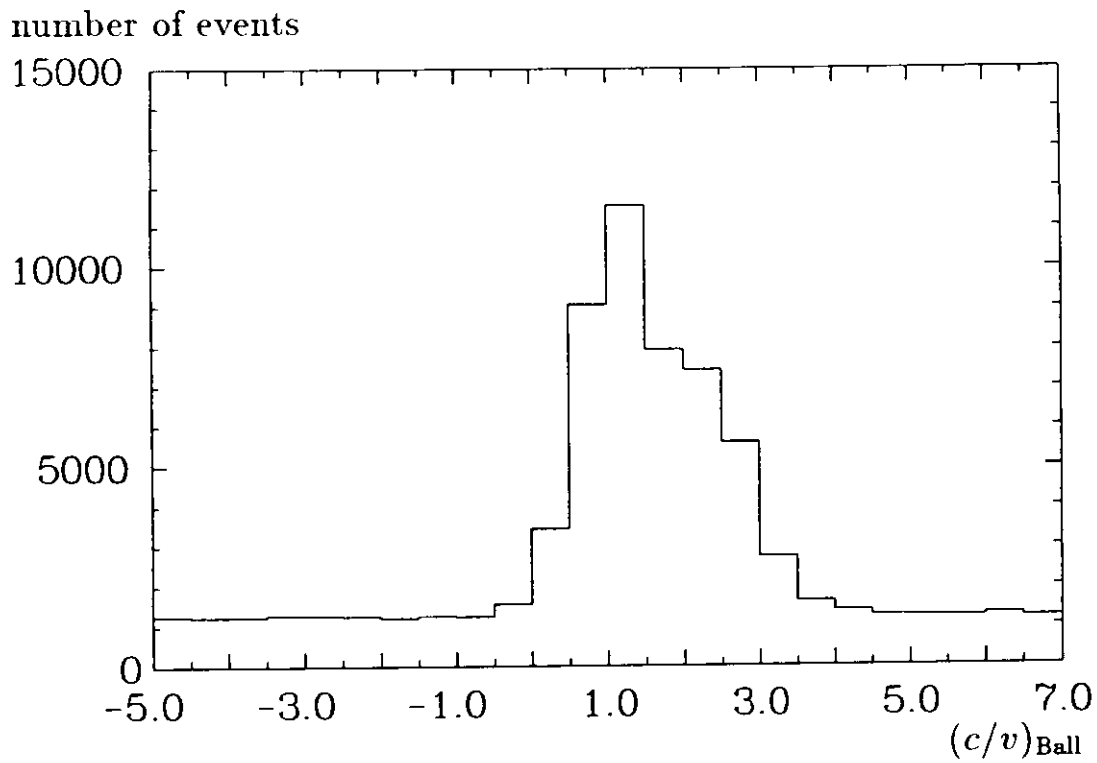


Figure 4.8: In the  $(c/v)_{\text{Ball}}$  distribution cosmic ray events show up as a flat background below the peak from beam-related events.

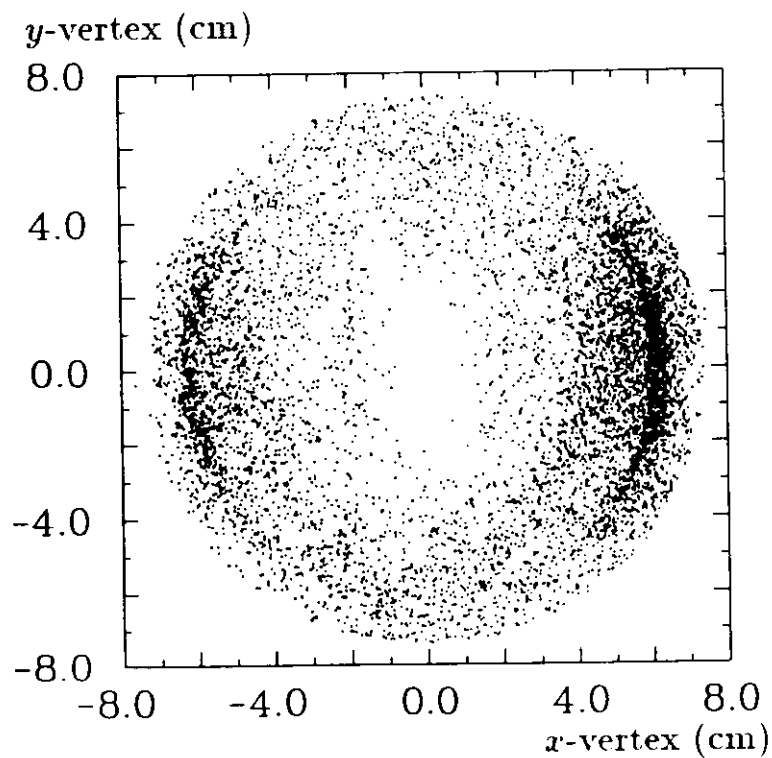


Figure 4.9: The image of the beam pipe in a preselected sample of  $\mu$ -pair candidate events.



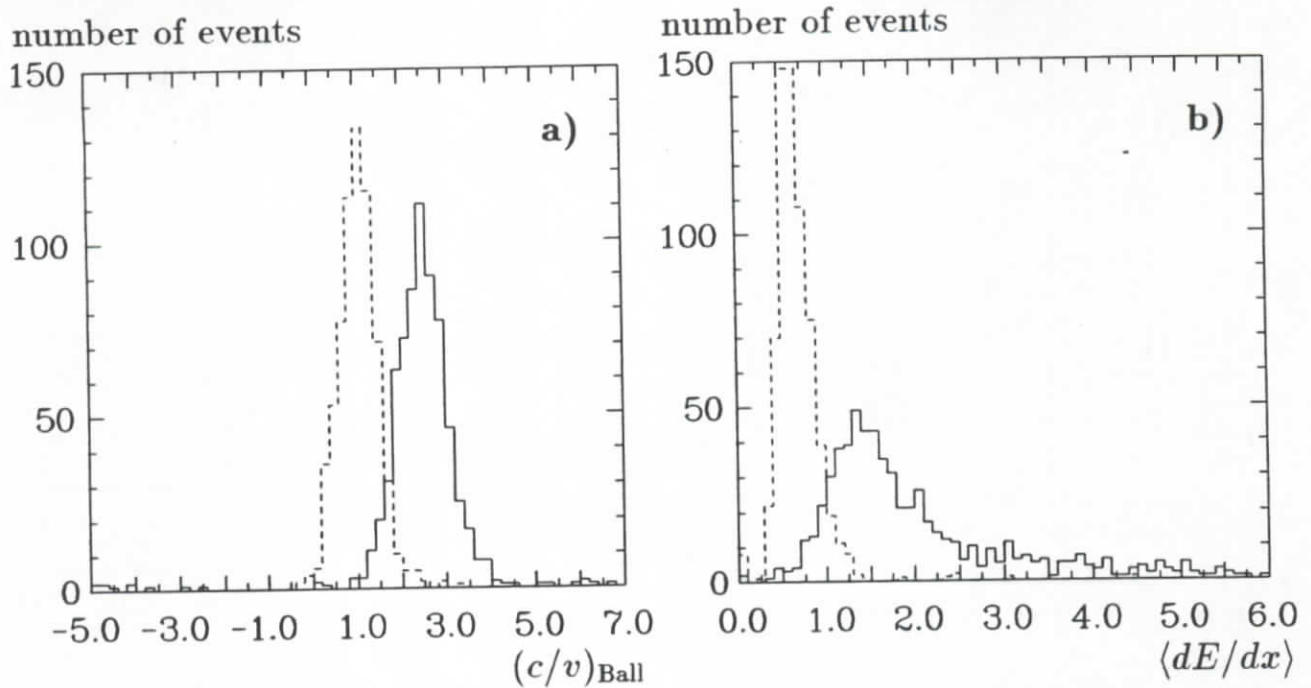


Figure 4.10: Distribution of  $(c/v)_{\text{Ball}}$  (a) and  $\langle dE/dx \rangle$  (b) for  $\mu$ -pair candidate events with one track pointing to the Roof-ToF counters. The solid lines are for off-axis events (mainly eN) and the dashed lines for on-axis events (mainly  $e^+e^- \rightarrow \mu^+\mu^-$ ).

Another feature, unique for particles from the eN background, is their average energy loss  $\langle dE/dx \rangle$  in the proportional chambers. We define this average energy loss  $\langle dE/dx \rangle$  as the truncated mean of the hit pulse heights  $S$ , combining both tracks according to

$$\left\langle \frac{dE}{dx} \right\rangle \equiv \begin{cases} \frac{1}{N-1} \sum_{i=1}^{N-1} \frac{S_i(\text{layer, run}) \sin \theta_i}{\langle S(\text{layer, run}) \sin \theta \rangle_e} & \text{for } N \geq 2 \\ \frac{S(\text{layer, run}) \sin \theta}{\langle S(\text{layer, run}) \sin \theta \rangle_e} & \text{for } N = 1. \end{cases} \quad (4.10)$$

The sum runs over all hits  $i$  in the *proportional* chambers<sup>4</sup>, which have been correlated to either of both muon clusters by the TAGTRK program. To correct for the dependence of the path length in the tube (cf. Appendix B), the total pulse height  $S_i$  of each hit is multiplied by  $\sin \theta_i$ , where  $\theta_i$  is the polar angle of the corresponding track. If more than one (correlated) hit in the proportional chambers is found in the event, the hit with the largest product  $S \sin \theta$  is excluded from the average in order to reduce effects from Landau fluctuations. Since the mean pulse height in the chambers depends on the layer and on time (run number) we normalize the pulse height of each hit to the average pulse height of 5 GeV electrons, which has been recorded in exactly the same layer at the same time of data taking. Fig. 4.10(b) shows the resulting distribution of  $\langle dE/dx \rangle$  for the samples described above. The  $\langle dE/dx \rangle$  of the eN events (solid line) is on an average clearly larger than that from genuine  $e^+e^- \rightarrow \mu^+\mu^-$  events (dashed line).

By plotting  $\langle dE/dx \rangle$  versus  $(c/v)_{\text{Ball}}$  for both samples, their composition emerges more clearly. Fig. 4.11(a) shows a horizontal band of cosmic ray events below the dominant contribution from eN events. Fig. 4.11(b) reveals a small eN background in the on-axis sample.

<sup>4</sup>In our  $\Upsilon(2S)$  data only two of the three double layers were operated in the proportional mode. Thus we have 4 layers of proportional tubes for the  $\Upsilon(2S)$  data and 8 layers for the  $\Upsilon(1S)$  and  $\Upsilon(4S)$  data.

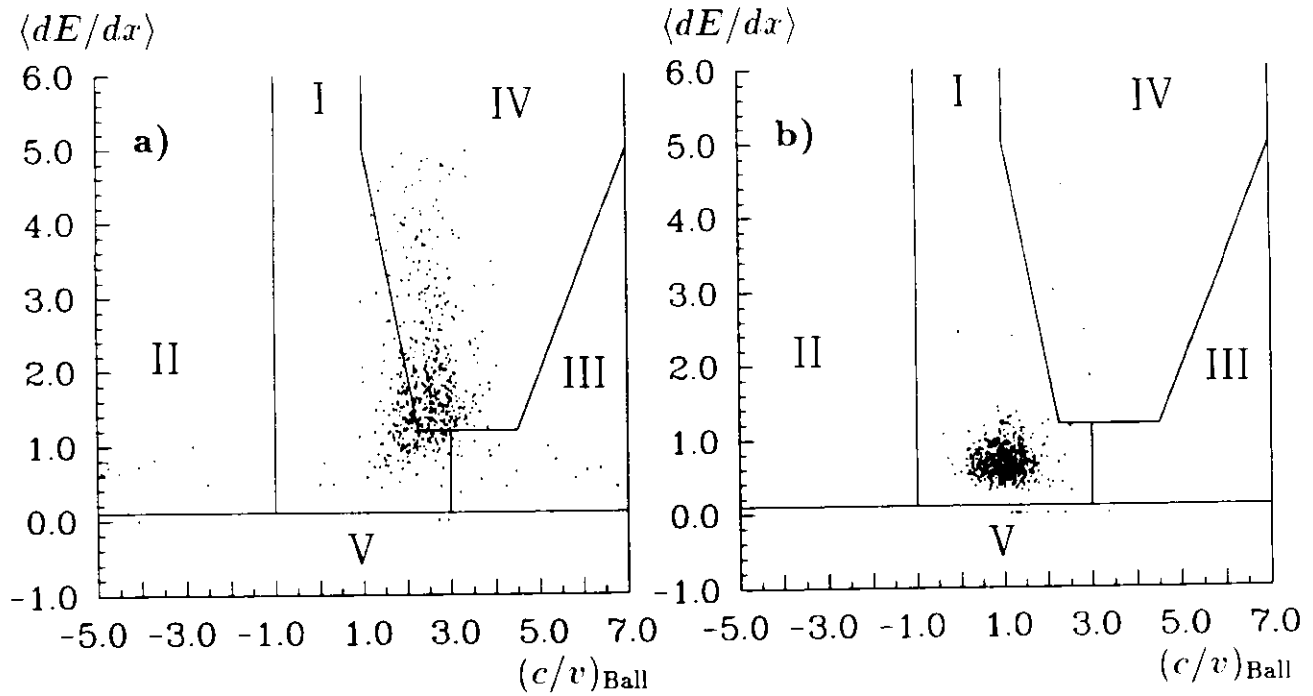


Figure 4.11: Distribution of  $\langle dE/dx \rangle$  versus  $(c/v)_{\text{Ball}}$  for the event sample with off-axis vertices (a, mainly  $eN$ ) and for the on-axis sample (b, mainly  $e^+e^- \rightarrow \mu^+\mu^-$ ). The various regions are explained in Section 4.5.2. The events have been selected from  $\Upsilon(2S)$  data where only 4 layers of proportional tubes were installed. An even better separation in  $\langle dE/dx \rangle$  is obtained with the 8 layers of proportional tubes available in the  $\Upsilon(1S)$  and  $\Upsilon(4S)$  data.

Events at  $\langle dE/dx \rangle = 0$  have no correlated tube hits.

The correlation plot of  $\langle dE/dx \rangle$  versus  $(c/v)_{\text{Ball}}$  can even lead to a sort of “particle identification”. The basis for that is the functional dependence  $d\widehat{E}/dl(\beta\gamma)$  of the most probable energy loss in a single tube on the incident particle momentum shown in Figure B.4 on page 150. Converting this figure to a dependence on  $1/\beta$  yields Figure 4.12. We have indicated by arrows the expected positions of 5 GeV electrons, of 5 GeV muons, of muons and pions with  $T = 200$  MeV (typical for  $\gamma\gamma \rightarrow \mu^+\mu^-, \pi^+\pi^-$ ), and of protons and deuterons with  $T = (150-200)$  MeV. Besides the electrons, which have been used for normalization, all these particles deposit  $\sim 200$  MeV in the calorimeter and can thus appear in our preselected sample of  $\mu$ -pair candidates.

In order to reliably identify from Fig. 4.11 the particle composition of the  $eN$  background, we would have to precisely determine the analogous dependence of the most probable value of  $\langle dE/dx \rangle$  (Eq. 4.10) on  $(c/v)_{\text{Ball}}$  (Eq. 4.9). However, for low-energy particles  $(c/v)_{\text{Ball}}$  is not equal to the inverse velocity  $1/\beta$  in the tubes. E.g. for two-photon generated muons (stopping in the ball) we measure  $(c/v)_{\text{Ball}} \approx 1.25$  somewhat larger than the value of  $1/\beta \approx 1.05$  predicted from their kinetic energy distribution. This effect reflects most probably the true deceleration of low-energy particles while penetrating the ball, since the Ball-ToF is extracted from their total energy deposition in the calorimeter, which is 40 cm deep.

In addition, even if the true velocity  $\beta$  could be measured, the functional dependence of  $\langle dE/dx \rangle(1/\beta)$  would still not be equal to the known dependence  $d\widehat{E}/dl(1/\beta)$  for a single tube hit. It is modified by averaging over all tube hits, and by excluding the largest hit in Eq. 4.10. A precise prediction for  $\langle \frac{dE}{dx} \rangle((\frac{c}{v})_{\text{Ball}})$ , which is mandatory for reliable particle identification, is therefore hampered.

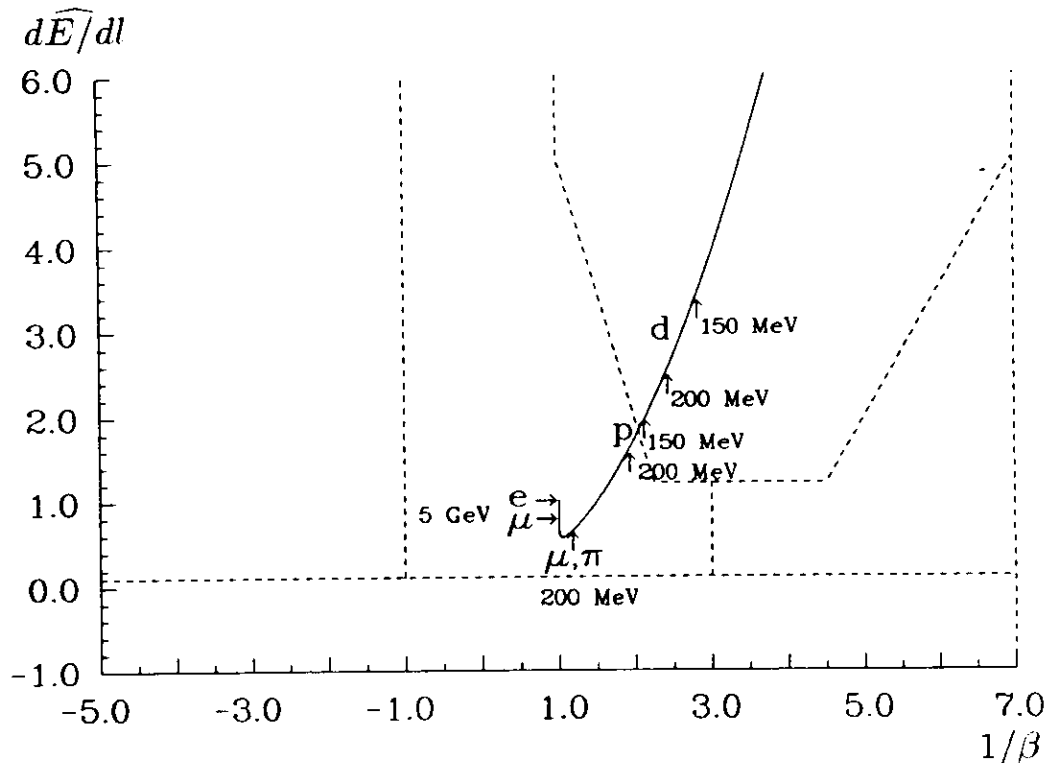


Figure 4.12: Most probable energy loss  $\widehat{dE}/dl$ , normed to 5 GeV electrons, in a single proportional tube versus  $1/\beta$ . For  $1/\beta \gtrsim 1.2$  this curve can be approximated by  $\widehat{dE}/dl = 0.43(1/\beta)^2$ .

However, for getting an idea of what particles are involved in eN events, the approximation

$$\left\langle \frac{dE}{dx} \right\rangle \left( \left( \frac{c}{v} \right)_{\text{Ball}} \right) \cong \frac{\widehat{dE}}{dl} \left( \frac{1}{\beta} \right)$$

should suffice. According to Fig. 4.12 low-energy muons and pions should be located around  $(1/\beta, \widehat{dE}/dl) = (1.05, 0.55)$ , protons with kinetic energy  $T$  ranging from 150 MeV to 200 MeV should lie between  $(2.0, 1.7)$  and  $(1.8, 1.4)$ , and deuterons of the same energy should appear between  $(2.7, 3.1)$  to  $(2.3, 2.3)$ , respectively. The best agreement with the observed peak value for eN events of  $((c/v)_{\text{Ball}}, \langle dE/dx \rangle) = (2.4, 1.4)$  is obtained for the proton hypothesis. The agreement even improves, if we assume that  $(c/v)_{\text{Ball}} > (1/\beta)_{\text{tube}}$  as suggested by the two-photon muons (see above). The most probable assignment for our eN background is thus production of proton pairs in a reaction  $eN \rightarrow ppX$ . Our final determination of the eN background in Section 5.1.2, however, will not rely on this assignment.

By the studies detailed above we have found two independent criteria to identify eN events. The first one is an off-axis vertex, if a cosmic ray event can be excluded by a Roof-ToF measurement. The second criterion is a pair of  $\langle dE/dx \rangle$  and  $(c/v)_{\text{Ball}}$  values, both larger than one. These features are met for most eN events, but rarely occur for other background. This fact will be exploited in the estimation of the residual eN background in our final sample. In addition to using the distributions of  $\langle dE/dx \rangle$  and  $(c/v)_{\text{Ball}}$ , eN events can be efficiently rejected by cuts on the amount  $E_{dep}$  of deposited energy, on the acollinearity, and on the debris energy  $E_{debris}$ . The latter is defined as the energy sum over all crystals in the Main Ball, besides those  $2 \times 13$  crystals which are adjacent to the crystal with the largest energy deposit of either muon candidate. A cut on the lateral pattern fractions  $F_2$  can not reduce the eN background. Typical distributions of these quantities, again compared to those of genuine  $e^+e^- \rightarrow \mu^+\mu^-$  events, are shown in Fig. 4.13(a)-(d).

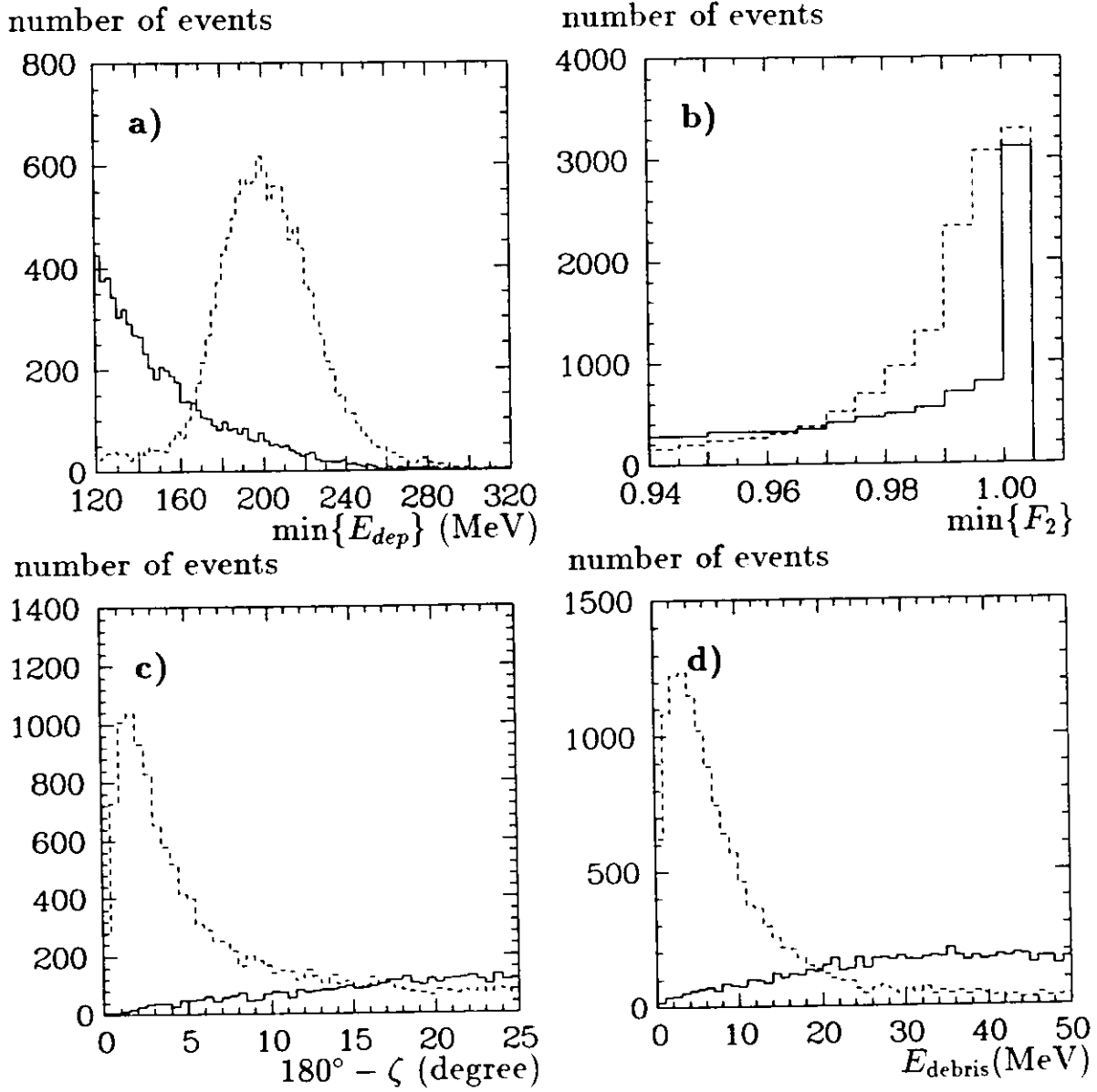


Figure 4.13: Distributions of  $E_{dep}$  (a),  $F_2$  (b), acollinearity  $180^\circ - \zeta$  (c), and  $E_{debris}$  (d) for our samples of (mainly) eN events (solid histograms) and (mainly)  $e^+e^- \rightarrow \mu^+\mu^-$  events (dashed histogram). For plots (a) and (b) the minimum value of both particles is plotted.

## 4.5.2 The Selection Criteria

Our selection exploits the above discussed event characteristics from the calorimeter, tube chamber, and ToF information to separate the background sources from genuine  $e^+e^- \rightarrow \mu^+\mu^-$  events. Since we finally want to subtract continuum data from on-resonance data, the time dependence of the selection acceptance should be accurately reproducible, as is discussed in more detail in the next chapter. Hence, our selection criteria have to meet two requirements. First, they should suppress all background sources well below the level of the continuum process  $e^+e^- \rightarrow \mu^+\mu^-$ . Second, they should introduce time dependences of the selection acceptance, which are either negligible or can be reproduced by MC methods. We apply the following set of cuts.

### Calorimeter Information

- 1.) **There are two energy depositions in the Main Ball fulfilling the requirements of both, the Major and the Minor Triangle Trigger with software thresholds at 160 MeV and 120 MeV, respectively, and less than 30 MeV in each Tunnel Region.**

The software thresholds are designed such that the hardware trigger efficiency for the selection cuts is indistinguishable from 100.0%. An energy deposition of 160 MeV is about 2.5 standard deviations below the peak value expected for 5 GeV muons.

- 2.) **Both energy depositions are smaller than 400 MeV, and the total energy deposited in the Main Ball plus Tunnel Regions plus Endcaps is less than 1000 MeV.**

This cut rejects only few genuine  $e^+e^- \rightarrow \mu^+\mu^-$  events, e.g. if one muon generates a high-energy  $\delta$ -electron above  $\gtrsim 200$  MeV, or if a high-energy (initial state) photon with  $E \gtrsim 500$  MeV hits the Endcaps.

- 3.) **More than 94.5% of each energy deposition is contained in two crystals.**

As can be read off Fig. A.3, this is fulfilled for about 95% of 5 GeV muons, but only for 74% of low-energy muons from two-photon production.

- 4.) **Debris energy in the ball, as defined above, is less than 30 MeV.**

In genuine  $e^+e^- \rightarrow \mu^+\mu^-$  events debris energy arises from photons radiated off from the initial and/or final state particles under large enough angles. In addition, some energy deposited by strayed beam-related particles appears in each event.

### Roof-ToF Information

- 5.) **For energy clusters associated with a Roof-ToF hit the measured inverse velocity of the particles,  $(c/v)_{\text{Roof}}$ , must not lie in the range between  $-1.6$  and  $-0.4$ .**

This corresponds to a 4 standard deviations (s.d.) window around  $(c/v)_{\text{Roof}} = -1$ , which is expected for cosmic rays. Annihilation events are separated from this range by about 10 s.d.

### Ball-ToF Information versus Chamber Pulse Heights

- 6.) The average energy loss  $\langle dE/dx \rangle$  in the chambers and the inverse particle velocity  $(c/v)_{\text{Ball}}$  as measured by the Ball-ToF have to lie in the Region I as indicated in Fig. 4.11.

This cut rejects events with both energy depositions regarded by TAGTRK as to originate from neutral particles (Region V, where  $\langle dE/dx \rangle = 0$ ). It is further effective for eN events mainly located in Region IV, and for cosmic ray events (Regions II and III) outside of a 4 s.d. window around  $(c/v)_{\text{Ball}} = 1$ , which is the expected value for annihilation events. This cut keeps about 99.9% of  $e^+e^- \rightarrow \mu^+\mu^-$  events.

### Chamber Information

- 7.) The event vertex is required to lie on the beam axis with a TAGTRK on-axis significance (cf. Section 3.4)  $\kappa > -0.2$ .

This cut in the on-axis significance keeps more than 99.9% of events originating from the beam axis [85], but is still effective in finding off-axis events. For more than 70% of the eN events in Region IV we detect off-axis vertices. Cosmic ray events with impact parameters to the beam axis of larger than 1 cm can be detected with more than 95% efficiency.

- 8.) The particle directions are measured to be back-to-back within 12 degree.

For exactly back-to-back particles ( $\zeta = 180^\circ$ ) this corresponds to about 3.5 times the experimental resolution. The real acollinearity due to photon radiation is small for most  $\mu$ -pair events, since  $\pi - \zeta \leq x$  holds for small photon energy fractions  $x$ . (A 100 MeV photon ( $x=0.02$ ) induces an acollinearity of  $(180^\circ - \zeta) \lesssim 1^\circ$ .)

Applying the above cuts, we select  $26.6 \times 10^3$  events from  $45.8 \text{ pb}^{-1}$  of data taken on and around the  $\Upsilon(1S)$ ,  $17.5 \times 10^3$  events from  $37.2 \text{ pb}^{-1}$  taken on and around the  $\Upsilon(2S)$ , and  $31.9 \times 10^3$  events from  $72.2 \text{ pb}^{-1}$  of data collected on and below the  $\Upsilon(4S)$ . As will be shown in detail below, most of these events are from the continuum process  $e^+e^- \rightarrow \mu^+\mu^-$ .

Our selection cuts on acollinearity, deposited energy, and lateral pattern reduce the two-photon background to levels of 20%, 2%, and 0.2% for  $\gamma\gamma \rightarrow \mu^+\mu^-$ ,  $\gamma\gamma \rightarrow \pi^+\pi^-$ , and  $\gamma\gamma \rightarrow e^+e^-$ , respectively, measured in terms of the observed continuum cross-section for  $e^+e^- \rightarrow \mu^+\mu^-$ . This corresponds to suppression factors of 300, 300, and 20000 for these three channels, respectively.

The  $\tau^+\tau^-$  background is, similar to the two-photon background, suppressed by the cuts on acollinearity, deposited energy in the calorimeter, and lateral pattern. Our cuts reduce it to about 0.45% of the observed  $e^+e^- \rightarrow \mu^+\mu^-$  continuum cross-section. Including all  $\tau^+\tau^-$  decay channels this corresponds to a reduction by a factor 200. (If we only consider decays of both taus to one charged particle plus neutrinos, the reduction factor is still about 50.)

The cosmic ray background is efficiently rejected by the selection criteria (5)–(7), based on vertex and timing information. A residual cosmic ray background of about 2% corresponds to a reduction factor of about 100 compared to preselected  $\mu$ -pair events.

Finally, the eN background is rejected by cuts (1), (4), and (6)–(8) on calorimeter, chamber, and ToF information. From our background determination below we find a typical eN background of 0.1% in our selected sample. This corresponds to a reduction by a factor of about 300 compared to our preselected  $\mu$ -pair sample.

Altogether, our selection cuts reduce all background sources other than the continuum process  $e^+e^- \rightarrow \mu^+\mu^-$  by at least a factor 100. The fraction of  $\mu$ -pairs from  $\Upsilon$  decays in our



final sample, however, is still relatively small. As will be shown below, it is 21% of the observed continuum cross-section on the  $\Upsilon(1S)$  resonance and only 4.4% on the  $\Upsilon(2S)$  resonance. The observed continuum cross-section is in turn mainly composed of  $e^+e^- \rightarrow \mu^+\mu^-$  events, but has a sizable contribution of  $\gamma\gamma \rightarrow \mu^+\mu^-$  events.

As can be concluded from the short discussions of each cut, the selection criteria were designed to cut a few standard deviations away from the most probable values for genuine  $e^+e^- \rightarrow \mu^+\mu^-$  events. This leads to a high selection efficiency and minimizes rundependent changes in acceptance, which can for example be introduced by a variation of the widths of these distributions with time.

# Chapter 5

## Background Determination

*“Alice laughed. ‘There is no use trying’, she said.  
‘One cannot believe impossible things’.  
‘I dare say you haven’t had much practice’, said the Queen...  
‘... sometimes I have believed as many as  
six impossible things before breakfast !’ ”*

L. Carroll, “Alice in Wonderland”

In the preceding chapter we have identified various background processes to  $e^+e^- \rightarrow \Upsilon \rightarrow \mu^+\mu^-$ . We have shown that backgrounds other than the continuum process  $e^+e^- \rightarrow \mu^+\mu^-$  can be effectively suppressed. The residual background from these sources plus the proper continuum  $e^+e^- \rightarrow \mu^+\mu^-$  has now to be subtracted from the number of  $\mu$ -pair events from on-resonance data in order to extract the observed number of  $\Upsilon$ -resonance decays to muons.

Since the muonic signals from  $\Upsilon$  decays rise only marginally above the total continuum background, it is not sufficient to scale off-resonance data merely by luminosity times the theoretical  $W$ -dependence of the cross-section, and to subtract then the scaled off-resonance numbers from on-resonance data. Any fractional error on the subtracted continuum background will cause a much larger fractional error on the observed number of resonant muons, since the latter number is small compared to the continuum background. Time dependent changes in the detector acceptance, the selection efficiency for  $\mu$ -pairs, or the background level may thus play an important role.

For a precision measurement we have instead to determine the continuum background specific for the given on-resonance running conditions. For example, variations in the eN background, cosmic ray background, tube chamber performance, size and position of the  $e^+e^-$  intersection region must be monitored and taken into account. If possible, the continuum background will be determined separately for each of the 45 data sets of different c.m. energy, which resulted from our determination of the DORIS beam energy described in Section 4.2 and Appendix C.

For the determination of background not originating from  $e^+e^-$  interactions, i.e. cosmic ray and eN events, we exploit the plot of the mean hit pulse height  $\langle dE/dx \rangle$  versus the inverse particle velocity  $(c/v)_{\text{Ball}}$ , as described in Section 5.1.

Yet, the main background to resonant  $\mu$ -pairs stems from  $e^+e^-$  interactions. We use a MC simulation to predict the observed cross-sections and their time dependence for all backgrounds from  $e^+e^-$  interactions as detailed in Section 5.2. This background prediction covers a twofold dependence of the observed  $e^+e^-$  cross-section on the c.m. energy  $W$ , the physical variation of cross-sections  $\sigma(W) \approx \sigma(\sqrt{s})$ , and the variation of the selection efficiency  $\epsilon(W_i)$  for each of our data sets. Our MC simulation is designed to reproduce both dependences,



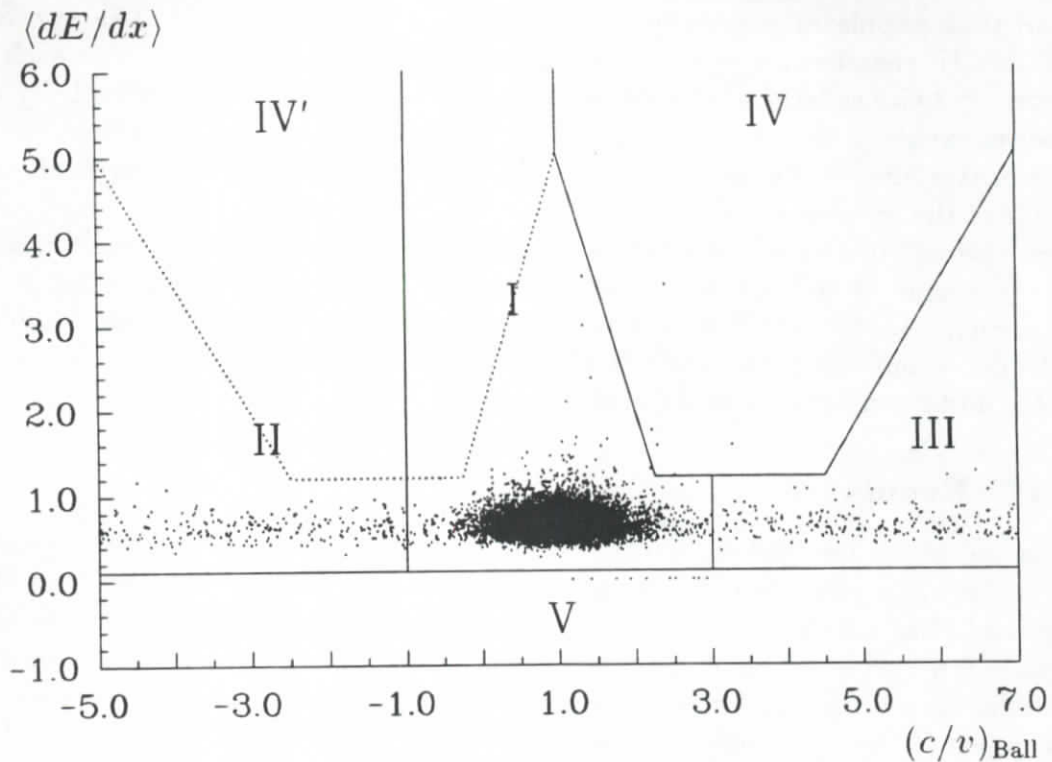


Figure 5.1: Correlation between  $\langle dE/dx \rangle$  and  $(c/v)_{\text{Ball}}$  after all selection cuts for a subsample of events.

since time dependent changes in beam-related background, tube chamber performance, position and size of the  $e^+e^-$  intersection region have been included (cf. Section 3.5).

These MC predictions for each of our 45 data sets still do not yield a precise enough prediction for the continuum background from  $e^+e^-$  interactions. Even if they perfectly reproduce the acceptance variations, the mean MC prediction for the observed cross-sections may systematically deviate by a few percent from the data due to inaccuracies in the event generators, the detector simulation, or the luminosity determination. This would spoil a precision measurement for  $\Upsilon \rightarrow \mu^+\mu^-$  for the same reasons, which prevented us to simply subtract off-resonance data. Thus neither the MC prediction, nor the continuum cross-section observed off-resonance is accurate enough to serve as a decent prediction for the background. Only by combining both informations we are able to predict the background cross-section for each data set precisely enough. The way of combining data and MC and the estimation of its systematic error will be explained in Section 5.3.

## 5.1 Backgrounds other than $e^+e^-$ -Interactions

The correlation plot of mean pulse height  $\langle dE/dx \rangle$  versus inverse particle velocity  $(c/v)_{\text{Ball}}$  serves as a key to determine the amount of cosmic ray and eN background. Fig. 5.1 shows this correlation plot for a subsample of our  $\Upsilon(4S)$  data. Besides the cut which is based on this plot (cut (6) in Section 4.5.2) all other selection criteria have already been applied.

### 5.1.1 Cosmic Ray Events

As discussed in Section 4.5.1, cosmic ray events are flatly distributed in  $(c/v)_{\text{Ball}}$ . Their mean pulse height  $\langle dE/dx \rangle$  is similar to that of high-energy muons. In Fig. 5.1 the cosmic ray

background thus populates a horizontal band around  $\langle dE/dx \rangle \approx 0.6$ . The two Sideband Regions II and III together are spanning a range of  $(c/v)_{\text{Ball}}$  values which is at each value of  $\langle dE/dx \rangle$  exactly twice as large as the corresponding range in the Signal Region I. By counting the number of events in the sideband regions and dividing by two we determine the residual cosmic ray background in the signal region for each of the 45 data sets. It typically amounts to about 2% of the selected events.

The feedthrough of annihilation events into the sideband regions is negligible, since their borders at  $(c/v)_{\text{Ball}}=-1$  and  $(c/v)_{\text{Ball}}=3$  are more than 4 standard deviations away from the signal at  $(c/v)_{\text{Ball}}=1$ . Misidentifications due to bad timing hardware have been excluded. This renders the determination of the amount of cosmic ray background and its time dependence very reliable and its systematic error negligible.

### 5.1.2 eN Events

The estimation of the residual eN background is more difficult, since its distribution in the  $\langle dE/dx \rangle$  vs.  $(c/v)_{\text{Ball}}$  plane is not known a priori and may moreover depend on the beam conditions and thus on time. Evidence for a small eN contamination in the final sample comes from a few events visible in Region IV of Fig. 5.1. These events cannot be explained from annihilation and/or cosmic ray sources, since a comparable number of events should then also appear in the symmetric Region IV' (dotted boundaries) on the left side of Fig. 5.1.

To estimate the number of eN events in the Signal Region I we exploit the fact, that we have two independent criteria to identify eN events (cf. Section 4.5.1). The first criterion is an entry in Region IV in the  $\langle dE/dx \rangle$  vs.  $(c/v)_{\text{Ball}}$  plane. The second is an off-axis vertex, if a cosmic ray event can be excluded by the Roof-ToF measurement. As sketched in Table 5.1, we count the numbers  $A$ ,  $B$ , and  $C$  of events, which fulfill certain combinations of both criteria.

Table 5.1: Definition of event numbers for the estimation of the residual eN background.

Region Number in Fig. 5.1	Off-Axis and no Cosmic Ray	On-Axis
IV	$C$	$B$
I	$A$	$X$

We have corrected for non-eN “contaminations” in these eN event samples, so that the numbers  $A$ ,  $B$ , and  $C$  really refer to eN events, only. A small cosmic ray contribution<sup>1</sup> to the number  $A$  has been subtracted with the help of the  $(c/v)_{\text{Ball}}$  sidebands. Similarly, we subtracted a small number of events found in Region IV' from the numbers  $B$  and  $C$ .

Since the two criteria for eN events are independent, we can assume that the ratios of on-axis and off-axis eN events ( $X/A=B/C$ ) are identical in Regions I and IV, or, equivalently, the ratios of eN events in Regions I and IV ( $X/B=A/C$ ) are identical for on-axis and off-axis events. In any case we find the residual eN background  $X$  in our final data sets by

$$X = \frac{AB}{C}. \quad (5.1)$$

However, even if we combine all data sets around the respective  $\Upsilon$  resonances, the numbers  $A$ ,  $B$ , and  $C$  after all cuts are so small ( $\sim 10$ ), that their statistical errors render the calculation

<sup>1</sup>The cosmic ray contamination would have been overwhelmingly large, if we had not restricted ourselves to the solid angle of the Roof-ToF counters, where the cosmic ray events can be efficiently suppressed.

of  $X$  very unreliable. We thus rewrite Eq. (5.1) as

$$X = A\left(\frac{B}{C}\right) = \left(\frac{A}{C}\right)B \quad (5.2)$$

and determine the ratios  $B_C \equiv B/C$  respectively  $A_C \equiv A/C$  with larger statistics: This larger statistics of eN events is gained by temporarily loosening two cuts and thereby increasing the eN background in the selected data samples. The maximum  $E_{\text{debris}}$  was loosened from 30 MeV to 60 MeV, and the minimum Major Triangle energy from 160 MeV to 110 MeV (cf. Figs. 4.13(a) and (d)). This procedure was chosen to keep the cuts applied for the background estimation as close as possible to our final selection criteria. To allow for a time dependence of the eN background we combined the continuum data samples below each  $\Upsilon$  resonance and the data samples on and around each resonance, respectively. We find both ratios,  $A_C$  and  $B_C$  to be of the order of one in all combined data samples.

With the help of these ratios we derive estimates for the residual eN background after all cuts via

$$\begin{aligned} X_A &\equiv AB_C & \text{and} \\ X_B &\equiv BA_C. \end{aligned} \quad (5.3)$$

The estimates  $X_A$  and  $X_B$  slightly differ from each other, because for  $X_A$  we combine the number  $A$  after all cuts with  $B_C = B/C$  deduced from the loosened cuts, whereas  $X_B$  is composed of the number  $B$  after all cuts and  $A_C = A/C$  from the loosened cuts. We take the mean value of the numbers  $X_A$  and  $X_B$  as an estimation  $X$  for the eN background and their difference as a measure of the systematic error according to

$$X = \frac{1}{2}(X_A + X_B) \quad \text{and} \quad (5.4)$$

$$\Delta X = \frac{1}{2}|X_A - X_B|. \quad (5.5)$$

The numbers of residual eN events from Eq. (5.4) are listed in Table 5.2 together with their statistical errors and the systematic errors from Eq. (5.5). The resulting background level corresponds to an  $e^+e^-$  cross-section of less than 1 pb for all periods. This is  $\lesssim 0.2\%$  of the observed continuum cross-section for  $e^+e^- \rightarrow \mu^+\mu^-$ .

Table 5.2: Residual eN background in the final data samples. We list the number of eN events for each  $10 \text{ pb}^{-1}$  of data.

Comb. Data Set	Below 1S	On 1S	Below 2S	On 2S	Below 4S	On 4S
# of Data Sets	1	27	1	12	3	1
$\mathcal{L}/\text{pb}^{-1}$	8	38	2	35	16	57
eN Evts./ $10\text{pb}^{-1}$	< 3 (90% CL)	$9 \pm 2 \pm 4$	$9 \pm 7 \pm 2$	$8 \pm 2 \pm 2$	$5 \pm 3 \pm 1$	$2 \pm 1 \pm 0.5$

## 5.2 Continuum Backgrounds from $e^+e^-$ -Interactions

All backgrounds from  $e^+e^-$  interactions are simulated with MC methods. The generated events are passed through a complete detector simulation, reconstructed, and subjected to the same cuts as real data. For the two most prominent backgrounds from  $e^+e^-$  interactions, namely  $e^+e^- \rightarrow \mu^+\mu^-$  and  $e^+e^- \rightarrow e^+e^-\mu^+\mu^-$ , we simulate each of the 45 data sets

separately. As explained in Section 3.5 we use for each data set input of tube chamber performance, beam spot parameters and beam related background specific to the contributing runs to model systematic acceptance variations. For the less prominent  $e^+e^-$  background sources the statistical MC errors would largely dominate, if each data set was simulated separately. Therefore we combined their MC simulation for all energies around the  $\Upsilon(1S)$ ,  $\Upsilon(2S)$ , and  $\Upsilon(4S)$ , respectively. The simulation of time dependences in these three samples is still included, but is combined for all runs contributing.

### 5.2.1 The Continuum Process $e^+e^- \rightarrow \mu^+\mu^-$

A prediction for the observed continuum cross-section  $\sigma^{ee \rightarrow \mu\mu}$  has been derived from our modified DYMU2 generator as described in Section 2.3.4. For each data set we have created a number of MC events which corresponds to about 6 times the data luminosity amounting to a total of more than  $10^6$  MC events. The generated cross-sections are 1.293 nb, 1.157 nb, and 1.042 nb at c.m. energies of 9.461 GeV, 10.024 GeV, and 10.580 GeV, respectively. They have to be compared to the Born cross-sections of 0.970 nb, 0.864 nb, and 0.776 nb for the same c.m. energies. The events around the  $\Upsilon(2S)$  were generated with a transverse beam polarization of 75%, which is observed in the data [95].

The result for  $\sigma^{ee \rightarrow \mu\mu}$  after the selection cuts is plotted as dots in Fig. 5.2. As expected we observe significant point-to-point variations of this prediction.

A selection efficiency for the continuum process cannot be given, since we did not generate the complete phase space of initial state radiation, but restricted the  $v$ -parameter below  $v_1 = 0.99$  (see Section 2.3.4). A number for the selection efficiency would thus be specific for our value of  $v_1$ . It would be meaningless to compare such a ill-defined continuum selection efficiency to other experiments, which usually apply different cuts on  $v$  or equivalent quantities in their MC generators. The only fixed reference cross-section for all experiments is the Born cross-section  $\sigma_{\text{Born}}$ . The fraction  $\sigma^{ee \rightarrow \mu\mu} / \sigma_{\text{Born}}$ , however, cannot be called “efficiency”.

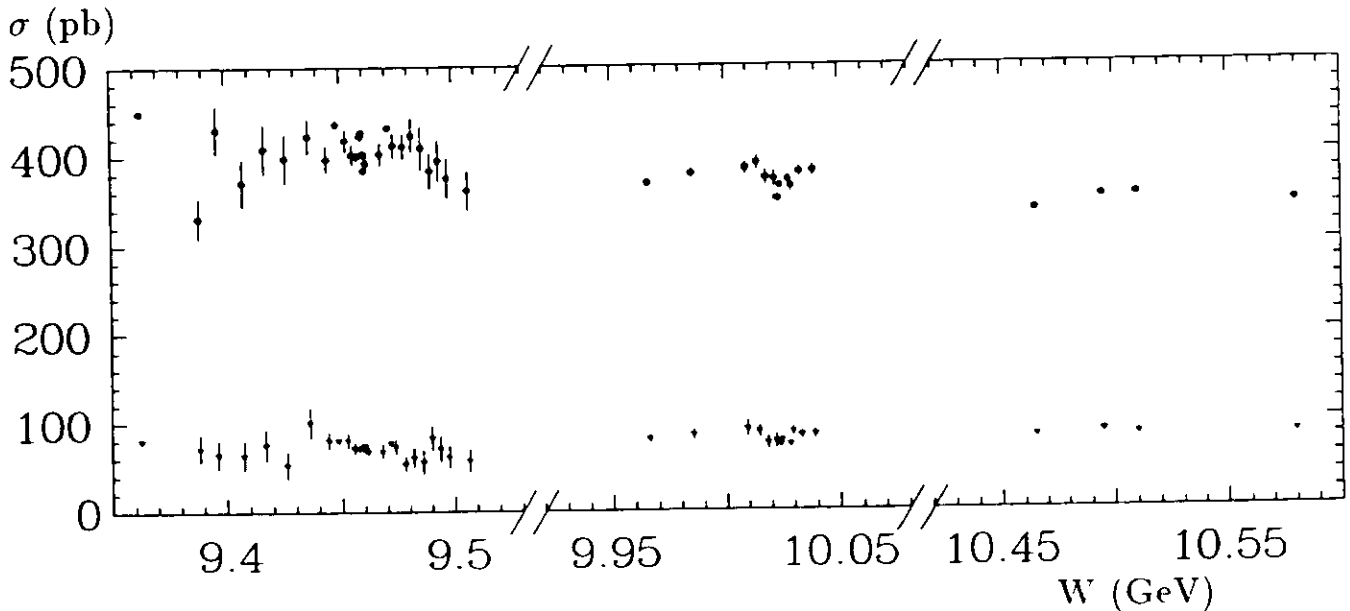


Figure 5.2: Monte Carlo prediction for the observed cross-section from  $e^+e^- \rightarrow \mu^+\mu^-$  (dots) and  $e^+e^- \rightarrow e^+e^-\mu^+\mu^-$  (triangles) for each of our data sets after applying all selection criteria.

### 5.2.2 The Two-Photon Process $e^+e^- \rightarrow e^+e^-\mu^+\mu^-$

The prediction for the observed background cross-section  $\sigma^{ee \rightarrow ee\mu\mu}$  from two photon  $\mu$ -pairs has been calculated from events  $e^+e^- \rightarrow (\gamma)e^+e^-\mu^+\mu^-$ , generated according to Ref. [97]. This generator simulates the two “multiperipheral” diagrams of Fig. 4.4, but allows in addition for initial state radiation of one photon. Since the total cross-section for  $e^+e^- \rightarrow e^+e^-\mu^+\mu^-$  is much larger than for  $e^+e^- \rightarrow \mu^+\mu^-$ , we already exclude on the generator level events from a further simulation, which are in phase space regions where our acceptance is zero. Applying cuts on the invariant  $\gamma\gamma$  mass of  $M_{\gamma\gamma}^2 > 20m_\mu^2$ , and angular cuts on the muons of  $|\cos\theta| < 0.90$  for the polar angles and  $\cos\zeta < -0.87$  ( $\cong \zeta \gtrsim 150^\circ$ ) for the acollinearity angle of the muon pair, the generated cross-sections are 1.381(3) nb, 1.417(4) nb, and 1.450(3) nb for the c.m. energies 9.461 GeV, 10.024 GeV, and 10.580 GeV, respectively. The figure in parentheses gives the statistical MC error on the last digit. These cross-sections are still larger than the continuum cross-section for  $e^+e^- \rightarrow \mu^+\mu^-$ .

Initial state photons were created down to  $k_s = E_\gamma/E_{\text{beam}} = 6 \times 10^{-4}$  ( $\cong 3$  MeV) with a  $k_0$  parameter [97] of  $10^{-2}$ . About 24% of the generated events have a photon above this cutoff. However, only about 0.5% of these photons are emitted under large enough angles with respect to the beams so that they appear in the Crystal Ball calorimeter.

For each data set we create a number of MC events, which corresponds to about 4 times the data luminosity amounting to a total of  $0.6 \times 10^6$  MC events. The prediction for the observed background cross-section  $\sigma^{ee \rightarrow ee\mu\mu}$  after our selection cuts is plotted as triangles in Fig. 5.2. As a function of c.m. energy the contribution of  $e^+e^- \rightarrow e^+e^-\mu^+\mu^-$  events ranges from 18% to 24% of the observed cross-section for  $e^+e^- \rightarrow \mu^+\mu^-$ .

### 5.2.3 The Two-Photon Process $e^+e^- \rightarrow e^+e^-\pi^+\pi^-$

Our generator [98] for  $e^+e^- \rightarrow e^+e^-\pi^+\pi^-$  sums the continuum process  $\gamma\gamma \rightarrow \pi^+\pi^-$  and the resonant process  $\gamma\gamma \rightarrow f_2(1270) \rightarrow \pi^+\pi^-$ . We again apply cuts on the generator level to reduce the amount of simulated events. These cuts are  $|\cos\theta| < 0.90$  for both pions and  $\cos\zeta < -0.70$  ( $\cong \zeta \gtrsim 135^\circ$ ). We find corresponding cross-sections of 0.670(2) nb, 0.687(2) nb, and 0.696(3) nb for the c.m. energies 9.461 GeV, 10.024 GeV, and 10.580 GeV, respectively. We create about 75,000 events for each of these c.m. energies corresponding to about twice the data luminosity. After applying the selection cuts we find a contribution of  $e^+e^- \rightarrow e^+e^-\pi^+\pi^-$  events ranging from 1.4% to 1.9% of the observed cross-section for  $e^+e^- \rightarrow \mu^+\mu^-$ , depending on  $W$ . The values for  $\sigma^{ee \rightarrow ee\pi\pi}$  are listed in Table 5.3.

### 5.2.4 The Two-Photon Process $e^+e^- \rightarrow e^+e^-e^+e^-$

The process  $e^+e^- \rightarrow e^+e^-e^+e^-$  was generated according to the Equivalent Photon Approximation [99]. The huge total cross-section of about 400 nb was reduced on the generator level by cuts on the electron energy  $E_e > 140$  MeV,  $|\cos\theta| < 0.90$  for both electrons, and  $\cos\zeta < -0.92$  ( $\cong \zeta > 157^\circ$ ) to 2.585(13) nb, 2.635(13) nb, and 2.690(13) nb at  $W = 9.461$  GeV, 10.024 GeV, and 10.580 GeV, respectively. Since this background is efficiently reduced by our cuts, we only generated 25,000 events for each of these c.m. energies, corresponding to about one fifth of the data luminosity. The residual background from this source ranges from 0.15% to 0.19% of  $\sigma^{ee \rightarrow \mu\mu}$  after the selection cuts. The resulting values of  $\sigma^{ee \rightarrow ee ee}$  are also listed in Table 5.3.

Table 5.3: Monte Carlo prediction for the observed cross-sections from the less prominent sources of continuum background.

$W$	(GeV)	9.461	10.024	10.580
$\sigma^{ee \rightarrow ee\pi\pi}$	(pb)	$5.4 \pm 0.2$	$5.7 \pm 0.2$	$6.6 \pm 0.3$
$\sigma^{ee \rightarrow eeee}$	(pb)	$0.6 \pm 0.2$	$0.6 \pm 0.2$	$0.6 \pm 0.2$
$\sigma^{ee \rightarrow \tau\tau}$	(pb)	$1.8 \pm 0.2$	$1.6 \pm 0.2$	$1.5 \pm 0.2$

### 5.2.5 The Continuum Process $e^+e^- \rightarrow \tau^+\tau^-$

Tau-pair events are simulated according to Ref. [100]. No cuts were applied on the generator level. One initial or final state photon was generated explicitly, if  $E_\gamma > 3$  MeV. The generated cross-section corresponds to 1.13 nb, 1.01 nb, and 0.90 nb at  $W = 9.461$  GeV, 10.024 GeV, and 10.580 GeV, respectively. We simulated the detector behaviour at these c.m. energies for 50,000 events, each, which is about the number expected from the data luminosity. The resulting predictions for the observed cross-section  $\sigma^{ee \rightarrow \tau\tau}$  are again listed in Table 5.3. They correspond to a level of 0.45% of  $\sigma^{ee \rightarrow \mu\mu}$ .

## 5.3 Continuum Background Subtraction

Since the  $\Upsilon$  resonances rise only marginally above the continuum background, the precision of the background reproduction constitutes the dominant systematic error in our analysis. The only background which can be reliably subtracted with a negligible systematic error is that from cosmic rays. We thus subtract the cosmic ray events according to Section 5.1.1 before further studying the background.

Fig. 5.3(a) shows the resulting observed  $\mu$ -pair cross-section  $\sigma_i^{\mu\mu}$  after our selection for each of the 45 values  $W_i$ . The dotted lines shows a typical behaviour of the observed cross-section, which would be expected if the detector acceptance was a constant in time. We observe significant point-to-point variations deviating by typically 10% from such a smooth cross-section.

Fig. 5.3(b) shows the background prediction  $\sigma_i^{BG}$  for the same data points. It has been obtained by summing the MC predictions of Fig. 5.2 and Table 5.3<sup>2</sup> and the estimations of the eN background from Table 5.2. Like Fig. 5.3(a), this prediction also reveals significant point-to-point variations. In the following we study the accuracy of the mean amplitude of this prediction as well as its ability to reproduce the background variations.

The systematic errors of the mean amplitudes of the observed cross-section  $\sigma^{\mu\mu}$  in Fig. 5.3(a) and of the background prediction in Fig. 5.3(b) are both 2.5%. The former arises from the luminosity measurement (see Section 4.4) and the latter is dominated by the accuracy of event generators and detector simulation (see Section 6.1). Directly subtracting  $\sigma_i^{BG}$  from  $\sigma_i^{\mu\mu}$  would thus result in a systematic error of 3.5%. As already emphasized in the beginning of Chapter 5, such an error would spoil a precision measurement of  $\Upsilon(1S) \rightarrow \mu^+\mu^-$  and even render a significant measurement of  $\Upsilon(2S) \rightarrow \mu^+\mu^-$  impossible, since the latter resonance enhancement rises only 4.4% above the continuum (see below).

We instead combine the information from off-resonance data and background prediction

<sup>2</sup>A slight  $W$ -dependence of the cross-sections for the backgrounds from Table 5.3 across the respective resonance regions has been taken into account.

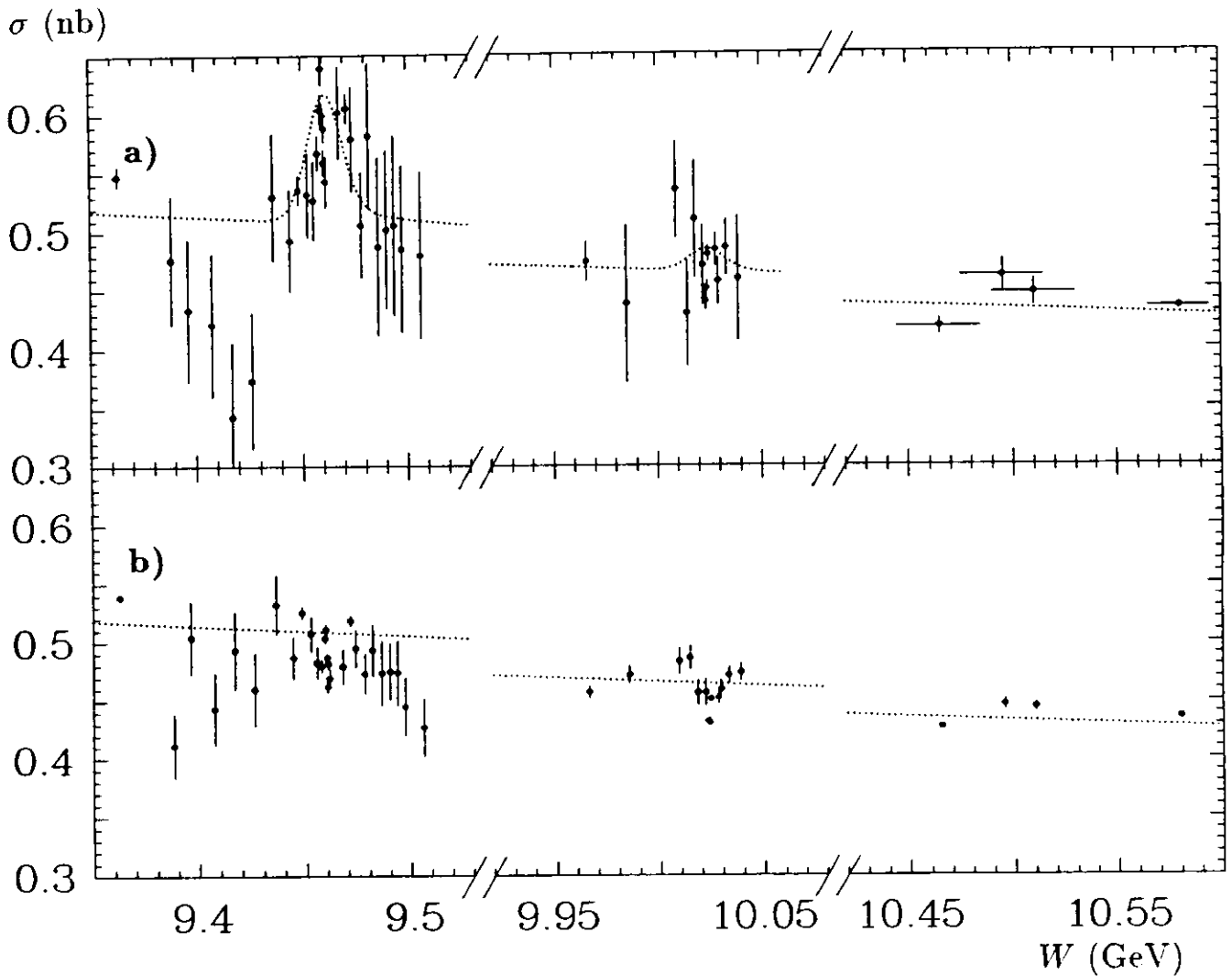


Figure 5.3: Measured cross-section for  $\mu$ -pairs (a) and the prediction of the continuum background (b) versus c.m. energy  $W$ . The background prediction is the sum of all continuum background processes. It does not include the resonant process  $\Upsilon \rightarrow \mu\mu$ . The fluctuations arise from variations of the detector acceptance with time. The dotted curves show typical expectations for a constant detector acceptance. A good correlation between the data (a) and the background prediction (b) is observed from the respective variation of the high statistics points around these dotted lines.

by defining a scaling factor

$$C \equiv \left\langle \frac{\sigma_j^{\mu\mu}}{\sigma_j^{BG}} \right\rangle_{off}, \quad (5.6)$$

where “off” denotes the average over the off-resonance c.m. energies  $W_j$ . Since  $\sigma_j^{\mu\mu}$  should be equal to  $\sigma_j^{BG}$  off resonance, the resulting value of  $C$  has to be equal to one within its systematic error of 3.5%. It thus represents a crucial consistency check of our analysis.

In addition, this scaling factor considerably reduces our systematic error on the background subtraction. By multiplying each point of the background prediction with the same factor  $C$ , obtained from Eq. (5.6), we fix the mean amplitude of the subtracted background to that level which has been observed in the data. The main systematic error on the background subtraction then arises from the reproduction of the point-to-point variations. This can be proven by rewriting Eq. (5.6) as

$$C \approx \frac{N_{off}^{\mu\mu}}{\mathcal{L}_{off} \sigma_{off}^{BG}}, \quad (5.7)$$

where  $N_{off}^{\mu\mu}$  is the number of observed  $\mu$ -pair events summed over the off-resonance c.m. energies,  $\mathcal{L}_{off}$  is the sum of the corresponding luminosities, and  $\sigma_{off}^{BG} \equiv \langle \sigma_j^{BG} \rangle_{off}$  is the mean predicted off-resonance (background) cross-section. We obtain the observed number  $N_i^{\Upsilon-\mu\mu}$  of resonance decays to muons for each  $W_i$  by

$$N_i^{\Upsilon-\mu\mu} = N_i^{\mu\mu} - C \mathcal{L}_i \sigma_i^{BG} \quad (5.8)$$

$$\approx N_i^{\mu\mu} - N_{off}^{\mu\mu} \frac{\mathcal{L}_i}{\mathcal{L}_{off}} \frac{\sigma_i^{BG}}{\sigma_{off}^{BG}}. \quad (5.9)$$

This way of background subtraction no longer depends on the absolute values of  $\mathcal{L}_i$  and  $\sigma_i^{BG}$ . Their systematic errors are thus eliminated. Instead we see from Eq. (5.9) that now the errors on the *ratios*  $\mathcal{L}_i/\mathcal{L}_{off}$  and  $\sigma_i^{BG}/\sigma_{off}^{BG}$  as well as the error on the measured number  $N_{off}^{\mu\mu}$  are relevant. These errors are all smaller than the 2.5% uncertainties of  $\mathcal{L}_i$  and  $\sigma_i^{BG}$  alone.

In the following we first determine the value of  $C$  (Section 5.3.1) and then investigate the errors on the luminosity ratios (Section 5.3.2) and on the ratios of the background predictions (Section 5.3.3). Special emphasis has been layed on a thorough calculation of both errors. Since we subtract in Eq. (5.8) two large numbers from each other, an error on the subtracted background  $N_i^{BG} \equiv C \mathcal{L}_i \sigma_i^{BG}$  has a strong impact on the result for  $N_i^{\Upsilon-\mu\mu}$ . *Fractional* errors on  $\mathcal{L}_i/\mathcal{L}_{off}$  and  $\sigma_i^{BG}/\sigma_{off}^{BG}$  cause a *fractional* error on the number  $N_i^{\Upsilon-\mu\mu}$  which is larger by a factor of  $\lambda = N_i^{BG}/N_i^{\Upsilon-\mu\mu}$ . Summing over c.m. energies  $W_i$  within  $\pm 10$  MeV of the resonance peaks in Fig. 5.3, we find the values  $\lambda(1S)=4.8$  and  $\lambda(2S)=23$ . This means that the resonances rise only by  $1/\lambda(1S)=21\%$  and  $1/\lambda(2S)=4.4\%$  above the continuum background (cf. also Table 6.3 in Section 6.2.2). A combined error of only 1% from the two ratios  $\mathcal{L}_i/\mathcal{L}_{off}$  and  $\sigma_i^{BG}/\sigma_{off}^{BG}$  would for example affect our result of  $N^{\Upsilon-\mu\mu}$  by already 4.8% and 23% for the  $\Upsilon(1S)$  and the  $\Upsilon(2S)$ , respectively.

For the estimation of  $\Delta(\mathcal{L}_i/\mathcal{L}_{off})$  and  $\Delta(\sigma_i^{BG}/\sigma_{off}^{BG})$  we thus study all effects, which potentially could introduce variations of more than 0.1% (one per mil) in the detector acceptance or the amount of background.

### 5.3.1 The Scaling Factor $C$

We determine  $C$  from Eq. (5.6) and Fig. 5.4 by averaging over 6 off-resonance points, using the data sets of  $8 \text{ pb}^{-1}$  at the lowest continuum c.m. energy below the  $\Upsilon(1S)$ ,  $2 \text{ pb}^{-1}$  at the lowest continuum c.m. energy below the  $\Upsilon(2S)$ , and  $9 \text{ pb}^{-1}$ ,  $3 \text{ pb}^{-1}$ ,  $4 \text{ pb}^{-1}$ , and  $57 \text{ pb}^{-1}$



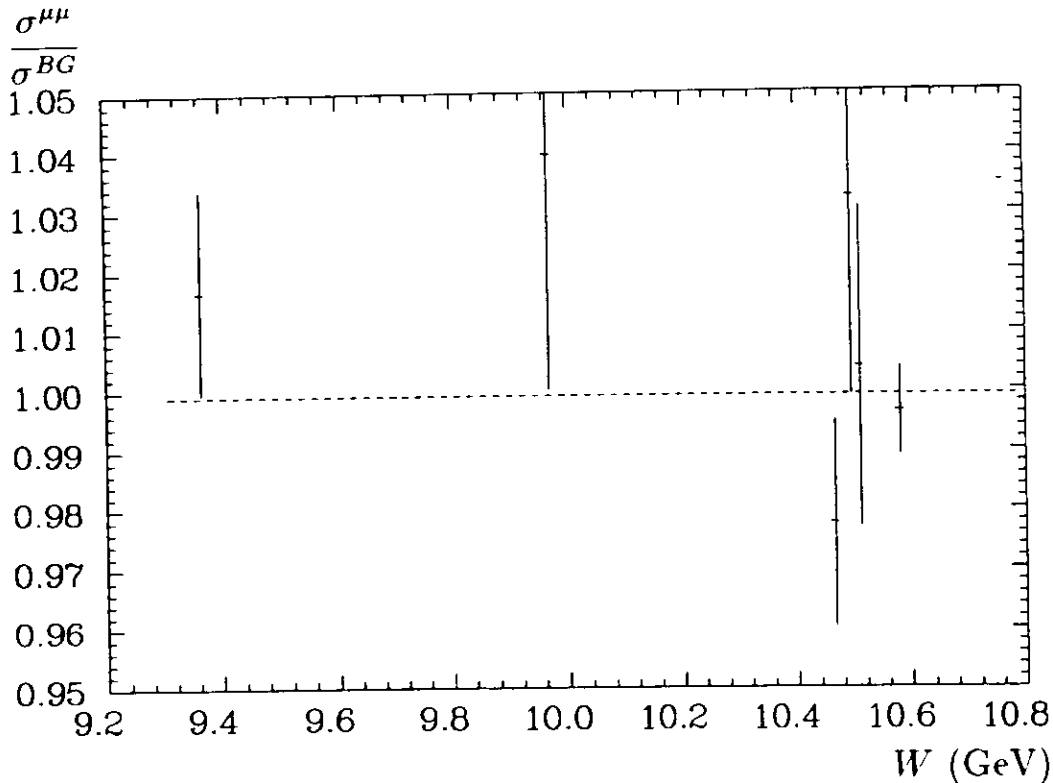


Figure 5.4: Determination of the scaling factor  $C$  by a fit to 6 off-resonance data sets.

at the c.m. energies below and on the  $\Upsilon(4S)$ . (As has been shown in Section 2.3.1, the muonic branching ratio of the  $\Upsilon(4S)$  is small enough that the latter data can be regarded as continuum.)

A fit to the ratios  $\sigma^{\mu\mu}/\sigma^{BG}$  for these 6 points to a constant  $C$  has a confidence level of 44% and results in

$$C = 0.999 \pm 0.006.$$

The error of this number is dominated by the data statistics. It contains in addition small contributions from MC statistics, from the statistics of luminosity events, and from the uncertainty  $\Delta W = 15$  MeV at  $W = 10580$  MeV, which enters through the  $\Upsilon(4S)$  interference with the continuum<sup>3</sup> (cf. Fig. 2.11).

The fit result shows that our prediction for the amplitude of the observed cross-section is in excellent agreement with the off-resonance data. The prediction even turns out to reckon the data much better than expected from its systematic uncertainty of 3.5%.

We stress that  $C$  and its error are no measures for the precision in predicting the point-to-point variations in the amount of background, because they express the precision of the *mean* prediction for the off-resonance data. Nevertheless, the good confidence level of the fit over 6 different points may be taken as a first hint on the smallness of point-to-point errors. The statistical errors of the 6 points included in the fit, however, restrict its sensitivity to point-to-point errors of  $\gtrsim 2\%$ .

With the help of the scaling factor  $C$  we obtain the observed cross-section  $\sigma_i^{e^+e^- \rightarrow \Upsilon \rightarrow \mu\mu}$  for both the  $\Upsilon(1S)$  and the  $\Upsilon(2S)$  as a function of  $W$  by subtracting the background spectrum from Fig. 5.3(b), scaled by  $C$ , from the observed  $\mu$ -pair cross-section  $\sigma_i^{\mu\mu}$  in Fig. 5.3(a)

$$\sigma_i^{e^+e^- \rightarrow \Upsilon \rightarrow \mu\mu} = \sigma_i^{\mu\mu} - C\sigma_i^{BG}. \quad (5.10)$$

<sup>3</sup>The interference effects from the other 5 points have been corrected for. They influence the resulting  $C$  by less than 0.001.

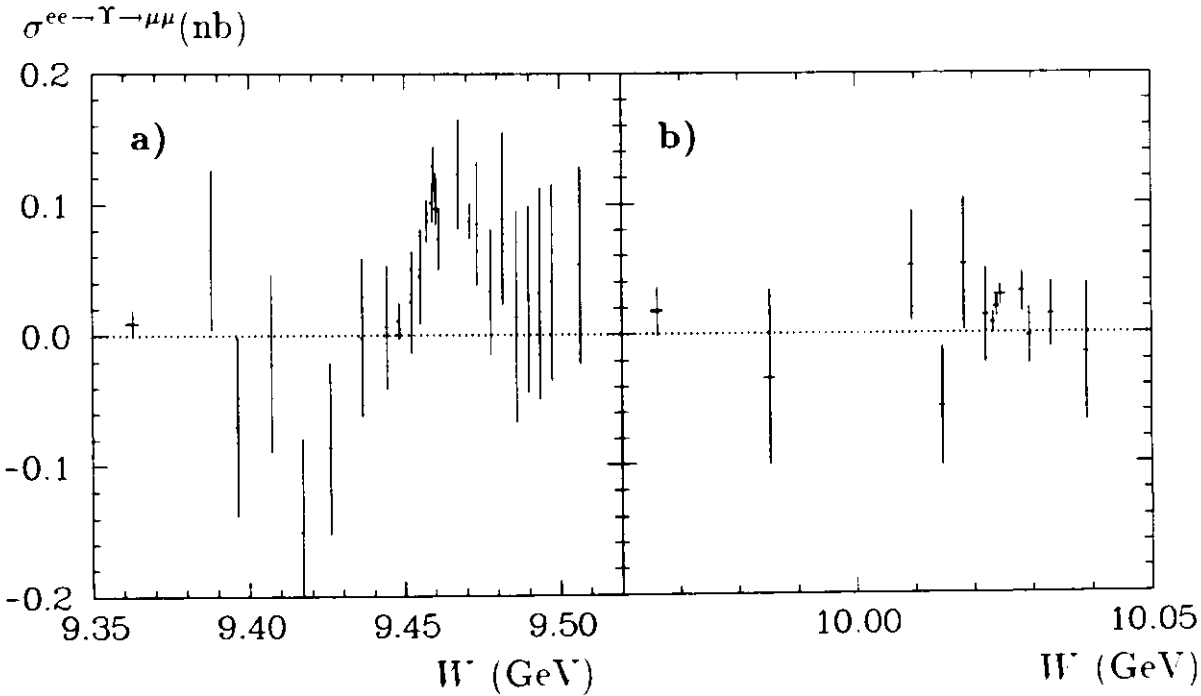


Figure 5.5: The “raw” observed cross-section spectrum for  $e^+e^- \rightarrow \Upsilon \rightarrow \mu^+\mu^-$  in the energy regions of the  $\Upsilon(1S)$  (a) and of the  $\Upsilon(2S)$  (b). It has been obtained by subtracting the background prediction of Fig. 5.3(b), scaled with  $C = 0.999$ , from the observed  $\mu$ -pair cross-section of Fig. 5.3(a). It is not yet corrected for selection efficiency.

The result is shown in Fig. 5.5. In the subtracted spectrum the point-to-point variations are largely reduced. This fact also indicates a good correlation between data and background prediction, which will be finally confirmed by our fits to this cross-section (after efficiency correction), which have confidence levels of 99% and 65%, respectively (see Section 6.3.1 and Figs. 6.2 and 6.3). Quantitative estimates for the point-to-point errors on  $\mathcal{L}_i/\mathcal{L}_{off}$  and  $\sigma_i^{BG}/\sigma_{off}^{BG}$  can not be deduced from any of these arguments, however. They will be determined in the following from detailed studies of possible error sources.

### 5.3.2 The Systematic Error on the Luminosity Ratio

The luminosity ratio  $\mathcal{L}_i/\mathcal{L}_{off}$  is affected by the variation of the  $\cos\theta$  acceptance for Bhabha events due to the variation of the vertex spread  $l$  with time, by the non-leading energy dependence of the Bhabha cross-section, by the amount of  $\Upsilon \rightarrow e^+e^-$  decays contributing to the number of observed electron pairs on resonance, by a period of non-linear performance of the electronic crystal readout in the  $\Upsilon(1S)$  data, and by the statistics of luminosity events. The contributions of these error sources to the error on the luminosity ratio are collected in Table 5.4.

They sum to errors of  $\Delta(\mathcal{L}_{\Upsilon(1S)}/\mathcal{L}_{off})=0.24\%$  and  $\Delta(\mathcal{L}_{\Upsilon(2S)}/\mathcal{L}_{off})=0.18\%$ , which propagate into errors of

$$\lambda(1S)\Delta(\mathcal{L}_{\Upsilon(1S)}/\mathcal{L}_{off}) = 1.2\%$$

and

$$\lambda(2S)\Delta(\mathcal{L}_{\Upsilon(2S)}/\mathcal{L}_{off}) = 4.1\%$$

on the amount of observed  $\Upsilon \rightarrow \mu^+\mu^-$ -decays. The smallness of  $\Delta(\mathcal{L}_i/\mathcal{L}_{off})$  reflects the fact that we have explicitly corrected our luminosity measurement (see Section 4.4) for effects

Table 5.4: Contributions to the error on luminosity ratios.

Source	$\Upsilon(1S)$	$\Upsilon(2S)$
$l_i - l_{off}$	0.10 %	
$\sigma^{ee \rightarrow ee} \propto 1/s$	0.05 %	
$\Upsilon \rightarrow e^+e^-$	0.15%	0.10%
Bad Readout	0.12%	—
Statistics	0.10 %	
$\Delta(\mathcal{L}_i/\mathcal{L}_{off})$	0.24%	0.18%
$\cong \Delta N^{\Upsilon \rightarrow \mu\mu}$	1.2%	4.1%

from a variation of the vertex spread  $l$ , for the  $\Upsilon \rightarrow e^+e^-$  contribution, and for the bad crystal readout. We briefly discuss each error source of Table 5.4 below.

$l_i - l_{off}$ : The residual error from the vertex spread  $l$  along the beam axis bases on the assumption that we model  $l$  and its time dependence with an accuracy of  $\Delta l = 0.15$  mm (cf. Fig. 3.7). This leads to  $\Delta(l_i - l_{off}) = 0.21$  mm which in turn results in the listed error on  $\mathcal{L}_i/\mathcal{L}_{off}$  by inserting this number into Eq. (4.7). We checked that the variation of the mean vertex position ( $\langle x \rangle, \langle y \rangle, \langle z \rangle$ ) influence the selection efficiency of Bhabha events by less than 0.1%.

$\sigma^{ee \rightarrow ee} \propto 1/s$ : The deviation of the Bhabha cross-section from a  $1/s$  dependence is much smaller than that of  $e^-e^- \rightarrow \mu^+\mu^-$  for two reasons. First, the  $s$ -channel annihilation diagram, which is influenced by vacuum polarization and interference with the  $\Upsilon$  resonances, contributes only 5% to the cross-section. Second, the  $t$ -channel scattering diagram is dominated by very small momentum transfers  $q^2$ , where deviations from  $1/s$  are negligible. Our estimate of an 0.05% deviation from  $\sigma^{ee \rightarrow ee} \propto 1/s$  is an educated guess based on the corresponding deviation of 0.5% in  $\sigma^{ee \rightarrow \mu\mu}$  if we change  $\sqrt{s}$  from 9.46 GeV to 10.58 GeV (see Section 2.3.1).

$\Upsilon \rightarrow e^+e^-$ : The error from the subtraction of  $\Upsilon \rightarrow e^+e^-$  has already been discussed in Section 4.4.

**Bad Readout:** The effect of the nonlinear crystal readout on the efficiency for the luminosity event selection was obtained from simulating the nonlinearity for each single crystal by MC methods [101] on the one hand, and from investigating inclusive features of the selected events [83] on the other hand. For those 40% of our  $\Upsilon(1S)$  data, which are affected by this nonlinearity, we find from these two independent methods a reduction of the Bhabha efficiency by 2.4% and 2.7%, respectively. The difference between these estimates, multiplied with the fraction of data affected, is taken as systematic error.

**Statistics:** We regard the (statistical) error on the ratio of Bhabha events on- and off-resonance as systematic error and combine it with the other errors<sup>4</sup>.

<sup>4</sup>As statistical errors for our analysis we only regard the errors on the number of muons and multi-hadrons, which enter directly in Eq. (4.1). Other statistical errors from luminosity events and Monte Carlo events are more conveniently included in our systematic error.

**Calorimeter Calibration:** The only cut in the selection of luminosity events, which is sensitive to the calorimeter calibration is  $E_{dep} > 0.7E_{beam}$  for both electromagnetic showers (cf. Section 4.4). Since the energy resolution for 5 GeV showers is only 1.5%, this cut is about 20 standard deviations away from the peak. Changes in the *resolution* can thus not affect the selection efficiency for luminosity events.

The shower energy distribution, however, exhibits a tail towards lower energies due to initial (and final) state photon radiation. Changes in the *peak position*  $E_{peak}$ , i.e. variations of  $E_{peak}/E_{beam}$ , may therefore influence the fraction of the tail which is above  $0.7E_{beam}$ . We have estimated that this effect is less than 0.1%. We thus neglect this error.

### 5.3.3 The Systematic Error on the Background Ratio

“ ‘What are You currently working on?’, Mr. K. was asked.  
‘Oh, I’m very busy. I’m preparing my next error.’ ”

B. Brecht

The contributions to the systematic error on the ratio  $\sigma_i^{BG}/\sigma_{off}^{BG}$  can be grouped into uncertainties of the cross-section dependence on  $s$ , into inaccuracies in reproducing variations of the detector acceptance, and in the error from MC statistics. The amount of errors from these sources, which will be derived in detail below, are listed in Table 5.5.

Table 5.5: Contributions to the error on background ratios.

Source	$\Upsilon(1S)$	$\Upsilon(2S)$
Cross-Section( $s_i$ )	0.19%	0.16%
Detector Acceptance ( $W_i$ )	0.44%	0.45%
MC Statistics	0.41%	0.41%
$\Delta(\sigma_i^{BG}/\sigma_{off}^{BG})$	0.63%	0.63%
$\cong \Delta N^{\Upsilon-\mu\mu}$	3.0%	14.5%

They sum to an error of  $\Delta(\sigma_i^{BG}/\sigma_{off}^{BG})=0.63\%$  for both, the  $\Upsilon(1S)$  and the  $\Upsilon(2S)$  data. This errors, together with the errors on  $\mathcal{L}_i/\mathcal{L}_{off}$  in Table 5.4, mean that we are able to reproduce the observed point-to-point variations of  $\sigma^{\mu\mu}(W_i)$  in Fig. 5.3(a) with a precision of better than 0.7%. Given point-to-point variations of  $\mathcal{O}(10\%)$  this is a remarkably high precision, which is mainly owing to our rundependent MC simulation (see Section 3.5) of beam-related background, of length and position of the  $e^+e^-$  intersection region, and of the chamber performance.

Just like the errors  $\Delta(\mathcal{L}_i/\mathcal{L}_{off})$  the errors  $\Delta(\sigma_i^{BG}/\sigma_{off}^{BG})$  have to be multiplied with  $\lambda(1S)=4.8$  and  $\lambda(2S)=23$  in order to derive their influence on the observed number of resonance decays to muons. This results in errors of

$$\lambda(1S)\Delta(\sigma_{\Upsilon(1S)}^{BG}/\sigma_{off}^{BG}) = 3.0\%$$

and

$$\lambda(2S)\Delta(\sigma_{\Upsilon(2S)}^{BG}/\sigma_{off}^{BG}) = 14.5\%,$$

which are the dominant systematic errors in our analysis. Therefore they deserve an (even more) detailed description which is given below.

### The $s$ -Dependence of the Background Cross-Section

This item encloses the precision in modeling all genuine variations of the background cross-sections with  $W_i$ , i.e. those variations which are not due to detector acceptance effects.

**$\Upsilon(4S)$  Interference:** The genuine cross-section uncertainty for  $e^+e^- \rightarrow \mu^+\mu^-$  is dominated by the interference effect of the (rare) decay  $\Upsilon(4S) \rightarrow \mu^+\mu^-$  with the continuum. It has a maximum of  $\pm 0.30\% \times \sigma_{\text{Born}}^{e^+e^- \mu^+\mu^-} \approx \pm 0.24\% \times \sigma^{BG}$  at  $W = m_{\Upsilon(4S)} \pm 20$  MeV (see dotted line<sup>5</sup> in Fig. 2.11). Given an error of  $\Delta W = 15$  MeV for data taken on the  $\Upsilon(4S)$ , which represent about 70% of our continuum sample, the interference correction may change  $\sigma_{\text{off}}^{BG}$  by 0.13%.

We note, that all 1-loop corrections to  $e^+e^- \rightarrow \mu^+\mu^-$ , even those with initial state photons, are modeled by our modified DYMU2 generator. They influence the  $s$ -dependence of the continuum background from  $e^+e^- \rightarrow \mu^+\mu^-$  by about 0.5% (cf. Fig. 2.12). Higher order corrections are suppressed by  $\alpha$  and should thus be negligible.

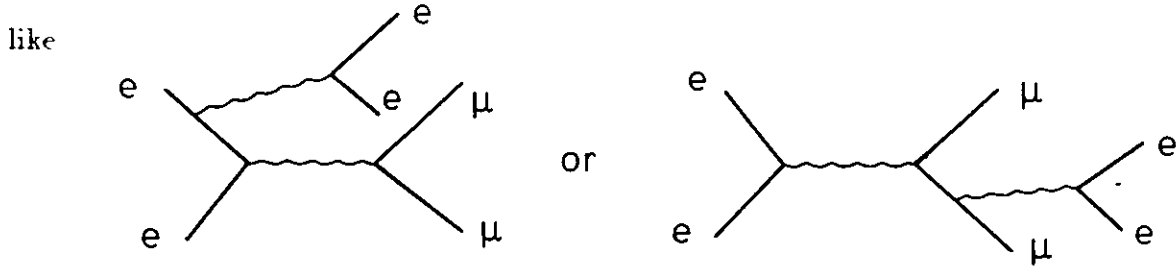
**$C_1 \neq C_2$ :** As we saw from Eq. (5.8) the scaling factor  $C$  eliminates the error on the *mean amplitude* of the background prediction  $\sigma^{BG}$ . However, the systematic MC error on the two-photon background may (due to generator, energy loss, lateral pattern) be slightly different from that of one-photon annihilation. To eliminate the MC error we would in fact need two scaling factors,  $C_1$  for one-photon annihilation and  $C_2$  for two-photon processes. Here it is important, that we model both the detector signatures for low-energy and high-energy muons with comparably good precision. A precision of about 2% for our set of cuts (cf. Section 6.1.2) has been obtained through our upgrade of the GHEISHA simulation of particle interactions (see Appendix A).

Since the fractional abundances  $f_1$  and  $f_2$  of one- and two-photon processes are different at different c.m. energies, the scaling factor  $C = f_1 C_1 + f_2 C_2$  acquires a  $W$ -dependence if  $C_1 \neq C_2$ . From Section 6.1.2 we conclude that  $C_1$  and  $C_2$  may differ by about 2.5% from each other. Our determination of  $C$  in Fig. 5.4 mainly relies on  $\Upsilon(4S)$  data. A short calculation shows that we have to estimate the error of using this  $C$  for all data by the expression  $|f_1(4S) - f_1(nS)| |C_1 - C_2|$ . It yields 0.10% for the  $\Upsilon(1S)$  and 0.05% for the  $\Upsilon(2S)$  data.

**eN Variations:** As determined in Section 5.1.2, also the “cross-section” for eN events varies with  $W$ . These variations are due to different beam conditions at different c.m. energies  $W_i$ . From the systematic errors of the eN background listed in Table 5.2, we find a contribution to  $\Delta(\sigma_i^{BG}/\sigma_{\text{off}}^{BG})$  of 0.08% and 0.04% for the  $\Upsilon(1S)$  and the  $\Upsilon(2S)$ , respectively.

**$\sigma^{e^+e^- \rightarrow e^+e^-\mu^+\mu^-}(s)$ :** A further error source is the amount of increase of  $\sigma^{e^+e^- \rightarrow e^+e^-\mu^+\mu^-}(s)$  from  $\sqrt{s} = m_{\Upsilon(1S)}$  and  $\sqrt{s} = m_{\Upsilon(2S)}$  to  $\sqrt{s} = m_{\Upsilon(4S)}$ . It is predicted for our cuts on generator level to be  $5.0 \pm 0.3\%$  and  $2.3 \pm 0.4\%$ , respectively, by our two-photon generator in Section 5.2. We use the (statistical) errors of this increase to estimate its accuracy. (With a more detailed generator [102] we have checked that systematic errors like omission of diagrams

<sup>5</sup>The amplitude of 0.35% of this curve is reduced by radiative corrections to the 0.30% cited here.



are of negligible influence.) Given the amount of about 16% two-photon muons in  $\sigma^{BG}$  we find contributions to  $\Delta(\sigma_i^{BG}/\sigma_{off}^{BG})$  of  $0.16 \times 0.3\% = 0.05\%$  and of  $0.16 \times 0.4\% = 0.06\%$  for the  $\Upsilon(1S)$  and the  $\Upsilon(2S)$ , respectively. Since the contributions of other processes ( $e^+e^- \rightarrow e^+e^-\pi^+\pi^-$ , ...) to  $\sigma^{BG}$  are much smaller than 16%, their corresponding errors are negligible.

Summarizing the above errors in Table 5.6, we find a combined error of 0.19% for the  $\Upsilon(1S)$  and 0.16% for the  $\Upsilon(2S)$ .

Table 5.6: (Sub-)Contributions to the error on the  $s$ -dependence of the background cross-section.

Source	$\Upsilon(1S)$	$\Upsilon(2S)$
$\Upsilon(4S)$ Interference	0.13%	0.13%
$C_1 \neq C_2$	0.10%	0.05%
eN Variations	0.08%	0.04%
$\sigma^{ee \rightarrow ee\mu\mu}(s)$	0.05%	0.06%
Cross-Section( $s_i$ )	0.19%	0.16%

### The Variation of the Detector Acceptance

The sources of acceptance variations for the background are the relative positions of the detector and the event vertices, the calorimeter calibration, the beam-related background in each event, the detector resolution and the triggers. In the following we discuss, why these sources can lead to changes in the detector acceptance and estimate their influence on  $\Delta(\sigma_i^{BG}/\sigma_{off}^{BG})$ .

**The Relative Position of Detector and Event Vertex** The probability that a  $\mu$ -pair event passes our data selection depends on the relative position of its event vertex with respect to the calorimeter. The farther the event vertex is away from the ball center at  $(x,y,z)=(0,0,0)$ , the more events are missed by the Triangle Triggers. The reason for this is that the ball coordinates of the energy depositions are not identical to the particle directions for  $(x,y,z) \neq (0,0,0)$ . First, back-to-back muons may thus appear in calorimeter triangles which are not back-to-back. Second, one of the muons may not end up in the Main Ball, even if both momentum directions are within  $|\cos\theta| < 0.84$ . A small additional effect on our selection efficiency is introduced by the fact that muons from  $(x,y,z) \neq (0,0,0)$  do not traverse a crystal along its axis. Thus, the probability of crossing crystal boundaries and widening the lateral energy pattern increases. However, by cutting in the  $F_2$  pattern fraction rather than in  $F_1$  we considerably lower our sensitivity to this effect [85].

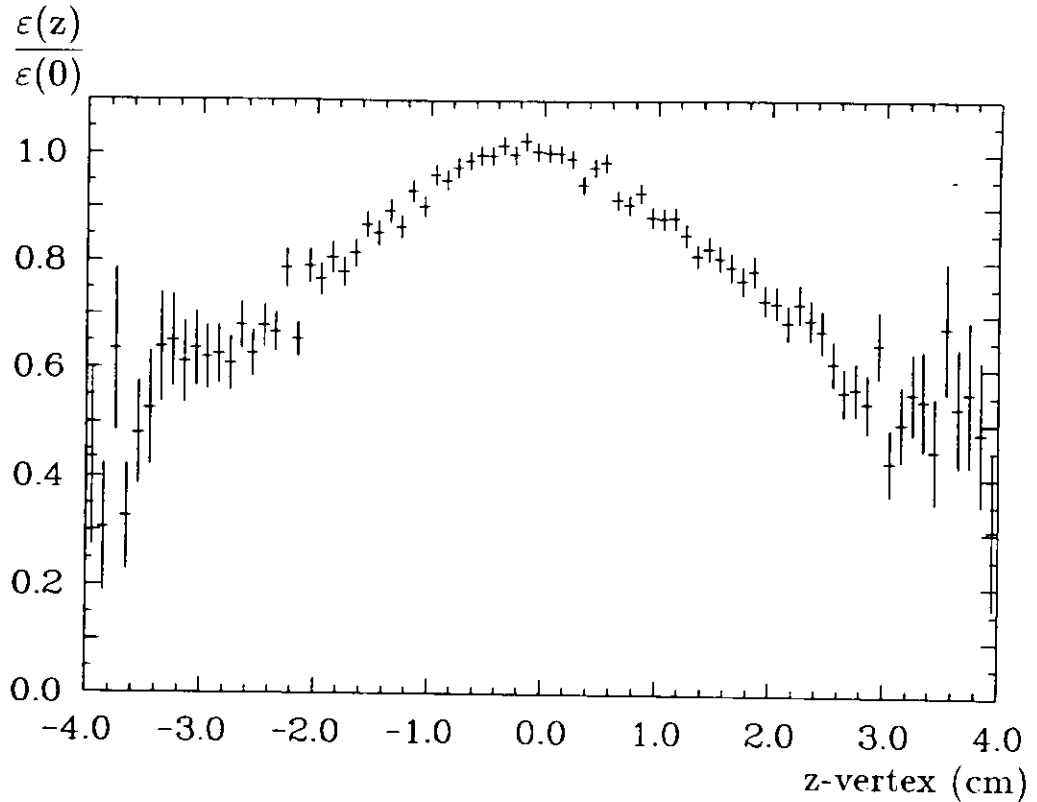


Figure 5.6: *Dependence of the selection efficiency on the z-vertex, where a given  $\mu$ -pair was created.*

Variations in the distribution of the relative positions of event vertex and calorimeter between different times of data taking can change the selection acceptance for the above reasons. These variations may be due to shifts of either vertex or detector. In our MC simulation we have modeled the variation of the mean relative coordinates ( $\langle x \rangle, \langle y \rangle, \langle z \rangle$ ) of the event vertices with respect to the ball center and the variation of the vertex spread  $l$  along the beam. From Fig. 3.7 we estimate residual uncertainties of  $\Delta\langle x \rangle = 1.0$  mm,  $\Delta\langle y \rangle = 0.2$  mm,  $\Delta\langle z \rangle = 0.4$  mm, and  $\Delta l = 0.15$  mm.

The variation of the air gap  $g$  between the upper and the lower ball hemisphere<sup>6</sup> is another error source. It was not larger than  $\Delta g = 1$  mm around its mean value of  $\langle g \rangle = 6$  mm [103].

For our error  $\Delta(\sigma_i^{BG}/\sigma_{off}^{BG})$  we used the uncertainties of the *differences* between on- and off-resonance data, which are then  $\Delta\langle x \rangle = 1.4$  mm,  $\Delta\langle y \rangle = 0.3$  mm,  $\Delta\langle z \rangle = 0.6$  mm,  $\Delta l = 0.21$  mm, and  $\Delta\langle g \rangle = 1.4$  mm. Note that systematic errors common for on- and off-resonance data drop out by forming differences.

Fig. 5.6 demonstrates the strong dependence of the selection efficiency  $\varepsilon$  for each single event as a function of its z-vertex. The efficiency has been normalized to that at  $z=0$ . The overall selection efficiency depends on the distribution of z-vertices  $p(z) \propto \exp[-(z - \langle z \rangle)^2/2l^2]$ , i.e. on  $\int p(z)\varepsilon(z)dz$ . From Figs. 5.6 and 3.7(d) we find an impact of  $\Delta l$  on  $\Delta(\sigma_i^{BG}/\sigma_{off}^{BG})$  of

$$\Delta \left( \frac{\sigma_i^{BG}}{\sigma_{off}^{BG}} \right)_l = 1.3\% \times \frac{\Delta l}{\text{mm}} = 0.27\%,$$

where we have inserted  $\Delta l = 0.21$  mm.

<sup>6</sup>The two calorimeter hemispheres were frequently moved apart in order to shield them with lead during beam injection or high-intensity DORIS running for the HAMBURG SYNCHROTRON LABORATORY. The abrasion of the mechanical opening mechanism may result in a variation of the gap between the hemispheres.

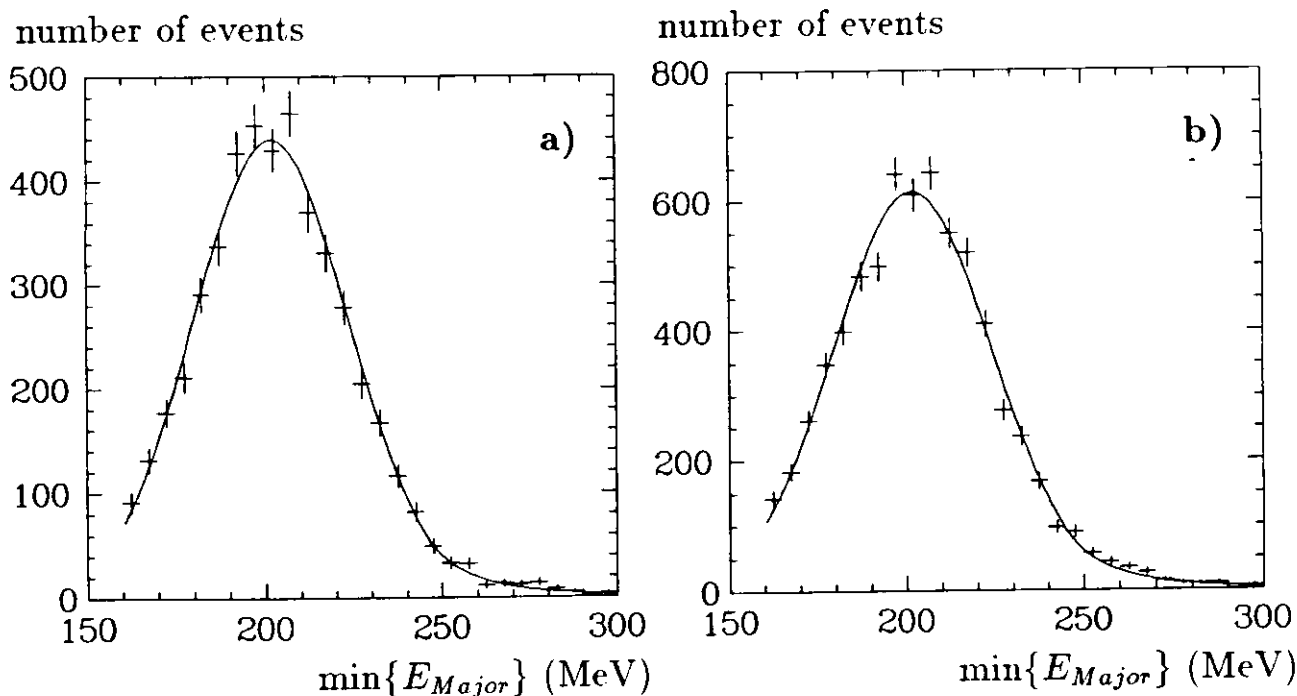


Figure 5.7: Two of the fits to Major Triangle energies to determine the variation in the calorimeter calibration.

Analogously we obtain with  $(\Delta\langle\rho\rangle)^2 \equiv (\Delta\langle x\rangle)^2 + (\Delta\langle y\rangle)^2 + (\Delta\langle z\rangle)^2 = 2.4 \text{ mm}^2$

$$\Delta\left(\frac{\sigma_i^{BG}}{\sigma_{off}^{BG}}\right)_\rho = 0.055\% \times \frac{(\Delta\langle\rho\rangle)^2}{\text{mm}^2} = 0.13\%.$$

(In contrast to the vertex spread  $l$ , the vertex position enters quadratically in this error, since the efficiency  $\epsilon(\rho) \sim \epsilon(z)$  can be approximated by a parabolic curve around  $z = 0$ .)

The influence of the gap variation is more involved. We re-simulated our complete MC datasets for the  $\Upsilon(1S)$  and the  $\Upsilon(2S)$  of about  $0.5 \times 10^6$  events with a different detector geometry, where we have enlarged the gap by 3 mm. The results of the tube chamber simulation of the original events were left completely unchanged. The (marginally significant) changes in efficiency were scaled to  $\Delta\langle g\rangle = 1.4 \text{ mm}$  resulting in

$$\Delta\left(\frac{\sigma_i^{BG}}{\sigma_{off}^{BG}}\right)_g = \begin{cases} 0.12\% & \text{for the } \Upsilon(1S) \text{ data} \\ 0.16\% & \text{for the } \Upsilon(2S) \text{ data.} \end{cases}$$

(For the  $\Upsilon(2S)$  we expect a larger effect due to the 75% beam polarization creating more  $\mu$ -pairs near the plane of the equator, where the efficiency is more sensitive to the gap size  $g$ .)

**Calorimeter Calibration** Time variations in the calorimeter calibration may slightly change the position and width of the measured energy loss distribution. The cut, which is most sensitive to such changes is the requirement of more than 160 MeV deposited in both Major Triangles hit by the muons. We selected the smaller one of both Major Triangle energies from each event and fitted their distribution for several subperiods of data, as shown for two examples in Fig. 5.7.

The mean peak position of  $E_{\text{peak}} = 202.0 \text{ MeV}$  (for  $\Upsilon(4S)$  data) was found to vary by only 0.2 MeV ( $\cong 0.1\%$ ) from period to period and the mean Gaussian width  $\sigma_E = 22.2 \text{ MeV}$  varied



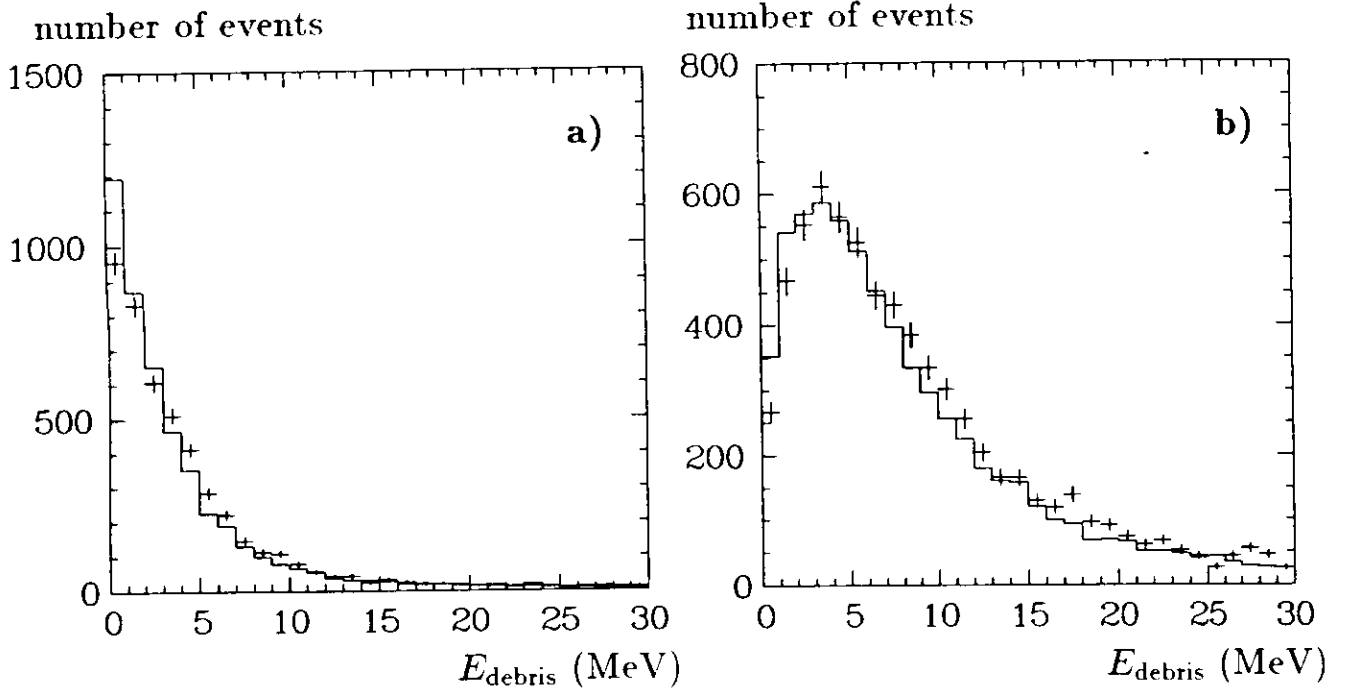


Figure 5.8: Distribution of debris energy in subsamples of  $\Upsilon(4S)$  data (a) and  $\Upsilon(2S)$  data (b). The crosses are data, and the histogram shows the corresponding MC prediction.

by typically 0.5 MeV ( $\cong 2\%$ ). Our cut at 160 MeV is about  $1.9\sigma_E$  below  $E_{\text{peak}}$ . From the variations of width and peak position we deduce for such a cut

$$\Delta \left( \frac{\sigma_i^{BG}}{\sigma_{off}^{BG}} \right)_{\sigma_E} = 0.27\%$$

and

$$\Delta \left( \frac{\sigma_i^{BG}}{\sigma_{off}^{BG}} \right)_{E_{\text{peak}}} = 0.05\%.$$

These errors are conservative estimates, since the variations of  $E_{\text{peak}}$  and  $\sigma_E$  are partially of statistical origin.

**Background Energy** As can be seen from Fig. 5.8, which shows the distribution of the debris energy in a subperiod of the  $\Upsilon(4S)$  data (a), and a subperiod of the  $\Upsilon(2S)$  data (b), the variation in the amount of this energy is well reproduced by the MC simulation. Most of this debris energy is coming from the beam-related background, which is included in the MC simulation by merging background events obtained with the DBM trigger (cf. Section 3.5). We estimate the systematic error on this simulation by repeating the merging process with independent samples of DBM background events, still taken from the same runperiod. We obtain variations of

$$\Delta \left( \frac{\sigma_i^{BG}}{\sigma_{off}^{BG}} \right)_{E_{\text{debris}}} = 0.10\%.$$

**Chamber resolution** Our selection cut on the measured acollinearity  $\zeta > 180^\circ - 12^\circ$  corresponds to 3.6 times the resolution  $\sigma_\zeta \equiv \sqrt{\sigma_{\Delta\theta}^2 + \sigma_{\Delta\varphi}^2}$ , where  $\sigma_{\Delta\theta}$  and  $\sigma_{\Delta\varphi}$  are the resolutions for the projected opening angles  $\Delta\theta$  and  $\Delta\varphi$  (see Fig. B.21(a) and (b)). Due to our loose

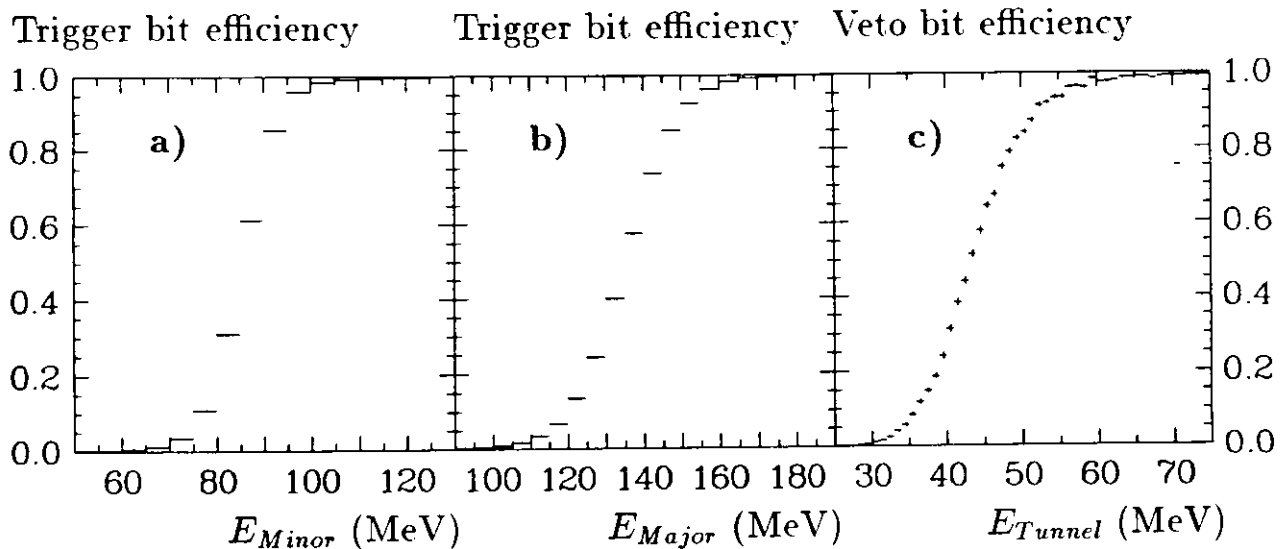


Figure 5.9: Threshold curves for the Minor Triangle Bit (a), the Major Triangle Bit (b), and the Tunnel Veto Bit (c).

cut we are fairly insensitive to small inaccuracies in modeling the time dependence of  $\sigma_{\Delta\theta}$  and  $\sigma_{\Delta\varphi}$ . Varying these resolutions by the expected E.T.MC accuracy of 4% (Eq. (B.41)) and 7.5% (Eq. (B.42)), we find from Fig. B.21(c) an influence on our ratio of background cross-sections of

$$\Delta \left( \frac{\sigma_i^{BG}}{\sigma_{off}^{BG}} \right)_{\theta, \varphi} = 0.04\%.$$

Both the  $\theta$  and  $\varphi$  errors contribute about equally. The time dependent tube chamber simulation considerably helped to achieve such a small error.

**Trigger Efficiencies** The threshold curves for the Crystal Ball trigger bits are rather steep and approach an efficiency of 100% very soon above the nominal threshold. In Fig. 5.9 we have plotted typical threshold curves for the Minor Triangle and the Major Triangle bit and for the Tunnel veto bit (cf. Section 3.2). Our software thresholds of more than 120 MeV and 160 MeV in both Minor and Major Triangles, hit by the muons (see Section 4.5.2), respectively, and less than 30 MeV in each of both Tunnel Regions, are already well above (below) the nominal trigger thresholds. We obtain trigger efficiencies of above 99.95% for the Minor Triangle Trigger and efficiencies ranging from 99.0% to 100.0% for the Major Triangle Trigger depending on the data sample. They have been obtained by weighting for each data sample the corresponding threshold curves with the energy distributions of the  $\mu$ -pair events. The ‘OR’ of both triggers thus misses less than each  $10^{-5}$ th event which would pass our selection cuts. Changes in the trigger efficiency from period to period are therefore negligible. Exceptions are 13  $\text{pb}^{-1}$  of  $\Upsilon(1S)$  data where only the Major Triangle Trigger was enabled with an efficiency of  $(99.7 \pm 0.1)\%$ , and 8  $\text{pb}^{-1}$  of  $\Upsilon(2S)$  data, where two Minor Triangles were not properly included in both triggers, resulting in an ‘OR’ efficiency of  $(97.2 \pm 0.2)\%$ . The systematic errors for these periods contribute

$$\Delta \left( \frac{\sigma_i^{BG}}{\sigma_{off}^{BG}} \right)_{\text{trigger}} = 0.05\%$$

to the error of our detector acceptance ratio.

**Other Sources** We have checked, that the systematic error on detector acceptance ratios induced from all other cuts are negligible even on the 0.1% level. Our cut in the  $(c/v)_{\text{Ball}}$  vs.  $\langle dE/dx \rangle$  plane rejects only about 0.1% of events from  $e^+e^-$  interactions. Since the variations of  $\langle dE/dx \rangle$  with time of data taking are properly included in the E.T.MC, the residual error is well below 0.1%.

Below 0.1%, likewise, is the probability that for an event from  $e^+e^-$  interactions a Roof-Timing of  $(\frac{c}{v})_{\text{Roof}} \approx -1$  consistent with a cosmic ray event is found, e.g. due to a malfunction of a Roof-ToF counter. This has been achieved by surveying each of the 94 Roof-ToF counters for all our data and excluding the timing information of those counters, which are found to be unreliable<sup>7</sup>. The cosmic rays passing through bad counters are properly subtracted via the  $(c/v)_{\text{Ball}}$  sidebands. A similar survey was performed for the Ball-Timing.

Finally, the faking of off-axis vertices by the TAGTRK program was also found to be less than 0.1% for our cut in the “on-axis significance”.

All errors from detector acceptance variations contributing to  $\Delta(\sigma_i^{BG}/\sigma_{off}^{BG})$  are collected in Table 5.7. Their quadratic sum amounts to 0.44% for the  $\Upsilon(1S)$  data and to 0.45% for the  $\Upsilon(2S)$  data.

Table 5.7: (Sub-)Contributions to the error on the reproduction of variations of the detector acceptance.

Source	$\Upsilon(1S)$	$\Upsilon(2S)$
$l$ -Vertex	0.27 %	
$(x,y,z)$ -Vertex	0.13 %	
Hemisphere Gap	0.12%	0.16%
$\sigma_E$ -Calibration	0.27 %	
$E_{\text{peak}}$ -Calibration	0.05 %	
$E_{\text{debris}}$	0.10 %	
$\theta, \varphi$ -Resolution	0.04 %	
Triggers	0.05 %	
Detector Acceptance ( $W_i$ )	0.44%	0.45%

### Monte Carlo Statistics

The last contribution to the error on  $\sigma_i^{BG}/\sigma_{off}^{BG}$  is the statistic of MC events. With the large amount of  $\sim 2 \times 10^6$  MC events we end up with statistical errors of 0.34% for the on-resonance MC data and 0.23% for the off-resonance MC data. They combine to an error of 0.41%, which is a factor of 2.5 less than the corresponding statistical error from the real data.

## 5.4 Resonant Background from $\Upsilon \rightarrow \mu^+ \mu^- X$

Before Fig. 5.5, where the continuum background has been subtracted, can be corrected for the selection efficiency for  $\Upsilon \rightarrow \mu^+ \mu^-$ , we have to account for possible resonant background. There are two sources for such a background, the decay  $\Upsilon(2S) \rightarrow X \Upsilon(1S) \rightarrow X \mu^+ \mu^-$ , where  $X = (\gamma\gamma, \pi\pi, \dots)$ , and the decay  $\Upsilon(1S, 2S) \rightarrow \tau^+ \tau^-$ . We will see that both resonant background

<sup>7</sup>Depending on the data sample we found 0-4 of such bad counters.

sources are small and lead to corrections for  $N^{\Upsilon \rightarrow \mu\mu}$  of only 0.45% on the  $\Upsilon(1S)$  and 2.3% on the  $\Upsilon(2S)$ . (Such a correction on the continuum subtracted spectrum changes  $N^{\Upsilon \rightarrow \mu\mu}$  by about the same amount as an 0.1% increase in the subtracted continuum would do.)

#### 5.4.1 The Process $\Upsilon \rightarrow \tau^+ \tau^-$

In Section 5.2 we have found that the continuum background from  $e^+e^- \rightarrow \tau^+ \tau^-$  is 0.45% of our observed continuum cross-section for  $e^+e^- \rightarrow \mu^+ \mu^-$ . Due to the large tau mass there are differences between  $\mu$ -pairs and  $\tau$ -pairs when we scale the continuum process, which includes initial state radiation, to the resonant process, which is lacking all high-energy initial state radiation. However, this differences occur for initial state photon energies of  $E_\gamma \approx [1 - (2m_\tau/m_\Upsilon)^2]E_{\text{beam}} = 0.86E_{\text{beam}}$ , where our acceptance for  $e^+e^- \rightarrow (\gamma)\mu^+ \mu^-$  is zero. Thus we conclude that the process  $\Upsilon \rightarrow \tau^+ \tau^-$  also contributes 0.45% to our observed resonance peaks.

#### 5.4.2 The Process $\Upsilon(2S) \rightarrow \Upsilon(1S)X$

The process  $\Upsilon(2S) \rightarrow X\Upsilon(1S) \rightarrow X\mu^+ \mu^-$  can “feed down” into our  $\mu$ -pair sample if the particles  $X=(\gamma\gamma, \text{ or } \pi^+\pi^-, \text{ or } \pi^0\pi^0 \rightarrow 4\gamma)$  are all not observed in the calorimeter but escape under angles  $|\cos\theta| > 0.93$ . From 160 events of this process (contained in a MC sample of about 20,000  $\Upsilon(2S)$  decays) only 2 events pass our selection cuts. With the measured branching ratios of the  $\Upsilon(2S)$  from Ref. [22] and our  $\Upsilon \rightarrow \mu^+ \mu^-$  selection efficiency from Section 6.1 below we convert this number to a resonant background of  $(1.8 \pm 1.3)\%$  in the continuum subtracted  $\Upsilon(2S)$  sample.

## Chapter 6

### Results for the Decay $\Upsilon \rightarrow \mu^+ \mu^-$

After correcting for the selection efficiency for  $\Upsilon \rightarrow \mu^+ \mu^-$  (Section 6.1) we determine two quantities from the observed cross-section  $\sigma^{e\bar{e} \rightarrow \Upsilon \rightarrow \mu\mu}(W)$  in Fig. 5.5. First, the area  $A$  under the excitation curves of the  $\Upsilon$  resonances is connected via Eq. (2.126) with the quantity

$$\frac{\Gamma_{\mu\mu}\Gamma_{ee}}{\Gamma} = \frac{1}{6\pi^2} m_\Upsilon^2 A. \quad (6.1)$$

The product  $\Gamma_{\mu\mu}B_{ee} = \Gamma_{\mu\mu}\Gamma_{ee}/\Gamma$  is thus determined from a fit to the cross-section as a function of  $W$  in Section 6.3.

Second, the  $\mu$ -pair branching ratios  $B_{\mu\mu}(1S)$  and  $B_{\mu\mu}(2S)$  are obtained by dividing the number of resonant  $\mu$ -pairs by the total number of produced  $\Upsilon$  resonances (Section 6.2). As has been already discussed in Section 4.2, we have to account for the fact that the cross-section for resonance decays to muons and the total number of produced  $\Upsilon$  decays are differently affected by the interference of resonance and continuum. For each c.m. energy  $W_i$  we correct the cross-section of resonance decays to  $\mu$ -pairs by the interference term  $\sigma_i^{\tilde{I}}$  and the  $\Upsilon$  production cross-section by  $(3 + R)\sigma_i^{\tilde{I}}$ . The factor 3 accounts for the three leptonic decay modes and  $R$ , the ratio of the hadronic continuum cross-section over the Born cross-section of  $\mu$ -pair production, relates the  $q\bar{q}$  decay of the  $\Upsilon$  to its leptonic decays. The value of  $\sigma_i^{\tilde{I}}$  mainly depends on  $\sqrt{\Gamma_{\mu\mu}\Gamma_{ee}}$  and the c.m. energy spread  $w$ . It was calculated from the modified DYMU2 generator as the difference between the cross-sections generated with and without interference, as explained in Section 2.3.4. We then obtain  $B_{\mu\mu}$  from

$$B_{\mu\mu} = \frac{\sum_i \left( \frac{N_i^{\Upsilon \rightarrow \mu\mu}}{\varepsilon_i^{\Upsilon \rightarrow \mu\mu}} - \mathcal{L}_i \sigma_i^{\tilde{I}} \right)}{\sum_i \left( \frac{N_i^{\Upsilon \rightarrow \text{had}}}{\varepsilon_i^{\Upsilon \rightarrow \text{all}}} - \mathcal{L}_i (3 + R) \sigma_i^{\tilde{I}} \right)}, \quad (6.2)$$

where  $i$  runs over all c.m. energies  $W_i$  within 10 MeV of the resonance peak.  $N_i^{\Upsilon \rightarrow \mu\mu}$  is the number of observed  $\Upsilon$  decays to muons, and  $\varepsilon_i^{\Upsilon \rightarrow \mu\mu}$  is their detection efficiency. The observed number  $N_i^{\Upsilon \rightarrow \text{had}}$  of  $\Upsilon$  decays to hadrons and the fraction  $\varepsilon_i^{\Upsilon \rightarrow \text{all}}$  of *all*  $\Upsilon$  decays, which pass our multi-hadron selector, will be derived in Section 6.2.1. We first describe the determination of  $\varepsilon_i^{\Upsilon \rightarrow \mu\mu}$ , which is needed for both the  $B_{\mu\mu}$  and the  $\Gamma_{\mu\mu}B_{ee}$  measurement.

## 6.1 The Selection Efficiency for $\Upsilon \rightarrow \mu^+ \mu^-$

“Siehst Du den Mond dort stehen?  
 Er ist nur halb zu sehen,  
 Und ist doch rund und schön:  
 So ist's mit manchen Sachen,  
 Die wir getrost belachen,  
 Weil uns're Augen sie nicht seh'n.”

‘Efficiencies’ à la M. Claudius

### 6.1.1 The Efficiency Dependence on the C.M. Energy

The selection efficiency for  $\mu$ -pairs from resonance decays has been determined for each c.m. energy value  $W_i$  separately. The dependence of  $\epsilon^{\Upsilon \rightarrow \mu\mu}(W_i)$  is again twofold. First, there is the same time dependence due to detector acceptance variations, which we have already discussed in Section 5.3.3.

Second, there is a genuine dependence on  $W_i$  due to the allowed energy range of initial state photons in the process  $e^+e^- \rightarrow (\gamma\gamma\dots)\Upsilon \rightarrow (\gamma\gamma\dots)\mu^+\mu^-(\gamma\dots)$ . Since the c.m. energy spread  $w$  is much larger than the total resonance widths  $\Gamma(1S)$  and  $\Gamma(2S)$ , the distribution of c.m. energies  $W$  above  $m_\Upsilon$  determines the range of the energy sum  $\sum_{\text{initial state}} E_\gamma$  for initial state photons. Resonance production is only possible if the  $e^+e^-$  c.m. energy  $\sqrt{s_e}$  after initial state radiation is  $\sqrt{s_e} \approx m_\Upsilon \pm \Gamma$ .

For c.m. energies  $W \approx m_\Upsilon$  the range of this energy sum is thus approximately determined by  $w \sim 8$  MeV. For  $W - m_\Upsilon \gg w$ , on the other hand, initial state photon energies are distributed around a mean value of  $\sum_{\text{initial state}} E_\gamma = W - m_\Upsilon$  with a typical width  $w$ . These higher photon energies influence our selection efficiency as soon as they amount to  $\sum_{\text{initial state}} E_\gamma \gtrsim 30$  MeV, because we allow for at most 30 MeV deposited apart from the muon clusters in the calorimeter (see Section 4.5.2). The effect should be perceptible for our largest  $\Upsilon(1S)$  energies, which range up to 46.3 MeV above the  $\Upsilon(1S)$  mass. This is confirmed by studying the efficiency behaviour, if  $W$  is varied in our MC simulation (Section 2.3.4) of  $e^+e^- \rightarrow (\gamma\gamma)\Upsilon \rightarrow (\gamma\gamma)\mu^+\mu^-(\gamma)$ . All time dependent quantities (beam spot parameters, chambers, beam related background), which further influence the acceptance, are left constant in this study. The result in Fig. 6.1 shows a clear decrease of the selection efficiency  $\epsilon^{\Upsilon \rightarrow \mu\mu}$  around  $W - m_\Upsilon \approx 25$  MeV. For  $W - m_\Upsilon < 22$  MeV we observe no significant variation of  $\epsilon^{\Upsilon \rightarrow \mu\mu}(W)$ .

This helps to overcome a cumbersome technical difficulty. For the generation of  $e^+e^- \rightarrow (\gamma\gamma)\Upsilon \rightarrow (\gamma\gamma)\mu^+\mu^-(\gamma)$  in our modified DYMU2 generator we did not adjust the sampling of the initial state photon spectrum to a sharply peaking resonance behaviour. Instead, we simply drop the bulk of events, namely all those which do not lead to  $\Upsilon$  production. The CPU time consumption for generating a sufficient amount of  $e^+e^- \rightarrow (\gamma\gamma)\Upsilon \rightarrow (\gamma\gamma)\mu^+\mu^-(\gamma)$  events to calculate the selection efficiency for each of our c.m. energies  $W_i$  would thus have been very large. We instead use for the efficiency calculation at each  $W_i$  that subsample of our corresponding *continuum* MC events  $e^+e^- \rightarrow (\gamma\gamma)\mu^+\mu^-(\gamma)$ , which has an energy sum of  $\sum_{\text{initial state}} E_\gamma < 10$  MeV. We cross-checked that efficiencies obtained with this method agree with those from proper resonance generation within their statistical errors of  $\sim 1\%$ . Only for  $W - m_\Upsilon > 22$  MeV we explicitly generate events  $e^+e^- \rightarrow (\gamma\gamma)\Upsilon \rightarrow (\gamma\gamma)\mu^+\mu^-(\gamma)$ . The simulation of time dependences in the detector acceptance was included specific for each  $W_i$  as usual.

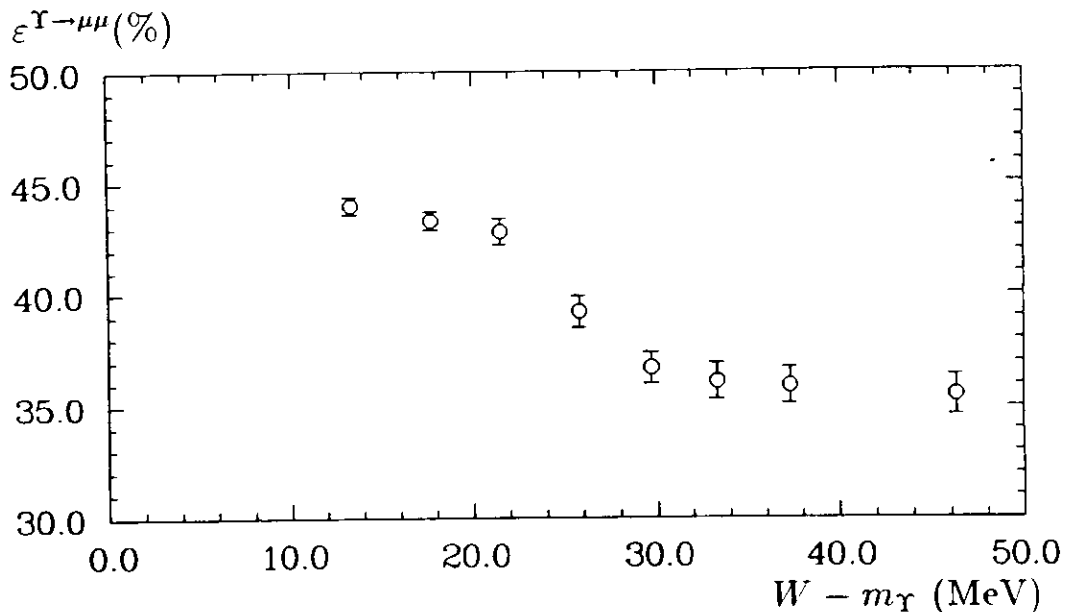


Figure 6.1: Dependence of the selection efficiency for resonant muons on the c.m. energy  $W$ , as predicted by MC for a constant set of all other beam- and detector-related parameters.

Note that the *final* state photons have to be generated over their complete energy spectrum, since  $B_{\mu\mu}$  is defined as the branching ratio to  $\mu^+ \mu^-$  plus an arbitrary number of photons with arbitrary energies. Any other definition would be of no use, since due to the Bloch-Nordsieck Theorem (Section 2.3.2) the branching ratio for  $\Upsilon \rightarrow \mu^+ \mu^- + 0\gamma$  is exactly zero. Since our  $\mu$ -pair selection is very sensitive to additional photons in the event, our selection efficiency is lowered by  $\sim 10\%$  due to final state radiation.

Averaged over either resonance region we obtain selection efficiencies of

$$\langle \epsilon^{\Upsilon(1S) \rightarrow \mu\mu} \rangle = 44.6\% \pm 1.1\%$$

and

$$\langle \epsilon^{\Upsilon(2S) \rightarrow \mu\mu} \rangle = 44.1\% \pm 1.1\%.$$

The cited systematic errors on these efficiencies are determined below.

### 6.1.2 The Systematic error on the Efficiency

The systematic error on the *mean amplitude* of our selection efficiency  $\epsilon_i^{\Upsilon \rightarrow \mu\mu}$  has three sources, namely the uncertainty in the MC generator, the simulation of the detector response, and the statistics of MC events. We discuss them in turn.

The generator uncertainty is dominated by the uncertainty in modeling the final state photon radiation. In absence of a better generator for final state radiation<sup>1</sup> we conservatively estimate the uncertainty by comparing the yield of final state photons between the first order exponentiated spectrum of DYMU2 and the non-exponentiated spectrum of the MMG1 generator [51] (see Section 2.3.3). After modeling the angular acceptance of our cuts on the generator level we observe that the MMG1 program generates about 25% more final state photons above 30 MeV than the DYMU2 generator. Since an exponentiated spectrum is clearly closer to the reality than any non-exponentiated spectrum (cf. Fig. 2.15 and the discussion in Section 2.3.2), we estimate the systematic error on the generator by half of the observed

<sup>1</sup>The KORALZ generator [65] (cf. Section 2.3.3) was not yet available at the time of our analysis.

difference. Given the  $\sim 10\%$  sensitivity of the selection efficiency to final state radiation, the generator thus contributes an error of 1.3% to the fractional error  $\Delta \epsilon^{\Upsilon \rightarrow \mu\mu} / \epsilon^{\Upsilon \rightarrow \mu\mu}$ .

The error on the detector acceptance was estimated from a comparison of MC distributions and data for all variables used in our selection cuts. Such comparisons are for example plotted in Figs. 5.8, A.3, A.6, and B.21. We find a combined fractional error of 2.1%; where the dominant sources are an 1.2% error from the inaccuracy in reproducing the debris energy (Fig. 5.8), and a 1.0% error of the pattern fraction efficiency (Fig. A.3) for a cut at  $F_2 > 0.945$ .

Finally, the MC statistics, combined over either resonance, contributes 0.5% to the error on the mean amplitude of  $\epsilon_i^{\Upsilon \rightarrow \mu\mu}$ .

The errors add up to a total fractional error of 2.5% (Table 6.1) corresponding to the absolute error of 1.1% on our selection efficiency, which was cited above.

Table 6.1: Contributions to the fractional error on the selection efficiency for resonant muons.

Source	fractional error
Generator	1.3%
Detector Simulation	2.1%
MC Statistics	0.5%
$\Delta \epsilon^{\Upsilon \rightarrow \mu\mu} / \epsilon^{\Upsilon \rightarrow \mu\mu}$	2.5%

## 6.2 The Determination of $B_{\mu\mu}$

Figures 6.2(b) and 6.3(b) present our final spectra for the efficiency corrected cross-section  $\sigma^{ee \rightarrow \Upsilon \rightarrow \mu\mu}(W)$ , which have been obtained by dividing for each  $W_i$  the observed cross-section from Fig. 5.5 by  $\epsilon_i^{\Upsilon \rightarrow \mu\mu}$ . They are listed in numerical form in Appendix D. The fits to the spectra are explained in Section 6.3. For the determination of  $B_{\mu\mu}$  we only use the numbers of resonant  $\mu$ -pairs which are the basis of this measured cross-section.

From the efficiency corrected number of resonant  $\mu$ -pairs measured within 10 MeV of the resonance peaks, and the corresponding number of  $\Upsilon$  decays we determine  $B_{\mu\mu}$  according to Eq. (6.2). The number of  $\Upsilon$  decays within 10 MeV of the resonance peaks is in turn derived from the observed hadronic cross-section, shown in Figs. 6.2(a) and 6.3(a), as detailed below.

### 6.2.1 The Number of $\Upsilon$ Resonances

#### Continuum Subtraction

The observed hadronic cross-sections in Fig. 6.2(a) and Fig. 6.3(a) are based on  $447 \times 10^3$  and  $253 \times 10^3$  multi-hadron events in the energy regions of the  $\Upsilon(1S)$  and  $\Upsilon(2S)$ , respectively. The data are identical to those which have been utilized to determine the c.m. energy in Appendix C. The observed hadronic cross-section is now plotted for each of the combined c.m. energies  $W_i$ , which resulted from this determination (see Sections 4.2 and C.5). In addition, we have now corrected the cross-section at each  $W_i$  for the contribution of decays  $\Upsilon \rightarrow e^+e^-$  to the number of luminosity events (cf. Section 4.4).

To the observed hadronic cross-section we fit a continuum

$$\sigma^{ee \rightarrow q\bar{q}}(W) = \sigma^{ee \rightarrow q\bar{q}}(W_{\text{peak}}) \frac{W_{\text{peak}}}{W^2} \quad (6.3)$$



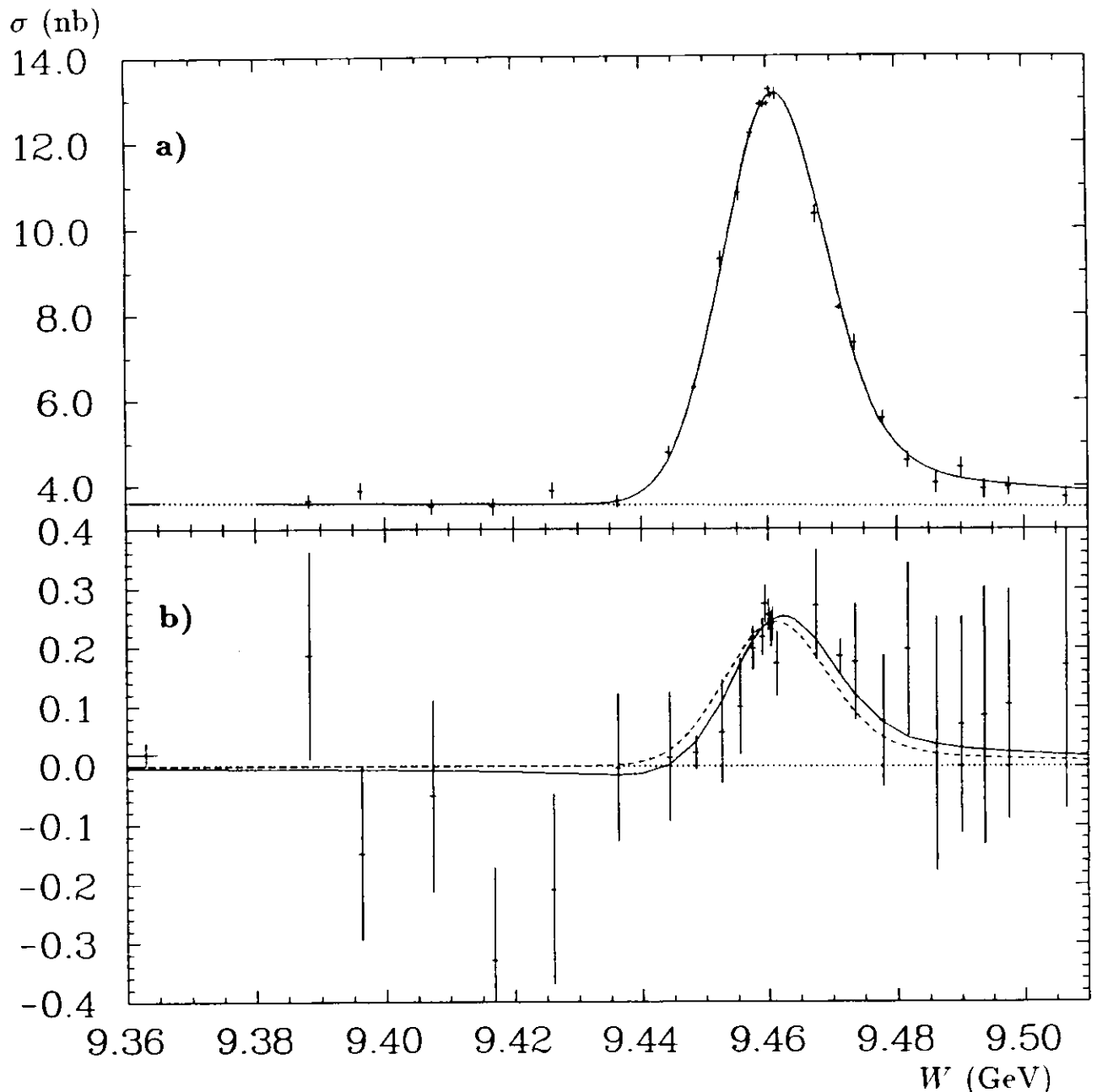


Figure 6.2: a) Observed hadronic cross-section in the region of the  $\Upsilon(1S)$  resonance. The solid line is a fit result with the parameters listed in Table 6.2. The dotted line shows the continuum contribution  $\sigma^{e^+e^- \rightarrow q\bar{q}}$  to the fit.

b) Measured cross-section of  $ee \rightarrow \Upsilon \rightarrow \mu\mu$  in the region of the  $\Upsilon(1S)$  resonance. It has been obtained by correcting the observed cross-section from Fig. 5.5(a) point-by-point with the detection efficiency  $\epsilon_{\Upsilon \rightarrow \mu\mu}^{\Upsilon}$ . The lines are fitted to the cross-section as described in Section 6.3. The dashed line is a fit without, the solid line is a fit with interference.

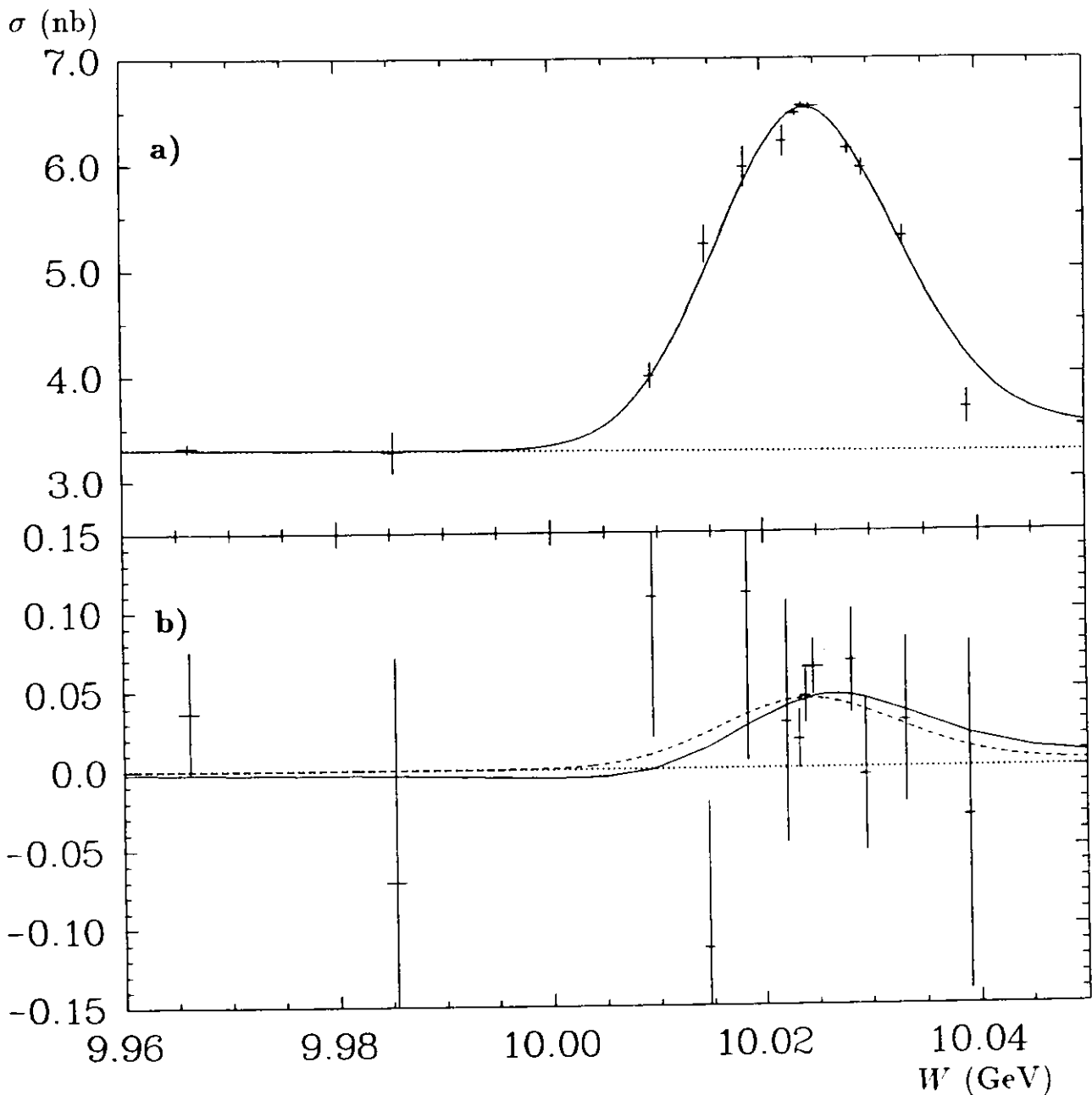


Figure 6.3: a) Observed hadronic cross-section in the region of the  $\Upsilon(2S)$  resonance. The solid line is a fit result with the parameters listed in Table 6.2. The dotted line shows the continuum contribution  $\sigma^{ee \rightarrow q\bar{q}}$  to the fit.

b) Measured cross-section of  $ee \rightarrow \Upsilon \rightarrow \mu\mu$  in the region of the  $\Upsilon(2S)$  resonance. It has been obtained by correcting the observed cross-section from Fig. 5.5(b) point-by-point with the detection efficiency  $\epsilon_{\Upsilon \rightarrow \mu\mu}^I$ . The lines are fitted to the cross-section as described in Section 6.3. The dashed line is a fit without, the solid line is a fit with interference.

plus a radiatively corrected resonance shape with free peak position  $W_{\text{peak}}$ , peak height  $\sigma^{\Upsilon \rightarrow \text{had}}(W_{\text{peak}})$ , and c.m. energy spread  $w$ . The small interference effect between hadronic resonance decays and continuum production was not included in the fit, because its influence on the fit results can be neglected. The parameters obtained from the fit procedure are listed in Table 6.2.

Table 6.2: Resulting parameters from the fit to the observed hadronic cross-section in Figs. 6.2(a) and 6.3(a).

		$\Upsilon(1S)$		$\Upsilon(2S)$	
$m_{\Upsilon}$	(MeV/ $c^2$ )	9460.3	$\pm 0.2$	10023.2	$\pm 0.3$
$w$	(MeV)	7.9	$\pm 0.2$	8.2	$\pm 0.3$
$\sigma^{\Upsilon \rightarrow \text{had}}(W_{\text{peak}})$	(pb)	9566	$\pm 58$	3263	$\pm 51$
$\sigma^{e\bar{e} \rightarrow q\bar{q}}(W_{\text{peak}})$	(pb)	3544	$\pm 22$	3267	$\pm 47$

Note, that the  $\Upsilon$  masses derived from  $m_{\Upsilon} = W_{\text{peak}} - 1.0$  MeV (Eq. (4.3)) have to agree with the PDG values [22] of  $m_{\Upsilon(1S)} = 9460.3$  MeV and  $m_{\Upsilon(2S)} = 10023.3$  MeV, since these were put in the determination of  $W_i$ . Our values for the c.m. energy spread  $w$  are in good agreement with those obtained in Ref. [96].

The observed number  $N_i^{\Upsilon \rightarrow \text{had}}$  of  $\Upsilon$  decays to hadrons is evaluated by subtracting the continuum contribution from the total number  $N_i^{\text{had}}$  of multi-hadron events observed at each c.m. energy  $W_i$  according to

$$N_i^{\Upsilon \rightarrow \text{had}} = N_i^{\text{had}} - \mathcal{L}_i \sigma^{e\bar{e} \rightarrow q\bar{q}}(W_i), \quad (6.4)$$

where  $\sigma^{e\bar{e} \rightarrow q\bar{q}}(W_i)$  was derived from Eq. (6.3) inserting the fit results from Table 6.2. This results in a total number of observed hadronic  $\Upsilon$  decays of  $N^{\Upsilon \rightarrow \text{had}}(1S) = (272.3 \pm 1.0) \times 10^3$  and  $N^{\Upsilon \rightarrow \text{had}}(2S) = (110.4 \pm 1.7) \times 10^3$  for the data points within  $\pm 10$  MeV of the resonance peaks. The errors are statistical only.

### Efficiency Determination

To obtain the total number of produced  $\Upsilon$  decays, we have to divide  $N_i^{\Upsilon \rightarrow \text{had}}$  by the fraction  $\epsilon_i^{\Upsilon \rightarrow \text{all}}$  of all  $\Upsilon$  decays which pass our multi-hadron selection. This fraction is calculated from the relative abundances of all  $\Upsilon$  decay channels together with the efficiency of the multi-hadron selector for each channel. The branching fraction for decays to fermion-antifermion ( $f\bar{f}$ ) pairs is given by  $B_{f\bar{f}} = (3 + R)B_{\mu\mu}$ . The branching fraction to all other channels (ggg,  $\gamma$ gg, transitions to lower lying  $b\bar{b}$  states) is then  $B_{\text{oth}} = 1 - B_{f\bar{f}}$ . The abundance of  $f\bar{f}$  events in  $N_i^{\Upsilon \rightarrow \text{had}}$  is modified to  $B_{f\bar{f}}(1 + \sigma_i^{\bar{I}}/\sigma_i^{\bar{R}})$  by the interference with the continuum production of  $f\bar{f}$ . Here,  $\sigma_i^{\bar{I}}/\sigma_i^{\bar{R}}$  is the ratio of the (muonic) interference cross-section to the (muonic) resonance cross-section at each c.m. energy  $W_i$ . We thus find

$$\epsilon_i^{\Upsilon \rightarrow \text{all}} = \frac{B_{\text{oth}}\epsilon_{\text{oth}} + B_{f\bar{f}}(1 + \sigma_i^{\bar{I}}/\sigma_i^{\bar{R}})\epsilon_{f\bar{f}}}{1 + B_{f\bar{f}}\sigma_i^{\bar{I}}/\sigma_i^{\bar{R}}}, \quad (6.5)$$

where the denominator restores the normalization of the branching fractions. The efficiencies  $\epsilon_{\text{oth}}$  and  $\epsilon_{f\bar{f}}$  of the hadron selector have been determined from a MC simulation of  $\Upsilon$  decays with an appropriate mixture of decay channels. The hadronic decays were generated with the LUND program and subjected to a complete detector simulation. We averaged the efficiencies

obtained with the string fragmentation in the JETSET 6.2 version [104] and those from the JETSET 6.3 program modeling parton shower fragmentation [105]. The resulting values are

$$\varepsilon_{\text{oth}}(1\text{S}) = 94.3\%, \quad \varepsilon_{\text{ff}}(1\text{S}) = 45.7\%$$

and

$$\varepsilon_{\text{oth}}(2\text{S}) = 92.1\%, \quad \varepsilon_{\text{ff}}(2\text{S}) = 45.1\%.$$

The  $\text{ff}$  efficiencies include all fermionic decay channels with respective efficiencies of  $\varepsilon_{\text{qq}} \approx 81\%$ ,  $\varepsilon_{\tau\tau} \approx 11\%$ , and  $\varepsilon_{\text{ee}} = \varepsilon_{\mu\mu} = 0\%$ . The branching fraction to fermion pairs was determined from  $R=3.48$  [96] together with our final results for  $B_{\mu\mu}$  (Eq. (6.6)) as  $B_{\text{ff}}(1\text{S}) = 15.0\%$  and  $B_{\text{ff}}(2\text{S}) = 7.9\%$ . Finally, the interference cross-section  $\sigma_i^{\text{I}}/\sigma_i^{\text{R}}$  was derived from the DYMU2 generator as described in Section 2.3.4 and plotted in Fig. 2.16.

For the various c.m. energies  $W$  we find efficiencies  $\varepsilon_i^{\text{I}\rightarrow\text{all}}$  ranging from 85.7% to 88.5% for the  $\Upsilon(1\text{S})$  data, and from 87.3% to 89.8% for the  $\Upsilon(2\text{S})$  data. Dividing the observed numbers  $N_i^{\text{I}\rightarrow\text{had}}$  of hadronic  $\Upsilon$  decays point-by-point by the efficiency  $\varepsilon_i^{\text{I}\rightarrow\text{all}}$  we obtain total numbers of produced  $\Upsilon$  decays of  $(312.7 \pm 1.1) \times 10^3$  and  $(124.8 \pm 1.9) \times 10^3$  for the data sets within  $\pm 10$  MeV of the  $\Upsilon(1\text{S})$  and the  $\Upsilon(2\text{S})$ , respectively. This corresponds to mean efficiencies of

$$\varepsilon^{\text{I}\rightarrow\text{all}}(1\text{S}) = 87.1\% \pm 1.2\%$$

and

$$\varepsilon^{\text{I}\rightarrow\text{all}}(2\text{S}) = 88.5\% \pm 1.5\%.$$

These mean values are very close to the values of 87.0% and 88.4%, which would have been obtained without correcting for interference. The interference correction is so small, because only fermionic  $\Upsilon$  decays contribute, and because the interference effects below and above the resonances essentially cancel. The systematic errors cited for these efficiencies are determined below.

### Systematic Errors and Results

The quantity  $\varepsilon_i^{\text{I}\rightarrow\text{all}}$  in Eq. (6.5) is constructed such that  $N_i^{\text{I}\rightarrow\text{had}}/\varepsilon_i^{\text{I}\rightarrow\text{all}}$  is the number of produced  $\Upsilon$  resonances  $\#(\Upsilon)$  plus a (positive or negative) contribution  $\mathcal{L}_i(3+R)\sigma_i^{\text{I}}$  of fermion pairs, which comes from the interference effect. This contribution has still to be subtracted (cf. Eq. (6.2)). With  $\sigma_i^{\text{I}}$  again obtained from the DYMU2 generator we find a total interference contribution of  $-(0.5 \pm 0.5) \times 10^3$  and  $-(0.2 \pm 0.2) \times 10^3$  resonances, summed over the data sets within  $\pm 10$  MeV of the  $\Upsilon(1\text{S})$  and the  $\Upsilon(2\text{S})$  resonances, respectively. This correction is again very small and moreover partially compensated by the interference effect on  $\varepsilon^{\text{I}\rightarrow\text{all}}$ . Its systematic error arises from the error of  $\Delta W = 0.5$  MeV on our c.m. energy measurement in Appendix C.

The dominant systematic error on  $\#(\Upsilon)$ , however, arises from the systematic uncertainty  $\Delta\varepsilon^{\text{I}\rightarrow\text{all}}$ . It has contributions from the observed differences between the LUND hadronization models (0.4%), from uncertainties in the detector response to hadrons (0.7%), and from the error on our final  $B_{\mu\mu}$  value (0.5% and 1.0% for the  $\Upsilon(1\text{S})$  and the  $\Upsilon(2\text{S})$ , respectively). The error on the modeling of the detector response was obtained from varying the parametrization of light quenching, negative particle absorption, and energy loss in our upgraded GHEISHA program. Since some of our GHEISHA upgrades (especially that of light quenching in scintillators) have been verified by comparing MC events from the LUND program to Crystal Ball data, we account for possible correlations between the first two errors by adding them linearly. The errors on  $B_{\mu\mu}$  are then added in quadrature resulting in systematic errors of

$\Delta\epsilon^{\Upsilon\rightarrow\text{all}}(1\text{S}) = 1.2\%$  and  $\Delta\epsilon^{\Upsilon\rightarrow\text{all}}(2\text{S}) = 1.5\%$ , which were cited above. With these errors and the interference correction we obtain numbers of produced  $\Upsilon$  resonances of

$$\#(\Upsilon(1\text{S})) = (313.2 \pm 1.1 \pm 4.4) \times 10^3$$

and

$$\#(\Upsilon(2\text{S})) = (125.0 \pm 1.9 \pm 2.1) \times 10^3.$$

The fractional systematic errors  $\Delta(\#(\Upsilon))/\#(\Upsilon)$  are thus 1.4% and 1.7% for the  $\Upsilon(1\text{S})$  and the  $\Upsilon(2\text{S})$ , respectively.

### 6.2.2 The Number of Resonant $\mu$ -Pairs

The procedure of calculating the number of resonant  $\mu$ -pairs  $\#(\Upsilon \rightarrow \mu^+\mu^-)$  follows the same line as the calculation of  $\#(\Upsilon)$  above. An overview is given in Table 6.3, where always the sum over the data samples within 10 MeV of the resonance peaks is given.

We first subtract the scaled continuum prediction  $C \sum \mathcal{L}_i \sigma_i^{BG}$  and the resonant background  $\sum N_i^{\Upsilon\rightarrow\mu\mu^X}$ , which have been determined in Sections 5.3 and 5.4, respectively, from the total number  $\sum N_i^{\mu\mu}$  of observed  $\mu$ -pair events. (As in Fig. 5.3(a) we have already subtracted the cosmic ray background in  $N_i^{\mu\mu}$ .) We are left with  $(3.19 \pm 0.16 \pm 0.10) \times 10^3$  and  $(0.66 \pm 0.15 \pm 0.10) \times 10^3$   $\mu$ -pair events from  $\Upsilon(1\text{S})$  and  $\Upsilon(2\text{S})$  decays, respectively. Their systematic errors arise mainly from  $\Delta(\mathcal{L}_i/\mathcal{L}_{\text{off}})$  and  $\Delta(\sigma_i^{BG}/\sigma_{\text{off}}^{BG})$ . Following Eq. (6.2) the numbers  $N_i^{\Upsilon\rightarrow\mu\mu}$  are corrected for each  $W_i$  by the detection efficiency  $\epsilon_i^{\Upsilon\rightarrow\mu\mu}$ , which has been determined together with its systematic error in Section 6.1.

Given our systematic error on the c.m. energy of  $\Delta W = 0.5$  MeV, we are able to determine the interference correction  $\sum \mathcal{L}_i \sigma_i^I$  to the resulting number  $\sum N_i^{\Upsilon\rightarrow\mu\mu}/\epsilon_i^{\Upsilon\rightarrow\mu\mu}$  of muonic resonance decays with a precision<sup>2</sup> of about 1% for the  $\Upsilon(1\text{S})$  and about 2% for the  $\Upsilon(2\text{S})$ . The total correction  $\sum \mathcal{L}_i \sigma_i^I$ , however, is not significantly different from zero, because we selected the data in a symmetric range of 10 MeV around the resonances, cancelling out most of the interference effect. Omitting a precise determination of  $W$  on the other hand, the distribution of the c.m. energies with respect to the resonance peak would have been unknown. In this case we would have had to allow for an error of at least  $\Delta W = w/3 = 2.7$  MeV (cf. Section 4.2), which would have increased the corresponding error on  $B_{\mu\mu}$  by more than a factor five. The resulting errors of at least 5% and 10% for  $B_{\mu\mu}(1\text{S})$  and  $B_{\mu\mu}(2\text{S})$ , respectively, would have been one of our dominant systematic error sources (see Table 6.4).

After the small interference correction we end up with a total number of resonant  $\mu$ -pairs of  $(7.22 \pm 0.36 \pm 0.30) \times 10^3$  and  $(1.52 \pm 0.35 \pm 0.23) \times 10^3$  for the  $\Upsilon(1\text{S})$  and  $\Upsilon(2\text{S})$ , respectively. Dividing these numbers by the total numbers of produced resonances, we obtain for the two lowest lying  $\Upsilon$  states values of

$$\begin{aligned} B_{\mu\mu}(1\text{S}) &= (2.31 \pm 0.12 \pm 0.10)\% \\ B_{\mu\mu}(2\text{S}) &= (1.22 \pm 0.28 \pm 0.19)\%. \end{aligned} \tag{6.6}$$

The relative influences of the various error sources are collected in Table 6.4.

<sup>2</sup>This precision is obtained from Eq. (4.5) if we allow to shift all values of  $W_i$  by 0.5 MeV up or down. It is conservative, since such a shift would create a 2 s.d. discrepancy of the fitted  $m_\Upsilon$  values in Table 6.2 away from their PDG values [22].

Table 6.3: Summary of results for the calculation of  $B_{\mu\mu}$ .

	$\Upsilon(1S)$	$\Upsilon(2S)$
$\sum N_i^{\mu\mu}$	$18680 \pm 140$	$16076 \pm 130$
$- C \sum \mathcal{L}_i \sigma_i^{BG}$	$15477 \pm 82 \pm 104$	$15404 \pm 82 \pm 101$
$- \sum N_i^{\Upsilon \rightarrow \mu\mu X}$	$14 \pm 0 \pm 2$	$15 \pm 0 \pm 9$
$\sum N_i^{\Upsilon \rightarrow \mu\mu}$	$3189 \pm 162 \pm 104$	$657 \pm 154 \pm 101$
$\sum N_i^{\Upsilon \rightarrow \mu\mu} / \epsilon_i^{\Upsilon \rightarrow \mu\mu}$	$7143 \pm 364 \pm 295$	$1491 \pm 350 \pm 232$
$- \sum \mathcal{L}_i \sigma_i^{\bar{I}}$	$-80 \pm 0 \pm 72$	$-29 \pm 0 \pm 30$
$\#(\Upsilon \rightarrow \mu\mu)$	$7223 \pm 364 \pm 304$	$1520 \pm 350 \pm 234$
$: \#(\Upsilon) / 10^3$	$313.2 \pm 1.1 \pm 4.4$	$125.0 \pm 1.9 \pm 2.1$
$B_{\mu\mu} / \%$	$2.31 \pm 0.12 \pm 0.10$	$1.22 \pm 0.28 \pm 0.19$

Table 6.4: Contributions of the various error sources to the fractional error on our  $B_{\mu\mu}$  measurements.

statistical errors	$\Upsilon(1S)$	$\Upsilon(2S)$
$\Delta N^{\Upsilon \rightarrow \text{had}}$	0.4%	1.6%
$\Delta N_{off}^{\mu\mu}$	2.5%	12.3%
$\Delta N_i^{\mu\mu}$	4.3%	19.5%
total $\Delta B_{\mu\mu} / B_{\mu\mu}$	5.0%	23.1%
systematic errors	$\Upsilon(1S)$	$\Upsilon(2S)$
$\Delta N^{\Upsilon \rightarrow \mu\mu X}$	0.1%	1.3%
$\Delta \epsilon^{\Upsilon \rightarrow \text{all}}$	1.4%	1.7%
$\Delta W$	1.0%	1.9%
$\Delta \epsilon^{\Upsilon \rightarrow \mu\mu}$	2.5%	2.5%
$\Delta(\mathcal{L}_i / \mathcal{L}_{off})$	1.2%	4.1%
$\Delta(\sigma_i^{BG} / \sigma_{off}^{BG})$	3.0%	14.5%
total $\Delta B_{\mu\mu} / B_{\mu\mu}$	4.4%	15.5%

## 6.3 The Determination of $\Gamma_{\mu\mu}B_{ee}$

### 6.3.1 The Fit to the Muonic Cross-Section

As we have already noted in Eq. (6.1) the quantity

$$\hat{A} \equiv \frac{\Gamma_{\mu\mu}\Gamma_{ee}}{\Gamma} = \Gamma_{\mu\mu}B_{ee} \quad (6.7)$$

is connected with the area  $A = \int \sigma^{ee \rightarrow \Upsilon \rightarrow \mu\mu}(W) dW$  under the muonic resonance cross-section.  $\hat{A}$  can thus be obtained from a fit of  $\sigma^{\bar{R}}(W) + \sigma^{\bar{I}}(W)$  (Fig. 2.16) to the measured cross-section  $\sigma^{ee \rightarrow \Upsilon \rightarrow \mu\mu}(W)$  (Figs. 6.2(b) and 6.3(b)). The fit function is a convolution of the non-radiative cross-section  $\sigma_0$  (Eq. (2.90)) with the Gaussian distribution of the c.m. energy and a Bremsstrahlung spectrum accounting for initial state photon radiation. As we have shown in Section 2.3.1 the non-radiative cross-section  $\sigma_0$  includes vacuum polarization, resonance, and interference terms. Since the resulting convoluted fit function is not analytic, we employ the DYMU2 generator (Section 2.3.4) to predict the cross-section  $\sigma^{ee \rightarrow \Upsilon \rightarrow \mu\mu}(m_\Upsilon, B_U, w, \hat{A})$  for each single c.m. energy  $W_i$  encountered in our data.

The parameter set  $(m_\Upsilon, B_U, w, \hat{A})$  is sufficient to describe this process, since we can write the resonant and interference terms of the *non-radiative* cross-section (Eqs. (2.84)–(2.86)) as

$$\begin{aligned} \sigma^I &\propto 2\Re B_n = 2 \frac{3\hat{A}}{\alpha B_U m_\Upsilon} \frac{s(s - m_\Upsilon^2)}{(s - m_\Upsilon^2)^2 + m_\Upsilon^2 (\hat{A}/B_U^2)^2} \\ \sigma^R &\propto |B_n|^2 = \frac{9\hat{A}^2}{\alpha^2 B_U^2 m_\Upsilon^2} \frac{s^2}{(s - m_\Upsilon^2)^2 + m_\Upsilon^2 (\hat{A}/B_U^2)^2}, \end{aligned} \quad (6.8)$$

where we have assumed lepton universality  $B_U = B_{\mu\mu} = B_{ee}$ . Initial state radiation and c.m. energy spread  $w$  are properly folded onto these non-radiative cross-sections by the DYMU2 generator. This leads to the predicted behaviour of  $\sigma^{ee \rightarrow \Upsilon \rightarrow \mu\mu} = \sigma^{\bar{R}} + \sigma^{\bar{I}}$ , which has been already plotted in Fig. 2.16 for the PDG values as input parameters.

We now vary  $\hat{A}$  as the only free parameter<sup>3</sup> in fitting the DYMU2 prediction to the measured data in Figs. 6.2(b) and 6.3(b). The values for  $m_\Upsilon$  and  $B_U$  have been fixed to their table values [22], and the c.m. energy spread  $w$  has been fixed to the values from Table 6.2, which were obtained from our hadronic cross-section.

The fit results to our muonic cross-section are shown as solid lines in Figs. 6.2(b) and 6.3(b). They have confidence levels of 99% and 65% for the  $\Upsilon(1S)$  and  $\Upsilon(2S)$  data, respectively. From these fits we obtain

$$\begin{aligned} \frac{\Gamma_{\mu\mu}\Gamma_{ee}}{\Gamma}(1S) &= (31.2 \pm 1.6 \pm 1.7) \text{ eV} \\ \frac{\Gamma_{\mu\mu}\Gamma_{ee}}{\Gamma}(2S) &= (6.5 \pm 1.5 \pm 1.0) \text{ eV.} \end{aligned} \quad (6.9)$$

Sources and size of the systematic errors for this measurement are essentially the same as for our determination of  $B_{\mu\mu}$  (see Table 6.4). Only the statistical error  $\Delta N^{\Upsilon \rightarrow \text{had}}$  on the number of multi-hadron events and the systematic error  $\Delta \epsilon^{\Upsilon \rightarrow \text{all}}$  on the hadron selection efficiency do not enter. An additional error of 2.5% originates from the luminosity measurement. The

<sup>3</sup>Actually,  $\hat{A}$  is guessed once, such that the predicted cross-section describes the data fairly well. We then fit a constant to the ratio of the measured and the predicted cross-section and obtain our final  $\hat{A}$  by multiplying the guessed  $\hat{A}$  with this constant.

uncertainty of 0.5 MeV in the c.m. energy of each data point has been taken into account in the fit by increasing the errors on the measured cross-section accordingly. This covers the error induced from fixing  $m_\Upsilon$  in the fit.

The errors from fixing  $w$  and  $B_{\mu\mu}$  are more difficult to estimate. Since the amplitude  $\bar{R}$  of the fit curve is governed by the high statistics points on top of the resonance, this amplitude will not change, when we *slightly* vary  $w$ . From Eqs. (6.1), (2.127), and (2.129) we deduce that  $\hat{A} \propto \bar{R}w^{1-\beta_\epsilon}$ , where  $\beta_\epsilon=0.087$  was defined in Eq. (2.97). Regarding  $\bar{R}$  as a constant, the errors on  $w$  from Table 6.2 contribute a fractional error of  $\Delta\hat{A}/\hat{A} = (1 - \beta_\epsilon)\Delta w/w$  yielding 2.3% and 3.4% for the  $\Upsilon(1S)$  and the  $\Upsilon(2S)$ , respectively.

The error induced from fixing  $B_{\mu\mu}$  is negligibly small. This can be understood from the fact, that  $B_{\mu\mu}$  enters only via the shape of the fit function. This shape depends on the relative amplitudes  $|\bar{I}/\bar{R}| \approx |I_0/R_0| = \alpha/3B_{\mu\mu}$  of interference and resonance cross-section (Eqs. (2.87) and (2.88)). As we have shown in Section 2.3.5, the ratio  $|\bar{I}/\bar{R}|$  is completely insensitive to  $\Gamma=\hat{A}/B_{\mu\mu}^2$ , as long as  $\Gamma \ll w$ . Actually, the fit results do only weakly depend on the ratio  $|\bar{I}/\bar{R}|$ , since our high-statistics data points are taken at c.m. energies, where the net interference effect is small. We find a change of only 1% for  $\hat{A}$ , if we modify  $B_{\mu\mu}$ , and thus  $|\bar{I}/\bar{R}|$ , by 40%. The errors on  $B_{\mu\mu}$  from Ref. [22] therefore induce negligible errors of 0.1% for  $\hat{A}(1S)$  and 0.5% for  $\hat{A}(2S)$ .

Note that this also means, that our determination of  $\hat{A}$  is essentially independent from the assumption of lepton universality in Eq. (6.8). All  $B_{\mu\mu}$  terms in this formulae arise from setting  $\sqrt{B_{ee}B_{\mu\mu}} \equiv B_{\mu\mu}$ . Since  $1.4B_{\mu\mu} = \sqrt{(2B_{ee})B_{\mu\mu}} = \sqrt{B_{ee}(2B_{\mu\mu})}$ , a violation of lepton universality by a factor of 2 has the same 1% effect on  $\hat{A}$  as a change of 40% in  $B_{\mu\mu}$ .

### 6.3.2 Evidence for Interference

By omitting the interference term in the generation of the  $\mu$ -pair cross-section, we can study, whether this term is really necessary to describe our data. The corresponding fit results are shown as dashed lines in Figs. 6.2(b) and 6.3(b). From the product of the probability densities for the deviations of each data point from the fits, we form a likelihood ratio for the hypotheses with and without interference. On the  $\Upsilon(2S)$  resonance our data have not sufficient statistics to discriminate between the two hypotheses, which is expressed in a likelihood ratio of 51:49 in favor of interference. However, on the  $\Upsilon(1S)$  the interference is favored by a likelihood ratio of 98:2, showing the first evidence for the expected interference between muonic  $\Upsilon$  decays and the continuum process  $ee \rightarrow \mu\mu$ . Following the arguments already made for the  $J/\psi$  [106], we thus confirm the assignment of  $J^{PC} = 1^{--}$  for the  $\Upsilon(1S)$ .

This evidence crucially depends on the size of the error bars in Fig. 6.2(b). We have included all errors in this plot, which can vary from point to point, for example all data and MC statistics, the 0.5 MeV error on each  $W_i$ , as well as the  $0.44\% \times \lambda(1S) = 2.1\%$  systematic error in reproducing the changes in the detector acceptance between each data point and the subtracted continuum (Table 5.7). Overall scaling errors, which are identical and correlated for all points, like  $\Delta\epsilon^{\Upsilon \rightarrow \mu\mu}$ ,  $\Delta\mathcal{L}$ , or  $\Delta N_{off}^{\mu\mu}$  (entering via the continuum subtraction) are not included. Those common scaling errors go into the same direction (up or down) on the left-hand side and on the right-hand side of the resonance (cf. Appendix D). They therefore must not be included if possible evidence for interference is to be tested. However, even including these errors, the evidence for interference would survive<sup>4</sup>, since they are considerably smaller than each of the error bars plotted in Fig. 6.2(b).

In contrast to that, an uncertainty  $\Delta W$  of a few MeV would destroy the significance of

<sup>4</sup>The likelihood ratio from above would change to 97:3.



the measured interference. However, the fact that the fit to the hadronic cross-section fixes the  $\Upsilon(1S)$  mass with a precision of 0.2 MeV (see Table 6.2), together with the fact that this fit does not allow to shift the two high statistics data points at 9448.4 MeV and 9471.2 MeV by more than 0.5 MeV to lower values of  $W$ , additionally supports our determination of the energy scale.

# Chapter 7

## Discussion of the Results

### 7.1 The Leptonic Branching Ratios of $\Upsilon(1S)$ and $\Upsilon(2S)$

#### 7.1.1 The New World Averages

We average our values of

$$B_{\mu\mu}(1S) = (2.31 \pm 0.16)\%, \quad (7.1)$$

$$B_{\mu\mu}(2S) = (1.22 \pm 0.34)\%, \quad (7.2)$$

with previous measurements of  $B_{\mu\mu}$  as displayed in Fig. 7.1 and listed in Table 7.1. Not including the preliminary MD-1 result [117] on  $B_{\mu\mu}(1S)$  we obtain new world averages of

$$B_{\mu\mu}(1S) = (2.52 \pm 0.07)\%, \quad (7.3)$$

$$B_{\mu\mu}(2S) = (1.30 \pm 0.21)\%, \quad (7.4)$$

where statistical and systematic errors have been added in quadrature. We note, that our result for  $B_{\mu\mu}(1S)$  is about 1.3 s.d. below the new world average (continuing an apparent trend of  $B_{\mu\mu}(1S)$  measurements decreasing with time). Our value of  $B_{\mu\mu}(2S)$  is the second significant measurement of this quantity. The previous number from CUSB [120] agrees well with our result.

Our determinations of  $B_{\mu\mu}(1S)$  and  $B_{\mu\mu}(2S)$  are the first measurements, which take into account the interference between resonant and nonresonant  $\mu$ -pair production. In Sections 4.2 and 6.2.2 we have shown that without a precise enough knowledge of the DORIS beam energy<sup>1</sup> this effect would have introduced considerable systematic errors. Basically independent from interference effects are only measurements from the ratio of exclusive ( $\Upsilon(n'S) \rightarrow \pi\pi\Upsilon(nS) \rightarrow \pi\pi\mu\mu$ ) and inclusive ( $\Upsilon(n'S) \rightarrow \pi\pi\Upsilon(nS) \rightarrow \pi\pi X$ ) pionic transitions to lower lying  $\Upsilon$  states, like the CLEO [112] and ARGUS [114] measurements of  $B_{\mu\mu}(1S)$ .

Assuming lepton universality we average the value of  $B_{\mu\mu}(1S)$  from Eq. (7.3) with measurements [22] of  $B_{ee}(1S) = (2.52 \pm 0.17)\%$  and<sup>2</sup>  $B_{\tau\tau}(1S) = (2.94 \pm 0.35)\%$  to a leptonic branching ratio of

$$B_{ll}(1S) = (2.53 \pm 0.06)\%. \quad (7.5)$$

Apart from  $B_{\mu\mu}$ , no other leptonic branching ratios of the  $\Upsilon(2S)$  have yet been significantly measured<sup>3</sup>.

<sup>1</sup>Other storage rings like CESR and VEPP-4 may have less problems in monitoring their beam energy.

<sup>2</sup>We rescaled  $B_{\tau\tau}$  after Ref. [22].

<sup>3</sup>The value for  $B_{ee}(2S)$  listed in [22] has been derived by  $B_{ee} = \Gamma_{ee}/\Gamma$ , and  $\Gamma$  has been calculated from  $\Gamma_{ee}/B_{ll}$ , where  $B_{ll}$  is strongly dominated by the value of  $B_{\mu\mu}$ . Thus  $B_{ee}$  and  $B_{\mu\mu}$  are not independent measurements [121].

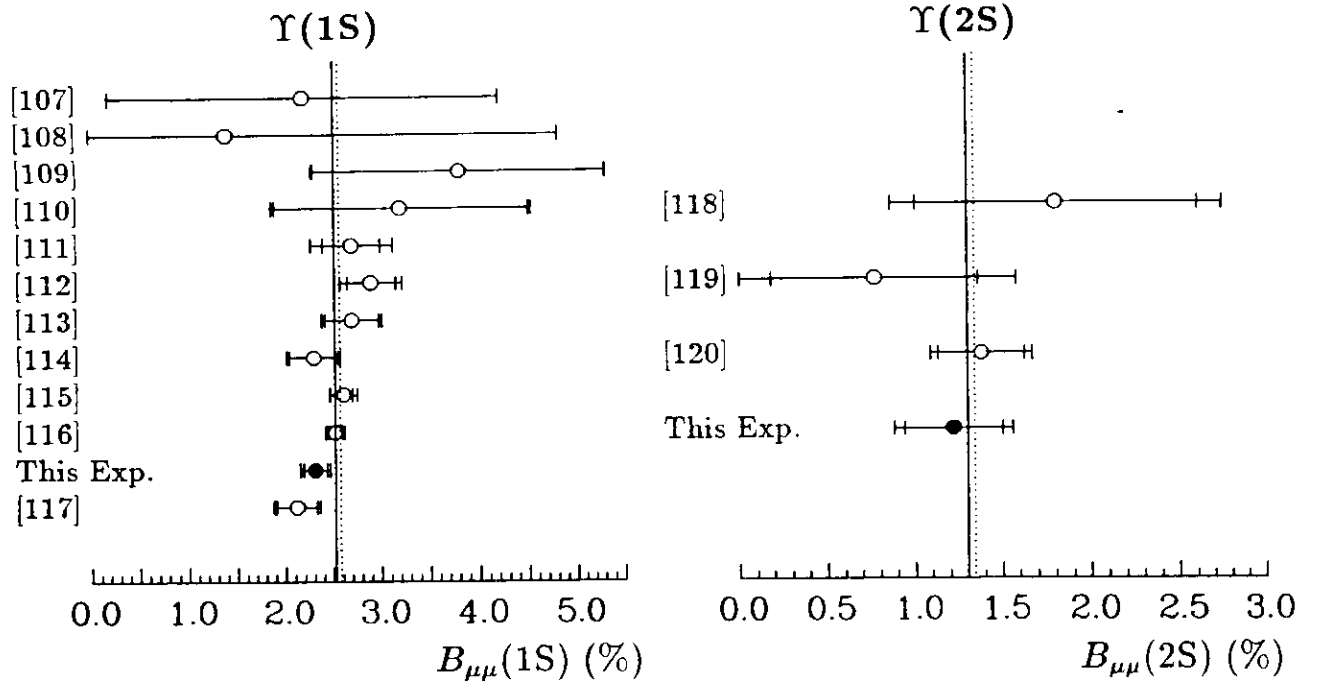


Figure 7.1: Graphical representation of  $B_{\mu\mu}$  measurements as listed in Table 7.1. The inner error bars show the statistical errors, only. The outer error bars are the quadratic sum of statistical and systematic errors. The new world average is shown as the solid vertical line, the previous average as the dashed line. The preliminary measurement  $B_{\mu\mu}(1S) = (2.12 \pm 0.21 \pm 0.11)\%$  [117] from MD-1 is included in neither of the two averages. It would change the new average to  $B_{\mu\mu}(1S) = (2.49 \pm 0.06)\%$ .

Table 7.1: Measurements of  $B_{\mu\mu}$  (in%). We disentangled the CLEO value of  $B_{\mu\mu}(1S) = (2.84 \pm 0.18 \pm 0.20)\%$  from [112] into a value for  $B_{e^+e^-}(1S) = (2.77 \pm 0.25 \pm 0.20)\%$  and the listed value for  $B_{\mu\mu}(1S)$ . The ARGUS  $\Upsilon(2S)$  value is scaled from the average  $\Upsilon(1S)$  value with  $B_{\mu\mu}(2S) = 1.57 \pm 0.59 \pm 0.53 + 2.1(B_{\mu\mu}(1S) - 2.9)$  (in %) [119].

Ref.	Exp. Year	$B_{\mu\mu}(1S)$ in %			Ref.	Exp. Year	$B_{\mu\mu}(2S)$ in %		
[107]	PLUTO 79	2.2	$\pm$	2.0	[118]	CLEO 84	1.8	$\pm$	0.8 $\pm$ 0.5
[108]	DESY-HD 80	1.4	$\pm$	$\begin{matrix} 3.4 \\ 1.4 \end{matrix}$	[119]	ARGUS 85	0.77	$\pm$	0.59 $\pm$ 0.55
[109]	LENA 82	3.8	$\pm$	1.5 $\pm$ 0.2	[120]	CUSB 89	1.38	$\pm$	0.25 $\pm$ 0.15
[110]	DASP 82	3.2	$\pm$	1.3 $\pm$ 0.3					
[111]	CLEO 83	2.7	$\pm$	0.3 $\pm$ 0.3	Prev. Average		1.35	$\pm$	0.26
[112]	CLEO 84	2.90	$\pm$	0.25 $\pm$ 0.20	This Experiment		1.22	$\pm$	0.28 $\pm$ 0.19
[113]	CUSB 87	2.70	$\pm$	0.28 $\pm$ 0.14	New Average		1.30	$\pm$	0.21
[114]	ARGUS 87	2.30	$\pm$	0.25 $\pm$ 0.13					
[115]	CUSB 89	2.61	$\pm$	0.09 $\pm$ 0.11					
[116]	CLEO 89	2.52	$\pm$	0.07 $\pm$ 0.07					
	Prev. Average	2.57	$\pm$	0.07					
	This Experiment	2.31	$\pm$	0.12 $\pm$ 0.10					
	New Average	2.52	$\pm$	0.07					

### 7.1.2 Consistency of $B_{\mu\mu}$ Values of Different Resonances

The widths for  $\Upsilon$  decays via  $b\bar{b}$  annihilation ( $(\Upsilon, q\bar{q}, \gamma g g, g g g)$ ) are all proportional to  $|\psi(0)|^2/m_\Upsilon^2$ , where  $\psi(0)$  is the (nonrelativistic) wave function at zero quark-antiquark separation (see e.g. Eqs. (2.67) and (2.68)). The normalized muonic branching ratios  $\widehat{B}_{\mu\mu} \equiv B_{\mu\mu}/B_{\text{anni}}$  are thus nearly identical for all  $\Upsilon$  resonances. The variation of  $|\psi(0)|$  and  $m_\Upsilon$  with the radial quantum number is cancelled in the above ratio to  $B_{\text{anni}}$ , which is the sum over all  $b\bar{b}$  annihilation channels. Corrections arise from the running coupling constant(s)  $\alpha_s$  (and  $\alpha_{em}$ ), and from relativistic effects. In principle, a scaling of  $B_{\mu\mu}$  to other quarkonia families, like the  $J/\psi$ , is also possible. We then have to account for the aforementioned corrections and for the quark charge  $|Q_c|=2/3$  compared to  $|Q_b|=1/3$ .

In Table 7.2 we have listed the branching ratios of the quark-antiquark annihilation decay channels in units of the muonic branching ratio of the  $\Upsilon(1S)$ , the  $\Upsilon(2S)$ , and the  $J/\psi(1S)$ . We used as an input the precisely measured value of  $B_{\mu\mu}(\Upsilon(1S)) = (2.52 \pm 0.07)\%$  from Eq. (7.3) and  $\frac{B_{\gamma g g}}{B_{\text{eff}}}(\Upsilon(1S)) = (2.77 \pm 0.15)\%$  [122]. The values  $R(m_\Upsilon) = 3.5 \pm 0.1$  and  $R(m_{J/\psi}) = 2.2 \pm 0.2$  are taken from a synopsis of  $R$  measurements [123]. The ratio  $B_{g g g}(\Upsilon(1S))/B_{\mu\mu}(\Upsilon(1S))$  was determined such that  $B_{\text{anni}} \equiv 1$ . (With the exception of a yet unmeasured decay  $\Upsilon(1S) \rightarrow \gamma \eta_b(1S)$  with a branching ratio of less than 0.5% the  $\Upsilon(1S)$  can only decay via  $b\bar{b}$  annihilation.) The ratio  $B_{\gamma g g}/B_{\mu\mu}$  was scaled to other resonances by multiplication with  $\alpha_s^2(\mu_{\text{eff}}^X)/\alpha_s^2(\mu_{\text{eff}}^{\Upsilon(1S)})$ , where  $\mu_{\text{eff}}$  denotes the (unknown) effective scale (cf. Eq. (2.60)) for evaluating  $\alpha_s$  for the gluonic decays of  $X=(\Upsilon(2S), J/\psi(1S))$  and of the  $\Upsilon(1S)$ . Accordingly we scaled the ratio  $B_{g g g}/B_{\mu\mu}$  with  $[\alpha_s^3(\mu_{\text{eff}}^X)/\alpha_s^3(\mu_{\text{eff}}^{\Upsilon(1S)})] \times (Q_b^2/Q_x^2)$ , where  $x=(b,c)$ . The running of  $\alpha_s$  was calculated from (see Eq. (2.44))

$$\alpha_s(\mu_{\text{eff}}^X) = \alpha_s(\mu_{\text{eff}}^{\Upsilon(1S)}) \times \left( 1 - \frac{\alpha_s(\mu_{\text{eff}}^{\Upsilon(1S)}) \beta_0}{\pi} \frac{1}{2} \ln \frac{\mu_{\text{eff}}^X}{\mu_{\text{eff}}^{\Upsilon(1S)}} \right)^{-1}. \quad (7.6)$$

For the calculation we set  $\mu_{\text{eff}}^X/\mu_{\text{eff}}^{\Upsilon(1S)} \equiv m_X/m_{\Upsilon(1S)}$  in Eq. (7.6). To cover the scale ambiguity we used the wide range  $0.14 \leq \alpha_s(\mu_{\text{eff}}^{\Upsilon(1S)}) \leq 0.22$ . This yielded<sup>4</sup>  $\alpha_s^2(\mu_{\text{eff}}^{J/\psi})/\alpha_s^2(\mu_{\text{eff}}^{\Upsilon(1S)}) = 1.6 \pm 0.2$  and  $\alpha_s^3(\mu_{\text{eff}}^{J/\psi})/\alpha_s^3(\mu_{\text{eff}}^{\Upsilon(1S)}) = 2.0 \pm 0.3$ . Naturally, a much smaller running of  $\alpha_s^3(\mu_{\text{eff}}^{\Upsilon(2S)})/\alpha_s^3(\mu_{\text{eff}}^{\Upsilon(1S)}) = 0.96 \pm 0.01$  emerges within the  $\Upsilon$  system.

To obtain  $B_{\mu\mu}$  we have to multiply the resulting values for  $\widehat{B}_{\mu\mu}$  with the fraction  $B_{\text{anni}}$  of resonance decays which proceed via quark-antiquark annihilation. We find from Ref. [22] that  $(44.9 \pm 2.1)\%$  of all  $\Upsilon(2S)$  decays are transitions to lower lying  $b\bar{b}$  bound states. For the  $J/\psi(1S)$  only one such transition exists, namely  $J/\psi \rightarrow \gamma \eta_c$  with a branching fraction of  $(1.3 \pm 0.4)\%$ .

Using this input<sup>5</sup> we predict  $B_{\mu\mu}(\Upsilon(2S)) = (1.43 \pm 0.07)\%$ , where the error is dominated by the 2.1% error on  $B_{\text{anni}}$ . The prediction agrees well with the world average value of  $B_{\mu\mu}(\Upsilon(2S)) = (1.30 \pm 0.21)\%$ . Let us mention, that a scaling of  $B_{\mu\mu}(\Upsilon(1S))$  to  $B_{\mu\mu}(\Upsilon(3S))$  (not listed in Table 7.2) also leads to good agreement with the measurements.

For the  $J/\psi(1S)$  we find  $B_{\mu\mu} = (4.5 \pm 0.5)\%$ . This differs by 2.3 standard deviations from the measured value [22] in Table 7.2. Since the measurement of  $B_{\mu\mu}(J/\psi)$  is supported by a (however, partially correlated) measurement of  $B_{ee}(J/\psi)$ , the most probable source for this

<sup>4</sup>The more exact procedure of using the second order expression for the running coupling constant, with additional terms [38] accounting for the opening of the  $c$ -flavor threshold between the  $J/\psi$  and the  $\Upsilon$ , agrees well with these results.

<sup>5</sup>An input of our result for  $B_{\mu\mu}(\Upsilon(1S))$  from Eq. (7.1) would have led to a prediction of  $B_{\mu\mu}(\Upsilon(2S)) = (1.31 \pm 0.10)\%$  in comparably good agreement with our measurement of this quantity (Eq. (7.2)).

Table 7.2: Predictions for  $B_{\mu\mu}(\Upsilon(2S))$  and  $B_{\mu\mu}(J/\psi)$  obtained by scaling the measured  $B_{\mu\mu}(\Upsilon(1S))$ .

channel	$B_{\text{channel}}/B_{\mu\mu}$	$\Upsilon(1S)$	$\Upsilon(2S)$	$J/\psi(1S)$
$l\bar{l}$	$n_{ll}$	3.0	3.0	2.0
$q\bar{q}$	$R$	$3.5 \pm 0.1$	$3.5 \pm 0.1$	$2.2 \pm 0.2$
$\gamma g g$	$(\frac{B_{\gamma g g}}{B_{g g g}})B_{g g g}/B_{\mu\mu}$	$0.9 \pm 0.1$	$0.9 \pm 0.1$	$1.4 \pm 0.2$
$g g g$	$\widehat{B}_{\mu\mu}^{-1} - (n_{ll} + R) - B_{\gamma g g}/B_{\mu\mu}$	$32.3 \pm 1.1$	$31.0 \pm 1.1$	$16.1 \pm 2.5$
	$1/\widehat{B}_{\mu\mu}$	$39.7 \pm 1.1$	$38.4 \pm 1.1$	$21.7 \pm 2.5$
	$\widehat{B}_{\mu\mu}$	$(2.52 \pm 0.07)\%$	$(2.60 \pm 0.08)\%$	$(4.6 \pm 0.5)\%$
	$\times B_{\text{anni}}$	1.00	$0.551 \pm 0.021$	$0.987 \pm 0.004$
	$B_{\mu\mu}$ predicted	— input —	$(1.43 \pm 0.07)\%$	$(4.5 \pm 0.5)\%$
	$B_{\mu\mu}$ measured	$(2.52 \pm 0.07)\%$	$(1.30 \pm 0.21)\%$	$(6.9 \pm 0.9)\%$

disagreement are relativistic  $v^2/c^2$  corrections [49,124,125] for the  $J/\psi$ , which we have not included. The disagreement cannot be due to the running of  $\alpha_{em}$ , which would even lower our prediction by 0.1%. On the other hand one might try to increase the range of values for  $\alpha_s(\mu_{\text{eff}}^{\Upsilon(1S)})$  in order to reduce the difference to the measured value to 1 standard deviation. This would require to insert  $\alpha_s(\mu_{\text{eff}}^{\Upsilon(1S)}) = 0.08$ , which is clearly beyond the range of sensible values, since then  $\mu_{\text{eff}}^{\Upsilon(1S)} \sim \mathcal{O}(1 \text{ TeV})$ ! Higher order  $\alpha_s$  corrections are mainly identical for  $\Gamma_{ggg}(J/\psi)$  and  $\Gamma_{ggg}(\Upsilon)$  and should thus not create problems as long as both quantities can be calculated within perturbative QCD. Since this has been already called into question for the  $\Upsilon$  (see, however, Section 7.4.1), it is even more uncertain for the  $J/\psi$ .

Summarizing we get good agreement in scaling  $B_{\mu\mu}$  within the  $\Upsilon$  system. A scaling to the  $J/\psi$  fails on the 2.3 s.d. level, however. The reason for that cannot be found without more work on both, the experimental and the theoretical side. (A successful attempt to include  $v^2/c^2$  corrections in a linear parametrization (i.e. without an explicit calculation) has been performed in Ref. [125]. It is, however, based on an older value of  $B_{\mu\mu}(\Upsilon(1S)) = (2.8 \pm 0.2)\%$  which somewhat reduces the discrepancy between the  $\Upsilon$  and the  $J/\psi$ .)

## 7.2 The Leptonic Widths of $\Upsilon(1S)$ and $\Upsilon(2S)$

### 7.2.1 Measurement of $\Gamma_{\mu\mu}(1S)$

In Section 6.3.1 we have measured the quantity  $\hat{A} = \Gamma_{\mu\mu}\Gamma_{ee}/\Gamma$  from fitting the energy dependence of the cross-section for  $\sigma^{e^+e^- \rightarrow \Upsilon \rightarrow \mu\mu}$  resulting in

$$\hat{A}(1S) = (31.2 \pm 2.3) \text{ eV}, \quad (7.7)$$

$$\hat{A}(2S) = (6.5 \pm 1.8) \text{ eV}. \quad (7.8)$$

where we have now added the errors in quadrature. This are the first direct measurements of these quantities from such a fit. Since

$$\hat{A} = \Gamma_{\mu\mu}B_{ee} = B_{\mu\mu}\Gamma_{ee} \quad (7.9)$$

we can compare our measurements with the product of the world averages for  $\Gamma_{ee}$  [22] and  $B_{\mu\mu}$  (Eqs. (7.3) and (7.4)). This product yields

$$\hat{A}(1S) = (33.8 \pm 1.4) \text{ eV}, \quad (7.10)$$

$$\hat{A}(2S) = (7.6 \pm 1.3) \text{ eV}. \quad (7.11)$$

in good agreement with our results.

By inserting  $B_{ee}$ ,  $B_{\mu\mu}$ , or  $\Gamma_{ee}$  in Eq. (7.9) we can determine in principle  $\Gamma_{\mu\mu}$ ,  $\Gamma_{ee}$ , or  $B_{\mu\mu}$  from our measurement of  $\hat{A}$ . However, by writing  $\Gamma_{ee} = \hat{A}/B_{\mu\mu}$  and inserting our  $B_{\mu\mu}$  measurement we would essentially calculate  $(N^{\Upsilon \rightarrow \mu\mu}/\mathcal{L})/(N^{\Upsilon \rightarrow \mu\mu}/N^{\Upsilon \rightarrow \text{had}}) = N^{\Upsilon \rightarrow \text{had}}/\mathcal{L}$ . Hence, this way of measuring  $\Gamma_{ee}$  would be exclusively based on the hadronic cross-section  $\sigma^{\Upsilon \rightarrow \text{had}}$ , whereas the number of  $\mu$ -pairs together with its errors would drop out. It would just repeat the  $\Gamma_{ee}$  determination from  $\sigma^{\Upsilon \rightarrow \text{had}}$ , which has been already published by the Crystal Ball Experiment [96].

Likewise, calculating  $B_{\mu\mu} = \hat{A}/\Gamma_{ee}$  and inserting the world average values for  $\Gamma_{ee}$  would yield no new information. Comparing this method to our determination of  $B_{\mu\mu}$  in Section 6.2.2 we notice that most of the errors are completely correlated. Those errors exclusively entering the above method ( $\Delta w$ ,  $\Delta\mathcal{L}$ ,  $\Delta\Gamma_{ee}$ ) are more than a factor of 2.5 larger than the errors ( $\Delta N^{\Upsilon \rightarrow \text{had}}$ ,  $\Delta\epsilon^{\Upsilon \rightarrow \text{all}}$ ) which are bound to the  $B_{\mu\mu}$  determination in Section 6.2.2. Averaging the results from both methods would therefore not reduce the overall error on  $B_{\mu\mu}$ , and not even perceptibly change the values of Eq. (6.6). We have checked, that both methods agree within their uncorrelated errors.

By dividing our measured  $\hat{A}(1S)$  by  $B_{ee}(1S)$ , however, we measure for the first time the muonic width of the  $\Upsilon(1S)$  from a fit to the muonic resonance cross-section. We obtain

$$\Gamma_{\mu\mu}(1S) = (1.24 \pm 0.06 \pm 0.11) \text{ keV}, \quad (7.12)$$

where the systematic error is dominated by the error on  $B_{ee}(1S) = (2.52 \pm 0.17)\%$  [22]. It is important to note that  $B_{ee}(1S)$  has been measured independently from  $B_{\mu\mu}(1S)$ . If this were not the case, we would obtain a mixture of  $\Gamma_{\mu\mu}$  and  $\Gamma_{ee}$ , since  $\hat{A}/B_{\mu\mu} = \Gamma_{ee}$ . For the  $\Upsilon(2S)$  we cannot derive  $\Gamma_{\mu\mu}$  from our analysis, since  $B_{ee}(2S)$  has not yet been measured (cf. footnote 3 on page 116).

Our result for  $\Gamma_{\mu\mu}(1S)$  is in good agreement with

$$\Gamma_{\mu\mu}(1S) = \Gamma_{ee}(1S)B_{\mu\mu}(1S)/B_{ee}(1S) = 1.34 \pm 0.11 \text{ keV}. \quad (7.13)$$

calculated from the current world averages of each quantity. It is independent from  $\Gamma_{ee}(1S)$  and  $B_{\mu\mu}(1S)$ , however. We also note that the error on  $\Gamma_{\mu\mu}(1S)$  in Eq. (7.13), which is deduced from averaging many experiments, is only marginally smaller than the error of our single measurement.

## 7.2.2 The New World Averages of $\Gamma_{\ell\ell}$

Our arguments from Section 6.3.1, showing that our measurement of  $\hat{A}$  is essentially independent from the assumption of lepton universality, are also valid for our measurement of  $\Gamma_{\mu\mu}(1S) = (1.24 \pm 0.12) \text{ keV}$ , since it has been directly deduced from  $\hat{A}(1S)$ . A comparison with the world average of  $\Gamma_{ee}(1S) = (1.34 \pm 0.04) \text{ keV}$  [22] therefore represents a successful test of lepton universality.

Assuming lepton universality on the other hand, we can combine both values to a leptonic width of

$$\Gamma_{\ell\ell}(1S) = (1.33 \pm 0.04) \text{ keV}. \quad (7.14)$$

For the  $\Upsilon(2S)$  only  $\Gamma_{ee}=(0.586\pm 0.029)$  keV [22] is known, which has been obtained from measurements of  $\Gamma_{ee} \cdot B_{\text{had}}$ , where  $B_{\text{had}} \equiv (1 - 3B_{\mu\mu})$ . We update this value with the new world average for  $B_{\mu\mu}(2S)$  from Eq. (7.4) yielding

$$\Gamma_{ee}(2S) = (0.584 \pm 0.028) \text{ keV}. \quad (7.15)$$

### 7.3 The Total Widths of $\Upsilon(1S)$ and $\Upsilon(2S)$

Combining all new averages of leptonic widths and branching ratios from above we determine the total widths of the  $\Upsilon$  resonances as

$$\Gamma(1S) = \frac{\Gamma_{\ell\ell}(1S)}{B_{\ell\ell}(1S)} = (52.5 \pm 1.9) \text{ keV} \quad \text{and} \quad (7.16)$$

$$\Gamma(2S) = \frac{\Gamma_{ee}(2S)}{B_{\mu\mu}(2S)} = (45.0 \pm 7.5) \text{ keV}. \quad (7.17)$$

The widths correspond to a mean lifetime of about  $1.3 \times 10^{-20}$  s. Both calculations assume lepton universality. The total width of the  $\Upsilon(1S)$  can also be calculated separately from the  $ee$  and  $\mu\mu$  channels yielding

$$\Gamma(1S) = \frac{\Gamma_{ee}(1S)}{B_{ee}(1S)} = (53.2 \pm 3.9) \text{ keV} \quad \text{and} \quad (7.18)$$

$$\Gamma(1S) = \frac{\Gamma_{\mu\mu}(1S)}{B_{\mu\mu}(1S)} = (49.2 \pm 5.0) \text{ keV}. \quad (7.19)$$

They are in good agreement with each other.

The total widths of the  $\Upsilon$  resonances are the basis for deriving partial decay widths other than  $\Gamma_{\ell\ell}$  from the measured branching ratios. Partial decay widths are in turn the only quantities which can be predicted by theory. A precise knowledge of  $\Gamma$  for the  $\Upsilon$  states is thus essential for a comparison of theory and experiment.

### 7.4 The Determination of $\alpha_s$ and $\Lambda$

We have already shown in Eq. (2.70) in Section 2.2.3 that the ratio

$$\begin{aligned} P_1^{\overline{\text{MS}},\mu}(\Upsilon \rightarrow \mu^+ \mu^-) &= F \frac{\Gamma_{\text{ggg}}}{\Gamma_{\mu\mu}} \\ &= \left( \frac{\alpha_s^{\overline{\text{MS}}}(\mu)}{\pi} \right)^3 \left[ 1 + \frac{\alpha_s^{\overline{\text{MS}}}(\mu)}{\pi} \left( (2.78 - \frac{3}{2} \ln \frac{m_\Upsilon}{\mu}) \beta_0 - 14.1 \right) \right], \end{aligned} \quad (7.20)$$

where

$$F \equiv \frac{9\alpha_{em}^2(m_\Upsilon)}{10\pi^2(\pi^2 - 9)} = 6.01 \times 10^{-6} \quad \text{for } \alpha_s^{-1}(m_\Upsilon) = 132.1 \text{ (see Table 2.6)}. \quad (7.21)$$

has the standard form of a perturbative expansion in  $\alpha_s$ . From measuring  $\Gamma_{\text{ggg}}/\Gamma_{\mu\mu} = B_{\text{ggg}}/B_{\mu\mu}$  and inserting the result in Eq. (7.20) we can therefore derive a value of the strong coupling constant  $\alpha_s^{\overline{\text{MS}}}$  or, alternatively, for the QCD scale parameter  $\Lambda^{\overline{\text{MS}}}$ , which is connected to  $\alpha_s^{\overline{\text{MS}}}$  via Eqs. (2.36) or (2.38). The evaluation of  $\alpha_s^{\overline{\text{MS}}}$  is performed at the (arbitrary) renormalization scale  $\mu$ . In Eqs. (2.51) and (2.52) we have shown that in next-to-leading order in

$\alpha_s$ , all dependences on the renormalization scheme  $\text{RS}=(\text{RC},\mu)$  can be absorbed in the dependence on  $\mu$ . Without restricting the general validity we can thus limit our discussion on the study of the  $\mu$ -dependence in a single renormalization convention (RC). For convenience we choose the  $\overline{\text{MS}}$  convention.

Since  $\mu$  is in principle a completely arbitrary scale parameter without any physical meaning (beside the fact that we calculate  $\alpha_s$  at this scale  $\mu$ ), our result should not depend on  $\mu$  at all. This means that  $\alpha_s$  runs with  $\mu$  as expected from the 1-loop level Equation (2.44), respectively from corresponding equations in higher loop orders. Equivalently, the parameter  $\Lambda$ , calculated from  $\alpha_s(\mu)$  following e.g. the 2-loop level Equation (2.36), should be a constant for a given number  $n_F$  of accessible flavors, and should thus not depend on  $\mu$ . Because the latter can be checked more easily, it is more convenient to plot  $\Lambda$  versus  $\mu$  than to plot  $\alpha_s(\mu)$ . Clearly, since the calculation of the perturbative expansion stops at finite order, we will not find  $\Lambda$  being constant, but (artificially) depending on  $\mu$ .

The basic problem is therefore, how to select a “sensible” (range of)  $\mu$ -value(s), where  $\Lambda$  is to be calculated. We have discussed this question already in some detail in Section (2.2.2). There we have also indicated that for the ratio  $B_{\text{ggg}}/B_{\mu\mu}$  the dependence of  $\Lambda$  on  $\mu$  is dramatic. We will now discuss the scale dependence of the  $\alpha_s$  determination from  $B_{\text{ggg}}/B_{\mu\mu}$  in more detail.

We base our discussion on the value

$$\begin{aligned} P^{\text{CB}}(\Upsilon(1\text{S}) \rightarrow \mu^+ \mu^-) &\equiv F \frac{B_{\text{ggg}}}{B_{\mu\mu}}(1\text{S}) \\ &= 6.01 \times 10^{-6} \cdot (35.9 \pm 3.0) = (2.16 \pm 0.18) \times 10^{-4}, \end{aligned} \quad (7.22)$$

which has been derived from our Crystal Ball (CB) measurement of  $B_{\mu\mu}(1\text{S})$  in Eq. (7.1) via (cf. Table 7.2)

$$\frac{B_{\text{ggg}}}{B_{\mu\mu}} = \frac{B_{\text{anni}}}{B_{\mu\mu}} - (n_U + R) - \frac{B_{\gamma\text{gg}}}{B_{\mu\mu}}. \quad (7.23)$$

Analogous studies can be based on our  $\Upsilon(2\text{S})$  value of

$$P^{\text{CB}}(\Upsilon(2\text{S}) \rightarrow \mu^+ \mu^-) = F \cdot (37.8 \pm 12.7) = (2.27 \pm 0.76) \times 10^{-4}, \quad (7.24)$$

or on values derived from the respective world averages (WA) of  $B_{\mu\mu}(1\text{S})$  and  $B_{\mu\mu}(2\text{S})$ . These are

$$P^{\text{WA}}(\Upsilon(1\text{S}) \rightarrow \mu^+ \mu^-) = F \cdot (32.3 \pm 1.1) = (1.94 \pm 0.07) \times 10^{-4} \quad (7.25)$$

and

$$P^{\text{WA}}(\Upsilon(2\text{S}) \rightarrow \mu^+ \mu^-) = F \cdot (35.0 \pm 7.0) = (2.10 \pm 0.42) \times 10^{-4}. \quad (7.26)$$

### 7.4.1 Study of the Renormalization Scheme Dependence

In Fig. 7.2 we have plotted the solution for  $\Lambda_4^{\overline{\text{MS}}}$  versus the scale  $\mu$  obtained from inserting  $P^{\text{CB}}(\Upsilon(1\text{S}) \rightarrow \mu^+ \mu^-)$  into Eq. (7.20) and solving the resulting equation for  $\alpha_s^{\overline{\text{MS}}}(\mu)$ . The QCD scale parameter  $\Lambda_4^{\overline{\text{MS}}}$  is extracted from  $\alpha_s^{\overline{\text{MS}}}(\mu)$  according to Eq. (2.36). Actually, the  $\overline{\text{MS}}$  convention for  $n_F$  would require us to use  $n_F=5$  for  $\mu > m_b \sim 4.8$  GeV (cf. page 17). The exact procedure to derive  $\Lambda_4^{\overline{\text{MS}}}$  for  $\mu > m_b$  would therefore be to replace in Eq. (7.20)  $\beta_0(n_F=4)$  by  $\beta_0(n_F=5)$  and  $-14.1$  by  $-14.1 + \frac{2}{3}(5-4)(2.78 - \frac{3}{2}\ln(m_\Upsilon/m_b)) = -12.9$ , so that the expression is unchanged at  $\mu=m_b$ . We then could derive  $\Lambda_5^{\overline{\text{MS}}}$  analogously to above and could afterwards convert it into  $\Lambda_4^{\overline{\text{MS}}}$  according to Ref. [38]. The resulting values for  $\Lambda_4^{\overline{\text{MS}}}$  would be lower by only about 10 MeV at  $\mu=10$  GeV, and by about 30 MeV at  $\mu=20$  GeV.



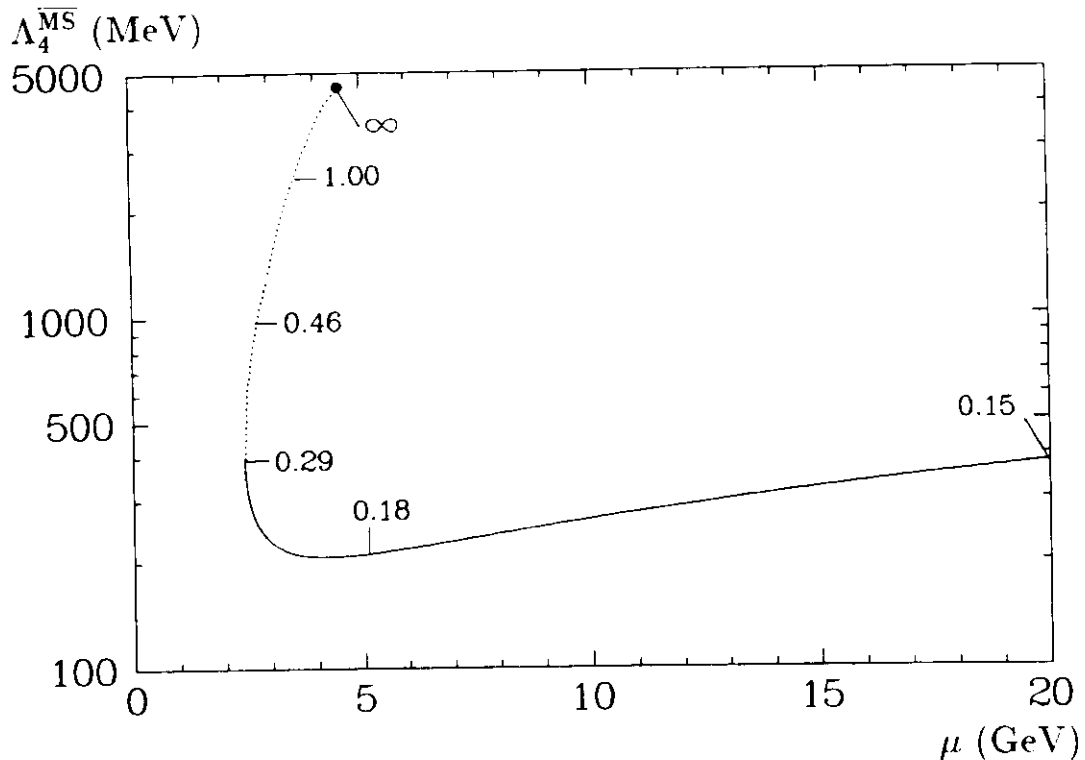


Figure 7.2: Solution for  $\Lambda_4^{\overline{\text{MS}}}$  versus renormalization scale  $\mu$  obtained from our measurement of  $B_{\mu\mu}(1S)$ . The dotted line gives the second solution below  $\mu=4.6$  GeV. Also indicated are some values for  $\alpha_s(\mu)$  along the curve.

These differences are small compared to the overall theoretical uncertainty on  $\Lambda$  (see below). We thus ignore all corrections from b-quark loops in the following by utilizing Eq. (7.20), which is strictly valid only for  $\mu \ll m_b$ , also for larger values of  $\mu$ .

In Fig. 7.2 we find below  $\mu = \mu_{\text{FAC}}^{\overline{\text{MS}}} = 4.6$  GeV no unique solution for  $\Lambda_4^{\overline{\text{MS}}}$ . This is remarkable, but perhaps tolerable, since it is clear from Fig. 7.2 that the smaller of both solutions for  $\Lambda^{\overline{\text{MS}}}$  should be taken in the range  $2.4 \text{ GeV} < \mu < 4.6$  GeV. The larger solution generally corresponds to values of  $\alpha_s$ , which are much too large to insert them in a perturbative QCD expression. More disturbing for some authors [45,32] was the fact that there is no solution at all below  $\mu = 2.4$  GeV. Since choosing the scale at  $\mu = 1.5$  GeV is recommended by the renormalization schemes  $(\overline{\text{MS}}, \mu_{\text{AVP}})$  and  $(\text{MOM}(3g), \mu_{\text{NAT}}^{3g})$  (cf. Section 2.2.3), this has cast doubt on the reliability of calculating  $\alpha_s$  and  $\Lambda$  from the next-to-leading order expression of  $\Gamma_{\text{ggg}}/\Gamma_{\mu\mu}$ .

However, it pays to study more closely the origin of the strong scale dependence. For that we rewrite Eq. (7.20) as

$$P_1^{\overline{\text{MS}},\mu}(\Upsilon \rightarrow \mu^+ \mu^-) = \left( \frac{\alpha_s^{\overline{\text{MS}}}(\mu)}{\pi} \right)^3 \left[ 1 - \frac{\alpha_s^{\overline{\text{MS}}}(\mu)}{\pi} \frac{3}{2} \beta_0 \ln \frac{\mu_{\text{FAC}}^{\overline{\text{MS}}}}{\mu} \right]. \quad (7.27)$$

where  $\mu_{\text{FAC}}^{\overline{\text{MS}}}$  is that scale where the first order correction vanishes (cf. Section 2.2.3). For  $0.15 \leq \alpha_s^{\overline{\text{MS}}} \leq 0.25$  the factor in front of the logarithm ranges from 0.60 to 1.00. This large coefficient is the origin of the strong scale dependence. If we want to assure that the first order correction is clearly smaller than the lowest order, we can vary  $\mu$  only in a small range around  $\mu_{\text{FAC}}^{\overline{\text{MS}}}$ . Since  $\mu$ , on the other hand, is in principle arbitrary, this creates an inconsistent situation.

In Eqs. (2.44)–(2.47) we have shown that the term

$$p\nu \equiv \frac{\alpha_s(\mu')}{\pi} p \frac{\beta_0}{2} \ln\left(\frac{\mu}{\mu'}\right) \quad (7.28)$$

in Eqs. (7.20) and (7.27) originates from the running of  $\alpha_s$  with  $\mu$ . The factor  $p=3$  is the power of  $\alpha_s$  in the lowest order process. This, however, means that the strong scale dependence of the ratio  $\Gamma_{\text{ggg}}/\Gamma_{\mu\mu}$  is not connected to any details of higher order corrections, specific for  $\Gamma_{\text{ggg}}$ . It merely emerges from the fact that the leading order of  $\Gamma_{\text{ggg}}/\Gamma_{\mu\mu}$  is  $p=3$ ! In fact, any other process  $\propto \alpha_s^3$  would have the same problem, since any process of that kind can be written in the form of Eq. (7.27). The only process dependent quantity is  $\mu_{\text{FAC}}^{\overline{\text{MS}}}$ .

This clearly reveals, why processes  $\propto \alpha_s^1$ , like  $\Gamma_{\text{ggg}}/\Gamma_{\gamma\text{gg}}$ , are much less sensitive to the choice of scale. To create the same change in the first order coefficient that is created for  $\Gamma_{\text{ggg}}/\Gamma_{\mu\mu}$  by going from  $\mu_{\text{FAC}}^{\overline{\text{MS}}}$  to  $\mu_{\text{FAC}}^{\overline{\text{MS}}}/f$ , we have to go to  $\mu_{\text{FAC}}^{\overline{\text{MS}}}/f^3$  for a process  $\propto \alpha_s^1$ . Or, in other words, by slightly varying  $\mu$  in a process  $\propto \alpha_s^3$ , the higher order corrections change rapidly. Explicitly calculating additional higher order corrections for  $\Gamma_{\text{ggg}}$  is a cumbersome task. Instead, one probably has to find a resummation procedure of the leading higher order terms, which has been successfully applied in QED (see for example the exponentiation of the Bremsstrahlung spectrum in Section 2.3.2).

In the following we will show, what *might* happen if we include higher order terms in  $\Gamma_{\text{ggg}}/\Gamma_{\mu\mu}$ . For that we rewrite Eq. (7.27) as

$$P_1^{\overline{\text{MS}},\mu}(\Upsilon \rightarrow \mu^+ \mu^-) = \left( \frac{\alpha_s^{\overline{\text{MS}}}(\mu)}{\pi} \right)^3 \left[ 1 + \frac{\alpha_s^{\overline{\text{MS}}}(\mu)}{\pi} \frac{3}{2} \beta_0 \ln \frac{\mu_{\text{FAC}}^{\overline{\text{MS}}}}{\mu} \right]^{-1}. \quad (7.29)$$

This expression is equivalent to Eq. (7.27) up to next-to-leading order in  $\alpha_s$ . On the first view it even looks physically better motivated, since it contains the correct scaling of  $\alpha_s$ , according to Eq. (2.44). From that equation we see that originally the term  $1 + p\nu$  was in the denominator. The deeper reason for that is the resummation of higher orders in the gluon propagator (Eq. (2.25)) analogously to the QED photon propagator (Eq. (2.17)).

However, this statement bases on the fact that we started out at  $\mu = \mu_{\text{FAC}}^{\overline{\text{MS}}}$ . If we had started at  $\mu = m_\Upsilon$  the above expression would be equivalent to writing the complete first order correction  $[1 + (\alpha_s/\pi)(\dots)]$  from Eq. (7.20) into the denominator. This would imply assumptions on the resummation of higher order corrections to  $\Gamma_{\text{ggg}}/\Gamma_{\mu\mu}$  which cannot be justified. Actually, we do know from the Renormalization Group Equation (2.32) and from its solution (2.35) and (2.36) that the term  $1 + (\alpha_s/\pi)(\beta_0/2)\ln(\mu/\mu')$  *must* go into the denominator if all higher orders are included, but we do not know about all the other terms which then appear in addition. In this sense the “inverted” Equation (7.29) can merely serve as an illustration what might happen by including higher orders.

Looking more closely at the inverted Equation (7.29) it is evident that the problem of a  $\mu$ -range without a solution for  $\Lambda$  will not appear, since the first order correction for small  $\mu$  is positive. In contrast to that, the term in brackets in our original Equation (7.27) becomes negative below  $\mu = 2.4$  GeV. In addition, we expect that the inverted expression is less sensitive to the scale  $\mu$ , since we have approximated the running of  $\alpha_s^3$ , which reads with  $\nu$  from Eq. (7.28)

$$\alpha_s^3(\mu) = \frac{\alpha_s^3(\mu')}{(1 - \nu)^3} = \frac{\alpha_s^3(\mu')}{1 + 3\nu + 3\nu^2 + \nu^3} = \alpha_s^3(\mu')(1 - 3\nu + 6\nu^2 - 10\nu^3 + \dots) \quad (7.30)$$

by

$$\alpha_s^3(\mu) = \frac{\alpha_s^3(\mu')}{1 + 3\nu}. \quad (7.31)$$

In the original expression the approximation is

$$\alpha_s^3(\mu) = \alpha_s^3(\mu')(1 - 3\nu), \quad (7.32)$$

which neglects higher order terms with larger coefficients.

This is confirmed by Fig. 7.3, where the solutions from the original Equation (7.27) (solid) and from the inverted Equation (7.29) (dashed) are plotted versus the scale  $\mu$ . Also indicated is the range of variation due to the experimental error on  $\Gamma_{ggg}/\Gamma_{\mu\mu}$ . The dashed solution is defined everywhere and reveals a weaker dependence on  $\mu$ . However, we also notice that the range of  $\mu$  values covered by the dashed curves is partially not contained in the range of solutions for the solid line. (Values of  $\Lambda \sim 180$  MeV are not covered there.) This means that the variation of  $\Lambda$  with  $\mu$  is not the whole story. Higher order corrections (like those effectively included in the dashed lines) may still extend the range of possible solutions for  $\Lambda$  perceptibly.

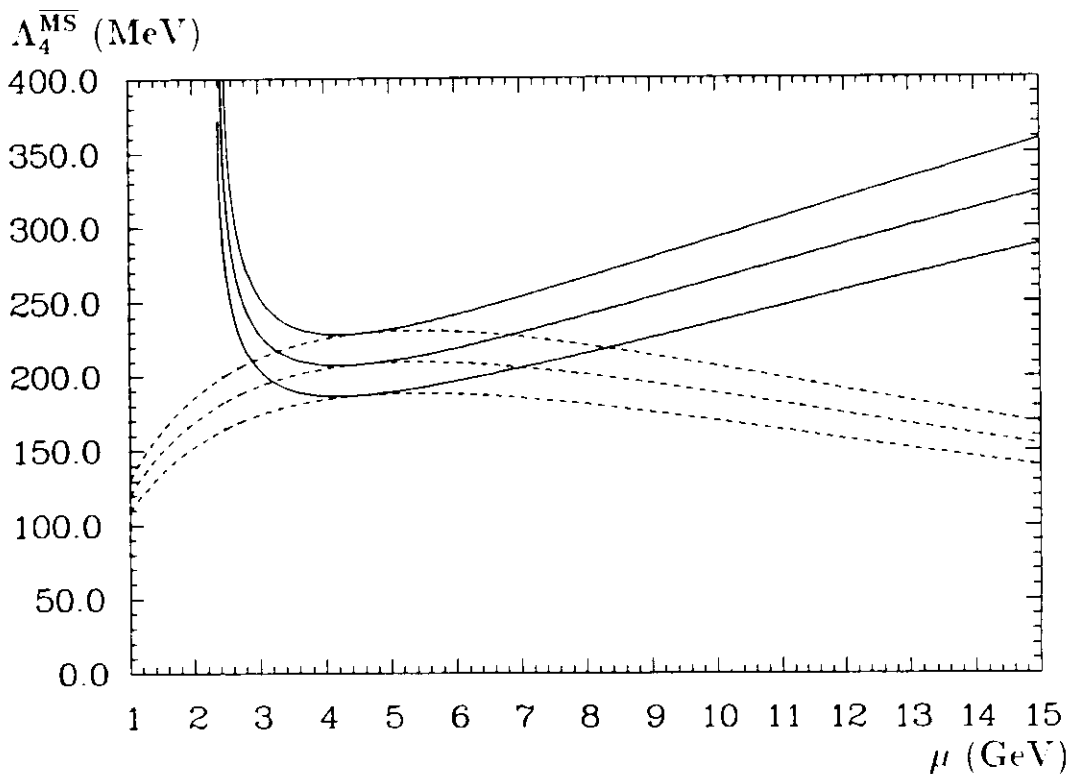


Figure 7.3: Solution for  $\Lambda_4^{\overline{MS}}$  versus renormalization scale  $\mu$  obtained from our measurement of  $B_{\mu\mu}(1S)$ . The solid lines are from the original expression for  $P(Y \rightarrow \mu^-\mu^-)$ , whereas the dashed lines are an illustrative example for the possible effects of higher order corrections. The bands indicate the experimental error on  $P$ . The second solution of the original expression below  $\mu = 4.6$  GeV is not shown.

This is, strictly spoken, true for every perturbative expression truncated at finite order. Even if the  $\mu$ -dependence of  $\Lambda$  is marginal, as e.g. for the ratio  $B_{ggg}/B_{\gamma gg}$  (see Fig. 2.6 and Ref. 122) which is linear in  $\alpha_s$ , one can in principle not be sure that higher order corrections do not change this picture. The true reason behind all this is clearly that  $\alpha_s$  is a relatively large quantity in the GeV range.

What can we learn from that? How can we test QCD as a theory for strong interactions if there are such severe ambiguities in comparing theoretical results with experimental measurements? The answer is: *Not from one process alone.* Each process, like  $\Gamma_{ggg}/\Gamma_{\mu\mu}$ ,  $\Gamma_{ggg}/\Gamma_{\gamma gg}$

— or, better, completely independent quantities, as discussed in the next section — delivers a solution for  $\Lambda_4^{\overline{\text{MS}}}$ . The theoretical error on  $\Lambda_4^{\overline{\text{MS}}}$  from a single process can basically not be quantified since the optimal choice for  $\mu$  is unknown in finite order of perturbation theory. All refined “guessworks” of choosing the optimal scale  $\mu_{\text{opt}}$  for a given process, which have been discussed in Section 2.2.3, can not exclude that there are large higher order corrections at their favorite scale  $\mu_{\text{opt}}$ .

The only way out is to calculate  $\Lambda_4^{\overline{\text{MS}}}$  from many independent processes allowing  $\mu$  to vary in a sensible range (see Eqs. (2.58) and (2.59)). If the resulting values of  $\Lambda_4^{\overline{\text{MS}}}$  cluster around a certain value this would mean a successful test of QCD. If *few* results for  $\Lambda_4^{\overline{\text{MS}}}$  significantly deviate from this “mean value”, it might be an indication for large higher order corrections in those special processes at the chosen scale  $\mu$ .

In this sense the determination of  $\alpha_s$  and  $\Lambda$  from the ratio  $\Gamma_{\text{ggg}}/\Gamma_{\mu\mu}$  is as appropriate as from any other process. There are no indications that this measurement leads to questionable values of the free QCD parameter. The only difference to other processes is that the sensible range of  $\mu$  values is somewhat smaller because of the power  $p=3$  in leading order. In the following we determine  $\Lambda_4^{\overline{\text{MS}}}$  and  $\alpha_s$  from our measurement of  $\Gamma_{\text{ggg}}/\Gamma_{\mu\mu}$  for the  $\Upsilon(1S)$ , and compare it to results from other methods in Section 7.4.2.

From studying Figures 7.2 and 7.3 we select “our” sensible range for choices of  $\mu$  as to be  $5 \text{ GeV} \lesssim \mu \lesssim 15 \text{ GeV}$ . The fact that there is no unique solution below  $\mu = \mu_{\text{FAC}}^{\overline{\text{MS}}} = 4.6 \text{ GeV}$  prevents us to use lower values for  $\mu$ . To “compensate” this restriction, we allow  $\mu$  to go as high as  $15 \text{ GeV}$  (corresponding to a MOM(3g) scale of  $2.16 \times 15 \text{ GeV} = 32 \text{ GeV}$ ). We determine our central value for  $\Lambda_4^{\overline{\text{MS}}}$  at  $5 \text{ GeV}$ , where the solid and dashed lines coincide, and estimate the theoretical error by the difference to the solutions of solid and dashed lines at  $\mu = 15 \text{ GeV}$ . We note that this range covers also the solution of the inverted expression (dashed) at the “famous” scale  $\mu = 1.5 \text{ GeV}$ , where the original expression (solid) failed completely<sup>6</sup>. The experimental error is obtained from the mean width of the 1 s.d. band between  $5 \text{ GeV}$  and  $15 \text{ GeV}$ . From this procedure we get

$$\Lambda_4^{\overline{\text{MS}}} = (210 \pm 25_{-50}^{+120}) \text{ MeV} = (210_{-75}^{+145}) \text{ MeV}, \quad (7.33)$$

where the first error is experimental and the second is theoretical. Their combined error is obtained from a linear sum, because the theoretical error surely does not follow a Gaussian distribution. This result corresponds to a value of the strong coupling constant of

$$\alpha_s^{\overline{\text{MS}}}(5 \text{ GeV}) = 0.184 \pm 0.006_{-0.013}^{+0.027} = 0.184_{-0.019}^{+0.033}. \quad (7.34)$$

It compares well with the value  $\alpha_s^{\overline{\text{MS}}}(5 \text{ GeV}) = 0.19 \pm 0.03$  (cf. Table 2.4) derived in Ref. [22]. (In principle we could have evaluated  $\alpha_s$  at any scale  $\mu$  from Eq. (7.33) and Eqs. (2.36) or (2.38). The scale of  $5 \text{ GeV}$  was chosen just because the central value of  $\Lambda$  was determined at this scale.)

We also calculate  $\Lambda_4^{\overline{\text{MS}}}$  from our measurement of  $B_{\mu\mu}(2S)$ . In this case the experimental error is still large. From Eq. (7.24) and an analogous procedure we obtain

$$\Lambda_4^{\overline{\text{MS}}} = (235 \pm 110_{-50}^{+120}) \text{ MeV} = (235_{-160}^{+230}) \text{ MeV}. \quad (7.35)$$

<sup>6</sup>Always keeping in mind that the inverted expression is sort of artificial.

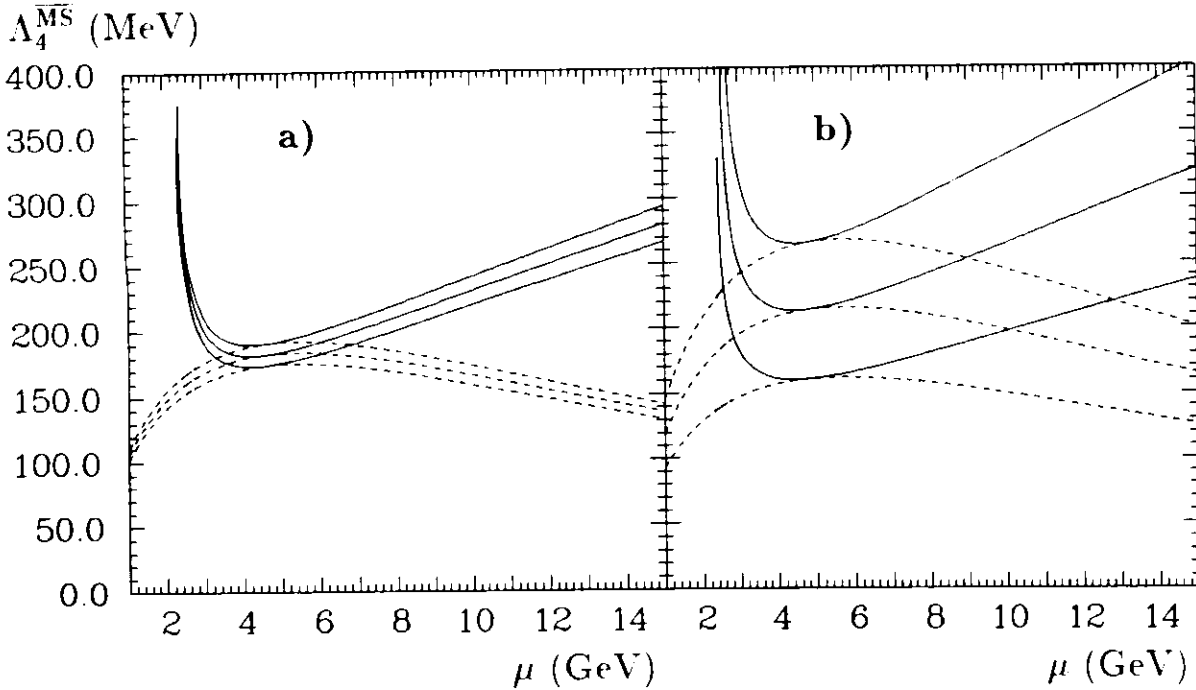


Figure 7.4: Solution for  $\Lambda_4^{\overline{\text{MS}}}$  versus renormalization scale  $\mu$  obtained from the world average values of  $B_{\mu\mu}(1S)$  (a) and  $B_{\mu\mu}(2S)$  (b). For a description of the curves see Fig. 7.3.

For completeness we list the results for  $\Lambda_4^{\overline{\text{MS}}}$  derived from the world averages of  $B_{\text{ggg}}/B_{\mu\mu}$  of the  $\Upsilon(1S)$  (Fig. 7.4(a)) and of the  $\Upsilon(2S)$  (Fig. 7.4(b)). They have considerably smaller experimental errors and read, utilizing Eq. (7.25) for the  $\Upsilon(1S)$ ,

$$\Lambda_4^{\overline{\text{MS}}} = (185 \pm 10_{-50}^{+120}) \text{ MeV} = (185_{-60}^{+130}) \text{ MeV} \quad (7.36)$$

and, utilizing Eq. (7.26) for the  $\Upsilon(2S)$ ,

$$\Lambda_4^{\overline{\text{MS}}} = (215 \pm 60_{-50}^{+120}) \text{ MeV} = (215_{-110}^{+180}) \text{ MeV}. \quad (7.37)$$

All results agree well within their experimental errors. The experimental errors on  $\Lambda_4^{\overline{\text{MS}}}$  from Eq. (7.36) are by far the smallest of any determination of  $\Lambda^{\overline{\text{MS}}}$  (see next section). Here, the large power  $p=3$  of  $\alpha_s$  in the leading order of  $\Gamma_{\text{ggg}}/\Gamma_{\mu\mu}$  is a clear advantage.

## 7.4.2 Comparison to Results for $\Lambda$ from Other Methods

Basically different methods to determine  $\alpha_s$  or  $\Lambda$  are measurements of the structure functions in deep inelastic lepton-hadron scattering (DIS), of the photon structure function  $F_2$  in  $\gamma-\gamma$ ,  $\gamma-q$ , or  $\gamma-g$  collisions, of the ratio  $R(s)$  in  $e^+e^-$  annihilation and of the rate of 2-, 3-, or 4-jet events in  $e^+e^-$  collisions via energy-energy correlations (EEC) or via other tools of jet identification. A discussion of all these methods leads beyond the scope of this work. A concise review with a comprehensive list of references can be found in the Review of Particle Properties [22]. In Fig. 7.5 we compare our result on  $\Lambda_4^{\overline{\text{MS}}}$  from the ratio  $B_{\text{ggg}}/B_{\mu\mu}$  of the  $\Upsilon(1S)$  (Eq. (7.33)) to values obtained from the other methods as collected in Ref. [22]. The two errors given in Ref. [22] are added in quadrature. We also list a result of  $\Lambda_4^{\overline{\text{MS}}} = (150 \pm 90) \text{ MeV}$  obtained recently by the Crystal Ball collaboration [122] from the ratio  $B_\gamma \equiv B_{\text{ggg}}/B_{\gamma\text{gg}}$ . Its error does not include scale dependences or uncertainties of higher order QCD corrections.

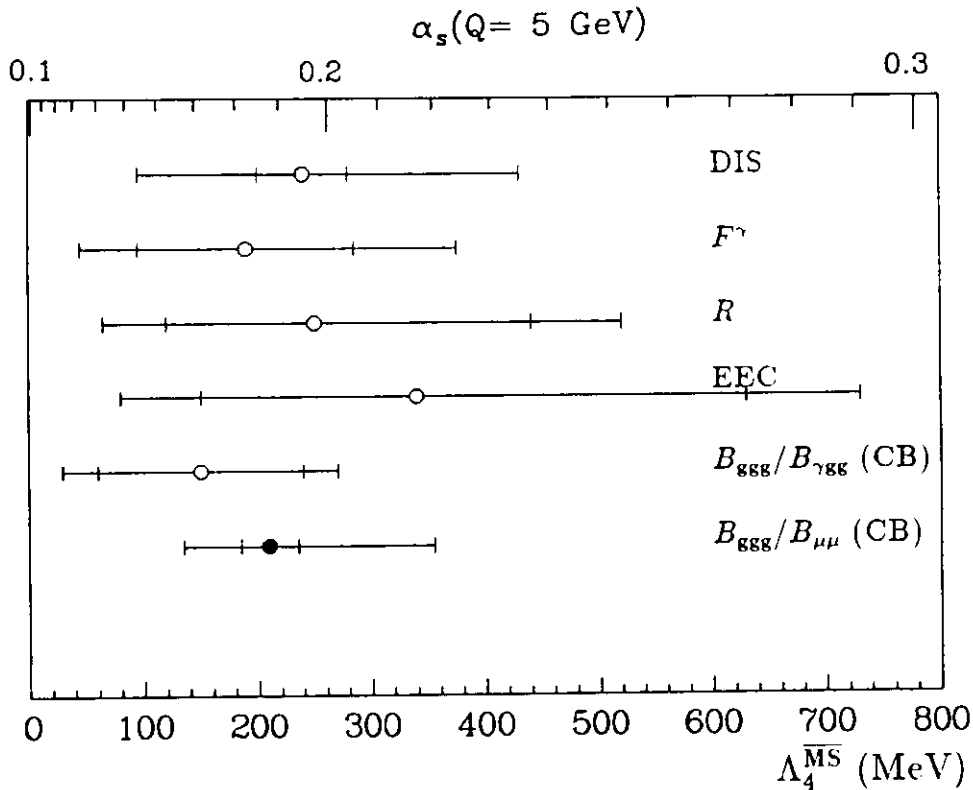


Figure 7.5: Solution for  $\Lambda_4^{\overline{\text{MS}}}$  from different methods as explained in the text. The larger error bars indicate estimates for additional uncertainties from scale ambiguities or higher order QCD corrections. For convenience, the top scale gives the value of  $\alpha_s^{\overline{\text{MS}}}(5 \text{ GeV})$  corresponding to the values of  $\Lambda_4^{\overline{\text{MS}}}$  at the bottom.

We linearly add an error of 30 MeV, estimated from the scale dependence of the dashed line in Fig. 2.6.

All determinations of  $\Lambda_4^{\overline{\text{MS}}}$  compare favorably among each other. They are all within one standard deviation consistent with a value of  $\Lambda_4^{\overline{\text{MS}}}$  between 135 MeV and 270 MeV (corresponding to  $\Lambda_5^{\overline{\text{MS}}}$  in the range from 90 MeV to 180 MeV). In spite of the large uncertainties of each single measurement their agreement is a clear success of perturbative QCD.

Note that for a more precise determination of  $\Lambda_4^{\overline{\text{MS}}}$  it is not enough to reduce the error on only one of these methods<sup>7</sup>. Since for a single quantity the higher order corrections are in principle unknown, one always needs a bunch of methods agreeing with each other within comparably small errors. Because the theoretical errors are large for most methods collected in Figure 7.5, an overall reduction of all errors is not possible without more work on the theoretical side.

<sup>7</sup>This is possible for  $B_{\text{ggg}}/B_{\gamma\text{gg}}$  by averaging the Crystal Ball measurement with previous results [126] from ARGUS, CLEO, and CUSB. Such an average is not straightforward since all experiments have partially correlated errors, e.g. from the shape of the photon spectrum.

# Chapter 8

## Summary

We were able to extract three types of quantities from studying the  $\mu$ -pair decay of the  $\Upsilon(1S)$  and the  $\Upsilon(2S)$  resonances.

First, the observed number of muon pairs and their cross-section led to measurements of the muonic branching ratio  $B_{\mu\mu}$  and of the product of electronic branching ratio and muonic width  $B_{ee}\Gamma_{\mu\mu}$  for both resonances. From the latter quantity we could deduce  $\Gamma_{\mu\mu}$  for the  $\Upsilon(1S)$  resonance.

Second, we obtained values for the total widths of the  $\Upsilon(1S)$  and the  $\Upsilon(2S)$  resonances from the leptonic widths and branching ratios. These total widths are the basis for converting theoretical predictions for partial widths into measurable branching ratios of the  $\Upsilon$  states.

Third, and most fundamental, we calculated the only free parameter of QCD, its coupling constant  $\alpha_s$ , respectively its scale parameter  $\Lambda$ , from the ratio of the muonic branching fraction and the branching fraction to three gluons.

We summarize the essential ingredients for these measurements below. The observation of a small excess of  $\mu$ -pairs from resonance decays above a large continuum background required a thorough understanding of systematic differences between on-resonance and off-resonance data samples. This triggered considerable effort to improve the Monte Carlo simulation of our data and the reproduction of variations with time. This effort led to distinct improvements in two program packages for the detector simulation, one for the calorimeter, and the other for the tube chambers. The reproduction of muonic energy depositions in the calorimeter was clearly improved by upgrading the simulation of particle interactions in the widely used GHEISHA program package. A bunch of corrections was introduced which should also improve the GHEISHA simulation of other detectors. Besides corrections of energy loss parameters and  $\delta$ -electron production we deduced an expression for the restricted energy loss with an extended range of validity. On the other hand the Crystal Ball tube chamber Monte Carlo was amended by modeling the time dependent behaviour of essentially each single tube.

Other systematic time dependences in the experiment, like length and position of the  $e^+e^-$ -intersection region or the amount of beam-related background signals in the detector had to be monitored to finally reproduce  $\sim 10\%$  changes in the detector acceptance with a precision of less than 0.7%. To calculate this number, more than 20 systematic effects were studied, which potentially influence the acceptance by 0.1% or more.

Another valuable ingredient to our analysis was the DYMU2 program for generating radiative  $\mu$ -pair events. We modified this generator such that it could be used as a efficient and flexible tool for calculating cross-sections and generating events for a variety of "boundary conditions".

In addition we noticed, that a precision measurement of the c.m. energy was mandatory to control effects which are introduced by interference between continuum and resonant  $\mu$ -pair

production. The precise determination of the DORIS beam energy finally enabled us not only to correct for this interference, but to present the first evidence for this interference in the  $\Upsilon$  system. It further opened the possibility to determine for the first time the product of electronic branching ratio and muonic width from a fit to the resonant  $\mu$ -pair cross-sections. Our values for  $B_{\mu\mu}$  are the first measurements, which take this interference into account. They are consistent with previous determinations of  $B_{\mu\mu}$ .

More than 13 years after the discovery of the  $\Upsilon$  system the world average value for  $B_{\mu\mu}(1S)$  has gained a high precision with an error of less than 3%. The leptonic branching ratios of the other narrow  $\Upsilon$  states, however, have somewhat larger errors of 10% ( $\Upsilon(3S)$ ) and 16% ( $\Upsilon(2S)$ ). In fact, our measurement of  $B_{\mu\mu}(2S)$  with a combined statistical and systematic significance of 3.6 standard deviations is up to now only the second measurement with an accuracy of better than two standard deviations. The precision of the  $B_{\mu\mu}(2S)$  and  $B_{\mu\mu}(3S)$  measurements should thus still be considerably improved, e.g. at a future  $\Upsilon/B$ -factory.

We have shown that a (straightforward) scaling of  $B_{\mu\mu}(\Upsilon(1S))$  to the  $J/\psi$  resonance does not result in a branching ratio which is in good agreement with the measurement of  $B_{\mu\mu}(J/\psi)$ . Improving the yet poor experimental precision of  $B_{\mu\mu}(J/\psi)$  together with theoretical work may give information about the source of this deviation. This would be of interest also for the determination of  $\alpha_s$  from  $\Upsilon$  decays, since higher order  $\alpha_s$  and  $v^2/c^2$  corrections to quarkonia decay widths are obvious candidates for causing trouble in the scaling from the  $\Upsilon$  to the  $J/\psi$ .

The determination of the QCD coupling constant  $\alpha_s$ , respectively of its scale parameter  $\Lambda$ , from the ratio  $B_{ggg}/B_{\mu\mu}$  exhibits a strong dependence on the renormalization scale  $\mu$ . We argued that this is not due to details of higher order corrections specific for this ratio. Thus, there is no indication that this ratio leads to questionable results for  $\alpha_s$  and  $\Lambda$ . A comparison to other methods of determining  $\Lambda$  in fact reveals a good agreement among all results. This represents a successful test of Quantum Chromo Dynamics as the theory of strong interaction. The uncertainty of the QCD scale parameter  $\Lambda$ , however, is still considerable. It can only be reduced with more work on the theoretical side, perhaps by a resummation of leading terms in higher orders of the perturbation series.



# Appendix A

## A Verified Upgrade of the GHEISHA Simulation of Particle Interactions

Comparing the GHEISHA 6/7 simulation of particle interactions [90] to experimental and theoretical knowledge, we were able to propose substantial improvements for the GHEISHA code [89], which have been already partially implemented in the recent update GHEISHA 8. Our changes concern the simulation of energy loss of charged particles,  $\delta$ -rays, multiple scattering, negative particle absorption, light quenching in scintillators, and neutron capture. They are supported by comparing the resulting detector simulation to Crystal Ball data. Below we will summarize those fields, which are most important for this analysis, namely the changes in the  $\delta$ -ray and energy loss simulation<sup>1</sup>. More details can be found in Ref. [89].

Due to the momentum dependence of energy loss,  $\delta$ -ray production, and multiple scattering, there are differences in the amount and the lateral pattern of the deposited energy for low and high energy muons. Our studies were triggered by the observation, that the default GHEISHA simulation was not able to reasonably describe these differences (see Figs. A.6 and A.3 below). With the help of our GHEISHA improvements we have been able to reduce that systematic error of our analysis, which is connected with the reproduction of dependences of the detector response on the incident muon energy (cf. Section 5.3.3 on page 95).

### A.1 Changes in the $\delta$ -Ray and Energy Loss Simulation

#### 1. Produce $\delta$ -rays in solids, too.

GHEISHA 7 generates them only in gases and liquids, GHEISHA 6 exclusively in chamber gas. For a finely segmented detector like the Crystal Ball, the lateral energy pattern of charged particles cannot be described without an explicit simulation of  $\delta$ -rays, since these knock-on-electrons may easily extend their electromagnetic showers into the adjacent crystals. The effect of this change is large for 5 GeV muons, which create  $\delta$ -rays up to a maximum electron energy of  $T_e^{max} = 1.4$  GeV, and still perceptible for 500 MeV muons, which have  $T_e^{max} = 25$  MeV (cf. Eq. (A.1)).

#### 2. Subtract the $\delta$ -ray energy from the energy of the tracked particle.

This was simply forgotten in GHEISHA 6/7. However, the energies  $T_e$  of most  $\delta$ -rays are much less than the maximum energy transfer  $T_e^{max}$ , which is in turn smaller than  $T/2$  for incident particles with kinetic energy  $T$ , mass  $m$ , and momentum  $\beta\gamma < m/2m_e$  (cf. Eq. (A.1)). Since one would expect sizable effects only for  $\delta$ -rays with  $T_e \sim T$ ,

---

<sup>1</sup>All formula refer to incident particles other than electrons. We use Gaussian units throughout this chapter, i.e.  $4\pi\epsilon_0 = 1$  so that  $\alpha = e^2/\hbar c$ .

this fix induces only marginal changes to the energy loss distribution of muons in the Crystal Ball.

3. **Use the correct relativistic formula for  $T_e^{max}$ .**

The maximum kinetic energy of knock-on electrons is given by

$$T_e^{max} = \frac{2m_e c^2 \beta^2 \gamma^2}{1 + 2\gamma \frac{m_e}{m} + \left(\frac{m_e}{m}\right)^2}, \quad (\text{A.1})$$

which can be deduced from Eq. (A.6) by setting  $\cos \theta = 1$ . GHEISHA 6/7 uses the approximation

$$T_e^{max} = 2m_e c^2 \beta^2 \gamma^2, \quad (\text{A.2})$$

which is only valid in the limit  $\gamma \ll m/2m_e$ . The correction of the  $T_e^{max}$  formula is very small for low-energy muons. Yet, for  $\beta\gamma = 45$  it reduces  $T_e^{max}$  by 30% from 2.0 GeV to 1.4 GeV. For  $\beta\gamma > m/2m_e$ , e.g. for muons with 11 GeV or more, the GHEISHA formula (A.2) would even violate energy conservation, since then  $T_e^{max} > T$ .

4. **Use the exact  $\delta$ -ray production rate.**

The number  $N_e$  of  $\delta$ -rays produced with energy  $T_e$  in a given thickness  $dx$  is given by [127]

$$\frac{d^2 N_e}{dx dT_e} = D \frac{Q^2}{\beta^2} \frac{1}{T_e^2} \left(1 - \beta^2 \frac{T_e}{T_e^{max}}\right), \quad (\text{A.3})$$

where  $Q$  is the electric charge of the incident particle in units of  $e$  and  $D$  is proportional to the electron density  $n_e$  of the traversed medium according to

$$D = \frac{2\pi e^4}{m_e c^2} n_e = 0.1536 \text{ MeV/cm} \left(\frac{\rho}{\text{g/cm}^3} \frac{Z}{A}\right). \quad (\text{A.4})$$

Here,  $\rho$  is the density and  $Z/A$  is the ratio of the charge to the mass number of the medium.

The production rate of  $\delta$ -rays in GHEISHA is described by

$$\frac{d^2 N_e}{dx dT_e} = D \frac{Q^2}{\beta^2} \frac{1}{T_e^2} \quad \text{for } T_e \leq T_e^{max} \quad (\text{A.5})$$

which misses the factor  $(1 - \beta^2 T_e/T_e^{max})$  compared to Equation (A.3). This has a big influence on the  $\delta$ -ray production rate near  $T_e^{max}$ .

5. **Use the correct relativistic ejection angle.**

The  $\delta$ -ray electrons are ejected under an angle  $\theta$  with respect to the incident particle direction which we obtain from 4-momentum conservation as

$$\begin{aligned} \cos \theta &= \left(1 + \frac{m_e}{\gamma m}\right) \frac{1}{\beta} \sqrt{\frac{T_e}{T_e + 2m_e c^2}} \\ &\approx \frac{1}{\beta} \sqrt{\frac{T_e}{T_e + 2m_e c^2}}. \end{aligned} \quad (\text{A.6})$$

Thus, for non-relativistic particle momenta ( $\beta\gamma \approx \beta \ll 1$ )  $T_e \ll 2m_e c^2$  holds for all  $T_e$ , and we get in the low momentum limit in agreement with the result of Reference [128]

$$\cos \theta = \sqrt{\frac{T_e}{T_e^{max}}}. \quad (\text{A.7})$$

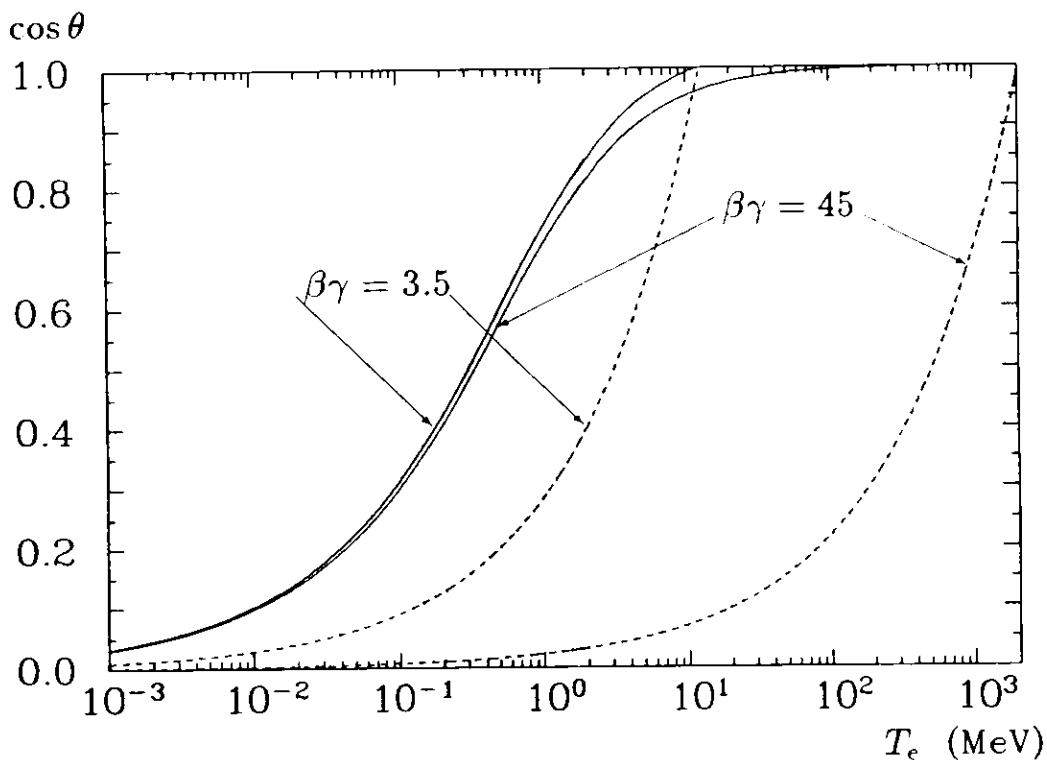


Figure A.1: Theoretical ejection angle for  $\delta$ -rays. The broken lines result from the nonrelativistic approximation (A.7), the solid lines show the prediction of the correct relativistic formula (A.6).

This nonrelativistic limit is used in GHEISHA 6/7.

The application of the correct formula for the  $\delta$ -ray ejection angle is the most important fix of the GHEISHA  $\delta$ -ray simulation. This can be seen from Figure A.1, where  $\cos \theta$  is plotted versus  $T_e$  for both the relativistic (A.6), and the nonrelativistic formula (A.7) indicated by solid and dashed lines, respectively. For a 20 MeV  $\delta$ -ray, one finds e.g. for  $\beta\gamma = 45$  almost orthogonal  $\theta$  values of  $\cos \theta = 0.10$  (nonrelativistic), and  $\cos \theta = 0.98$  (relativistic).

6. **Fluctuate the energy loss below the limit  $T_e^0$  for explicit  $\delta$ -ray generation with a Gaussian distribution.**

Simulating the energy loss in a given detector component, GHEISHA adds up smeared mean energy losses  $\Delta E$  in a couple of steps. The shape of the probability distribution  $p$  for the fluctuations in the single steps does neither depend on the step size, nor on the incident particle momentum, but is fixed to an approximation of the Landau distribution according to

$$p(\Delta E + 0.31\sigma\Lambda)d\Lambda = \frac{0.762}{\sqrt{2\pi}} \exp \left[ -\frac{1}{2} (\Lambda^\alpha + e^{-\Lambda}) \right] d\Lambda \quad (\text{A.8})$$

with  $\alpha = 1$  (0.85) for  $\Lambda < 0$  ( $> 0$ ). The only step size dependence lies in the width parameter  $\sigma$ , which is given by

$$\frac{\sigma}{\Delta E} = \frac{2}{\ln(1 + D\Delta x/7.5 \text{ eV})} \quad (\text{A.9})$$

Since the shape of the energy loss fluctuations of Eq. (A.8) is fixed, the energy loss distribution over a finite length, subdivided in several steps, depends on the number of these steps and not only on the overall length. Covering the whole distance with a single step would result in the Landau distribution of Eq. (A.8). But already for the about 20 steps of a high energy muon tracked through the NaI crystals of the Crystal Ball, GHEISHA cannot generate the proper Landau tail of the energy loss distribution. Instead, the result from summing the single Landau distributions from each step is a Gaussian distribution around the sum of the mean values of the single distributions, as follows from the central limit theorem (see dotted line in Fig. A.6).

In addition, these mean values  $(\Delta E)_{mean} = \Delta E + 0.66\sigma$  are systematically higher than the initial  $\Delta E$ . Thus, the mean value of the energy loss over a finite length composed of several steps comes out too large. GHEISHA 7 tries to avoid this incorrectness by multiplying the smeared  $\Delta E$  with a fixed correction factor `PARMAT(material,1)` for each material. Its default values range from 0.86 to 1.00 for solids, from 0.92 to 0.98 for liquids, and from 0.33 to 0.68 for gases.

Explicitly generating  $\delta$ -rays above a limit  $T_c^\circ$ , as done through our changes (1)–(5), results in a correct simulation of the Landau tail and of its dependence on the incident particle momentum. We even can find a peak correction factor of `PARMAT(NaI,1) = 0.745`, which reproduces the peak positions of low and high energy muons in the Crystal Ball. This result, however, is based on a purely fortuitous coincidence of several parameters in our given case (see below). It depends on the chosen step size as well as on the  $\delta$ -ray threshold  $T_c^\circ$ . Since the GHEISHA step size can vary by more than two orders of magnitude for different materials, different particles, or even for the same particle type at different momenta, it is impossible, to get a satisfactory description of the energy loss for all particles at all momenta with a fixed correction factor `PARMAT(material,1)`. Both unwanted dependences on the step size and on the  $\delta$ -ray threshold are removed by applying our corrected energy loss simulation, as described below.

As we saw, the dependence of the mean energy loss over a finite length on the step size  $\Delta x$ , in which this length is subdivided, is introduced in GHEISHA by an inadequate step size dependence of the distribution of energy loss fluctuations in Eq. (A.8). We correct the step size dependence by choosing Gaussian fluctuations for the energy loss below  $T_c^\circ$  according to

$$p(\Delta E + \sigma\Lambda)d\Lambda = \frac{1}{\sqrt{2\pi}} \exp\left[-\frac{1}{2}\Lambda^2\right] d\Lambda. \quad (\text{A.10})$$

Then the mean value of energy losses below  $T_c^\circ$  in single steps becomes  $(\Delta E)_{mean} = \Delta E$  and depends no longer on the width  $\sigma$ . The larger energy losses get the proper step size dependence via the explicit  $\delta$ -ray simulation. In addition the shape of the energy loss in each step is correct, as long as  $T_c^\circ$  is not much larger than the width  $\sigma$  of the Gaussian. (We have used  $T_c^\circ = \sigma = 2$  MeV for a step size of 2 cm in the NaI crystals.)

## 7. Use a correct formula for the restricted energy loss.

If energy losses above  $T_c^\circ$  are explicitly simulated via  $\delta$ -rays, the remaining mean energy loss  $\Delta E$  restricted to energy transfers below  $T_c^\circ$  in a step  $\Delta x$  is given by [89]

$$\Delta E = D \frac{Q^2}{\beta^2} \Delta x \left[ \ln \left( \frac{2m_e c^2 T_c^\circ}{I^2} \beta^2 \gamma^2 \right) - \beta^2 \left( 1 + \frac{T_c^\circ}{T_c^{max}} \right) - \delta \right], \quad (\text{A.11})$$

where  $I$  is the mean ionization potential of the medium, and  $\delta$  is the density effect correction. It describes the effect of the polarization of the traversed medium, which causes

a saturation of the restricted energy loss for high particle momenta. With the help of the material dependent Sternheimer parameters<sup>2</sup>  $\bar{C}$ ,  $b$ ,  $n$ ,  $Y_0$ , and  $Y_1$  it is expressed as [129]

$$\begin{aligned} \delta &= 0 & \text{for } \beta\gamma &\leq Y_0 \\ \delta &= \ln \beta^2 \gamma^2 - \bar{C} + b \left( \ln \frac{Y_1}{\beta\gamma} \right)^n & \text{for } Y_0 < \beta\gamma < Y_1 \\ \delta &= \ln \beta^2 \gamma^2 - \bar{C} & \text{for } Y_1 \leq \beta\gamma \end{aligned} \quad (\text{A.12})$$

The exponent  $n$  is close to 3 for most materials. The boundary momenta of the transition range between the uncorrected energy loss without density effect and the saturation value are formed by the parameters  $Y_0$  and  $Y_1$ . The boundary condition at  $\beta\gamma = Y_0$  fixes the parameter  $b$  to

$$b = (\bar{C} - \ln Y_0^2) \left( \ln \frac{Y_1}{Y_0} \right)^{-n}. \quad (\text{A.13})$$

Finally, the parameter  $\bar{C}$  is given by the fact, that for very high energies the energy loss no longer depends on the mean ionization potential  $I$  but merely on the electron density  $n_e$  [130], expressed in terms of the electron plasma frequency  $\omega_p$ . The theory yields the following expression for  $\bar{C}$  which cancels the  $I$  dependence of Eq. (A.11) for  $\beta\gamma > Y_1$ ,

$$\bar{C} = 2 \ln \left( \frac{I}{\hbar\omega_p} \right) + 1, \quad (\text{A.14})$$

where  $\hbar\omega_p$  is given by

$$\hbar\omega_p = \left( 2m_e c^2 D a_0 \right)^{\frac{1}{2}} = 28.8 \text{ eV} \left( \frac{\rho}{\text{g/cm}^3} \frac{Z}{A} \right)^{\frac{1}{2}}, \quad (\text{A.15})$$

and  $a_0 = \hbar^2 / e^2 m_e$  is the Bohr radius.

Formula (A.11) is usually cited [22] in the limit  $T_e^\circ \ll T_e^{\text{max}}$  as it was found by Bethe [131]. Compared to the result of Bethe our derivation of the restricted energy loss reveals an additional factor  $(1 + T_e^\circ / T_e^{\text{max}})$ , which extends the validity of Equation (A.11) to all  $T_e^\circ \leq T_e^{\text{max}}$ . The factor reduces for  $T_e^\circ \ll T_e^{\text{max}}$  the calculated value for the restricted energy loss by up to  $\sim 5\%$ . In addition, it creates a smooth continuation of the restricted energy loss into the mean energy loss (Eq. (A.20)) at  $T_e^\circ = T_e^{\text{max}}$ . This is needed for MC simulations of low energetic particles, whose values of  $T_e^{\text{max}}$  are close to the values, which are typically chosen for  $T_e^\circ$ .

The fact, that the GHEISHA energy loss simulation with explicit  $\delta$ -rays described our muons reasonably well, is due to the cancellation of four errors. This can be seen by confronting the GHEISHA energy loss simulation

$$\Delta E = \text{PARAMAT}(\text{mat.}, 1) D \frac{Q^2}{\beta^2} \Delta x \left[ \ln \left( \frac{2m_e c^2 T_e^{\text{max}}}{I^2} \beta^2 \gamma^2 \right) - 2\beta^2 - 2\delta \right], \quad (\text{A.16})$$

with the theoretically correct formula (A.11). The use of  $T_e^{\text{max}} = 2m_e c^2 \beta^2 \gamma^2$  instead of  $T_e^\circ = 2 \text{ MeV}$  together with the doubled density correction  $\delta$  from Equation (A.12) resulted in a plateau value for high momenta as expected from the correct formula. The resulting error in the amount of the relativistic rise was approximately cancelled by a wrong density effect parameter  $\bar{C}(\text{NaI}) = 3.40$  instead of the measured value  $\bar{C}(\text{NaI}) =$

<sup>2</sup>In comparison to the original Sternheimer parametrization using the parameters  $C$ ,  $a$ ,  $m$ ,  $X_0$ ,  $X_1$  our parameter set  $\bar{C}$ ,  $b$ ,  $n$ ,  $Y_0$ ,  $Y_1$  is defined by  $\bar{C} = -C$ ,  $b = a / (\ln 10)^m$ ,  $n = m$ ,  $Y_0 = 10^{X_0}$ , and  $Y_1 = 10^{X_1}$ .

Table A.1: Density effect parameters for NaI.

	$\bar{C}$	$n$	$Y_0$	$Y_1$	$b$
general expression	6.06	3.00	2.86	$1.00 \cdot 10^3$	$1.97 \cdot 10^{-2}$
material fits	6.06	3.04	1.32	$3.91 \cdot 10^3$	$0.99 \cdot 10^{-2}$

6.06 [132]. The overall amount of  $dE/dx$  was corrected by  $\text{PARMAT}(\text{NaI}, 1)$ . As pointed out above, this approximate cancellation happened just by chance, given our special  $T_c^\circ$  parameter choice, and detector setup.

The application of formula (A.11) guarantees the independence of the amount of energy loss from  $T_c^\circ$ . In addition it introduces the theoretically correct dependence of  $dE/dx$  on the particle momentum. This brings the peak correction factor  $\text{PARMAT}(\text{material}, 1)$  to the expected value of about 1 for all materials, given the right material parameters (see next changes for our case of NaI).

#### 8. Use the measured mean ionization potentials.

GHEISHA uses the approximation from Ref. [133] for the mean ionization potential  $I$  of materials with  $Z \geq 13$

$$I = \left( 9.76 \cdot Z + \frac{58.8}{Z^{0.19}} \right) \text{eV}. \quad (\text{A.17})$$

The results of this expression match very well with the measured values from Ref. [132] as far as pure elements are concerned. However, there may be substantial differences for compounds. Since the measured values of  $I$  and  $\bar{C}$  are related via Equation (A.14), we calculate  $I$  from  $\bar{C}$  according to

$$I = \hbar\omega_p e^{(\bar{C}-1)/2}. \quad (\text{A.18})$$

The correction of the mean ionization potential for NaI affects the total amount of  $dE/dx$  by about 2%, but has negligible effect on the momentum dependence of  $dE/dx$ .

#### 9. Use the density effect parameters from “material fits”.

Our final change is the replacement of the density effect parameters for NaI from the “general expression” [134], used by GHEISHA, by those from “material fits” [132], as listed in Table A.1. Note, that the parameters  $n$ ,  $Y_0$ ,  $Y_1$ , and  $b$  are highly correlated, and that even a large variation of these parameters may change the result only marginally. In our case the modification results in a decrease of the simulated relativistic rise of the energy loss between muon samples of  $\beta\gamma \approx 3.5$  and  $\beta\gamma = 45$  from 10.4% to 7.8%. The size of the decrease is consistent with the expected uncertainty of the “general expression” for the density effect.

Altogether the changes (1)–(9) generate a consistent simulation of  $\delta$ -rays,  $dE/dx$ , and its fluctuations, with no additional correction factors dependent on particle, momentum, or material. The simulation describes the energy loss distribution correctly independent of the actual simulation step sizes. This is confirmed by a comparison with our data.

## A.2 Verification with Crystal Ball Data

The various changes of the GHEISHA simulation of the energy loss of charged particles in NaI have been verified with the help of two Crystal Ball  $\mu^+ \mu^-$  data samples of different muon

energies. The high-energy  $\mu$ -pair sample comes from the annihilation process  $e^+e^- \rightarrow \mu^+\mu^-$  at beam energies around 5 GeV. The low-energy sample consists of  $\mu$ -pairs produced in the two-photon reaction  $e^+e^- \rightarrow e^+e^-\mu^+\mu^-$  where the final state electrons escape the detector under small angles. Here the muon energy typically lies in the range from 200 MeV to 500 MeV. The selection criteria were designed to give unbiased distributions of the muon energy depositions in the calorimeter [135]. The low energy muons were separated from the high energy muons by the requirement not to reach the Roof-ToF counters.

### A.2.1 The Lateral Energy Pattern

A useful test of our changes to the GHEISHA detector simulation is to compare the measured lateral energy pattern of the muons with those of the Monte Carlo. Besides the event vertex distribution along the beam axis, there are two major reasons why the deposited energy is generally not restricted to one single crystal: multiple scattering and  $\delta$ -ray production. While multiple scattering is the dominant effect for low-energy muons, the  $\delta$ -rays govern the lateral pattern distributions for the high-energy muons.

Figure A.2 shows various measured distributions of pattern fractions for both samples. They have been defined in Section 3.4. A general feature is, that the low energetic muons tend to extend their energy depositions over more crystals, which results in a tail to lower pattern fractions.

Integrating these distributions from right to left, we get the probability (or cut efficiency) for a muon, having at least a certain fraction of its deposited energy distributed among 1, 2, or 4 crystals (see crosses in Figure A.3). These integrated pattern distributions from the data are compared to the results of the GHEISHA simulation without  $\delta$ -rays (dotted) and with default GHEISHA  $\delta$ -rays (dashed). Especially for the high-energy muons the simulation without  $\delta$ -rays cannot describe the data and largely overestimates the cut efficiency. On the other hand, the default GHEISHA  $\delta$ -rays tend to underestimate the efficiency for the high-energy muons by  $\sim 5\%$  in the most commonly used range of cut values between 0.90 and 0.95.

After applying our changes to the GHEISHA  $\delta$ -ray simulation we observe a very good agreement of 1% to 2% between the integrated pattern fraction distributions of MC (solid line in Figure A.3) and data (crosses) below 0.96. Only for pattern fraction values near 1 deviations up to 15% for the low-energy and 5% for the high-energy muons still remain. These regions correspond to energy depositions of less than 8 MeV outside the considered crystals, which may be caused by photons radiated off by the final state muons. We estimate, that an appreciable part of the difference for the low-energy muons can be explained by this fact, since only the event generator for the high-energy muon sample includes final state radiation. The remaining differences in both samples may be attributed to inaccuracies in the event generators, in the EGS 3 shower simulation, the ball geometry code, or other error sources.

However, altogether Figure A.3 justifies and confirms the correctness of our changes by clearly showing an improvement over the default GHEISHA pattern simulation with and without  $\delta$ -rays through our corrected  $\delta$ -ray simulation.

### A.2.2 The Energy Loss Distribution

Having two muon samples with low- and high-energy muons, respectively, we are able to determine the relativistic rise of the energy loss peak positions between the two samples. The high-energy sample contains monoenergetic muons with  $\beta\gamma = 45$ , whereas the low energy muons, according to a Monte Carlo prediction, are distributed essentially between  $\beta\gamma = 2$

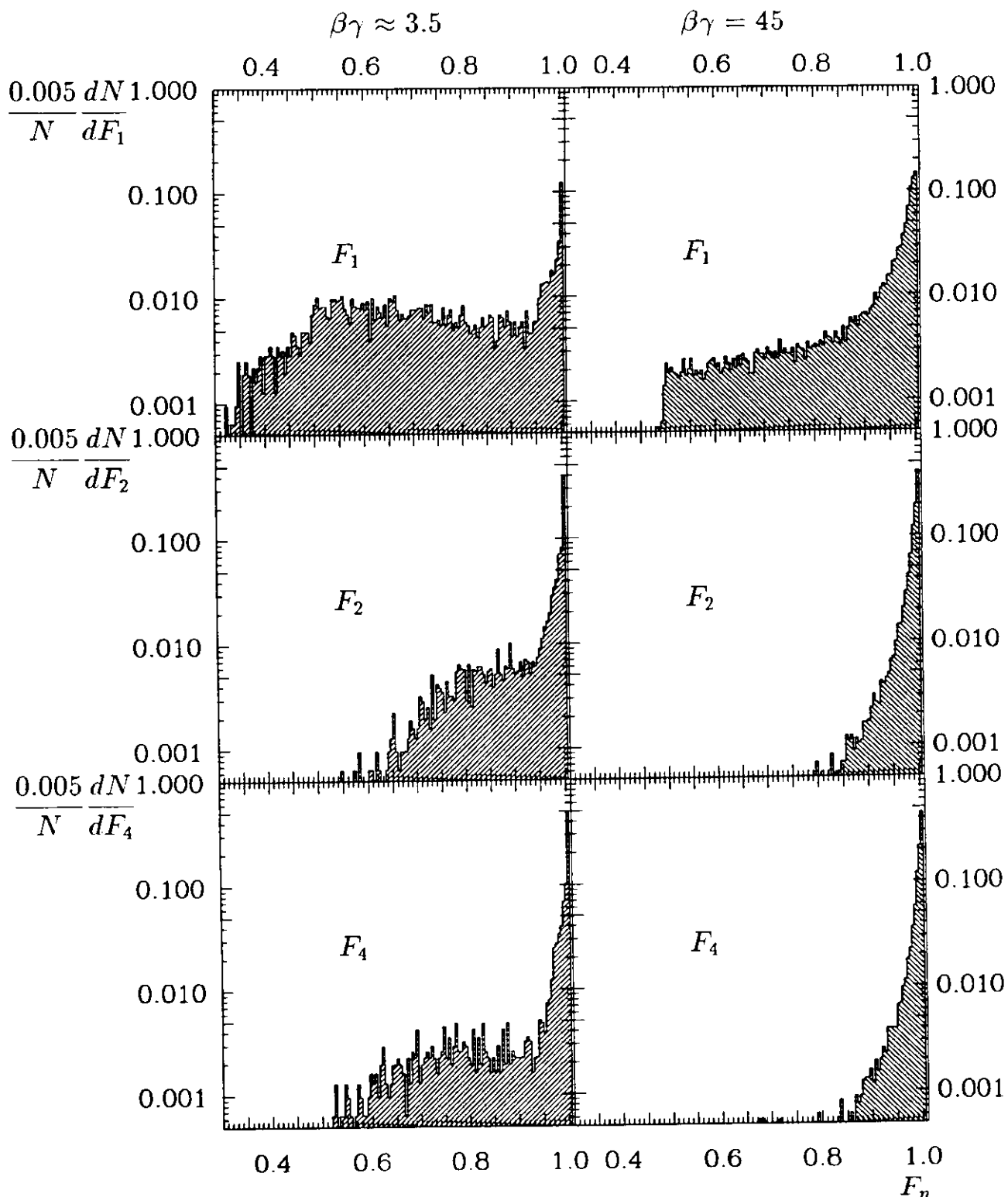


Figure A.2: Distribution of energy pattern fractions. The distributions on the left-hand side are obtained from the low-energy muon sample, those on the right-hand side come from the high-energy muon sample. For the definitions of variables see the text.



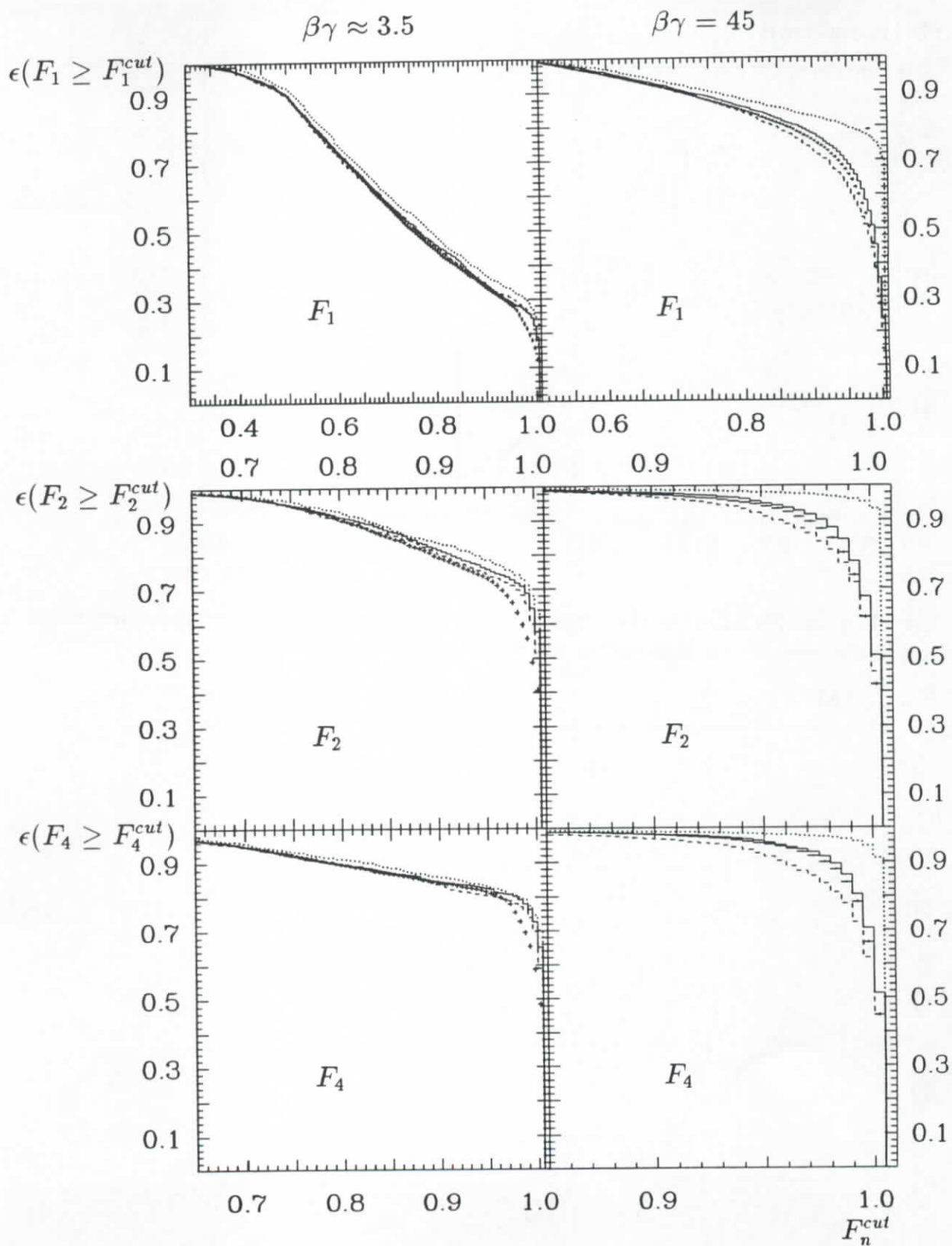


Figure A.3: Efficiency  $\epsilon$  versus cut on pattern fraction for the low-energy muon sample (left-hand side), and the high-energy muon sample (right-hand side). Crosses are data, solid line is final MC simulation, dots are MC without  $\delta$ -rays, and dashes are MC with default GHEISHA  $\delta$ -rays.

(arbitrary units)

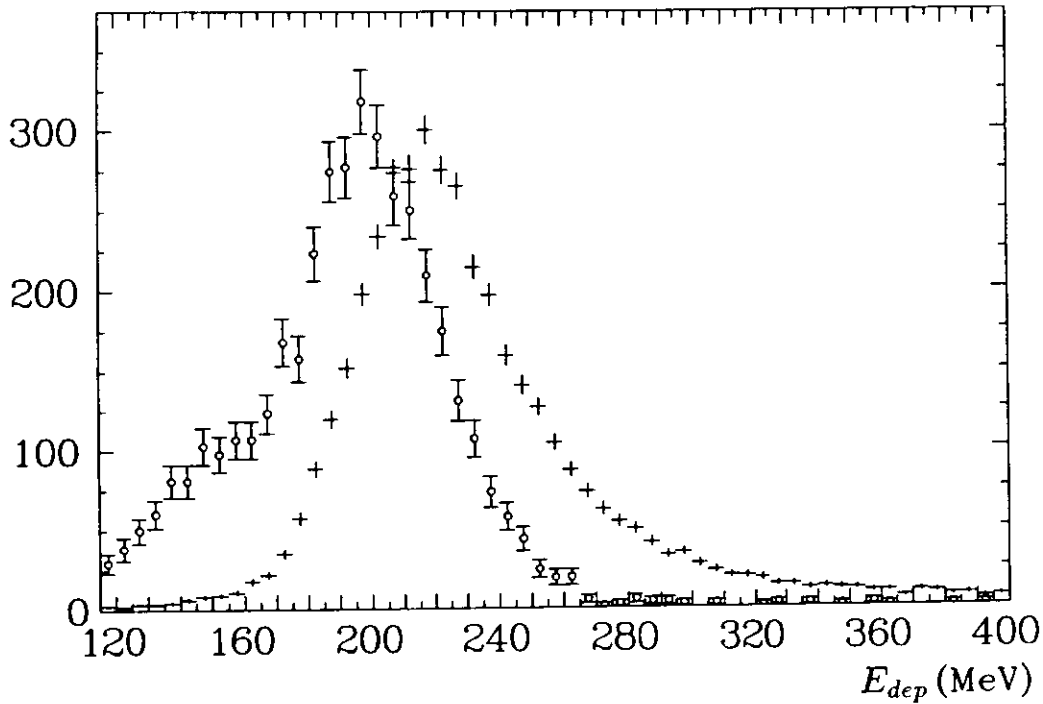


Figure A.4: Energy deposited in the Crystal Ball. The open circles show the low-energy muon sample, the crosses the high-energy muon sample.

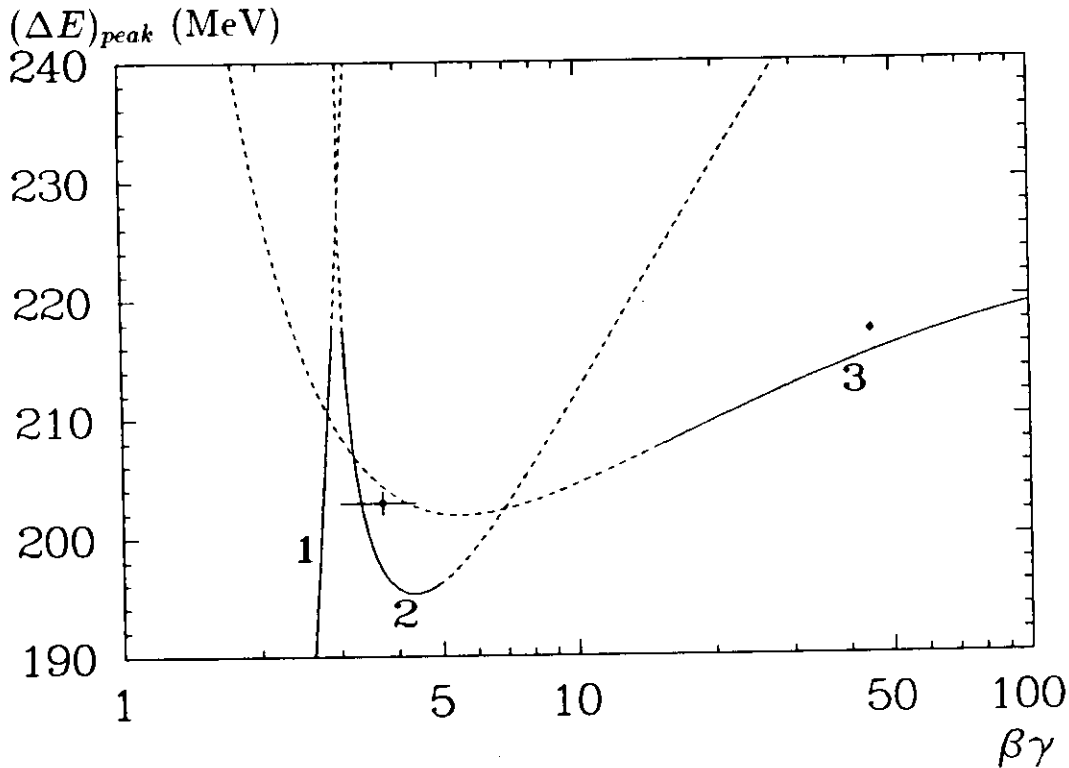


Figure A.5: Prediction for energy loss peak positions of muons in the Crystal Ball. The three curves show the kinetic energy (1), the integrated mean energy loss (2), and the most probable energy loss in thin layers (3). The solid parts indicate the momentum range, where the curves are relevant for the energy loss peak position. The dots are the observed peak values of  $E_{dep}$  and their statistical errors.

and  $\beta\gamma = 5$ . The measured distributions of the deposited energy  $E_{dep}$  for both samples are displayed in Fig. A.4.

The theoretical prediction for the energy loss peak position  $(\Delta E)_{peak}$  of muons in the Crystal Ball, as shown in Fig. A.5, reveals three momenta ranges, which have to be described by different expressions. Each of them has a counterpart in our muon samples. -

- The muons with  $\beta\gamma \lesssim 3$  stop in the ball and deposit all their kinetic energy  $T$ , so that

$$(\Delta E)_{peak} = T = mc^2 \left( \sqrt{\beta^2\gamma^2 + 1} - 1 \right) \quad (\text{A.19})$$

for any given value of  $\beta\gamma$ , as depicted in curve #1. This part of the low-energy muons, creates the broad distribution below the Gaussian peak in Fig. A.4.

- The Gaussian peak in the deposited energy distribution of the low-energy sample arises from the more energetic muons, which manage to traverse the ball. For these muons with  $3 \lesssim \beta\gamma \lesssim 5$  a Gaussian approximation for the energy loss fluctuations is appropriate in the Crystal Ball, since their maximum  $\delta$ -ray energy of 10 MeV  $\lesssim T_e^{max} \lesssim 25$  MeV is of the same order as the width  $\sigma$  of their energy loss distribution. Their mean energy loss including all energy transfers  $T_e$  to the atomic electrons up to the kinematic limit  $T_e^{max}$  is given as [131,136,129]

$$- \left( \frac{dE}{dx} \right)_{mean} = D \frac{Q^2}{\beta^2} \left[ \ln \left( \frac{2m_e c^2 T_e^{max}}{I^2} \beta^2 \gamma^2 \right) - 2\beta^2 - \delta \right]. \quad (\text{A.20})$$

The peak position of their energy loss distribution is then obtained by integrating this mean energy loss along their path through the crystals

$$(\Delta E)_{peak} = \int_{0\text{cm}}^{40.6\text{cm}} \left( \frac{dE}{dx} \right)_{mean}(x) dx \quad (\text{A.21})$$

yielding curve #2.

- In thin material layers the energy loss distribution is not Gaussian, and the energy loss peak position differs from  $\int (dE/dx)_{mean} dx$ . According to Landau [137] the most probable energy loss in thin layers is approximately given by the restricted energy loss of Equation (A.11), if the cutoff parameter  $T_e^o$  is chosen to be

$$T_e^o = \xi \equiv D \frac{Q^2}{\beta^2} \Delta x. \quad (\text{A.22})$$

The conditions for having a thin layer are  $\xi/T_e^{max} < 0.05$  and  $(\Delta E)_{peak} \ll T$ . The most probable energy loss is then given as

$$(\Delta E)_{peak} = \xi \left[ \ln \left( \frac{2m_e c^2 \xi}{I^2} \beta^2 \gamma^2 \right) - \beta^2 + 0.198 - \delta \right], \quad (\text{A.23})$$

where the contributions of energy transfers greater than  $\xi$  are accounted for by the numerical correction term 0.198 [138], which raises the peak position generally by about 1%.

The Crystal Ball calorimeter fulfills both conditions for a thin layer for incident particles of  $\beta\gamma \gtrsim 15$ . Then the energy loss peak position is given by curve #3 obtained from Eq. (A.23). In the intermediate range  $5 \lesssim \beta\gamma \lesssim 15$  none of our formulae is accurate.

The observed peak values lie at  $E_{dep} = 202.9 \pm 1.0$  MeV for those of the low-energy muons, which traverse the ball, and at  $E_{dep} = 217.2 \pm 0.4$  MeV for the high-energy muons. Since  $E_{dep}$  includes the final state photon radiation, an increase in  $\Delta x$  due to the finite vertex distribution, and the detector calibration, which alone may give rise to systematic errors of a few percent, their agreement with the predictions is excellent.

The essential quantity to test a detector MC, however, is the difference between the peak positions, since most systematic errors mentioned above cancel in the subtraction. The sensitivity of this test can be seen from the fact, that not only the three parts of the energy loss distributions are described by three different expressions, but also that the predicted  $(\Delta E)_{peak}$  of the muons of  $\beta\gamma \approx 3.5$  lies on a curve with a steeply falling slope. Therefore small inaccuracies in the detector simulation and its  $dE/dx$  parametrization, (but also in the underlying momentum distribution from the generator for  $e^+e^- \rightarrow e^+e^-\mu^+\mu^-$ ), can change the simulated peak value appreciably. To reproduce the relativistic rise of only 7% in the energy loss peak position from  $\beta\gamma \approx 3.5$  to  $\beta\gamma = 45$  correctly, it is crucial to exactly predict differences between  $dE/dx$  values for different momenta. Thus the use of an accurate expression for the energy loss is important, including a proper choice of the density effect parameters, which govern the momentum dependence of the energy loss in the relativistic range.

For the following comparisons we first adjusted the peak position and width for the energy loss distribution of the high-energy sample to match with the data. This was done with the help of `PARMAT(NaI,1)` for  $\Delta E$ , and by appending a correction factor `PARMAT(material,5)` to  $\sigma$  in Equation (A.9). Thus, the high-energy sample acts as a reference for the peak position and the width of the Gaussian part of the energy loss distribution of the low-energy muons.

For a correct  $dE/dx$  simulation, the factor `PARMAT(material,1)` should be very close to 1, and deviations, e.g. due to systematic detector calibration errors, should be less than a few percent. Having eliminated this overall systematic errors via `PARMAT(material,1)`, the peak position of the low-energy sample can be studied with high enough accuracy to test, if the simulation reproduces the 7% relativistic rise in the energy loss peak position between the two samples.

Fig. A.6 compares the data energy loss distributions (crosses) from Fig. A.4 to various versions of the MC simulation. The dotted line describes the default GHEISHA simulation without explicit  $\delta$ -rays, the dashed and dashed-dotted lines show intermediate stages of the MC simulation, and the full line is from our final simulation after all changes.

Fig. A.6 confirms, that our modified GHEISHA simulation can predict the momentum dependence of the energy loss distribution of charged particles in the Crystal Ball with high accuracy. The measured peak position, width, and shape of the energy loss distribution for both, the high and the low energy sample, are consistently described by our final simulation. The final value of the parameter for the peak adjustment, `PARMAT(NaI,1) = 0.995`, clearly indicates the correctness of our changes. The parameter `PARMAT(NaI,5)` for the width adjustment has the value 1.9. It accounts for inaccuracies in the amount of the simulated  $dE/dx$  fluctuations as well as for the detector resolution of the NaI crystals for ionizing particles. (We cannot test the validity of Equation (A.9) for  $dE/dx$  fluctuations, since the energy resolution for ionizing particles in the Crystal Ball is not known.)

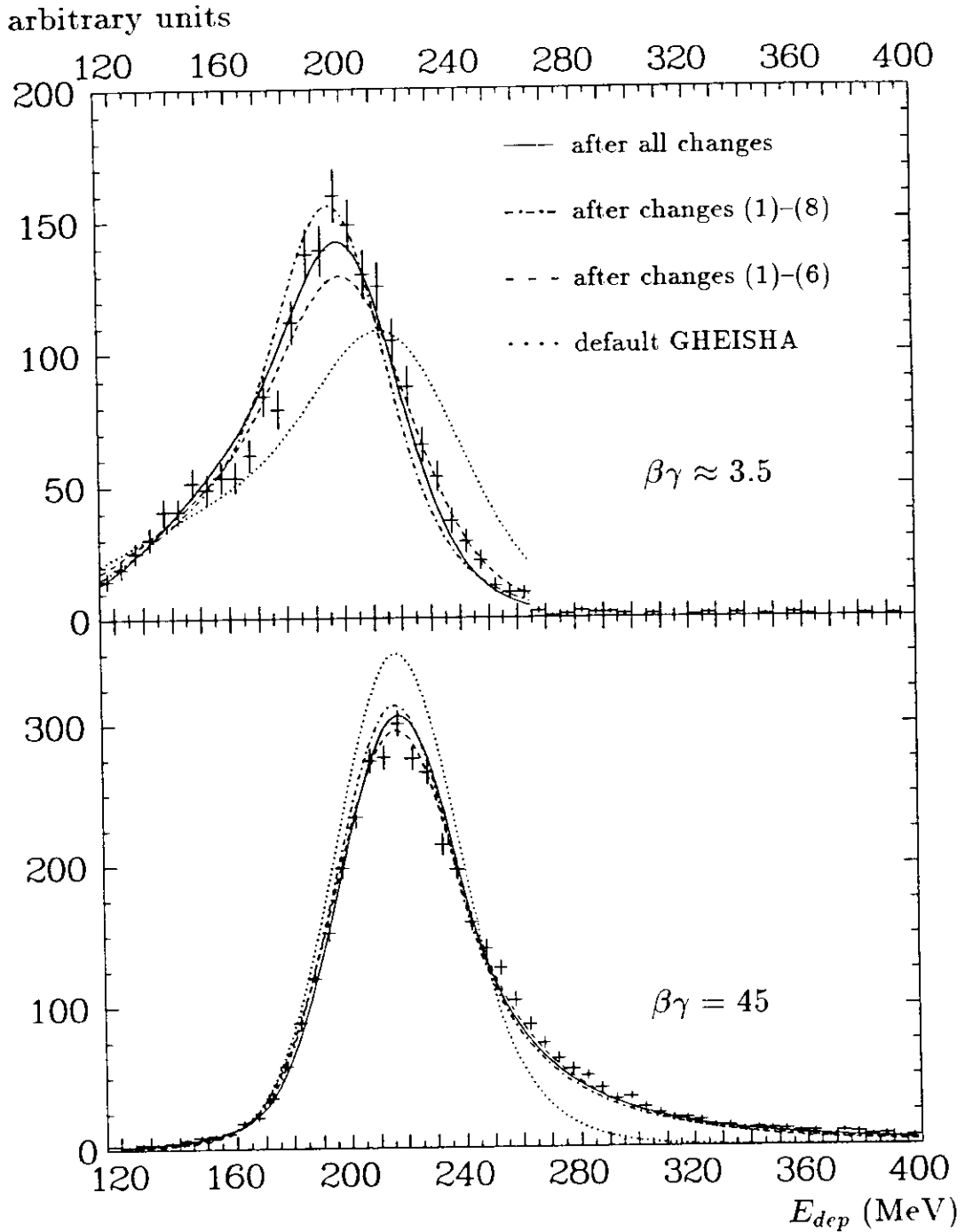


Figure A.6: Simulation of muon energy depositions in the Crystal Ball. The results for the low-energy muons are shown in the upper plot, those for the high-energy muons in the lower plot. Crosses are data, lines represent Gaussian fits to the results of various versions of MC simulation. In the upper plot we added another Gaussian with fixed position for the contribution of the stopping muons, in the lower plot we used power tails to describe the  $\delta$ -ray contribution on the right-hand side, and the small tail on the left-hand side caused by gaps in the detector.

# Appendix B

## The Erlangen Tube Chamber MC

For a realistic MC simulation of the Crystal Ball tube chamber it is not enough to cover the three different setups with their different modes of operation (cf. Section 3.1). Even within each setup there were large variations in the chamber performance. The old streamer tubes kept degrading through the growing of organic molecules on the wires, which forced the collaboration to lower the high voltage in order to prevent sparks. This made their response efficiency and their pulse height distribution time dependent.

After the replacement of the streamer tubes by new proportional tubes in a two-step upgrading process the efficiency was greatly improved. However, still a distinct time dependence of both, efficiency and pulse height, was observed, which also led to a variation of the  $z$ -resolution with time. The time dependences were introduced by repeated damage of the hybrid amplifiers through sparks, by changes in the high voltage setting in order to minimize sparking, and by other effects like pressure and temperature variations.

The Erlangen Tube chamber Monte Carlo (E.T.MC) is designed to model the chamber performance by thoroughly reproducing differential distributions and their time dependence. These distributions cover the interdependences between pulse heights,  $z$ -resolution, efficiencies, particle momenta, and directions. The E.T.MC replaces an older Crystal Ball tube chamber MC [139], which simulated only one typical snapshot of each chamber setup without a detailed reproduction of the above mentioned interdependences. The old code was adopted as a basis of our simulation and partially rewritten or extended.

In order to properly model the time-dependence of the tube chamber performance, we subdivided the Crystal Ball data sample into a total of 220 periods. Most period boundaries were defined by perceptible changes in the mean pulse height or in the efficiency of at least one of the double layers. In addition, new periods were started at any major change of beam energy or trigger setting. On an average, each period corresponds to about 50 runs (fills of the DORIS ring) equivalent to about 2 days of data taking. The actual size of a single period varies from 7 runs to 450 runs.

The E.T.MC input parameters, which are suited to model the pulse height distributions,  $z$ -resolution, and efficiency, and their dependences on particle momenta and directions, have to be extracted for each period from measured data. As a reference data set we select Bhabha events and perform a track reconstruction (i.e. assignment of hits and fitting of directions) with the help of the TAGTRK routine [85]. In order to obtain complete pulse height distributions we retrieve all hits down to pulse heights of 10 mV and 200 mV for the proportional and streamer tubes, respectively, from the raw data (cf. Section 3.4). This is well below the pulse height cuts applied in the Crystal Ball event reconstruction.

In the following we discuss in detail, how the E.T.MC input parameters have been extracted from the selected reference data, and how the parameters are employed to model the

complete performance of the tube chambers for arbitrary particle momenta and directions. A short summary of these details can be found in Section B.4. The results of the simulation are illustrated by distributions for the old setup, consisting of three double layers of streamer tubes, and for the new setup, composed of four double layers of proportional tubes. (The intermediate setup was composed of double layers #1 and #2 from the new setup and double layer #3 from the old one.) We use the symbols for various geometrical parameters as depicted in Fig. B.1.

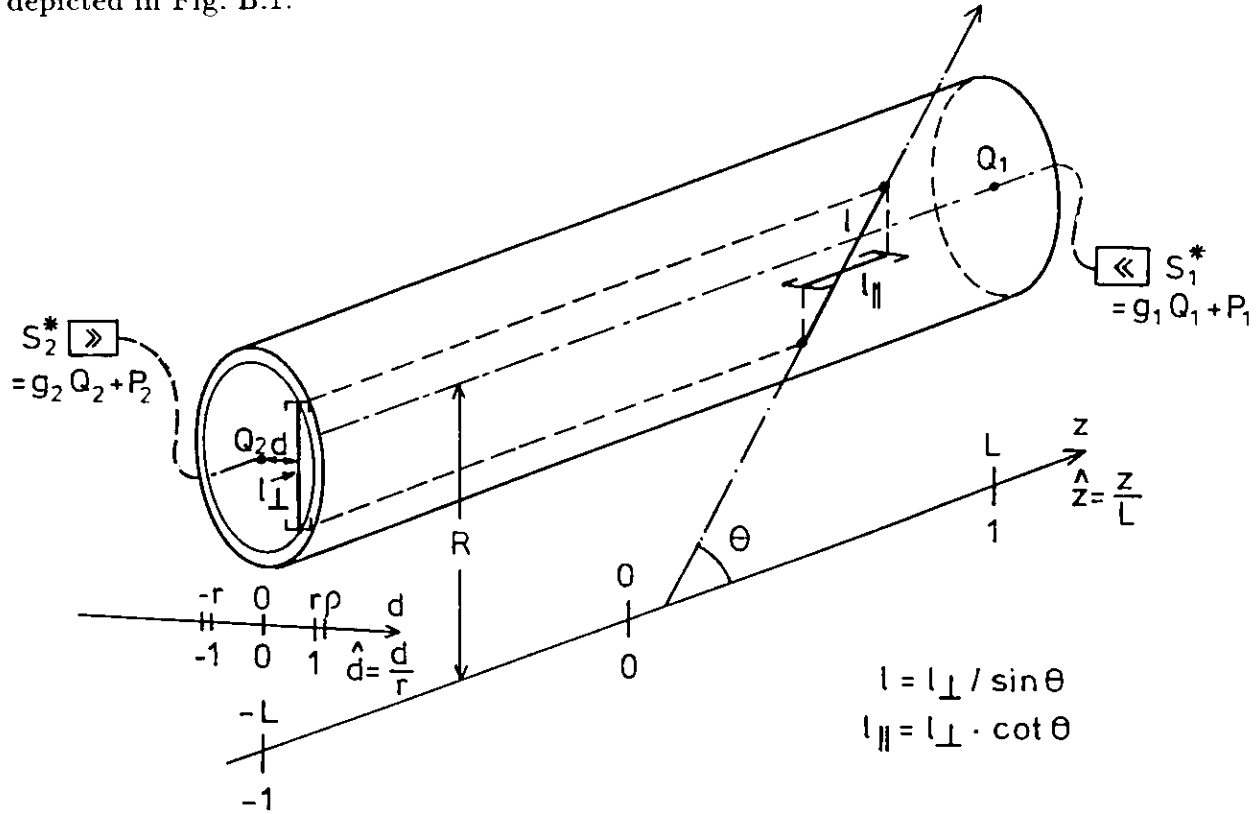


Figure B.1: Definition of various geometric parameters for the tube chamber simulation. The figure shows a single tube, traversed by a charged particle (dashed-dotted line). The  $z$ -axis is the beam line. The relative sizes of the tube length  $2L$ , the tube diameter  $2r$ , and the distance  $R$  to the beam line are not on scale.

## B.1 The Pulse Height Distributions

The basic output signal of each tube chamber hit are the pulse heights  $S_i$ , ( $i=1,2$ ), at both ends of the tube. They emerge from amplifying the charge signals  $Q_i$  at the ends of the resistive wire resulting in the respective measured pulse heights  $S_i^*$  (Fig. B.1) given by

$$S_i^* = g_i Q_i + P_i \quad (i=1,2), \quad (\text{B.1})$$

where  $g_i$  are the gain factors (of dimension  $1/\text{capacitance}$ ) and  $P_i$  are the pedestal voltages. The pulse heights  $S_i$  are determined from the measured pulse heights  $S_i^*$  by subtracting the mean pedestal voltages  $\langle P_i \rangle$

$$S_i = S_i^* - \langle P_i \rangle \approx g_i Q_i. \quad (\text{B.2})$$

The total pulse height  $S$  is then defined as the sum

$$S = S_1 + S_2. \quad (\text{B.3})$$

To separate genuine chamber hits of charged particles from noise or background, only those hits are used in the Crystal Ball event reconstruction, whose total pulse heights  $S$  exceed a (run-dependent) pulse height cut  $S_{cut}$ . The efficiency for chamber hits thus depends on the distribution of  $S$  for a given particle. Also the precision of extracting the  $z$ -position of a hit from its charge division into  $S_1$  and  $S_2$  is a function of  $S$ , as described in Section B.2 below. The correct modeling of pulse height distributions is thus an unconditional basis for reproducing the resolution of the  $z$ -position as well as the efficiencies with means of a MC simulation.

The pulse height measured for a charged particle traversing a *proportional* tube depends on its specific ionization  $dE/dl(\beta\gamma)$ , on the path length  $l(\theta, \hat{d})$  inside the tube, and in addition on some ‘‘edge effects’’  $e_S(\hat{z})$  in the vicinity of  $|\hat{z}| = 1$

$$S = S_{propo}(\beta\gamma, \theta, \hat{d}, \hat{z}). \quad (\text{B.4})$$

The pulse height in *streamer* tubes is in principle independent on the primary ionization (i.e. on  $dE/dl$  and  $l$ ). It is thus identical for all particles and particle momenta. We empirically observe, however, an approximate  $1/\sin\theta$  dependence, which may arise from the larger gas volume available for the formation of streamers at smaller values of  $\sin\theta$ . Thus,  $S$  is a function

$$S = S_{streamer}(\theta, \hat{z}), \quad (\text{B.5})$$

where the  $\hat{z}$  dependence again arises from edge effects at  $|\hat{z}| \approx 1$ .

We model the chamber pulse heights and their variation with time by simulating the pulse heights  $S$  starting from reference pulse height distributions  $S_{file}$ . These reference distributions are obtained from our Bhabha event sample for each simulation period and each layer. They are partitioned in about 50 bins, and recorded on the E.T.MC input file.

To serve as a reference,  $S_{file}$  must not be sampled over the full range of  $\beta\gamma, \theta, \hat{d}$ , and  $\hat{z}$  encountered in the Bhabha events. Instead,  $S_{file}$  should refer to fixed reference values  $dE/dl(\beta\gamma_{file}), l_{file}(\theta, \hat{d})$ , and  $e_{S,file}(\hat{z})$ , so that the dependence of  $S$  on these variables can be properly introduced afterwards. This condition is trivially fulfilled for

$$\frac{dE}{dl}(\beta\gamma_{file}) \equiv \frac{dE}{dl}(10000),$$

since  $dE/dl$  changes only very weakly from beam-energy electrons ( $\beta\gamma \approx 10000$ ) to lower energetic electrons in radiative Bhabha events (see Fig. B.4 below). The edge effects  $e_S(\hat{z})$  can be eliminated by requiring  $|\hat{z}| < 0.8$  yielding (cf. Eq. (B.9) below)

$$e_{S,file} \equiv e_S(|\hat{z}| < 0.8) = 1.$$

Thus, only the dependences of the observed pulse heights on  $l$  for the proportional tubes and on  $1/\sin\theta$  for the streamer tubes are left. Since the total path length  $l(\theta, \hat{d})$  inside the tube is given by  $l = l_{\perp}(\hat{d})/\sin\theta$  (see Fig. B.1) we can remove the  $\theta$ -dependence for both, the proportional and the streamer tubes, by multiplying the measured electron pulse height  $S_e$  for each hit with the corresponding value of  $\sin\theta$ . For the proportional chambers this multiplication scales the pulse height to a reference path length  $l_{file} = l_{\perp}(\hat{d})$ , which still depends on  $\hat{d}$ . To finally remove also this dependence, we collect only those hits, where the electron track intersects the tube within  $|\hat{d}| < 0.4$ , i.e. where  $l_{\perp} \approx 2r$ . A precise enough measurement of  $l_{\perp}(\hat{d})$  for each hit in order to explicitly remove the  $\hat{d}$  dependence analogously to the  $\theta$ -dependence is not possible. The effective reference path length is then  $l_{file} = \langle l_{\perp}(|\hat{d}| < 0.4) \rangle$ , which can be expressed with the help of a scale factor  $f$  slightly larger than 1 as

$$l_{file} = 2r/f.$$



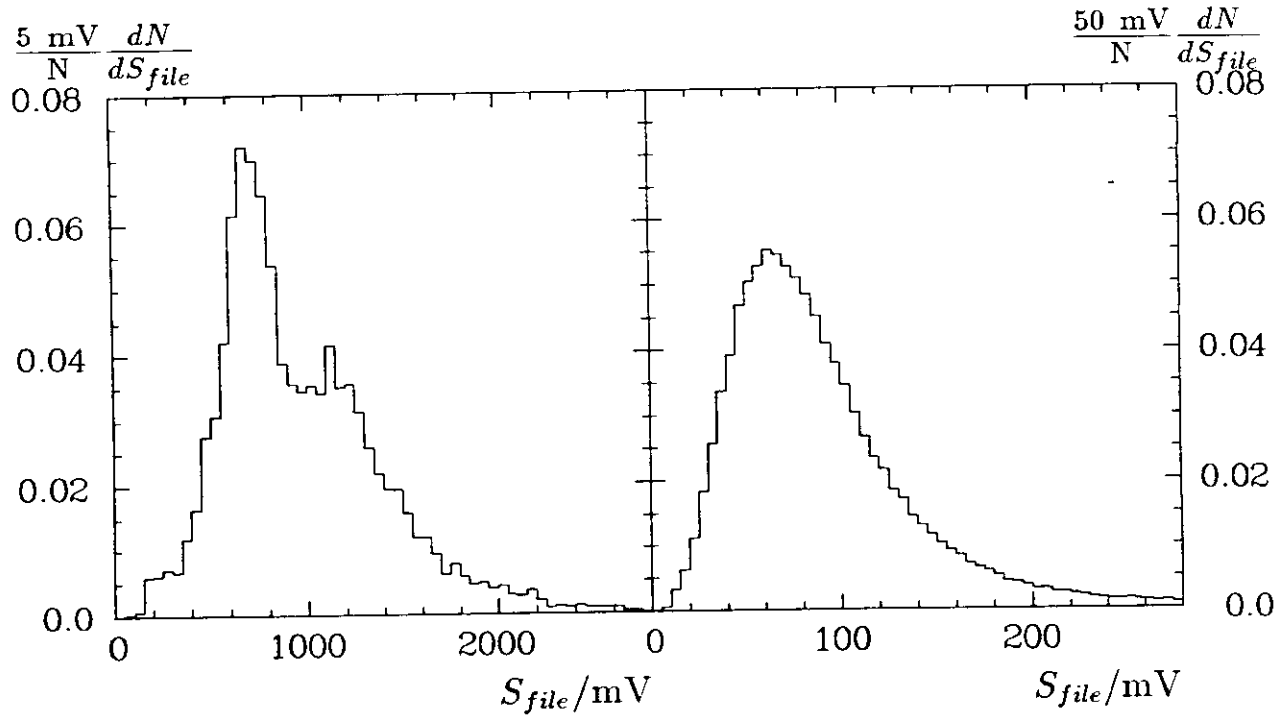


Figure B.2: Reference distributions  $S_{file}$  of the chamber pulse heights for streamer tubes (left) and proportional tubes (right) for one layer in one of the 220 E.T.MC simulation periods.

If  $\hat{d}$  could be measured exactly, our cut in  $|\hat{d}|$  would correspond to  $f = 1.03$ . Without a cut in  $\hat{d}$  — or, equivalently, for a very poor resolution  $\Delta d \gg r$  — we would have to average over all possible  $l_{\perp}$  values resulting in  $f = 4/\pi = 1.27$ . Practically, the finite  $\varphi$  resolution  $\Delta\varphi$  of the track reconstruction procedure<sup>1</sup> implies a finite resolution  $\Delta d = R\Delta\varphi$ . The factors  $f$  will thus depend on the layer radii  $R$ . We find values ranging from  $f = 1.12$  for the innermost double layer to  $f = 1.18$  for the outermost double layer of tubes.

Summarizing, we collect reference pulse height distributions  $S_{file}$  by recording the product of pulse height  $S_e$  and  $\sin\theta$  for those hits in Bhabha events, which have been assigned to an electron track and fulfill the above constraints, i.e.

$$S_{file} = \sin\theta \cdot S_e(\beta\gamma = 10000, \theta, [|\hat{d}| < 0.4], |\hat{z}| < 0.8), \quad (\text{B.6})$$

where the constraint in squared brackets is applied for proportional chambers, only. We show one example for the resulting distribution of  $S_{file}$  for a layer of streamer tubes and a layer of proportional tubes in Fig. B.2. The streamer pulse heights are by more than a factor 10 larger than those from the proportional tubes.

In our MC simulation these distributions are used as a probability density for generating a pulse height  $S_0$  for each tube hit in the given layer and data taking period. For the proportional tubes the final simulated pulse height is then obtained by scaling  $S_0$  with the ratio of path lengths  $l/l_{file} = (l_{\perp}/\sin\theta)/(2r/f)$ , with the ratio of specific ionizations  $\frac{dE}{dl}(\beta\gamma) \equiv \frac{dE}{dl}(\beta\gamma)/\frac{dE}{dl}(10000)$ , and by correcting for edge effects yielding

$$S_{propo} = \frac{S_0}{\sin\theta} \frac{fl_{\perp}}{2r} \frac{dE}{dl}(\beta\gamma) \epsilon_S(\hat{z}). \quad (\text{B.7})$$

<sup>1</sup> $\varphi$  is measured from a fit through all tube hits associated with a given track. We use only tracks with a large enough number of hits so that  $\hat{d}$  of the hit under study is determined accurately enough from all other associated hits.

For the streamer tubes this reduces to

$$S_{streamer} = \frac{S_0}{\sin \theta} e_S(\hat{z}). \quad (\text{B.8})$$

The functional form of the edge effect has been obtained by plotting  $\langle S \sin \theta \rangle$  versus  $\hat{z}$ . We find, that we can describe the data with

$$e_S(\hat{z}) = \begin{cases} 1 & \text{for } |\hat{z}| \leq 0.8 \\ 1 - \frac{|\hat{z}-0.8|}{1-0.8} & \text{for } |\hat{z}| > 0.8 \end{cases}. \quad (\text{B.9})$$

Figure B.3 confirms this ansatz by a comparison of tube hits from Bhabha electrons with their MC simulation according to Eqs. (B.7),(B.8), and (B.9). Away from the edges in  $\hat{z}$  we observe the expected flat behaviour of  $\langle S \sin \theta \rangle$ . The magnitude of the MC prediction agrees very well with the data. (The range of  $\hat{z}$  values plotted for each layer is dictated by the layer geometry and the range of possible  $\theta$  angles for the corresponding energy clusters in the calorimeter via  $\hat{z} \sim R \cot \theta / L$ .)

For the proportional chambers the pulse height dependence on the primary ionization  $dE/dl(\beta\gamma)$  is modeled according to Eq. (A.23). The resulting specific energy loss  $d\widehat{E}/dl(\beta\gamma)$  for the gas mixture in the proportional chambers is shown in Fig. B.4 together with the curves for pure Ar and pure CO<sub>2</sub>. We check the correctness of the pulse height simulation and its dependence on  $\beta\gamma$  with 5 GeV electrons from Bhabha events ( $\beta\gamma = 10000$ ), 5 GeV muons from  $e^+e^- \rightarrow \mu^+\mu^-$  events ( $\beta\gamma \approx 50$ ), and muons from the two-photon process  $ee \rightarrow ee\mu\mu$  with energies typically ranging from 0.25 to 0.5 GeV ( $2 \lesssim \beta\gamma \lesssim 5$ ). The measured distributions of hit pulse heights (collected without restrictions in  $\hat{z}$ ,  $\theta$ , and  $\hat{d}$ ) for these particles are shown in Fig. B.5 together with their E.T.MC predictions. We observe a good reproduction of the data behaviour.

Figure B.6 shows the reproduction of the changes in the mean pulse height with time for Bhabha events from the Y(2S) data. The data are averaged over 5 runs each, whereas the E.T.MC prediction is plotted for the range of runs corresponding to each simulation period.

## B.2 The $z$ -Resolution

The  $z$  position of the hit along the wire can be obtained from charge division by

$$\hat{z} = \frac{Q_1 - Q_2}{Q_1 + Q_2}, \quad (\text{B.10})$$

which can be expressed in terms of the pedestal subtracted measured pulse heights (Eq. (B.2)) as

$$\hat{z} = \frac{S_1 - \xi S_2}{S_1 + \xi S_2}, \quad (\text{B.11})$$

where  $\xi = \langle g_1/g_2 \rangle$  is the mean gain ratio, which changes from tube to tube and ranges typically from 0.8 to 1.2. In Eq. (B.11) we have neglected small effects introduced by the finite amplifier impedances (cf. Ref. [83]). The experimental error of the measurement of  $\hat{z}$  is introduced by the finite variations  $\Delta g_i/g_i$  of gains and  $\Delta P_i$  of pedestal voltages around their mean values for  $i=1,2$ . From Eqs. (B.1) and (B.2) we find

$$\begin{aligned} (\Delta S_i)^2 &= (\Delta P_i)^2 + (Q_i \Delta g_i)^2 \\ &\approx (\Delta P_i)^2 + \left(S_i \frac{\Delta g_i}{g_i}\right)^2. \end{aligned} \quad (\text{B.12})$$

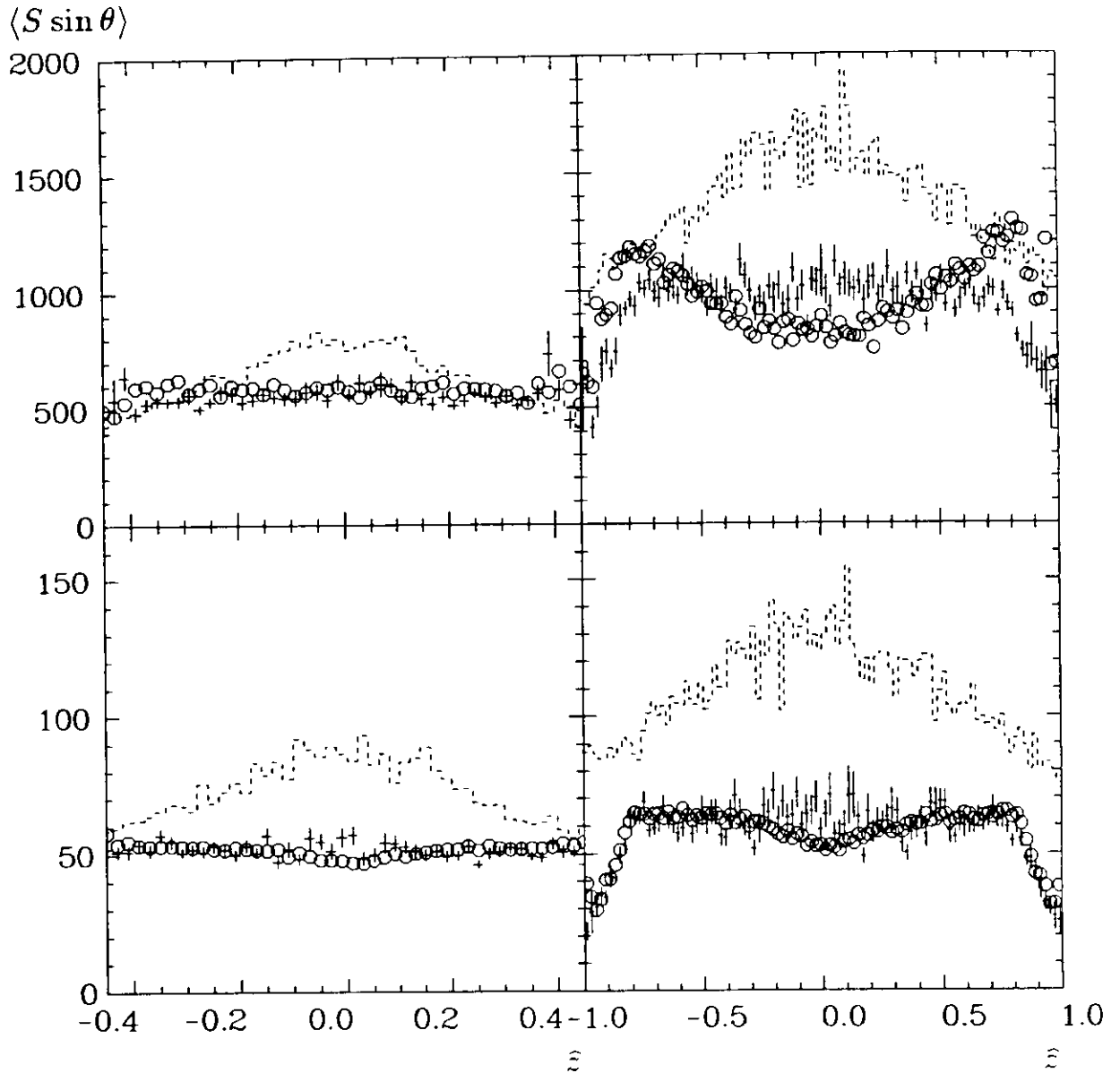


Figure B.3: Mean  $\langle S \sin \theta \rangle$  distributions for Bhabha electrons in the streamer tubes (upper plots) and the proportional tubes (lower plots) along the z-axis of the tubes. Open circles are data, crosses are E.T.MC, and the dashed line is the prediction of the older Crystal Ball tube chamber MC. The left-hand side is plotted for one of the innermost layers, the right-hand side for one of the outermost layers. With the exception of the outermost streamer layers, our ansatz for  $S(\theta, \tilde{z})$  is confirmed.

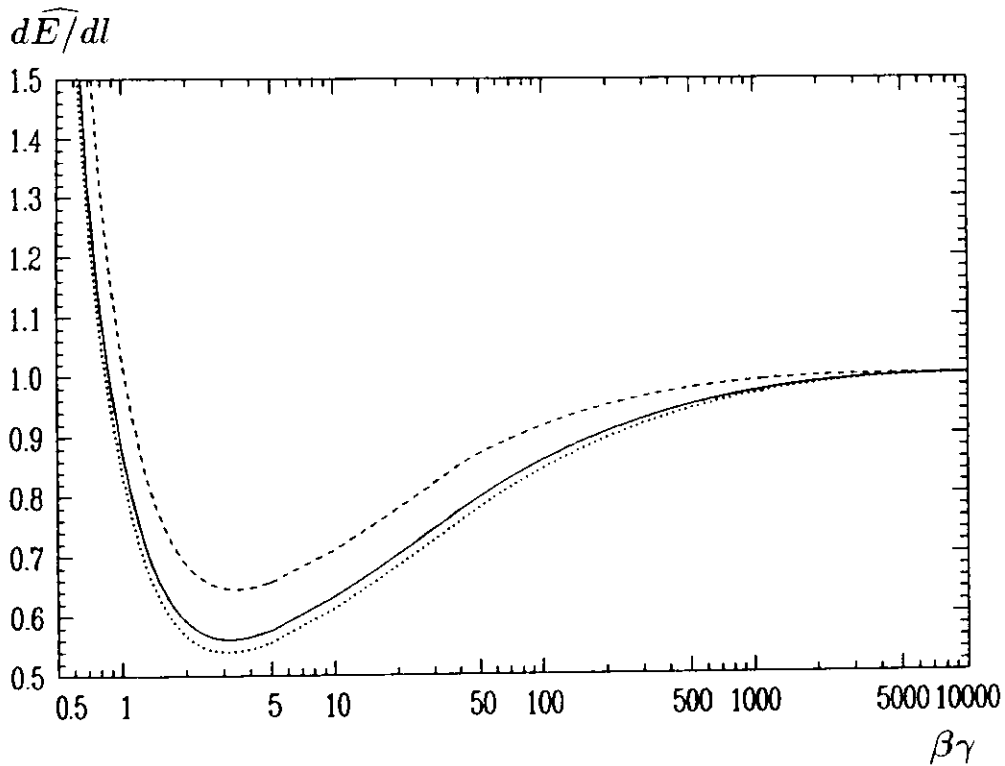


Figure B.4: Specific energy loss  $\widehat{dE/dl}(\beta\gamma)$  in the proportional tubes, normed to that of particles with  $\beta\gamma = 10000$ . The dotted line is for pure Ar, the dashed line describes pure  $\text{CO}_2$ , and the solid line is valid for a 80:20 mixture of both components.

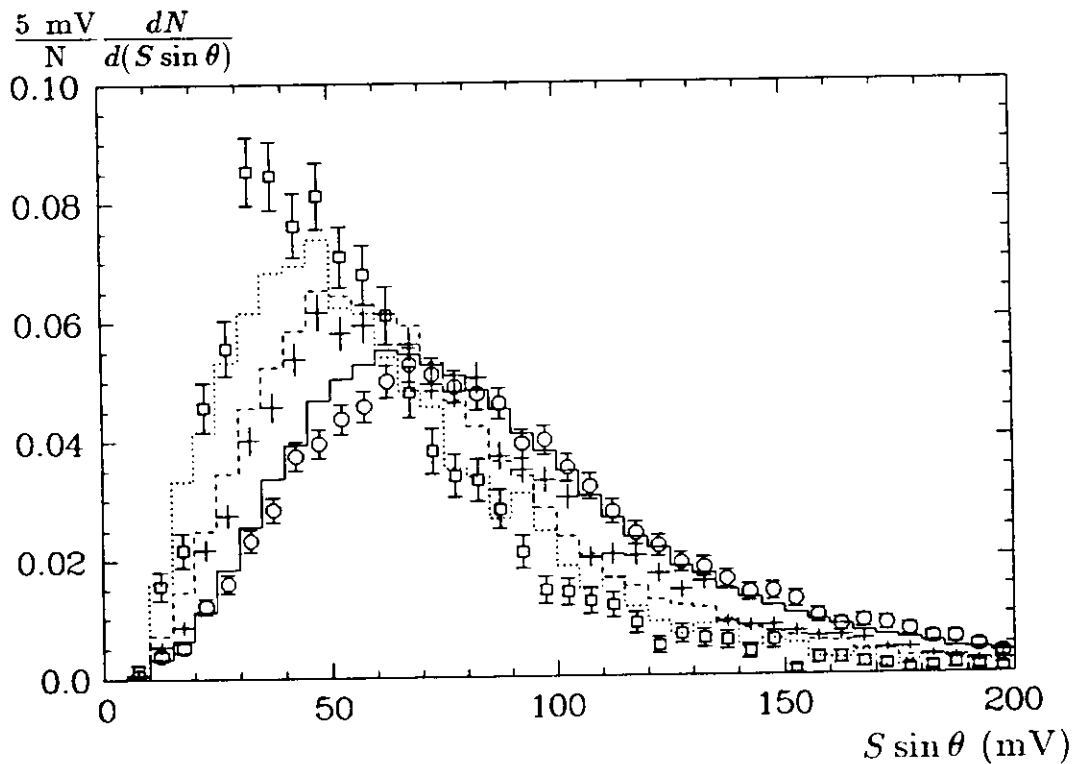


Figure B.5: Pulse height distributions  $S \sin \theta$  for electrons with  $\beta\gamma = 10000$  (data: solid, E.T.MC: open circles), for muons with  $\beta\gamma \approx 50$  (data: dashed, E.T.MC: crosses), and for muons with  $2 \leq \beta\gamma \leq 5$  (data: dotted, E.T.MC: open squares). The old Crystal Ball tube chamber MC did not simulate any  $\beta\gamma$ -dependence of  $S$ .

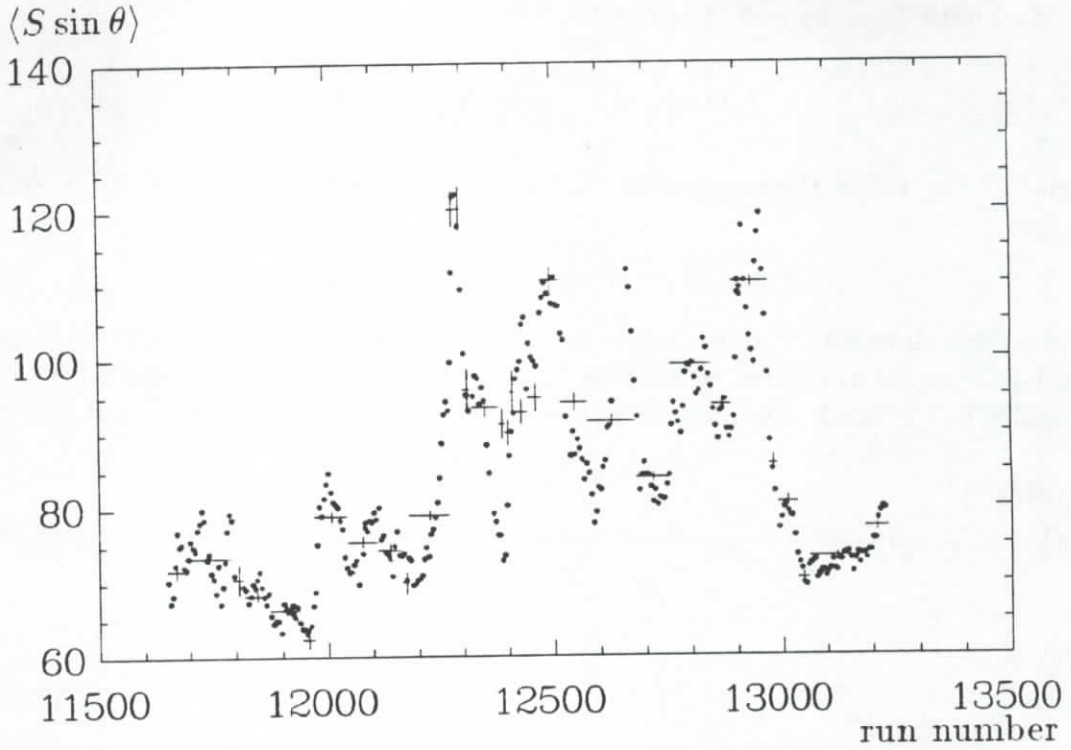


Figure B.6: Mean pulse heights of Bhabha electrons from data (dots) versus run number and their reproduction by the E.T.MC (crosses). The old Crystal Ball tube chamber MC did not simulate a run dependence within each chamber setup.

Since the  $\hat{\varepsilon}$  resolution is roughly the same for all tubes in a layer<sup>2</sup>, we do not parametrize the signal smearing  $\Delta S_i$  for each tube separately, but insert average values  $\Delta P_1 = \Delta P_2 \equiv \Delta P$  and  $\Delta g_1 = \Delta g_2 \equiv \Delta g$  for all tubes in a layer. In addition, already the initial charge  $Q_1 + Q_2$  is smeared out on the wire over a finite length  $l_{||} = l_{\perp} \cot \theta$  (cf. Fig. B.1). To account for the propagation of this smearing into the measured signals  $S_i$  we add a term  $\propto (S_1 + S_2) \cot \theta$  to the expression for  $\Delta S_i$ . It will be proven below to be justified. Thus we have

$$(\Delta S_i)^2 = (\Delta P)^2 + \left(S_i \frac{\Delta g}{g}\right)^2 - (cS \cot \theta)^2, \quad (\text{B.13})$$

where the constants  $\Delta P$ ,  $\Delta g/g$ , and  $c$  have to be determined for each layer in each simulation period.

Averaging over whole layers we find to good approximation  $\xi \approx 1$ . The experimental error on  $\hat{\varepsilon} \approx (S_1 - S_2)/(S_1 + S_2)$  then becomes

$$\begin{aligned} (\Delta \hat{\varepsilon})^2 &= \left(\frac{d\hat{\varepsilon}}{dS_1}\right)^2 (\Delta S_1)^2 + \left(\frac{d\hat{\varepsilon}}{dS_2}\right)^2 (\Delta S_2)^2 \\ &= \frac{4S_2^2}{S^4} [(\Delta P)^2 - (S_1 \frac{\Delta g}{g})^2 + (cS \cot \theta)^2] \\ &\quad - \frac{4S_1^2}{S^4} [(\Delta P)^2 - (S_2 \frac{\Delta g}{g})^2 + (cS \cot \theta)^2]. \end{aligned} \quad (\text{B.14})$$

It pays to study the behaviour of this expression at  $\hat{\varepsilon} \approx 0$  and  $|\hat{\varepsilon}| \approx 1$ . In the middle of the

<sup>2</sup>With the exception of effects induced by the DORIS synchrotron radiation discussed below.

tubes we find with  $S_1 = S_2 = S/2$  and  $\cot \theta = 0$

$$(\Delta \hat{\varepsilon})_{|\hat{\varepsilon}=0}^2 = 2 \frac{(\Delta P)^2}{S^2} + \frac{1}{2} \left( \frac{\Delta g}{g} \right)^2. \quad (\text{B.15})$$

At the end of the tubes the expression (B.14) becomes with  $S_1 = 0$ ,  $S_2 = S$ , or  $S_1 = S$ ,  $S_2 = 0$

$$(\Delta \hat{\varepsilon})_{|\hat{\varepsilon}=1}^2 = 4 \frac{(\Delta P)^2}{S^2} + (2c \cot \theta_{|\hat{\varepsilon}=1})^2. \quad (\text{B.16})$$

Both expressions show a  $1/S^2$  dependence for small  $S$  approaching a constant for large enough  $S$ . If we had omitted the term  $\propto \cot \theta$  in Eq. (B.13), we would have found  $(\Delta \hat{\varepsilon})^2 \rightarrow 0$  for  $S \rightarrow \infty$  and  $|\hat{\varepsilon}| \rightarrow 1$ . Such a behaviour is not observed in the data (see Fig. B.7).

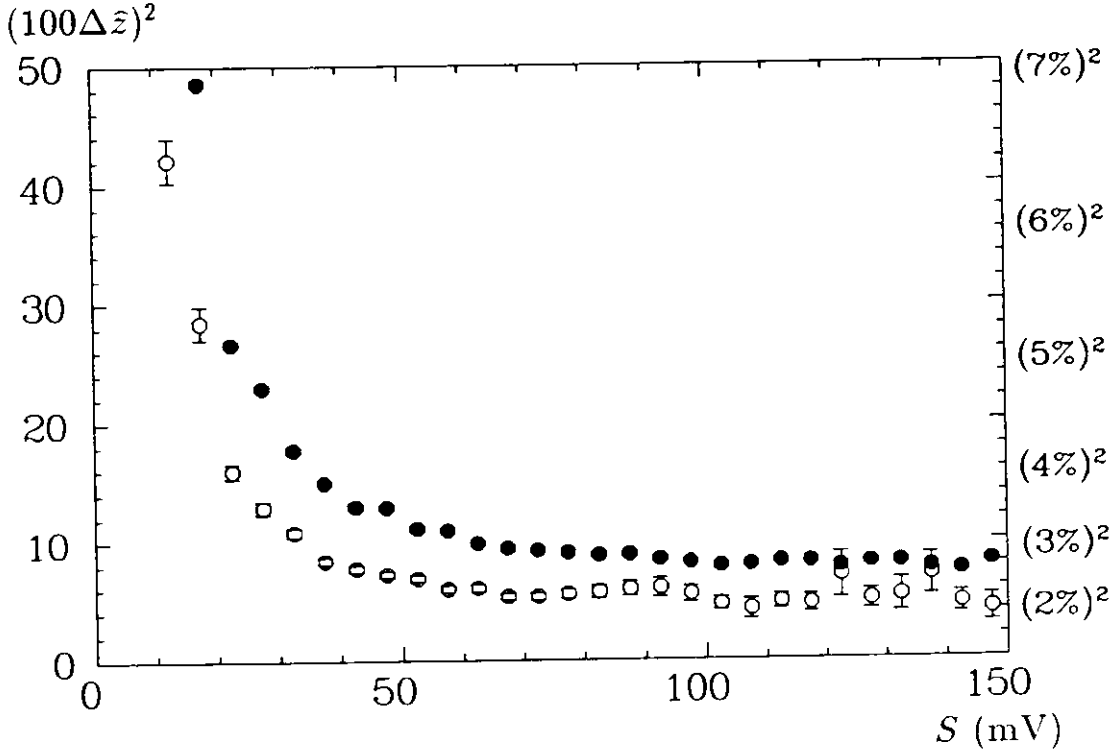


Figure B.7: Mean squared  $\hat{\varepsilon}$  deviation from the fitted track versus total pulse height  $S$  for tube hits in Bhabha events. The open circles are for  $\hat{\varepsilon} \approx 0$  and the filled circles are for  $|\hat{\varepsilon}| \approx 0.8$ .

For large pulse heights  $S$  we find instead the resolution  $(\Delta \hat{\varepsilon})^2$  for  $|\hat{\varepsilon}| \rightarrow 1$  to be even larger than around  $\hat{\varepsilon} \approx 0$ . From the ratio of both curves in Fig. B.7 and Eqs. (B.15) and (B.16) we find for the two outermost double layers a value of  $c \approx 0.4\Delta g/g$  stable for all run periods. We assume that the inner double layers can be described with the same value of  $c$ . (For these layers we cannot determine  $c$  from the resolution at  $|\hat{\varepsilon}| \approx 1$ , since the tracks of all particles entering the Main Ball intersect the chambers within  $|\hat{\varepsilon}| \lesssim 0.35$  and  $|\hat{\varepsilon}| \lesssim 0.45$ , respectively.)

Beyond  $|\hat{\varepsilon}| = 0.8$  the resolution is again influenced by edge effects. We parametrize

$$c = 0.4 \max \left( \frac{\Delta g}{g}, 0.8(|\hat{\varepsilon}| - 0.795) \right), \quad (\text{B.17})$$

so that  $c = 0.4\Delta g/g$  is valid for at least all  $|\hat{\varepsilon}| < 0.795$ . The functional dependence for  $|\hat{\varepsilon}| \rightarrow 1$  has been deduced from the data.

There are two more effects, which call for a modification of Eq. (B.13). First,  $\Delta\hat{z}$  is roughly identical for all tubes only within each of the outer double layers. For the two innermost double layers it reveals spikes around  $\varphi = 0$  and  $\varphi = 180^\circ$  (see Fig. B.13), which originate from small additional background charge deposits somewhere along the wire. They are caused by photo-electrons from synchrotron radiation, which is preferably emitted in the plane of the storage ring. These background charges are even too low to be sufficiently modeled by adding hits from background events to each MC event (cf. Section 3.5). They instead have to be put in by hand by parametrizing the  $\varphi$ -dependence of the simulated  $\Delta\hat{z}$  resolution as

$$\Delta\hat{z}(\varphi) = \Delta\hat{z}(90^\circ)(\sin\varphi)^{-0.35} \quad \text{for layers \#1 - \#4.} \quad (\text{B.18})$$

Second, the shape of the  $\Delta\hat{z}$  distribution is not Gaussian, but reveals tails both for the proportional and the streamer tubes (see Fig. B.10). The tails are more pronounced for the inner layers indicating also a beam-related origin. In the MC simulation we include both effects most easily by modifying the  $S_i\Delta g/g$  term in Eq. (B.13) as described below.

Summarizing, we obtain the smeared measured pulse heights  $S_1^*$  and  $S_2^*$  in the following way. First, according to the  $\hat{z}$  position of the hit, the total pulse height  $S$  is divided into  $S_1$  and  $S_2$ , which are essentially given by

$$S_1 \approx (1 + \hat{z})\frac{S}{2} \quad \text{and} \quad S_2 \approx (1 - \hat{z})\frac{S}{2}. \quad (\text{B.19})$$

In fact, all corrections from finite amplifier impedances and gain ratios  $\xi \neq 1$  are properly included in the program. The values of these parameters are taken from the data calibration files.

Second, the pulse heights are smeared by adding three randomly chosen quantities

$$S_i^* = S_i + S_Q + S_g + P_i, \quad (\text{B.20})$$

each corresponding to a term in Eq. (B.13). The initial charge smearing  $S_Q$  is modeled as a Gaussian with a probability distribution of

$$p(S_Q)dS_Q = \frac{1}{\sqrt{2\pi}\sigma_Q} e^{-\frac{1}{2}\left(\frac{S_Q}{\sigma_Q}\right)^2} dS_Q \quad (\text{B.21})$$

$$\sigma_Q = cS \cot\theta, \quad (\text{B.22})$$

where  $c$  is given in Eq. (B.17). The gain smearing  $S_g$  is described by a Gaussian with smoothly attached power tails according to

$$p(S_g)dS_g = \begin{cases} k(n)e^{-\frac{1}{2}\left(\frac{S_g}{\sigma_g}\right)^2} dS_g & \text{for } \left|\frac{S_g}{\sigma_g}\right| \leq \sqrt{n} \\ k(n)\left(\sqrt{\frac{n}{2}}\left|\frac{S_g}{\sigma_g}\right|\right)^{-n} dS_g & \text{for } \left|\frac{S_g}{\sigma_g}\right| > \sqrt{n} \end{cases} \quad (\text{B.23})$$

$$\sigma_g = \begin{cases} S_i \frac{\Delta g}{g} (\sin\varphi)^{-0.35} & \text{for layers \#1 - \#4} \\ S_i \frac{\Delta g}{g} & \text{for layers \#5 - \#8,} \end{cases} \quad (\text{B.24})$$

where  $k(n)$  is a normalization constant. For the power  $n$  we find

$$n = \begin{cases} 1.5 & \text{for layers} & \text{streamer} & \text{proportional} \\ 1.6 & \text{for layers} & 1, 2 & 1, 2 \\ 2.0 & \text{for layers} & 3, 4 & 3, 4 \\ 3.0 & \text{for layers} & 5, 6 & 5, 6, 7, 8. \end{cases} \quad (\text{B.25})$$

Finally, the pedestals are added at each end via

$$p(P_i)dP_i = \frac{1}{\sqrt{2\pi}\sigma_p} \exp\left[-\frac{1}{2}\left(\frac{P_i - \langle P_i \rangle}{\sigma_p}\right)^2\right] dP_i \quad (\text{B.26})$$

$$\sigma_p = \Delta P, \quad (\text{B.27})$$

where the mean pedestals  $\langle P_i \rangle$  are taken from the data calibration files.

The resulting pulse heights  $S_i^*$  can then be treated like real data, i.e. pedestal subtraction (Eq. (B.2)) and  $z$ -reconstruction (Eq. (B.11)) are done by the same programs using the data calibration files.

Since  $c$  and  $\Delta g/g$  are related via Eq. (B.17), the basic parameters for the simulation of the pulse height smearing are  $\Delta g/g$  for the streamer tubes, and both  $\Delta g/g$  and  $\Delta P$  for the proportional tubes. (The pulse heights of the streamer tubes (Fig. B.2) are so large that the  $\hat{z}$ -resolution has already approached a constant value independent from  $S$  (Fig. B.7), and thus from  $\Delta P$  (Eqs. (B.15) and (B.16)).) These input parameters have to be determined from the data separately for each layer and each simulation period.

The extraction from the measured resolutions, like those in Fig. B.7, is not straight forward. First, the measured  $(\Delta\hat{z})^2$  in a given layer is calculated as the mean square distance of the hits to the fitted tracks. It thus includes the resolution of the TAGTRK tracking routine, which in turn depends on the  $z$ -resolution in all other layers. Second, even for ideal resolution, the observed  $(\Delta\hat{z})^2$  at high pulse heights  $S$  and  $\hat{z} \approx 0$  (Eq. (B.15)) is actually not equal to  $(\Delta g/g)^2/2$ , but is increased due to the power tails in  $p(S_g)$  in Eq. (B.23).

In order to extract  $\Delta g/g$  and  $\Delta P$ , we fit the measured  $(\Delta\hat{z}(S))_{\hat{z}\approx 0}^2$  (e.g. the open circles in Fig. B.7) with the function

$$(\Delta\hat{z})_{\hat{z}\approx 0}^2 = 2\frac{a^2}{S^2} + \frac{1}{2}b^2, \quad (\text{B.28})$$

where  $a$  and  $b$  are free parameters (compare Eq. (B.15)). These parameters are a measure for  $\Delta P$  and  $\Delta g/g$ . We now search for that pair of values  $(\Delta P, \Delta g/g)$ , which has to be plugged into the MC simulation, so that the MC output is described by the same values  $(a, b)$  as the data. For each chamber setup and each layer we put 4 values of  $\Delta P$  and  $\Delta g/g$  into a MC simulation of  $e^+e^- \rightarrow e^+e^-$  and analyze the MC output like our Bhabha events. Fitting the above function (B.28) to the plot  $(\Delta\hat{z}(S))^2$  obtained from our MC events, we find the relations  $a(\Delta P)$  and  $b(\Delta g/g)$ . An example for one layer of the proportional chamber setup is shown in Fig. B.8. These dependences are fitted for each layer with the empirical function

$$\frac{a}{\text{mV}} = A \sqrt[p]{\frac{\Delta P}{\text{mV}}} \quad \text{and} \quad \frac{b}{\%} = B \sqrt[q]{\frac{\Delta g/g}{\%}}. \quad (\text{B.29})$$

Depending on the layer number we find  $A=0.8-1.0$ ,  $p=1.6$  and  $B=4-7$ ,  $q=2-3$  for the proportional tubes and slightly larger values of  $q=3-5$  for the streamer tubes.

The parameters  $\Delta P$  and  $\Delta g/g$  for each layer in each of the 220 simulation periods are now obtained by fitting the function (B.28) to the measured distributions  $(\Delta\hat{z}(S))_{\hat{z}\approx 0}^2$  as described above. We then convert the fit results  $a$  and  $b$  into the corresponding parameters  $\Delta P(a)$  and  $\Delta g/g(b)$  with the help of Eq. (B.29).

The distribution of these final input parameters for all layers in all periods is shown in Fig. B.9. We find typical values of  $\Delta P \approx 0.6$  mV and  $\Delta g/g \approx 0.5\%$  considerably varying, however, from period to period. The pedestal voltages span a smaller region than the gain



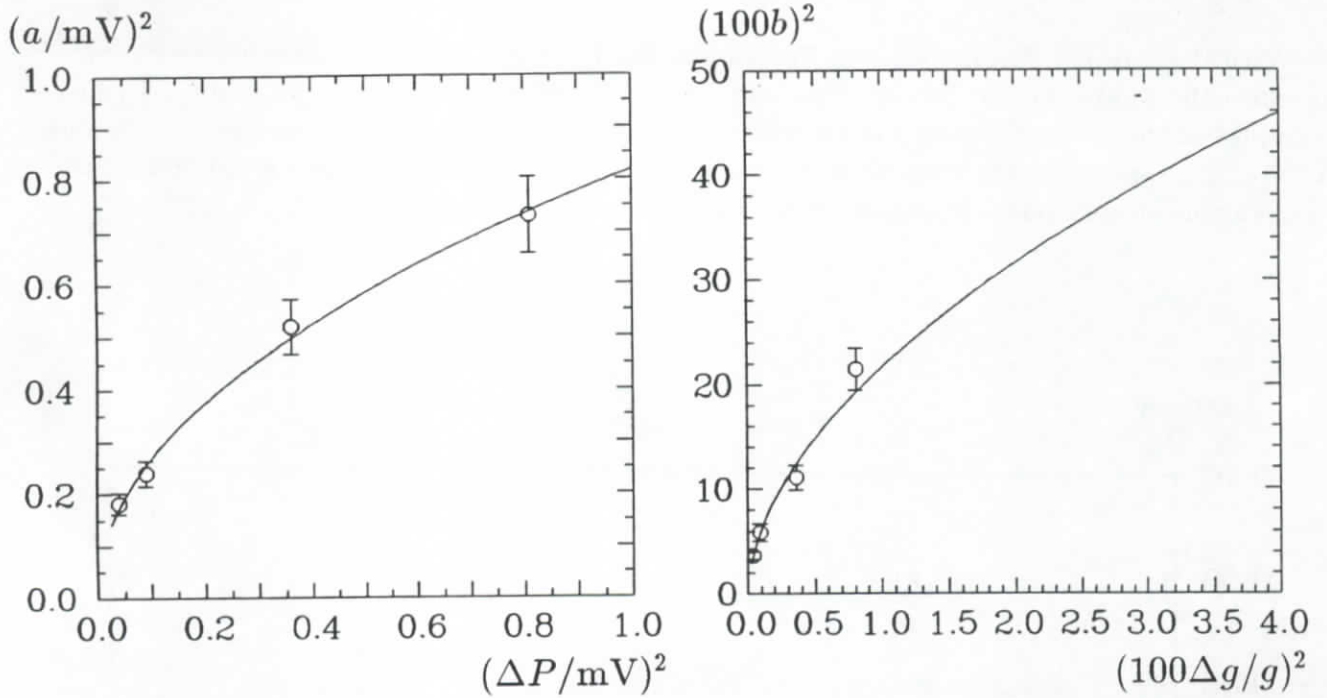


Figure B.8: Typical relation between the measured z-resolution parameters ( $a, b$ ) and the charge smearing parameters ( $\Delta P, \Delta g/g$ ) in the E.T.MC simulation.

Number of occurrences

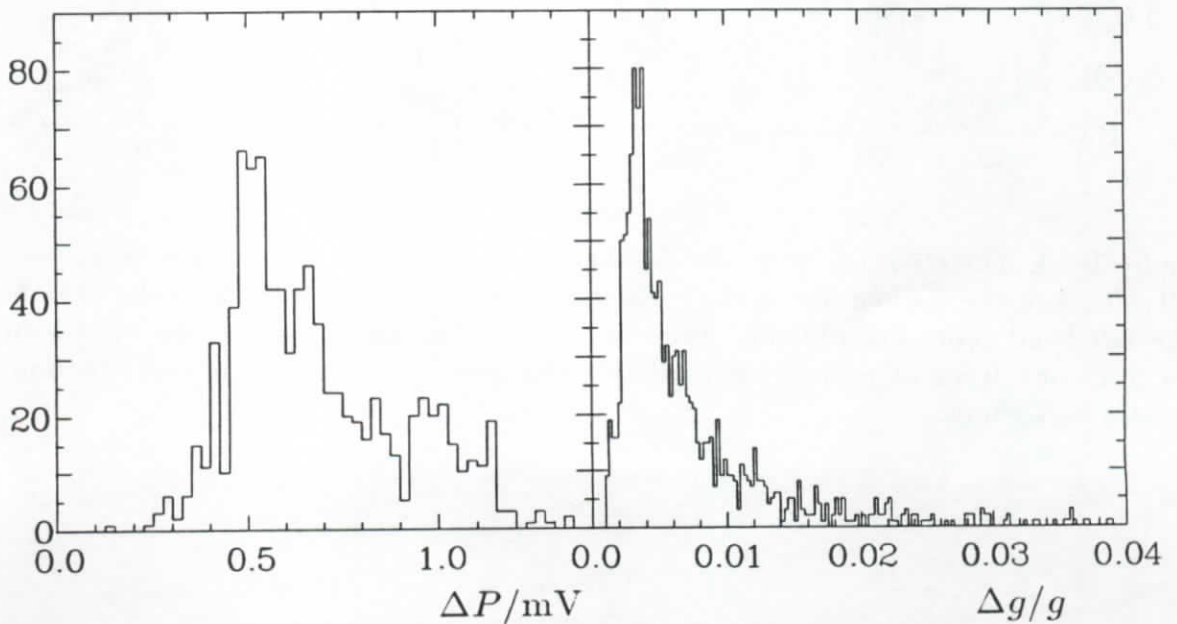


Figure B.9: The distribution of the charge smearing parameters  $\Delta P$ , and  $\Delta g/g$  entering the E.T.MC simulation.

widths. The range of gain widths even continues outside of Fig. B.9 up to  $\sim 8\%$  for 8 simulation periods ( $\cong 15 \text{ pb}^{-1}$  of data), where the tube chamber ADC was nonlinear<sup>3</sup>.

With these input parameters and Equations (B.20)–(B.27) and (B.17) above, we can now simulate the shape of the  $z$ -resolution and its dependence on  $S$ ,  $\varphi$ ,  $\hat{z}$ , and time. Typical examples of these dependences are shown in figs B.10 to B.14. The “microscopic” treatment of the charge smearing together with the correct charge distribution enables us to predict the  $z$ -resolution for any particle momentum, direction, and running conditions.

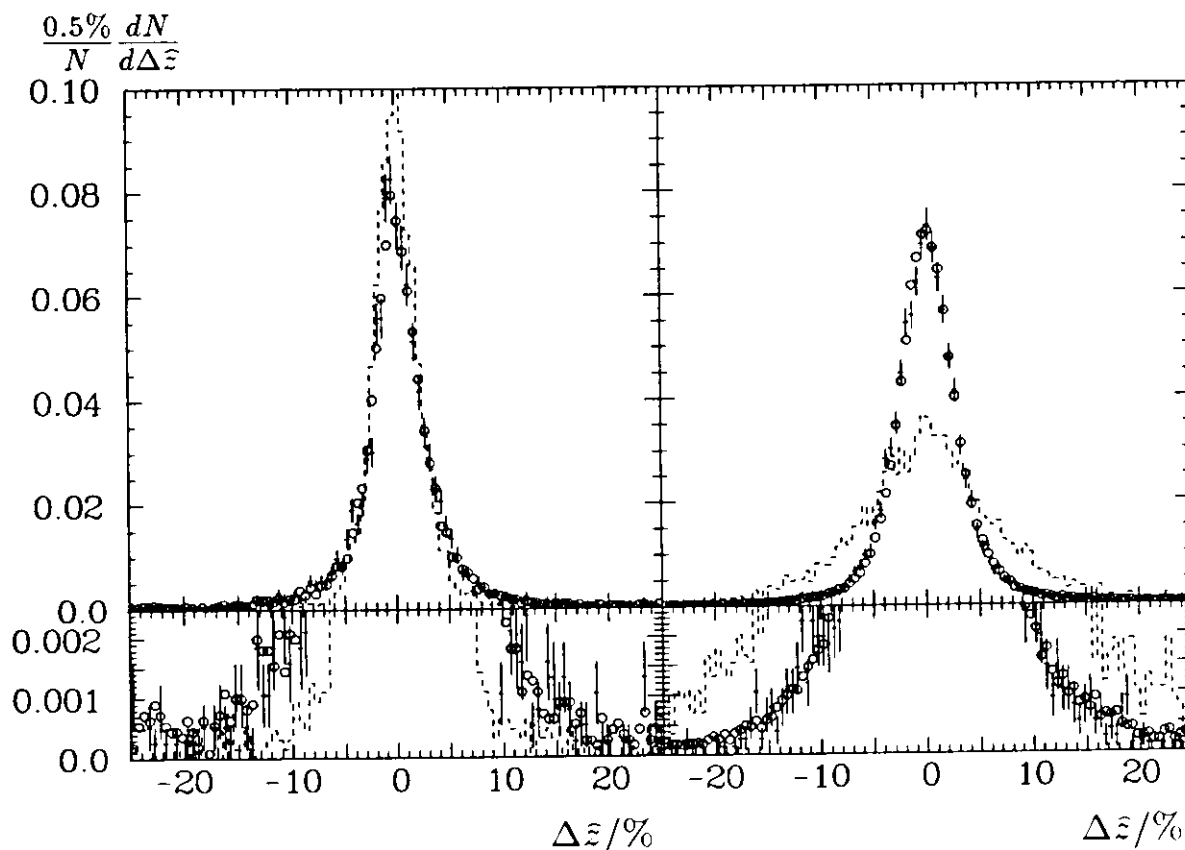


Figure B.10: Distribution of  $\Delta\hat{\varepsilon}$  for Bhabha electrons. Open circles are data, crosses are E.T.M.C, and the dashed line is the prediction of the older Crystal Ball tube chamber MC. The left-hand plots are obtained from one layer of streamer tubes, the right-hand plots are from one layer of proportional tubes. The lower plots show the reproduction of the non-Gaussian tails.

<sup>3</sup>Detailed systematic effects of this bad ADC, like nonlinearity only for certain values of  $S_i$ , corresponding to certain ranges in  $\hat{z}$ , are not modeled, however.

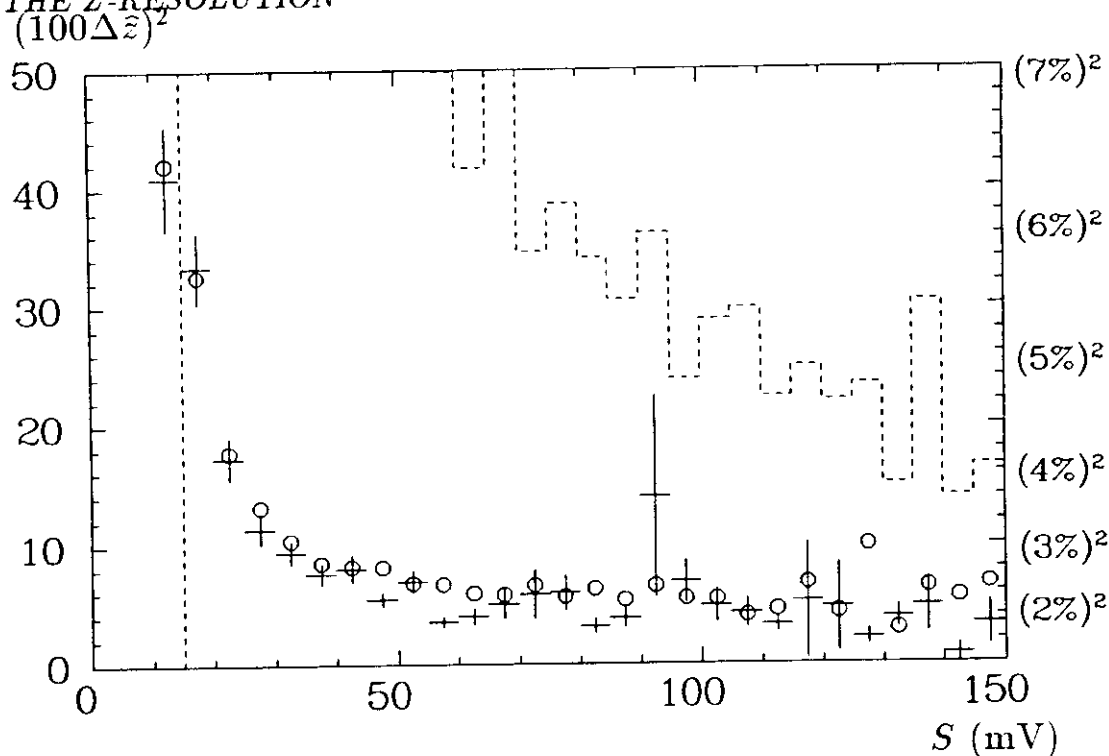


Figure B.11: Mean squared  $\hat{z}$  deviation from the fitted track for  $\hat{z} \approx 0$  versus total pulse height  $S$  for Bhabha electrons in one layer for one period of the proportional chamber setup. Open circles are data, crosses are E.T.MC, and the dashed line is the prediction of the older Crystal Ball tube chamber MC.

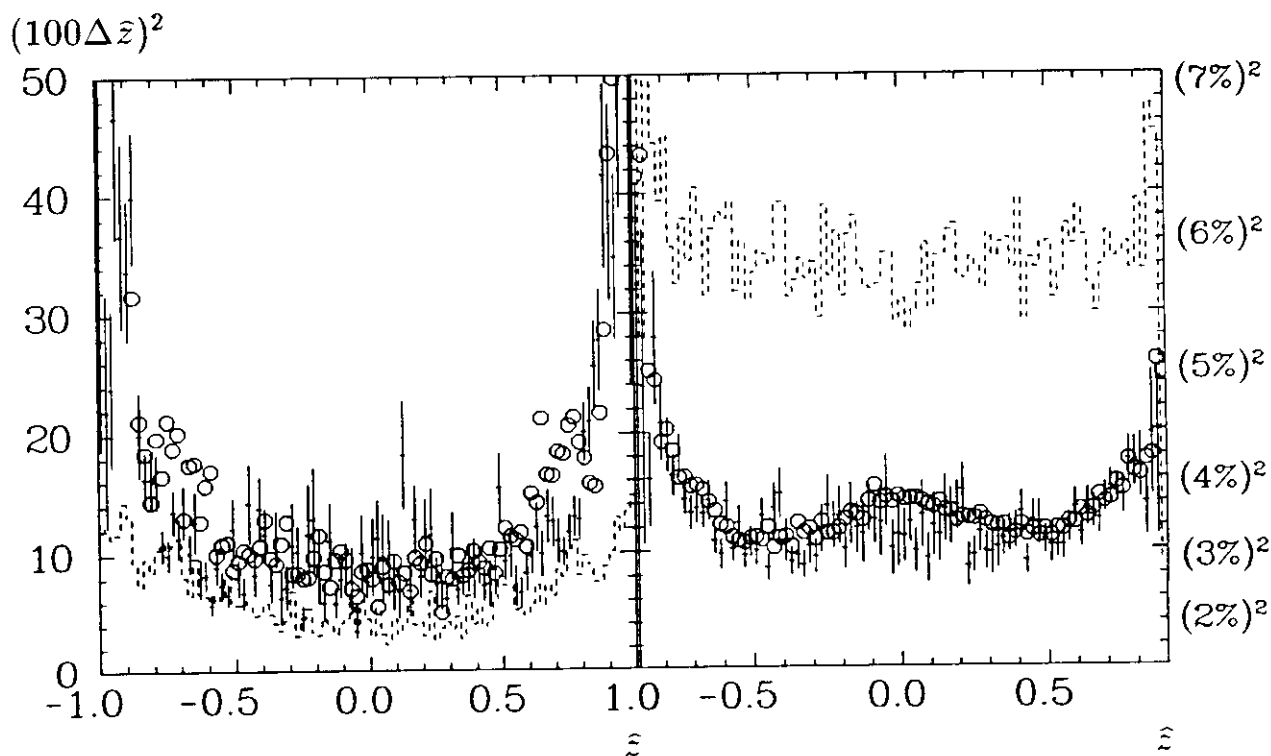


Figure B.12: Mean squared  $\hat{z}$  deviation from the fitted track versus  $\hat{z}$  for Bhabha electrons. Open circles are data, crosses are E.T.MC, and the dashed line is the prediction of the older Crystal Ball tube chamber MC. The left-hand plot is obtained from one layer of streamer tubes, the right-hand plot is from one layer of proportional tubes.

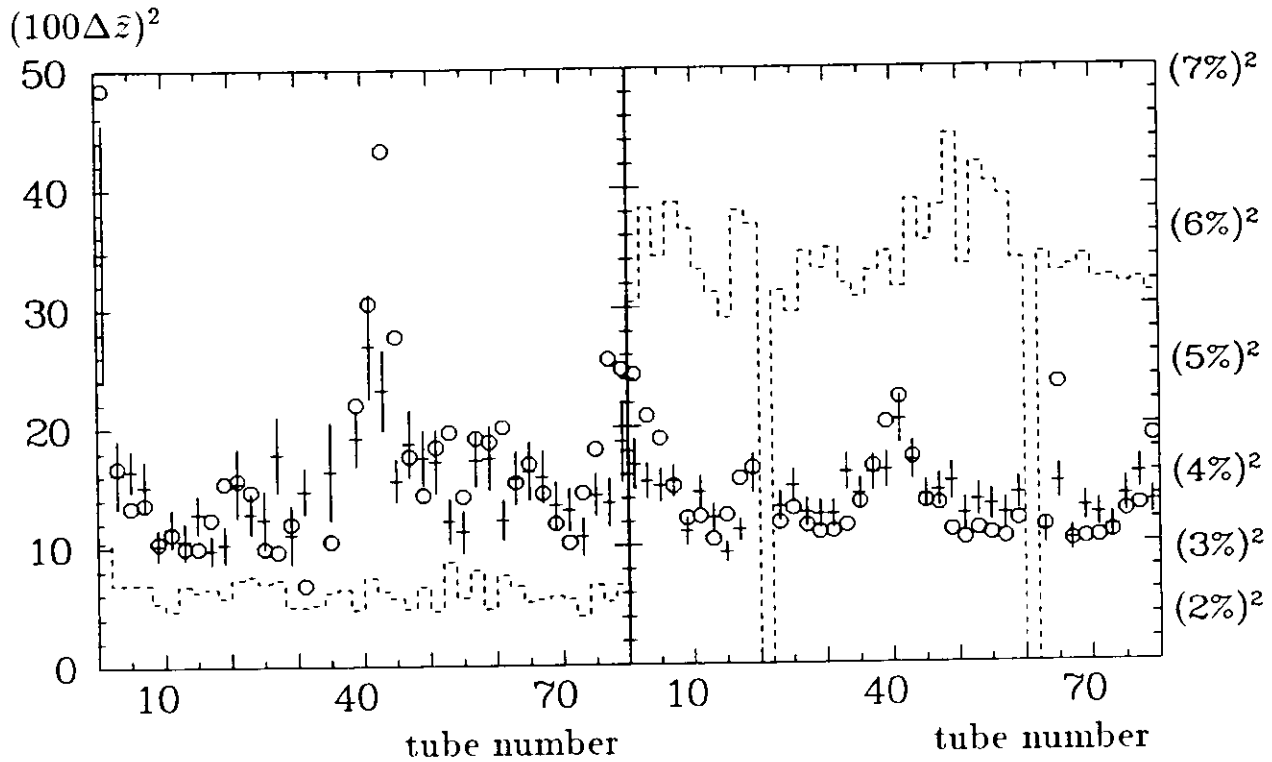


Figure B.13: Mean squared  $\hat{z}$  deviation from the fitted track versus  $\varphi$ , expressed in the tube number, for Bhabha electrons. The tube number 0 corresponds to  $\varphi = 0$ , the number 40 corresponds to  $\varphi = \pi$ . Open circles are data, crosses are E.T.MC, and the dashed line is the prediction of the older Crystal Ball tube chamber MC. The left-hand plot is obtained from one layer of streamer tubes, the right-hand plot is from one layer of proportional tubes. Missing entries on the right-hand side correspond to nonexistent tube numbers.

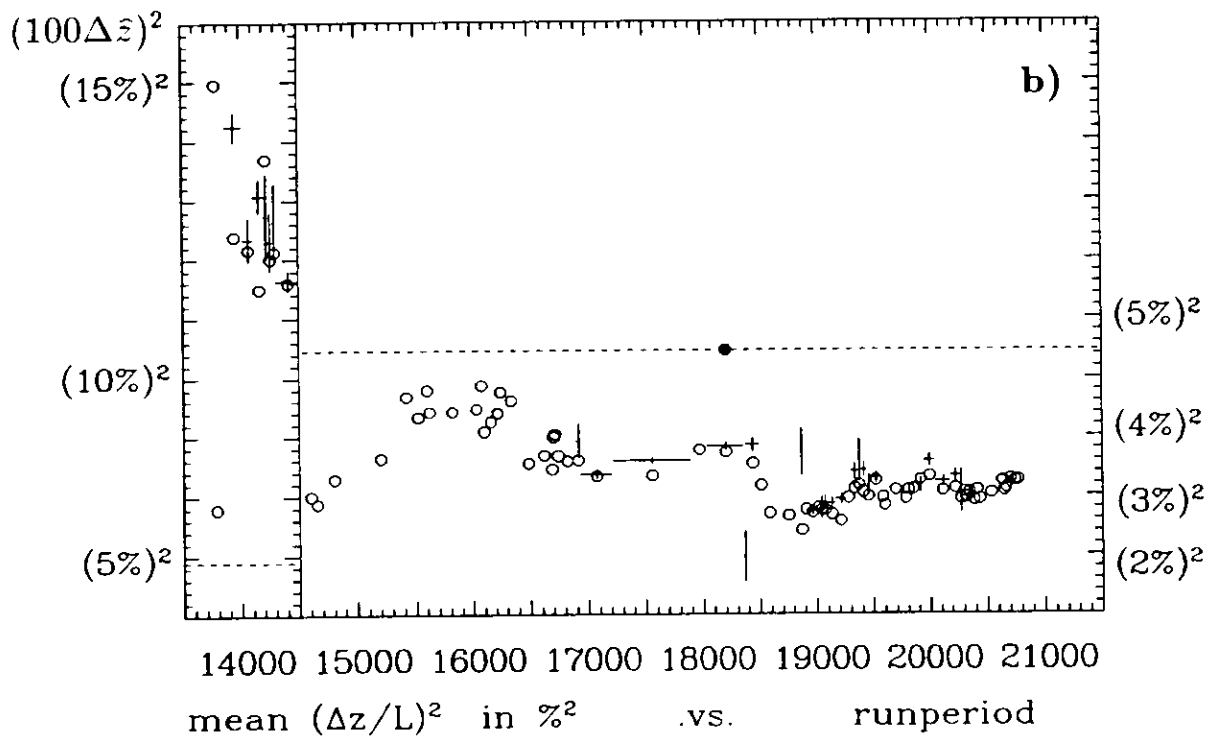
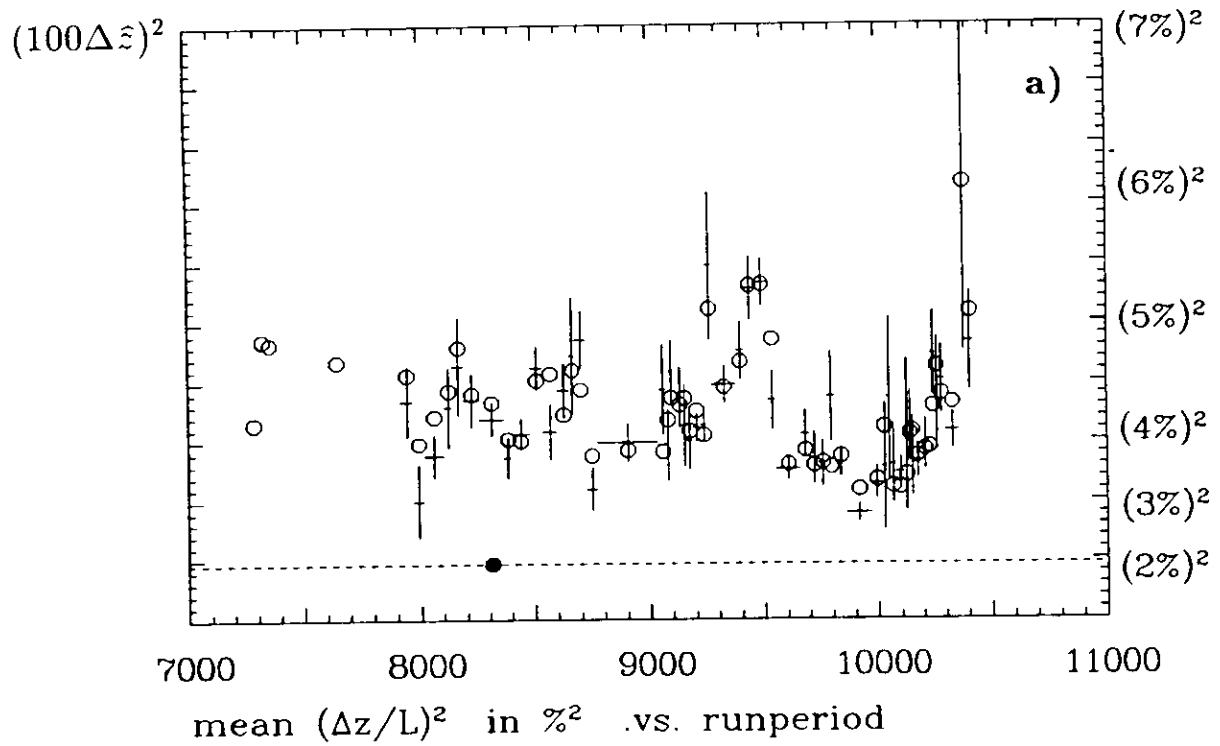


Figure B.14: Mean squared  $\varepsilon$  deviation of hits in layer #1 from the fitted electron tracks for run periods in the setup of streamer tubes (a) and proportional tubes (b). Open circles are data, crosses are *E.T.MC.* and the dashed line is the (constant) prediction of the older Crystal Ball tube chamber MC. Not all periods were included in the *E.T.MC.* simulation. In runs 13872 to 14566 a bad tube chamber ADC was installed.

### B.3 The Hit Efficiencies

The tube chamber simulation of pulse height and charge smearing is completed by the simulation of the hit efficiency  $\epsilon_{hit}$ , i.e. the probability that we will find a tube hit from a charged particle traversing a tube chamber layer. This probability is a function of tube geometry, pulse height cut  $S_{cut}$ , and of hardware features like edge effects  $\epsilon_e(\hat{d})$ ,  $\epsilon_e(\hat{z})$  or hardware inefficiencies of single tubes

$$\epsilon_{hit} = \epsilon(\text{geometry}, S_{cut}, \epsilon_{hardware}(\text{tube}, \hat{z}, \hat{d})). \quad (\text{B.30})$$

The tube geometry is implemented with tube positions taken from the  $\varphi$  calibration files, tube radii  $\rho = 5.6$  mm and 6.1 mm, and tube wall thicknesses of  $\rho - r = 0.08$  mm and 0.18 mm for the streamer and proportional tubes, respectively. (The streamer tubes in the innermost double layer had radii of  $\rho = 4.8$  mm, only.) Having simulated the tube geometry and the pulse height distributions correctly, a proper efficiency reproduction is obtained for those hits which are not influenced by edge effects or by bad hardware. We account for possible hardware faults (bad or broken amplifiers, bad or broken wires) by a factor  $\epsilon_{tube}$  for each single tube. This factor ranges from zero for dead tubes to one for fully efficient tubes. It is obtained for each tube in each of the 220 periods from monitoring tracks of Bhabha electrons, which intersect the respective tube in a large enough distance from its edges, i.e. at  $|\hat{d}| < 0.4$  and  $|\hat{z}| < 0.8$ . In contrast to the proportional tubes, where values below one are found for few tubes, only, considerable hardware inefficiencies are encountered for most of the streamer tubes. They were connected with the growth of organic molecules on the wires as mentioned in the beginning. Examples of  $\epsilon_{tube}$  values in one simulation period are plotted for one layer of streamer and proportional tubes, respectively, in Fig. B.15.

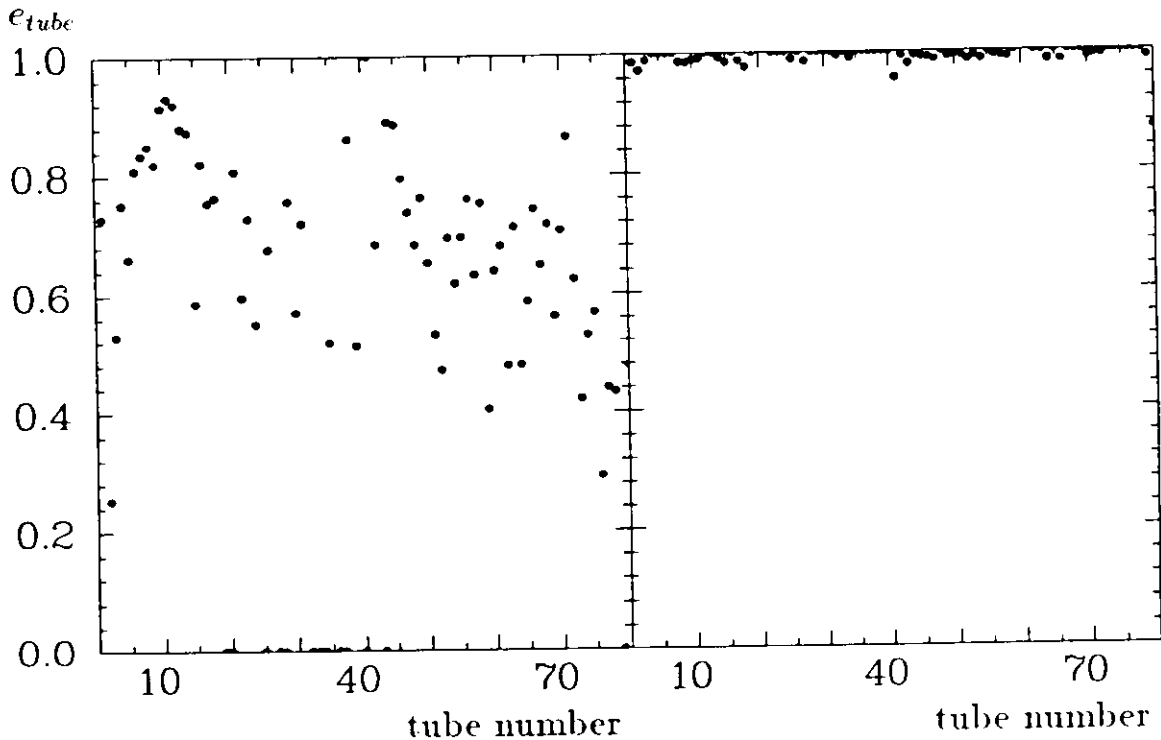


Figure B.15: Example for  $\epsilon_{tube}$  parameters entering the E.T.MC simulation. The left-hand side is for a layer of streamer tubes, the right-hand side for a layer of proportional tubes.

Additional inefficiencies arise at the end of the tubes and near their walls. We find that the decrease of efficiency at the end of the tubes cannot be completely attributed to the decrease in pulse height (cf. Eq. (B.9)). Instead, we have to introduce an additional edge correction  $\epsilon_c(\hat{z})$

$$\epsilon_c(\hat{z}) = \begin{cases} 1 & \text{for } |\hat{z}| \leq 0.83 \\ 1 - \frac{|\hat{z}| - 0.83}{0.93 - 0.83} & \text{for } |\hat{z}| > 0.83 \end{cases} \quad (\text{B.31})$$

Beyond  $|\hat{z}| = 0.93$  the tubes seem not to be active at all. This parametrization reproduces the functional dependence  $\epsilon(\hat{z})$ , which is found in the data (Fig. B.16).

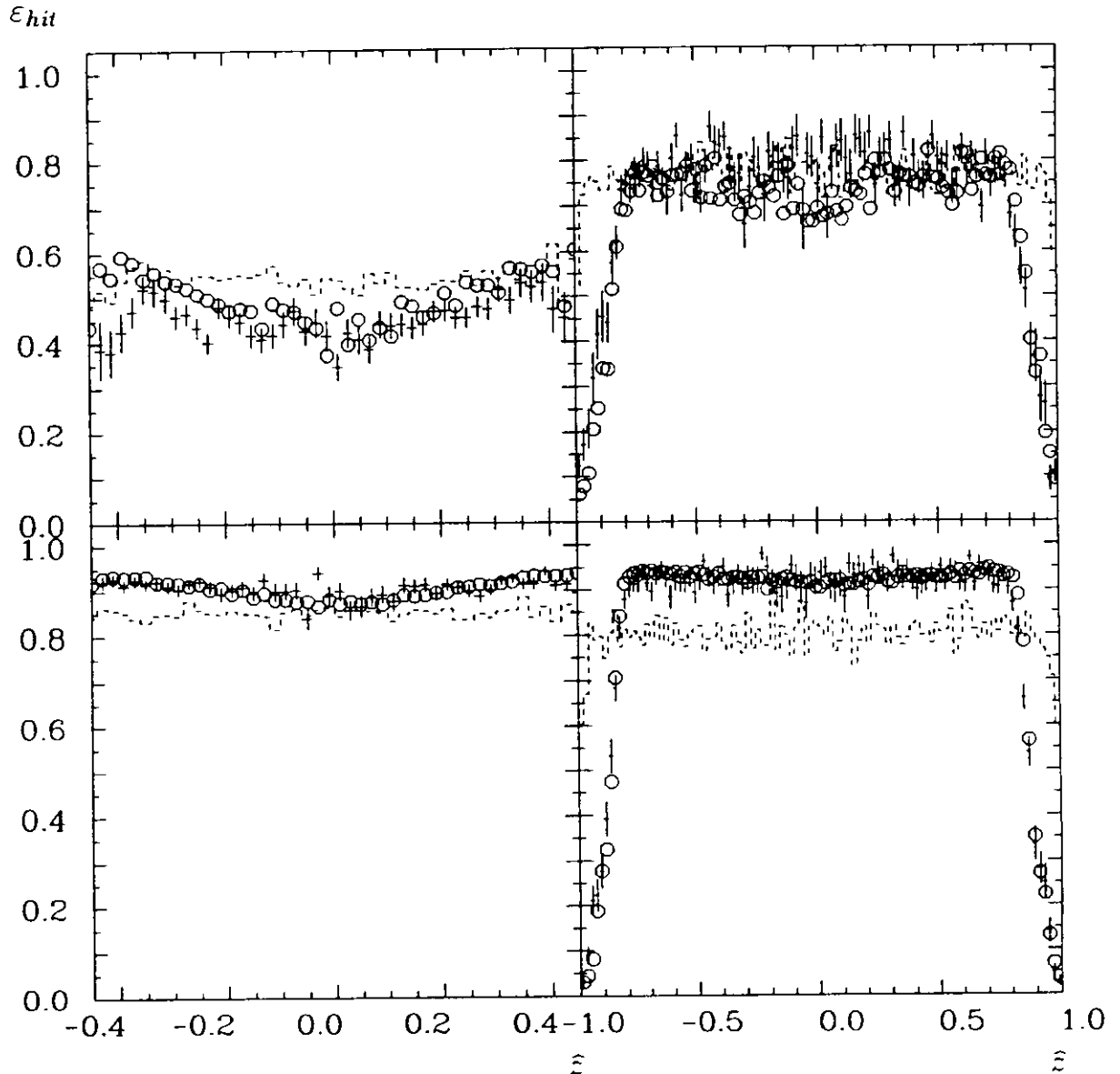


Figure B.16: The hit efficiency as a function of the measured  $\hat{z}$  for streamer tubes (upper plots) and proportional tubes (lower plots) along the  $z$ -axis of the tubes. Open circles are data, crosses are E.T.M.C., and the dashed line is the prediction of the older Crystal Ball tube chamber MC. The left-hand side is plotted for one of the innermost layers, the right-hand side for one of the outermost layers.

A success of our pulse height simulation is, that we do not need any edge correction  $\epsilon_c(\hat{d})$  for the proportional tubes. Instead, the functional dependence is fully explained by the pulse height cut  $S_{cut}$  rejecting more hits at large  $|\hat{d}|$ , since the path length  $l$  decreases as a function of  $|\hat{d}|$ . For the streamer tubes, however, we have to introduce an edge function  $\epsilon_c(\hat{d})$ , which has a width of  $\sim 0.1r$ , i.e. at  $\hat{d} = 0.9$  we model a 50% inefficiency. The reason for an inefficiency near the tube walls may be connected with a higher recombination probability of the ionized gas atoms. The resulting MC reproduction of  $\epsilon_{hit}(|\hat{d}|)$  is shown in Fig. B.17.

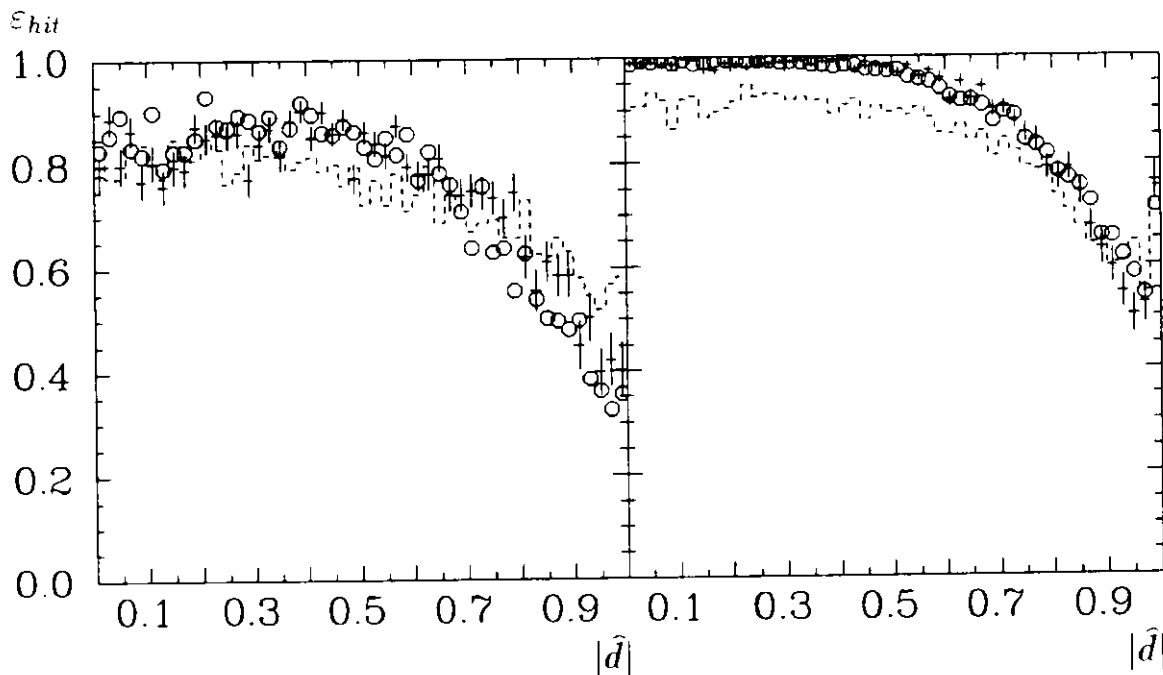


Figure B.17: The hit efficiency as a function of the measured  $|\hat{d}|$  for streamer tubes (left-hand side) and proportional tubes (right-hand side). Due to the finite resolution  $\Delta\hat{d}$  the measured efficiency at  $|\hat{d}|=1$  is not zero. Open circles are data, crosses are E.T.MC, and the dashed line is the prediction of the older Crystal Ball tube chamber MC.

In the E.T.MC simulation, we simulate a hit for a traversed tube with a probability  $\epsilon_{hardware}$  obtained from the product of the  $\epsilon$ -factors derived above

$$\epsilon_{hardware} = \epsilon_{tube} \epsilon_c(\hat{z}) [\epsilon_c(\hat{d})]. \quad (\text{B.32})$$

The factor in brackets is for streamer tubes, only. Together with the effect from the pulse height cut  $S_{cut}$  this simulation correctly reproduces the hit efficiency  $\epsilon_{hit}$  (Eq. B.30) for each tube together with its time dependence.

## B.4 Short Summary

We obtain a comprehensive reproduction of the tube chamber performance and its time dependence by extracting basic simulation parameters from Bhabha events. For each of 220 data periods and each of the 6(8) layers we determine

- hardware tube eff.  $\sim 100$  tubes/layer  $\times$  6(8) layers  $\times$  220 periods  $\approx$  150.000 parameters
- pulse height dist.  $\sim 50$  bins/layer  $\times$  6(8) layers  $\times$  220 periods  $\approx$  75.000 parameters
- gain widths  $\approx$  6(8) layers  $\times$  220 periods  $\approx$  1.500 parameters
- pedestal widths  $\approx$  6(8) layers  $\times$  220 periods  $\approx$  1.500 parameters
- other constants  $\approx$  30 parameters.



For each charged particle these parameters are employed as follows.

- Find the tubes intersected by the particle track.
- Calculate the hardware efficiency

$$\varepsilon_{hardware}(\text{tube}, \hat{z}, \hat{d}, \text{layer}, \text{period}) \quad \text{from Eq. (B.32),}$$

and decide, if a hit is simulated.

- Generate a pulse height

$$S(\beta\gamma, \theta, \hat{d}, \hat{z}, \text{layer}, \text{period}) \quad \text{from Eqs. (B.7) and (B.8).}$$

- Perform a charge division (Eq. (B.19)) and smear the divided charges  $S_1$  and  $S_2$  by

$$\Delta S_i(S_i, \varphi, \theta, \hat{z}, \text{layer}, \text{period}) \quad \text{from Eqs. (B.20) - (B.27).}$$

For photons we model the conversion before each layer  $j$  according to its probability  $p_{conv}$  induced by the traversed material thickness  $t = t_j / \sin\theta$

$$p_{conv}(E_\gamma) = \frac{7}{9} \frac{t}{X_0} K(E_\gamma). \quad (\text{B.33})$$

$X_0$  is the radiation length of the material, and  $t_j$  is the summed material thickness before layer  $j$  including the beam pipe and the tube support structure. E.g. in our three different chamber setups the summed material before the outermost layer is  $t_6 = 0.047X_0$ ,  $t_6 = 0.063X_0$ , and  $t_8 = 0.088X_0$  for the old and intermediate setups with 3 double layers and the new setup with 4 double layers, respectively. The function  $K(E_\gamma)$  is plotted in Fig. B.18. For the pulse height simulation in proportional tubes, a converted photon is treated as two electrons with  $E_e = E_\gamma/2$ .

The application of the E.T.MC in the frame of the Crystal Ball MC is very comfortable. An arbitrary subsample of the 220 periods can be selected for the simulation. The number of events simulated according to each selected period is determined from the integrated luminosity in each period. Background hits in the tube chambers are merged on the MC events from those DBM background events (sections 3.2 and 3.5), which have been collected exactly in the simulated data period. We are thus able to create a realistic picture of the tube chamber performance for any subsample of Crystal Ball data.

## B.5 Systematic Errors

To calculate systematic errors of Crystal Ball data analyses, the systematic errors of the E.T.MC for the description of inclusive quantities have to be known rather than the precision for single hits. These inclusive quantities are the efficiency to identify charged particles ("tagging efficiency"), the probability that enough hits are found to perform a fit of the track ("tracking efficiency"), the precision of this direction measurement, and the probability for tagging photons due to photon conversion. These items as well as errors for their ratios in different run periods are discussed in the following. We derive the errors from a comparison of the simulated events for  $e^+e^- \rightarrow \mu^+\mu^-$  with their E.T.MC prediction. Since the E.T.MC simulation relies on input from Bhabha events  $e^+e^- \rightarrow e^+e^-$  only, such a comparison tests also the precision of the momentum dependence of the simulation between  $\beta\gamma=10000$  and  $\beta\gamma=50$ .

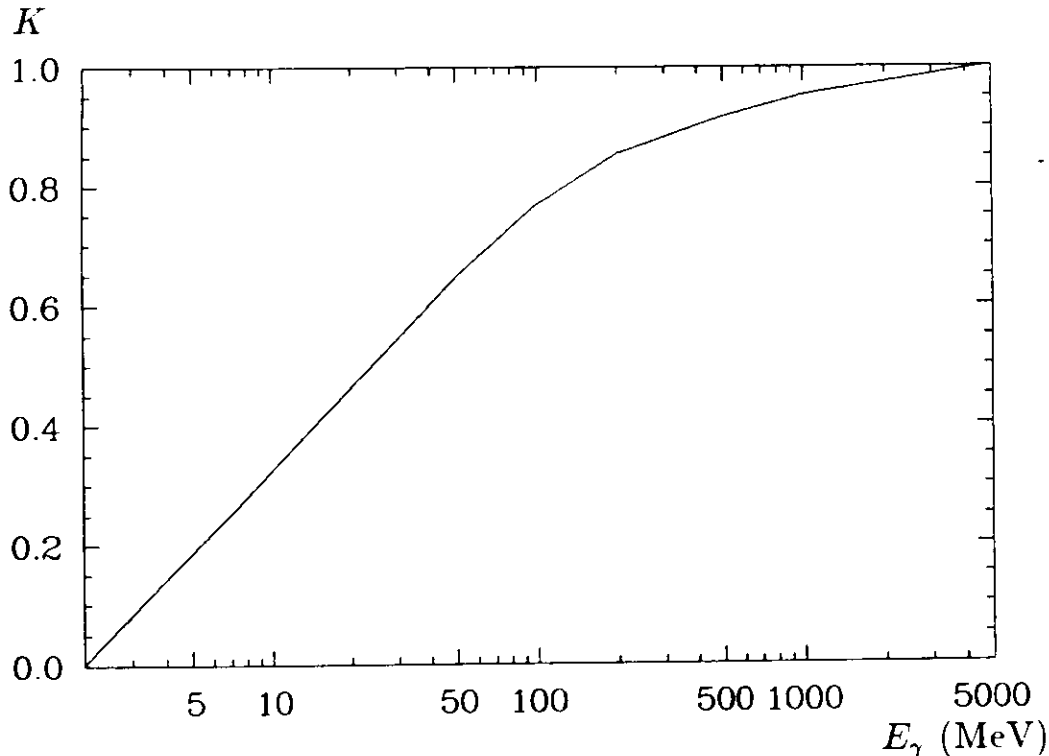


Figure B.18: The dependence of the conversion probability on the photon energy.

### B.5.1 Efficiencies

Most of the following plots show examples of inclusive efficiencies for the intermediate chamber setup, which was characterized by a proper performance of the two double layers of proportional tubes and a steady degradation of the streamer tube double layer. The plotted runs coincide essentially with our  $\Upsilon(2S)$  data sample.

There are two most widely used definitions for tagging and tracking of charged particles, the standard Crystal Ball reconstruction routines, and the TAGTRK program (see Section 3.4). The tagging efficiency for 5 GeV muons obtained by the standard Crystal Ball routines is plotted in Fig. B.19(b) together with the E.T.MC prediction. Since for the setup with 3 double layers only one hit is required by the standard tagging (similar to the TAGTRK tagging), we observe very high efficiencies of  $\varepsilon_{tag} \gtrsim 99\%$  for the intermediate tube chamber setup. Considerably lower efficiencies were only observed for the old streamer tube setup (Fig. B.19(a)), which is not used in this analysis. From Fig. B.19 we derive a systematic uncertainty of the E.T.MC of

$$\Delta\varepsilon_{tag} = 1\% - 2\%, \quad (\text{B.34})$$

where the lower error is valid for high efficiencies  $\gtrsim 90\%$ .

The probabilities  $\varepsilon_{track}$ , that a track fitting can be performed for a charged particle, are plotted in Fig. B.20 for the standard tracking and the TAGTRK tracking for runs from the intermediate chamber setup. Large differences are observed between the two efficiencies, which arise from the minimum number of hits required for track fitting. Whereas standard tracking needs at least 3 hits correlated with the energy deposition in the ball, TAGTRK can perform a straight line fit with already two hits, because the energy deposition in the ball is included in the fit. (A large difference in the hit efficiency for 2 and 3 hits resulted from the deterioration of the double layer of streamer tubes in the runs plotted, so that only two double layers were operating properly.) Both tracking efficiencies and their run dependences

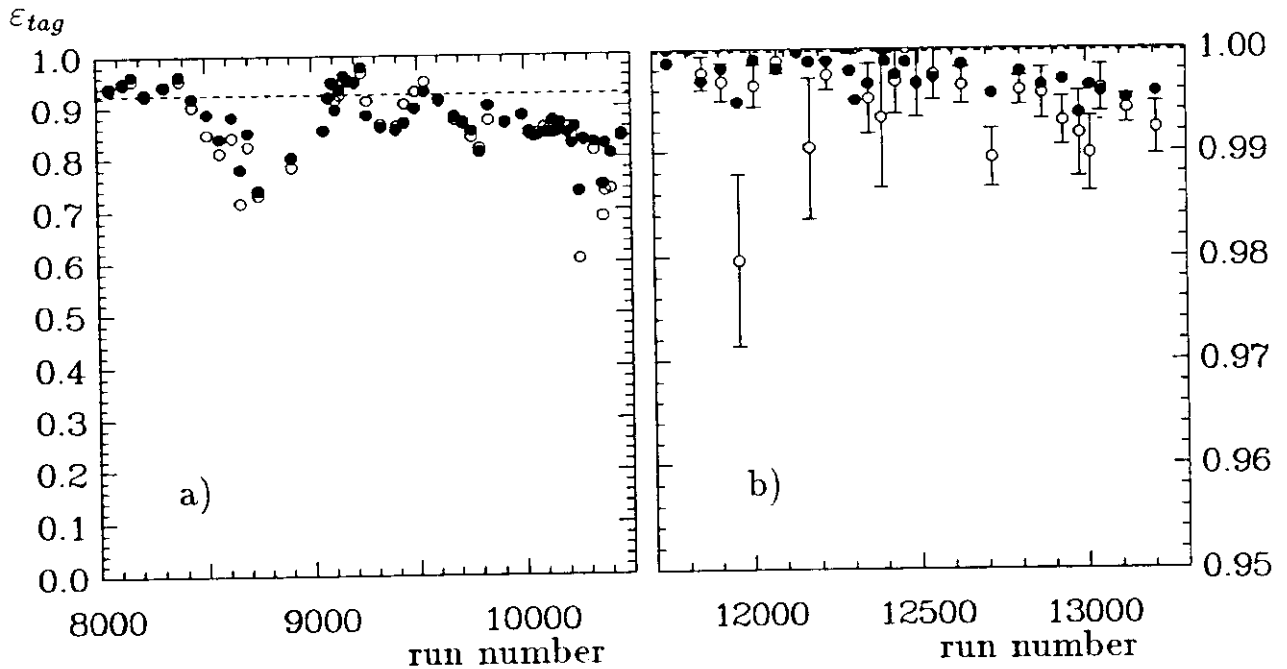


Figure B.19: Standard tagging efficiency for 5 GeV electrons in the old streamer tube chamber setup (a) and 5 GeV muons in the intermediate tube chamber setup (b), both selected within  $|\cos\theta| < 0.82$ . The open circles are the data values, the dots are the E.T.MC prediction, and the dashed line is the runindependent prediction from the old tube chamber MC. Note the different scales on the ordinates.

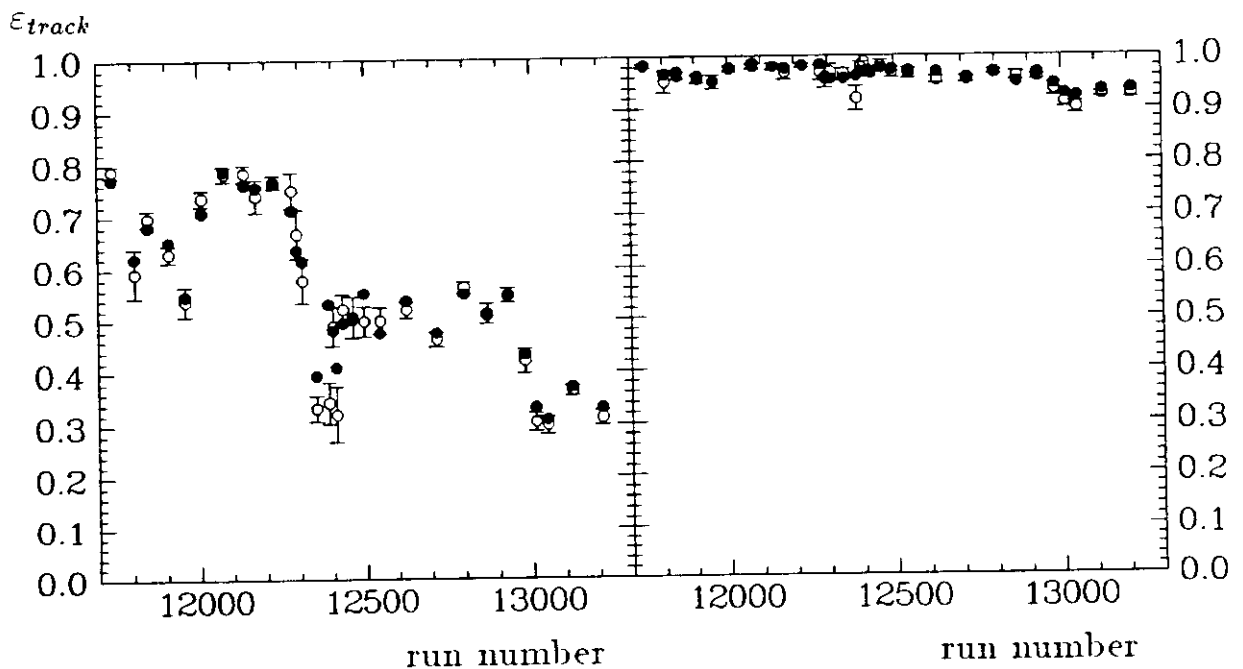


Figure B.20: Tracking efficiency for 5 GeV muons within  $|\cos\theta| < 0.82$  in the intermediate chamber setup as measured from data (open circles) and predicted by the E.T.MC (full dots). The left-hand plot is obtained with standard tracking, the right-hand plot is valid for the TAGTRK routine.

are well reproduced by the E.T.MC simulation with a typical systematic error of

$$\Delta\varepsilon_{track} = 2\% - 3\%, \quad (\text{B.35})$$

where the lower error is again valid for high efficiencies  $\sim 90\%$ .

### B.5.2 Precision of Direction Measurements

To measure, how accurate the resolution of track directions in  $\theta$  and  $\varphi$  are reproduced with the E.T.MC, we study the distribution of the projected opening angles  $\Delta\varphi$  and  $\Delta\theta$  as well as the total opening angle  $\zeta$  for our muons from  $e^+e^- \rightarrow \mu^+\mu^-$ , both for data and E.T.MC. The particle tracks have been fitted with the TAGTRK program. We determine the precision  $\Delta\sigma_{\Delta\theta}$  and  $\Delta\sigma_{\Delta\varphi}$  of the reproduction of the width  $\sigma$  of the distribution for the projected opening angles  $\Delta\varphi$  and  $\Delta\theta$ . Fig. B.21 shows examples for a relatively good and a relatively bad data reproduction, respectively. From corresponding plots for a series of data periods we obtain typical accuracies in reproducing the widths of the projected opening angles of

$$\frac{\Delta\sigma_{\Delta\theta}}{\sigma_{\Delta\theta}} = 8\% \quad \text{and} \quad \frac{\Delta\sigma_{\Delta\varphi}}{\sigma_{\Delta\varphi}} = 15\%. \quad (\text{B.36})$$

It has to be mentioned, that both numbers depend on the length and position of the intersection region of the beams, which is plugged into the MC simulation. We tried to reproduce as far as possible the measured vertex parameters (see Section 3.5). Especially the error for  $\sigma_{\Delta\varphi}$  mainly reflects the residual systematic error in  $\langle x \rangle$ -vertex. The reproduction of  $\sigma_{\Delta\varphi}$  from the E.T.MC alone is much better.

### B.5.3 Photon Conversion Probability

Photon conversion in the beam pipe or the tube chambers plays no role in our analysis. We treat the corresponding E.T.MC simulation only for completeness as a reference for other analyses. The thickness  $t$  of the tube chamber and beam pipe material is known with a precision of  $\Delta t/t = 10\%$ . This constitutes the dominant error for the reproduction of "neutral efficiencies". Neutral efficiencies are defined as the fraction

$$\varepsilon_{neut} = \sum_{i=0}^n \varepsilon_{i,N} \quad (\text{B.37})$$

of events with  $N$  photons, where at most  $n$  photons convert in the inner detector and are detected as charged particles. Here  $\varepsilon_{i,N}$  is the fraction of events with exactly  $i$  "charged" photons. The systematic error on  $\varepsilon_{neut}$ , as determined from the E.T.MC, can be found as follows.

- Find from

$$\varepsilon_{neut} = \sum_{i=0}^n \binom{N}{i} \varepsilon'_{1,1} (1 - \varepsilon_{1,1})^{N-i}$$

the probability  $\varepsilon_{1,1}$  for each single photon to be identified as charged.

- This probability is uncertain by  $\Delta t/t$  due to the error in the thickness of converting material. We define

$$\varepsilon'_{1,1} \equiv \varepsilon_{1,1} (1 - \Delta t/t).$$

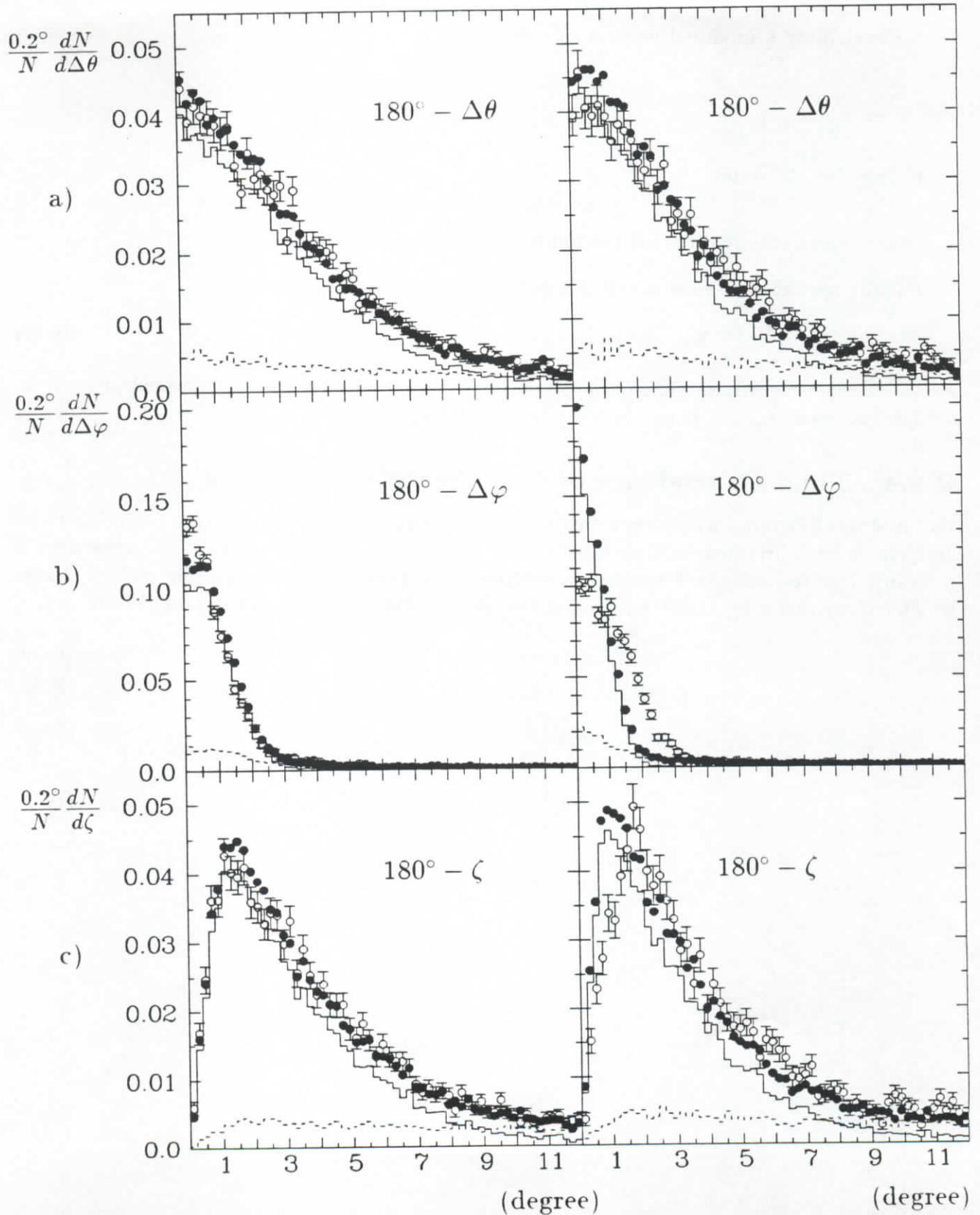


Figure B.21: Reproduction of opening angles for  $\mu$ -pairs from data (open circles) by the E.T.MC simulation (full dots). The MC prediction is a sum of  $e^+e^- \rightarrow \mu^+\mu^-$  (solid histogram) and  $e^+e^- \rightarrow e^+e^-\mu^+\mu^-\pi^+\pi^-$  (dashed histogram). The left-hand side shows a relatively good reproduction, the right-hand side is an example for a relatively bad reproduction.

- Recalculate a modified neutral efficiency

$$\varepsilon'_{neut} = \sum_{i=0}^n \binom{N}{i} \varepsilon'_{1,1}{}^i (1 - \varepsilon'_{1,1})^{N-i}.$$

- Take the difference

$$\Delta\varepsilon_{neut} \equiv \varepsilon_{neut} - \varepsilon'_{neut}$$

as the systematic error for the neutral efficiency.

For the special case with  $n = 0$  this procedure reduces to

$$\Delta\varepsilon_{neut} = \varepsilon_{neut} - [(1 + \Delta t/t) \sqrt[N]{\varepsilon_{neut}} - \Delta t/t]^N. \quad (\text{B.38})$$

As an example we would find from a predicted neutral efficiency for no “charged photon” in a 4-photon event  $\varepsilon_{neut} = \varepsilon_{0,4} = 75.0\%$  an error of  $\Delta\varepsilon_{neut} = 2.2\%$ .

### B.5.4 Time Dependence of Chamber Measurements

For analyses like ours, where event numbers obtained from different running periods,  $A$  and  $B$ , have to be subtracted from each other, the ratio or the difference of E.T.MC accuracies is relevant. Due to our time-dependent modeling of the tube chamber behaviour we are able to predict these ratios by about a factor of two better than the single quantities. We thus find

$$\Delta(\varepsilon_{tag}(A) - \varepsilon_{tag}(B)) = 0.5\% - 1\% \quad (\text{B.39})$$

$$\Delta(\varepsilon_{track}(A) - \varepsilon_{track}(B)) = 1\% - 1.5\% \quad (\text{B.40})$$

$$\Delta\left(\frac{\sigma_{\Delta\theta}(A)}{\sigma_{\Delta\theta}(B)}\right) = 4\% \quad (\text{B.41})$$

$$\Delta\left(\frac{\sigma_{\Delta\varphi}(A)}{\sigma_{\Delta\varphi}(B)}\right) = 7.5\%. \quad (\text{B.42})$$

# Appendix C

## The Determination of the Beam Energy

### C.1 The Method

In the following we show details of the fits to the observed hadronic cross-section as a function of the magnetic field  $B$  in a storage ring bending magnet, which yielded a determination of the beam energy for our on-resonance data. Performing these fits we introduced three simplifications, which led to  $\sim 1\%$  inaccuracies for both, the cross-section subjected to the fit, and for the fitting function. Such inaccuracies change our result on the c.m. energy  $W$  by only 0.1 – 0.2 MeV.

First, we calculated the observed hadronic cross-section without correcting for the contribution of  $\Upsilon \rightarrow e^+e^-$  in the luminosity events (cf. Section 4.4). Such a correction would have been only feasible in an iterative procedure, since it needs the c.m. energy, which we actually just want to determine.

Second, the fits should have been performed with a continuum term  $\propto 1/s \propto 1/B^2$  plus a Breit-Wigner resonance, corrected for initial state photon radiation and beam energy spread, plus a term accounting for the interference between qq production from  $\Upsilon$  decays and in the continuum. Since the interference term contributes at most 1% of the observed hadronic peak cross-section (cf. Section 6.2.1) it can be safely neglected.

Third, to achieve an even simpler (and analytic) fitting function, we approximate the resonance shape by a Gaussian with appended power tail on the high-energy side, which deviates from the exact curve again by at most 1% of the peak cross-section. It can conveniently be parametrized by the peak position  $B_{\text{peak}}$ , the observed continuum cross-section  $\sigma_{\text{cont}} \equiv \sigma^{e^+e^- \rightarrow \text{qq}}(B_{\text{peak}})$ , the observed resonance peak cross-section  $\sigma_{\text{res}} \equiv \sigma^{\Upsilon \rightarrow \text{had}}(B_{\text{peak}})$ , the peak width  $b$  and the exponent  $n \approx 1.8$  according to

$$\sigma^{\text{had}}(B) = \sigma_{\text{cont}} \left( \frac{B_{\text{peak}}}{B} \right)^2 + \sigma_{\text{res}} \begin{cases} \exp \left[ -\frac{1}{2} \left( \frac{B - B_{\text{peak}}}{b} \right)^2 \right] & \text{for } B \leq B_{\text{peak}} + b\sqrt{n} \\ \left[ \sqrt{\frac{\epsilon}{n}} \left( \frac{B - B_{\text{peak}}}{b} \right) \right]^{-n} & \text{for } B > B_{\text{peak}} + b\sqrt{n}. \end{cases} \quad (\text{C.1})$$

$B_{\text{peak}}$  is related by Eqs. (4.4) and (4.3) to the nominal  $\Upsilon$  mass by

$$m_{\Upsilon} = c_{\text{orbit}} B_{\text{peak}} - (1.0 \pm 0.1) \text{ MeV}. \quad (\text{C.2})$$

For the relation between the peak width  $b$ , which contains contributions from initial state radiation, and the true Gaussian width  $w$  of the c.m. energy we find for  $w \approx 8$  MeV

$$w = c_{\text{orbit}} b - (0.4 \pm 0.1) \text{ MeV}. \quad (\text{C.3})$$



The fits according to Eq. (C.1) were performed with  $B_{\text{peak}}$  as the only free parameter. The parameters  $\sigma_{\text{cont}}$ ,  $\sigma_{\text{res}}$ , and  $b$  were fixed to the averages of values from fits to the same data, where all parameters have been left free. This ensures, that changes in  $B_{\text{peak}}$  are not due to statistical changes in the parameters  $\sigma_{\text{cont}}$ ,  $\sigma_{\text{res}}$ , and  $b$ , which all should be constant in time.

From the fitted values of  $B_{\text{peak}}$  for each data period with constant  $c_{\text{orbit}}$  we obtain  $c_{\text{orbit}}$  from Eq. (C.2) as

$$c_{\text{orbit}} = \frac{m_{\Upsilon} + 1.0 \text{ MeV}}{B_{\text{peak}}} \quad (\text{C.4})$$

by inserting the PDG values [22]  $m_{\Upsilon(1S)} = 9460.3 \text{ MeV}$  and  $m_{\Upsilon(2S)} = 10023.3 \text{ MeV}$ . Each data point  $(B, \sigma^{\text{had}})$  was selected by scanning the data taking logbook<sup>1</sup> and grouping the runs of constant  $B$ , which are adjacent in time, to one point each. At breaks in the DORIS operation a new point was started to allow for a shift in  $c_{\text{orbit}}$ . We used the offline hadron selection, described in Section 4.1, for measuring  $\sigma^{\text{had}}$ , and divided the number of resulting multi-hadron events by the corresponding luminosity.

## C.2 Application to the $\Upsilon(2S)$ Data

The NMR reading was available for  $29.6 \text{ pb}^{-1}$  out of the sample of  $37.2 \text{ pb}^{-1}$  of  $\Upsilon(2S)$  data, which we have based our analysis on. For  $7.6 \text{ pb}^{-1}$  of  $\Upsilon(2S)$  data, taken before a regular NMR reading existed at DORIS, we applied different procedures to determine their c.m. energy  $W$ .

During the 1983  $\Upsilon(2S)$  scan (runs 11014 – 11065, corresponding to  $\mathcal{L}=2.3 \text{ pb}^{-1}$ ) the beam energy was directly determined with high precision by resonance depolarization measurements in the DORIS II ring [95,96]. This procedure resulted in 12 data points, for which we (conservatively) estimate a precision of  $\Delta W=0.5 \text{ MeV}$ .

The c.m. energy of the data taken directly before and after this scan (runs 10951 – 11013 and 11066 – 11078, corresponding to  $\mathcal{L}=1.8 \text{ pb}^{-1}$ ) was determined from their difference in the nominal beam energy to the data of the depolarization scan<sup>2</sup>. (We further corrected the resulting c.m. energy for some runs by  $0.5 \text{ MeV}$  to accommodate changes in the high frequency of the Klystrons.) From this data we got 5 points with an estimated precision of  $\Delta W=1.0 \text{ MeV}$ .

Finally, for an older on-resonance period without NMR reading (runs 10486 – 10777, corresponding to  $\mathcal{L}=6.7 \text{ pb}^{-1}$ ) we grouped runs between breaks of the DORIS operation and monitored their observed hadronic cross-section. For our analysis we selected a subset of groups ( $\mathcal{L}=3.5 \text{ pb}^{-1}$ ), so that their mean observed cross-section  $\langle \sigma^{\text{had}} \rangle = 6.57 \pm 0.05 \text{ nb}$  was equal to the expected peak value of  $\sigma_{\text{peak}} = \sigma_{\text{cont}} + \sigma_{\text{res}} = 6.53 \pm 0.02 \text{ nb}$  (see Table 6.2). We thus assumed their c.m. energy to be  $W = W_{\text{peak}}$ . The error on this assignment was estimated to be  $\Delta W=2.0 \text{ MeV}$ , which is supported by a resonance depolarization measurement in one of these runs.

For the bulk of our  $\Upsilon(2S)$  data, however, we could apply the initially introduced procedure of collecting data points  $(B, \sigma^{\text{had}})$  and fitting their functional dependence on  $B$ . For the  $\Upsilon(2S)$  runs between number 11650 and 13230, acquired in the years 1983 and 1984, we collected a total of 29 data points. Few runs with unknown  $B$ , and some runs taken with a different

<sup>1</sup>The handwritten values for  $B$  in this logbook were the only source for the NMR measurement for most of our data.

<sup>2</sup>The nominal DORIS beam energy is directly calculated from the magnet currents. Differences in this beam energy are a reliable measurement for c.m. energy differences for runs directly adjacent in time. Breaks in the DORIS operation alter the relation between current and magnetic field ( $\cong$  beam energy) due to hysteresis effects in the magnets.



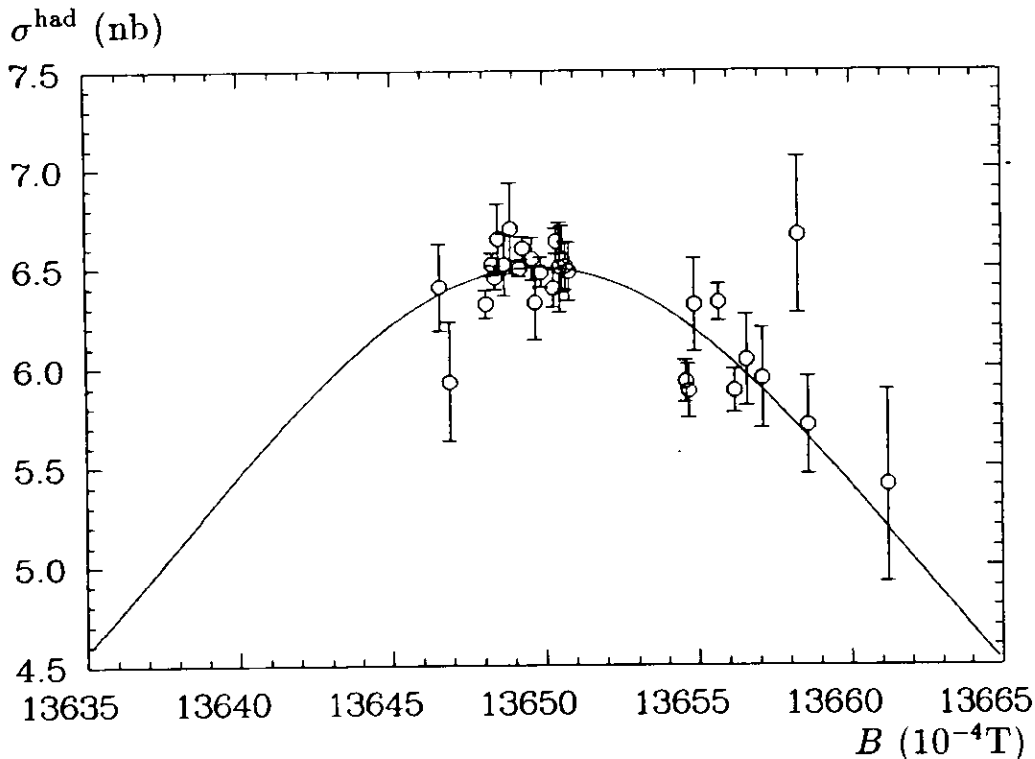


Figure C.1: Fit for the determination of the c.m. energy in our  $\Upsilon(2S)$  data.

beam optic in begin of 1984 were neglected. All 29 data points could be consistently fitted with a single conversion factor

$$c_{orbit} = (7344.0 \pm 0.2) \frac{\text{MeV}}{\text{T}}, \quad (\text{C.5})$$

where the error is only statistical. The corresponding fit is shown in Fig. C.1. We observe, that there were some (so called “on-resonance”) runs, where the c.m. energy was too high by about 5 MeV. If  $c_{orbit}$  has been proven to be constant, as in the case of our  $\Upsilon(2S)$  data, such an offset can be reliably noticed by monitoring  $B$ , only.

### C.3 Application to the $\Upsilon(1S)$ Data

In all of our  $\sim 50 \text{ pb}^{-1}$  of  $\Upsilon(1S)$  data, taken in the years 1984 and 1986, an NMR reading of  $B$  was available. We collected 158 data points of  $(B, \sigma^{had})$  and grouped them to 19 periods between DORIS breaks, so that within each period the conversion factor  $c_{orbit}$  could be regarded as a constant.

Some of these 19 periods contained no scan data, but only (so called) on-resonance data. For these periods a left-right ambiguity arises. Even, if the peak height  $\sigma_{peak}$  and width  $b$  in Eq. (C.1) are known, as in our case, it is not possible to decide from a single point  $(B, \sigma^{had})$ , whether this point lies on the left-hand or the right-hand side of the peak. A determination of  $c_{orbit}$  is not possible in this case. Luckily, most of our periods comprised a large enough range of  $B$  values<sup>3</sup> together with sufficient statistics, so that a clear rise or fall of  $\sigma^{had}$  as a function of  $B$  was visible (cf. Fig. C.3(d)) and resolved the left-right ambiguity. Only 2

<sup>3</sup>The changes of  $B$  may arise from the magnets’ warming up with time, even though all machine parameters are not changed in on-resonance running.

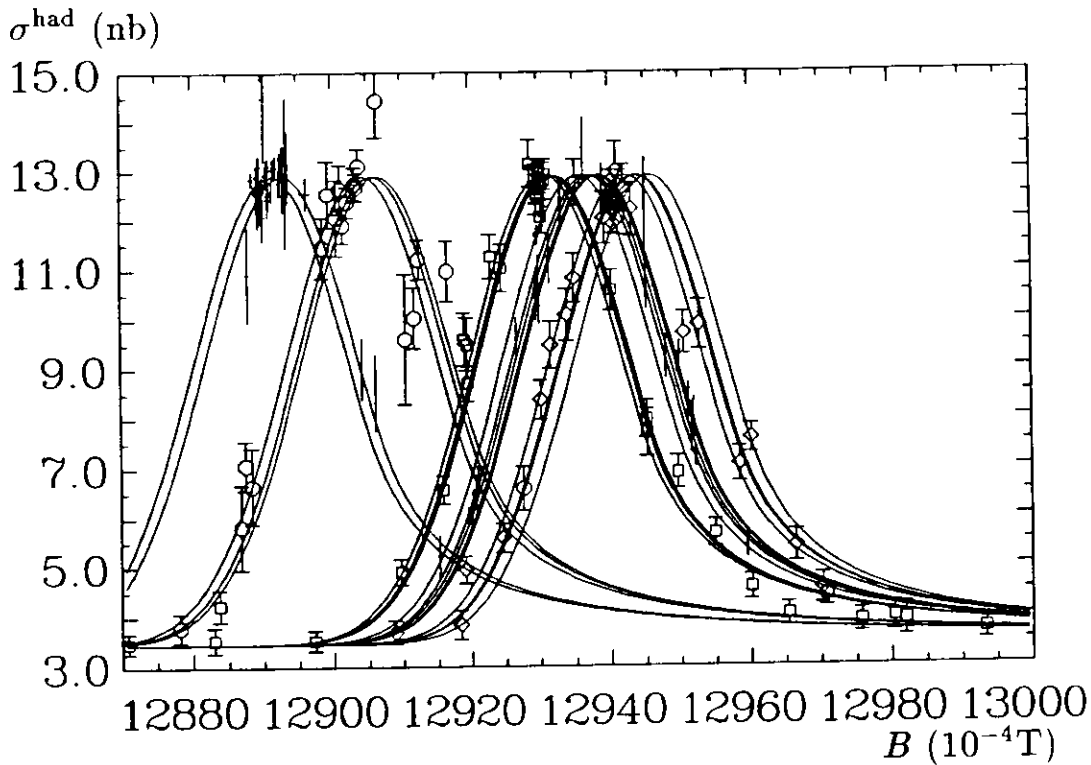


Figure C.2: All single fits to the 19 data periods for the determination of the c.m. energy in our  $\Upsilon(1S)$  data.

periods with  $\mathcal{L} = 3.4 \text{ pb}^{-1}$  did not yield a conclusive result and were thus not further used in the analysis.

The fit results for all 19 periods are shown in Fig. C.2. The most important message of this figure is, that  $c_{orbit}$  really changes in steps. At least 5 groups of fits are visible, which appear to have resonance fits consistent with each other. By closer looking at the respective errors of  $B_{peak}$  we found that we actually have to combine the 17 periods, left after rejecting those periods with unresolved left-right ambiguity, into 6 groups. The fit results for these combined periods are shown in Fig. C.3.

Table C.1: The conversion factors for the determination of the c.m. energy  $W$  from  $B$  for the 6 combined periods of  $\Upsilon(1S)$  data. Only the last 5 values enter our analysis, since the data from the runs 14207 - 14566 were not used due to a nonlinear tube chamber ADC.

Fig. C.3	Runs	$B_{peak}$ (mT)	$c_{orbit}$ (MeV/T)	$V$ (MeV)
(a)	14207 - 14315	$1290.54 \pm 0.04$	$7331.3 \pm 0.2$	16.4
(b)	14316 - 14934	$1289.19 \pm 0.02$	$7339.0 \pm 0.1$	6.5
(c)	17903 - 18391	$1293.15 \pm 0.02$	$7316.5 \pm 0.1$	35.6
(d)	18396 - 18479	$1293.57 \pm 0.02$	$7314.1 \pm 0.1$	38.6
(e)	18496 - 18731	$1293.79 \pm 0.01$	$7312.9 \pm 0.1$	40.2
(f)	19003 - 19073	$1294.32 \pm 0.03$	$7309.9 \pm 0.2$	44.2

The numerical results for the conversion factors are given in Table C.1. The last column in this table gives the offset  $V$  in the  $\Upsilon(1S)$  c.m. energy compared to that value, which would

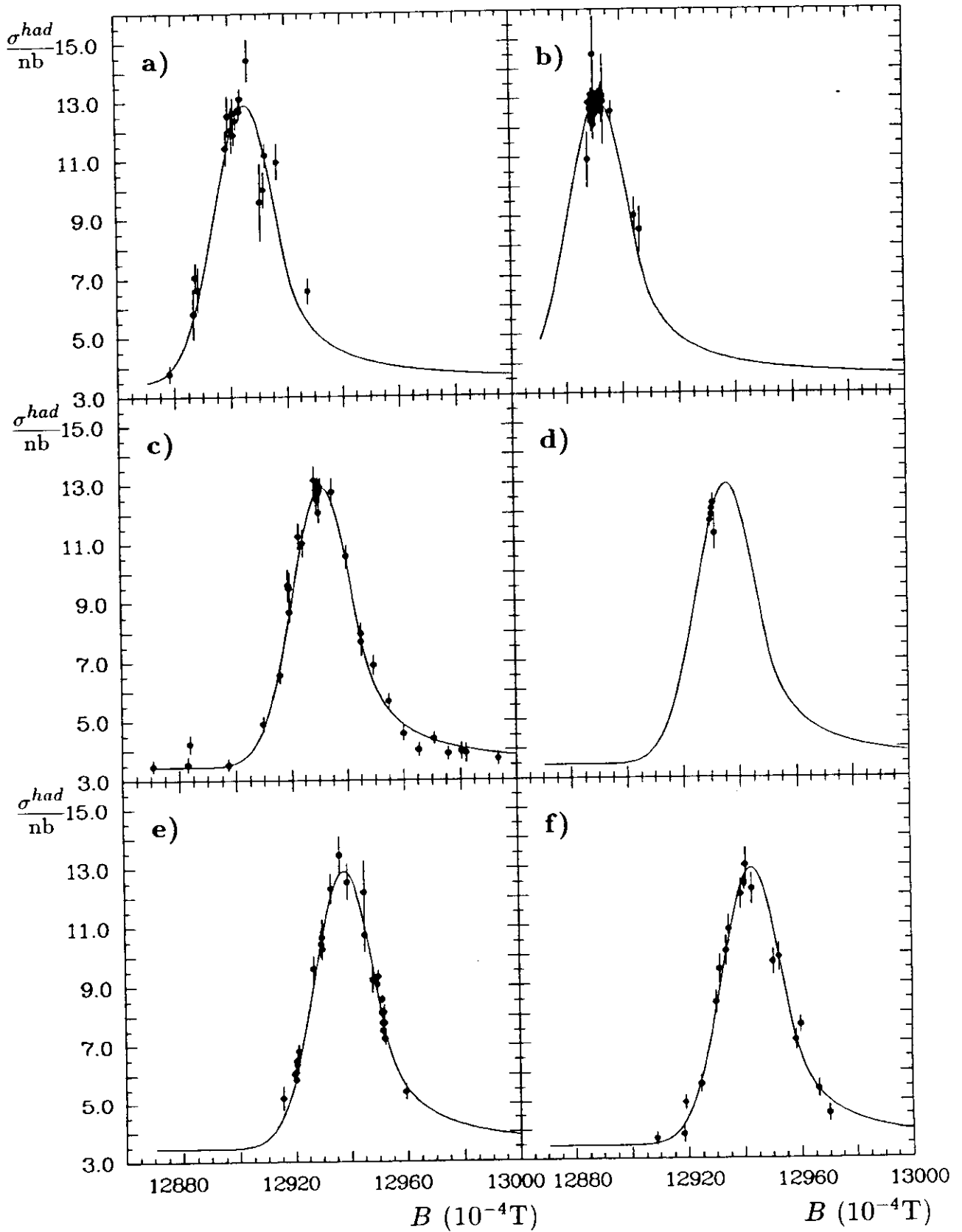


Figure C.3: The final fits to 6 combined data periods for the determination of the c.m. energy in our  $\Upsilon(1S)$  data.

have been obtained by utilizing the  $\Upsilon(2S)$  conversion factor from Eq. (C.5), i.e.

$$V_i = m_{\Upsilon(1S)} \left( \frac{c_{orbit}(2S)}{c_{orbit}(1S)_i} - 1 \right). \quad (C.6)$$

The resulting offsets  $V$  are substantial, if they are compared to the c.m. energy spread of  $w \approx 8$  MeV at DORIS. This result shows, that the c.m. energy  $W$  cannot be measured reliably in the  $\Upsilon(1S)$  energy region by only monitoring  $B$  in a DORIS ring bending magnet. Identical values of  $B$  may belong to c.m. energies, which differ by considerable fractions (or even multiples) of  $w$ . Besides  $B$  the monitoring of a second variable, in our case  $\sigma^{had}$ , was thus mandatory to determine  $W$ .

## C.4 Systematic Errors

All errors listed above are statistical errors as obtained from the fits. The systematic error on our determination of  $W$  was estimated from the variation of the  $B_{peak}$  results of each of the 17 single periods around the  $B_{peak}$  values from the combined fits in Table C.1. We find a r.m.s. variation of 0.10 mT ( $\cong 0.7$  MeV). From pure statistics we expect 0.07 mT ( $\cong 0.5$  MeV). We attribute the quadratic difference between these values to systematic error sources, resulting in an systematic error of our c.m. energy determination of

$$\Delta W = \sqrt{(0.7 \text{ MeV})^2 - (0.5 \text{ MeV})^2} = 0.5 \text{ MeV}. \quad (C.7)$$

This error was used for the c.m. energy determination of the  $\Upsilon(2S)$  data according to Eq. (C.5), likewise.

We note, that the fractional precision of a single  $B$  measurement with the NMR effect is  $5 \times 10^{-5}$  and thus happens to coincide with our value of  $\Delta W/W$ . However, this error does not contribute to  $\Delta W$ . Relevant for  $\Delta W$  are the errors of differences between the mean values of repeated measurements of  $B$ . These are much smaller and thus negligible.

## C.5 Combining the Data Points

After having determined  $W$  for each of the data points in each of the 6 combined periods, we have grouped data with nearby values of  $W$  from different periods together in order to obtain a clearer visualization of our analysis results as a function of  $W$  (see Section 4.2). To each such data set we assigned a luminosity weighted average c.m. energy  $W_i = \sqrt{\sum \mathcal{L} W^2 / \sum \mathcal{L}}$ . The number of different  $W$  values was thereby reduced from 47 to 13 and from 109 to 28 for the  $\Upsilon(2S)$  and the  $\Upsilon(1S)$  data, respectively. (49 data points from our initial number of 158 around the  $\Upsilon(1S)$  were not used in the analysis due to a bad tube chamber ADC (42 points) or due to the unresolved left-right ambiguity (7 points).)

## Appendix D

## The Efficiency Corrected Cross-Section

Table D.1: The spectrum of the efficiency corrected cross-section for  $e^+e^- \rightarrow \Upsilon(1S) \rightarrow \mu^+\mu^-$  and  $e^+e^- \rightarrow \Upsilon(2S) \rightarrow \mu^+\mu^-$  as measured in this analysis at the DORIS II storage ring as a function of the c.m. energy  $W$  (Figs. 6.2(b) and 6.3(b)). The errors listed on the cross-section are only those combined statistical and systematic errors, which are essentially independent from point to point. They include the errors on  $W$ , converted to an error on  $\sigma^{ee \rightarrow \Upsilon \rightarrow \mu\mu}(W)$ . They do not include, however, systematic errors common to all points. These common errors are fractional errors of 3.6% and 4.2%, dominated from the errors on selection efficiency and Luminosity, and absolute errors of 6.4 pb and 5.6 pb, mainly stemming from the number of off-resonance  $\mu$ -pairs observed in the data. The first value refers to the  $\Upsilon(1S)$ , the second to the  $\Upsilon(2S)$  resonance data.

$\Upsilon(1S)$				$\Upsilon(2S)$			
$W$	$\Delta W$	$\sigma^{ee \rightarrow \Upsilon \rightarrow \mu\mu}$	$\Delta\sigma^{ee \rightarrow \Upsilon \rightarrow \mu\mu}$	$W$	$\Delta W$	$\sigma^{ee \rightarrow \Upsilon \rightarrow \mu\mu}$	$\Delta\sigma^{ee \rightarrow \Upsilon \rightarrow \mu\mu}$
(MeV)	(MeV)	(pb)	(pb)	(MeV)	(MeV)	(pb)	(pb)
9362.9	2.0	19.5	19.7	9966.2	1.0	36.7	39.0
9388.3	0.5	186.4	175.5	9985.4	1.0	-70.9	142.3
9396.3	0.5	-148.5	145.7	10009.4	0.5	108.6	88.6
9407.4	0.5	-50.8	161.5	10014.6	0.5	-113.5	92.7
9416.9	0.5	-328.5	157.9	10018.4	0.5	111.1	106.5
9426.1	0.5	-208.5	161.0	10022.1	0.5	29.1	76.7
9436.2	0.5	-3.5	125.1	10023.3	0.5	18.0	18.8
9444.3	0.5	14.7	109.4	10023.9	0.5	45.3	17.0
9448.4	0.5	22.4	28.5	10024.6	1.0	63.7	17.3
9452.5	0.5	57.0	87.3	10028.2	0.5	67.6	32.6
9455.4	0.5	100.2	81.2	10029.5	0.5	-4.9	47.9
9457.5	0.5	198.7	36.5	10033.2	0.5	29.9	52.2
9459.1	0.5	218.1	31.5	10039.1	0.5	-30.7	110.3
9459.5	0.5	274.3	31.9				
9460.1	0.5	256.6	25.0				
9460.4	0.5	231.3	30.3				
9460.6	0.5	240.5	29.0				
9461.3	0.5	172.9	55.7				
9467.5	0.5	271.8	93.6				
9471.2	0.5	185.8	28.9				
9473.6	0.5	176.4	99.0				
9478.0	0.5	76.5	111.0				
9481.8	0.5	197.4	145.7				
9486.1	0.5	37.1	215.4				
9490.0	0.5	70.0	183.5				
9493.6	0.5	85.5	217.9				
9497.6	0.5	104.6	195.0				
9506.6	0.5	171.1	243.1				

# Acknowledgements

*"Can we actually 'know' the universe?  
My God, it's hard enough finding your way around Chinatown."*

Woody Allen, "Getting Even"

At this place I want to thank all those people who have helped me, on the one side, to know and to understand the Crystal Ball Experiment (which is not quite the universe) and, on the other side, to find my way in life and around Hamburg (which is, maybe, as hard as that around Chinatown).

At the first place I thank my advisor and 'Doktorvater' Prof. Horst Wegener for the chance of working in the field of high energy physics. His continuous support and interest in my work and his excitement about fundamental questions of particle physics were an invaluable incitation for this thesis. I will ever remember his advices and the true wisdom of his attitudes in so many aspects of life.

Working in the Erlangen high energy physics group together with Dr. Udo Volland, Jörg Schütte, Manfred Paulini, Klaus Reim, and Bernhard Brandl was real fun. The Erlangen Tube Chamber MC would never have been completed without Jörg Schütte's support. Udo Volland was present whenever a problem appeared to outgrow me. Mrs. Löhner guaranteed that the organizational connection to Erlangen was working across a distance of 600 km.

I thank the DESY directorate for refunding my travel expenses, and the Bundesministerium für Forschung und Technologie for its financial support. This funding was essential for this work and for attendances of schools and conferences.

The Crystal Ball experiment would not have been possible without the joint effort of many people, which are listed on the next page. I would like to thank all members of the Crystal Ball Collaboration for this effort and for years of good cooperation. Dr. Susan Cooper and Dr. Kay Königsmann created a fruitful working atmosphere in the Crystal Ball group at DESY. I'm grateful for their interest in and for their contributions to this analysis. I especially profited from discussions with Reinhardt Lekebusch, Manfred Reidenbach, and Zbyszek Jakubowski. I thank Prof. J.K. Bienlein for the encouragement to publish our Monte Carlo studies. **©THANKS** to Karl-Heinz Karch for the user support within the group.

I appreciate discussions with Prof. G. Kramer about radiative corrections in QED, and especially the advice of Prof. W. Buchmüller in my struggle with QCD renormalization. The patience of Jean-Eric Campagne in explaining details of his DYMU2 generator to me was an infinite one.

Karl Green assured me that the language in which I have written this thesis has something in common with English. Our secretary, Ursula Rehder, did all the hand-drawn plots. With her readiness to help, not only in this case, Mrs. Rehder contributed a lot of human warmth to the collaboration. Manfred Paulini was a magnificent 'ghostreader' of this thesis.

More important, Manfred Paulini and Helmut Marsiske have been true friends all through our common years in Hamburg. They left lasting footprints in my life and helped me in finding my way around Hamburg.

My wife Gaby and our six months old son Pascal created the connection between life and physics. Gaby's understanding and patience, her love and friendship was the by far most important contribution to this thesis and to my life. Gaby and Pascal provided all the color, happiness, and encouragement which was necessary to eventually complete this work. Therefore this thesis is devoted to both of them.

# The Crystal Ball Collaboration

D. Antreasyan<sup>9</sup>, H.W. Bartels<sup>5</sup>, D. Besset<sup>11</sup>, Ch. Bieler<sup>8</sup>, J.K. Bienlein<sup>5</sup>, A. Bizzeti<sup>7</sup>, E.D. Bloom<sup>12</sup>,  
I. Brock<sup>3</sup>, K. Brockmüller<sup>5</sup>, R. Cabenda<sup>11</sup>, A. Cartacci<sup>7</sup>, M. Cavalli-Sforza<sup>2</sup>, R. Clare<sup>12</sup>,  
A. Compagnucci<sup>7</sup>, G. Conforto<sup>7</sup>, S. Cooper<sup>12</sup>, R. Cowan<sup>11</sup>, D. Coyne<sup>2</sup>, A. Engler<sup>3</sup>, K. Fairfield<sup>12</sup>,  
G. Folger<sup>6</sup>, A. Fridman<sup>12</sup>, J. Gaiser<sup>12</sup>, D. Gelphman<sup>12</sup>, G. Glaser<sup>6</sup>, G. Godfrey<sup>12</sup>, K. Graaf<sup>8</sup>,  
F.H. Heimlich<sup>7</sup>, F.H. Heinsius<sup>8</sup>, R. Hofstadter<sup>12</sup>, J. Irion<sup>9</sup>, Z. Jakubowski<sup>5</sup>, H. Janssen<sup>10</sup>,  
K.H. Karch<sup>5</sup>, S. Keh<sup>13</sup>, T. Kiel<sup>8</sup>, H. Kilian<sup>13</sup>, I. Kirkbride<sup>12</sup>, T. Kloiber<sup>5</sup>, M. Kobel<sup>6</sup>, W. Koch<sup>5</sup>,  
A.C. König<sup>10</sup>, K. Königsmann<sup>13</sup>, R.W. Kraemer<sup>3</sup>, S. Krüger<sup>8</sup>, G. Landi<sup>7</sup>, R. Lee<sup>12</sup>, S. Leffler<sup>12</sup>,  
R. Lekebusch<sup>8</sup>, T. Lesiak<sup>4</sup>, A.M. Litke<sup>12</sup>, W. Lockman<sup>12</sup>, S. Lowe<sup>12</sup>, B. Lurz<sup>6</sup>, D. Marlow<sup>3</sup>,  
H. Marsiske<sup>5,12</sup>, W. Maschmann<sup>5</sup>, P. McBride<sup>9</sup>, F. Messing<sup>3</sup>, W.J. Metzger<sup>10</sup>, H. Meyer<sup>5</sup>,  
B. Monteleoni<sup>7</sup>, B. Muryn<sup>4</sup>, R. Nernst<sup>8</sup>, B. Niczyporuk<sup>12</sup>, G. Nowak<sup>4</sup>, C. Peck<sup>1</sup>, P.G. Pelfer<sup>7</sup>,  
B. Pollock<sup>12</sup>, F.C. Porter<sup>1</sup>, D. Prindle<sup>3</sup>, P. Ratoff<sup>1</sup>, M. Reidenbach<sup>10</sup>, B. Renger<sup>3</sup>, C. Rippich<sup>3</sup>,  
M. Scheer<sup>13</sup>, P. Schmitt<sup>13</sup>, J. Schotanus<sup>10</sup>, J. Schütte<sup>6</sup>, A. Schwarz<sup>12</sup>, D. Sievers<sup>8</sup>, T. Skwarnicki<sup>5</sup>,  
V. Stock<sup>8</sup>, K. Strauch<sup>9</sup>, U. Strohbusch<sup>8</sup>, J. Tompkins<sup>12</sup>, H.J. Trost<sup>5</sup>, B. van Uitert<sup>12</sup>,  
R.T. Van de Walle<sup>10</sup>, H. Vogel<sup>3</sup>, A. Voigt<sup>5</sup>, U. Volland<sup>6</sup>, K. Wachs<sup>5</sup>, K. Wacker<sup>12</sup>, W. Walk<sup>10</sup>,  
H. Wegener<sup>6</sup>, D. A. Williams<sup>9,2</sup>, P. Zschorsch<sup>5</sup>

<sup>1</sup> *California Institute of Technology, Pasadena, CA 91125, USA*

<sup>2</sup> *University of California at Santa Cruz, Santa Cruz, CA 95064, USA*

<sup>3</sup> *Carnegie-Mellon University, Pittsburgh, PA 15213, USA*

<sup>4</sup> *Cracow Institute of Nuclear Physics, PL-30055 Cracow, Poland*

<sup>5</sup> *Deutsches Elektronen Synchrotron DESY, D-2000 Hamburg, Germany*

<sup>6</sup> *Universität Erlangen-Nürnberg, D-8520 Erlangen, Germany*

<sup>7</sup> *INFN and University of Firenze, I-50125 Firenze, Italy*

<sup>8</sup> *Universität Hamburg, I. Institut für Experimentalphysik, D-2000 Hamburg, Germany*

<sup>9</sup> *Harvard University, Cambridge, MA 02138, USA*

<sup>10</sup> *University of Nijmegen and NIKHEF, NL-6525 ED Nijmegen, The Netherlands*

<sup>11</sup> *Princeton University, Princeton, NJ 08544, USA*

<sup>12</sup> *Department of Physics, HEPL, and Stanford Linear Accelerator Center,  
Stanford University, Stanford, CA 94309, USA*

<sup>13</sup> *Universität Würzburg, D-8700 Würzburg, Germany*

# Bibliography

- [1] R. Hofstadter, *Rev. Mod. Phys.* 28 (1956) 214.
- [2] R.E. Taylor, *Proc. 15<sup>th</sup> Int. Conf. on High Energy Phys., Kiev (1970)*, ed. R. Wilson; J.I. Friedman and R.W. Kendall, *Ann. Rev. Nucl. Part. Sci.* 22 (1972) 203.
- [3] J. Aubert et al., *Phys. Rev. Lett.* 33 (1974) 1404;  
J.E. Augustin et al., *Phys. Rev. Lett.* 33 (1974) 1406;  
G.E. Abrams et al., *Phys. Rev. Lett.* 33 (1974) 1453.
- [4] S.W. Herb et al., *Phys. Rev. Lett.* 39 (1977) 252;  
W.R. Innes et al., *Phys. Rev. Lett.* 39 (1977) 1240.
- [5] P. Söding and G. Wolf, *Ann. Rev. Nucl. Part. Sci.* 31 (1981) 231.
- [6] H. Plothow-Besch, CERN PPE/90-168 (1990).
- [7] M. Gell-Mann, *Phys. Lett.* 8 (1964) 214;  
G. Zweig, CERN reports TH-401 (1964) and TH-412 (1964).
- [8] J.D. Bjorken, *Phys. Rev.* 179 (1969) 1547;  
R.P. Feynman, *Phys. Rev. Lett.* 23 (1969) 1415.
- [9] Basic ideas for QCD were developed e.g. by  
H. Fritzsch, M. Gell-Mann, and H. Leutwyler, *Phys. Lett.* 47B (1973) 365;  
S. Weinberg, *Phys. Rev. Lett.* 31 (1973) 494, and *Phys. Rev. D*8 (1973) 4482;  
D.J. Gross and F. Wilczek, *Phys. Rev. D*8 (1973) 3633.
- [10] Pioneering works for QED were e.g.  
P.A.M. Dirac, *Proc. Royal Soc. London A*114 (1927) 243;  
P. Jordan and E. Wigner, *Z. Phys.* 47 (1928) 631;  
W. Heisenberg and W. Pauli, *Z. Phys.* 56 (1929) 1;  
E. Fermi, *Atti d. Reale Acc. Naz. d. Lincei* 12 (1930) 431.
- [11] S.L. Glashow, *Nucl. Phys.* 22 (1961) 579;  
A. Salam, *Proc. 8<sup>th</sup> Nobel Symp., Almquist and Wiksell, Stockholm (1968)* 367;  
S. Weinberg, *Phys. Rev. Lett.* 19 (1967) 1264.
- [12] G. 't Hooft, *Nucl. Phys.* B33 (1971) 173 and *Nucl. Phys.* B35 (1971) 167.
- [13] Updated from K. Bethge, U.E. Schröder, "Elementarteilchen",  
*Wiss. Buchgesellschaft, Darmstadt (1986)*, 182 and 188.
- [14] H.B. Jensen et al. (CDF), *Bull. Am. Phys. Soc.* 35 (1990) 943.



- [15] J. Feigenbaum, *Phys. Rev.* D43 (1991) 264.
- [16] B. Gittelmann and S. Stone in "High Energy Electron-Positron Physics", ed. A. Ali and P. Söding, World Scientific (1988) 273.
- [17] S. Okubo, *Phys. Lett.* 5 (1963) 165;  
G. Zweig, CERN reports TH-401 (1964) and TH-412 (1964);  
J. Iizuka et al., *Prog. Theo. Phys.* 35 (1966) 1061.
- [18] C.N. Yang, *Phys. Rev.* 77 (1950) 242;  
cf. also L.D. Landau and E.M. Lifschitz, "Lehrbuch d. Theo. Phys. Bd. IVa", Akad. Verlag Berlin <sup>2</sup>(1971) 32.
- [19] R.P. Feynman, "QED, the Strange Theory of Light and Matter", Princeton University Press, Princeton NJ (1985).
- [20] W. Majerotto, CBPF report M0-001/86, Rio de Janeiro (1986);  
cf. also D. Haidt, DESY report 84-108 (1984),  
publ. in *Proc. CERN School of Physics*, Lofthus, Norway (1984) 85.
- [21] G.S. Abrams et al. (MARK II), *Phys. Rev. Lett.* 63 (1989) 2173;  
B. Adeva et al. (L3), *Phys. Lett.* B231 (1989) 509;  
D. Decamp et al. (ALEPH), *Phys. Lett.* B231 (1989) 519;  
M.Z. Akrawy et al. (OPAL), *Phys. Lett.* B231 (1989) 530;  
P. Aarnio et al. (DELPHI), *Phys. Lett.* B231 (1989) 539.
- [22] Particle Data Group: Review of Particle Properties, *Phys. Lett.* B239 (1990) 1.
- [23] N. Cabibbo, *Phys. Rev. Lett.* 10 (1963) 531;  
M. Kobayashi and J. Maskawa, *Prog. Theo. Phys.* 49 (1973) 652.
- [24] P.W. Higgs, *Phys. Lett.* 12 (1964) 132 and *Phys. Lett.* 13 (1964) 508.
- [25] T.W.B. Kibble, *Phys. Rev.* 155 (1967) 1554.
- [26] M.Z. Akrawy et al. (OPAL), CERN report PPE/90-150 (1990).
- [27] C. Jarlskog, CERN report TH-5918/90 (1990),  
publ. in *Proc. 25<sup>th</sup> Int. Conf. on High Energy Phys.*, Singapore (1990).
- [28] S. Tomonoga, *Phys. Rev.* 74 (1948) 224;  
R.P. Feynman, *Phys. Rev.* 76 (1949) 749 and 769;  
J. Schwinger, *Phys. Rev.* 76 (1949) 790.
- [29] G. Bonneau, *Int. J. Mod. Phys. A*5 (1990) 3831.
- [30] J.C. Ward, *Phys. Rev.* 78 (1950) 1824;  
cf. also C. Itzykson, J.-B. Zuber "Quantum Field Theory",  
Mc Graw-Hill, New York NJ (1985), chapter 7-1.
- [31] W. Hollik, CERN report TH/90-5661 (1990),  
publ. in *Proc. CERN-JINR School of Physics 1989*, Egmond-aan-Zee, Netherlands.
- [32] D.W. Duke and R.G. Roberts, *Phys. Reports* 120 (1985) 277.

- [33] G. 't Hooft and M. Veltman, Nucl. Phys. B44 (1972) 189.
- [34] W.A. Bardeen, A.J. Buras, D.W. Duke, and T. Muta, Phys. Rev. D18 (1978) 3998.
- [35] W. Celmaster and R.J. Gonsalves, Phys. Rev. Lett. 42 (1979) 1435, and Phys. Rev. D20 (1979) 1420, see also [41,42];  
R. Barbieri, L. Caneschi, G. Curci, and E. d'Emilio, Phys. Lett. 81B (1979) 207.
- [36] Y.S. Tsai, SLAC-PUB-3129 (1983), publ. in Proc. 1<sup>st</sup> Asia-Pacific Phys. Conf. 1983, World Scientific, Singapore (1984) 1289, ed. A. Arima et al.
- [37] see e.g. A. Blumenfeld and M. Moshe, Phys. Rev. D26 (1982) 648, and references therein.
- [38] W.J. Marciano, Phys. Rev. D29 (1984) 580.
- [39] O.V. Tarasov, A.A. Vladimirov, and A.Y.Zharkov, Phys. Lett. 93B (1980) 429.
- [40] W. de Boer, SLAC-PUB-4428 (1987),  
publ. in Proc. 10<sup>th</sup> Warsaw Symp. on Elem. Part. Phys., Kazimierz (1987) 503.
- [41] W. Celmaster and R.J. Gonsalves, Phys. Rev. D21 (1980) 3112.
- [42] W. Celmaster and D. Sivers, Phys. Rev. D23 (1981) 227.
- [43] G. Grunberg, Phys. Lett. 95B, (1980) 70 and erratum loc. cit. 110B (1982) 501;  
Phys. Lett. 114B (1982) 271; and Phys. Rev. D29 (1984) 2315.
- [44] P.M. Stevenson, Phys. Rev. D 23 (1981) 2916.
- [45] S.J. Brodsky, P.B. Mackenzie, and G.P. Lepage, Phys. Rev. D28 (1983) 228.
- [46] R. van Royen and V.F. Weisskopf, Nuovo Cimento 50 (1967) 617.
- [47] R. Barbieri, R.Gatto, R. Kögerler, and Z. Kunszt, Phys. Lett. 57B (1975) 455;  
for a discussion of higher order  $\alpha_s$  corrections cf. [49].
- [48] P.B. Mackenzie and G.P. Lepage, Phys. Rev. Lett. 47 (1981) 1244;  
for a discussion of higher order  $\alpha_s$  corrections cf. [124].
- [49] W. Buchmüller and S.-H.H. Tye, Phys. Rev. D24 (1981) 132.
- [50] K. Königsmann, DESY report 87-151 (1987),  
publ. in Proc. Int. Symp. Heavy Flavors, Stanford (1987) 98.
- [51] F.A. Berends, R. Kleiss, and S. Jadach, Nucl. Phys. B202 (1982) 63;  
R. Kleiss, Ph.D. Thesis, Rijksuniversiteit te Leiden (1982);  
(MMG1 generator, essentially identical to Ref. [62]).
- [52] J.P. Alexander, G. Bonvicini, P.S. Drell and R. Frey, Phys. Rev. D37 (1988) 56.
- [53] Y.S. Tsai, Phys. Rev. 120 (1960) 269;  
N. Cabibbo and R. Gatto, Phys. Rev. 124 (1961) 1577;  
cf. also Ref. [69].

- [54] H. Burkhardt, F. Jegerlehner, G. Penso and C. Verzegnassi, *Z. Phys.* C43 (1989) 497; In our MC simulation and for all our plots we employed the routine PIHINT from the Berends and Kleiss generators [61,51,62], which interpolates the result of Ref. [74], and yields  $\Pi_{had}(9.46 \text{ GeV}) = 1.65 \times 10^{-2}$ . The small difference to the value in Table 2.6 is due to new measurements of  $\sigma^{ee \rightarrow had}$ .
- [55] F.A. Berends and G.J. Komen, *Nucl. Phys.* B115 (1976) 114.
- [56] F. Bloch and A. Nordsieck, *Phys. Rev.* 52 (1937) 54.
- [57] T. Kinoshita, *J. Math. Phys.* 3 (1962) 650;  
T.D. Lee and M. Nauenberg, *Phys. Rev.* 133 (1964) B1549.
- [58] O. Nicrosini and L. Trentadue, *Phys. Lett.* B196 (1987) 551.
- [59] D.R. Yennie, S.C. Frautschi, and H. Suura, *Ann. Phys.* 13 (1961) 379.
- [60] R. Kleiss, CERN report TH/89-5439, publ. in "Radiative Corrections for  $e^+e^-$  Collisions" (Proc. Ringberg Workshop 1989), ed. H.J. Kühn, Springer, Berlin (1989) 101.
- [61] F.A. Berends and R. Kleiss, *Nucl. Phys.* B177 (1981) 237, (BKMUON generator).
- [62] F.A. Berends, R. Kleiss and S. Jadach, *Comp. Phys. Comm.* 29 (1983) 185, (MUSTRAAL generator).
- [63] S. Jadach and B.F.L. Ward, *Comp. Phys. Comm.* 56 (1990) 351.
- [64] S. Jadach and B.F.L. Ward, TPJU report 89-19, Krakow (1989) and UTHEP report 89-0703, Knoxville TS (1989), (Workshop on Radiative Corrections, Brighton 1989); cf. also S. Jadach and B.F.L. Ward, in "Radiative Corrections for  $e^+e^-$  Collisions" (Proc. Ringberg Workshop 1989), ed. H.J. Kühn, Springer, Berlin (1989) 118.
- [65] S. Jadach, B.F.L. Ward, and Z. Was, CERN report TH/91-5994 (1991), subm. to *Comp. Phys. Comm.*
- [66] V.N. Gribov and L.N. Lipatov, *Sov. J. Nucl. Phys.* 15 (1972) 438 and 675.
- [67] E.A. Kuraev and V.S. Fadin, *Sov. J. Nucl. Phys.* 41 (1985) 466.
- [68] G. Altarelli and G. Parisi, *Nucl. Phys.* B126 (1977) 298.
- [69] M.E. Peskin, SLAC-PUB-5210 (1990), publ. in *Proc. 17<sup>th</sup> SLAC Summer Inst.*, Stanford (1989) 71, ed. E.C. Brennan.
- [70] J.E. Campagne and R. Zitoun, *Z. Phys.* C43 (1989) 469.
- [71] J.E. Campagne, Ph.D. Thesis, Universites Paris VI et VII (1989).
- [72] F.A. Berends, G. Burgers, and W.L. van Neerven, *Phys. Lett.* B185 (1987) 395.
- [73] F.A. Berends, G. Burgers, W. Hollik, and W.L. van Neerven, *Phys. Lett.* B203 (1988) 177.
- [74] F.A. Berends and G.J. Komen. *Phys. Lett.* B63 (1976) 432.

- [75] J.D. Jackson, D.L. Scharre, Nucl. Inst. Meth. 128 (1975) 13.
- [76] H.J. Bhabha, Proc. Roy. Soc. A154 (1935) 195.
- [77] E.D. Bloom and C.W. Peck, Ann. Rev. Nucl. Part. Sci. 33 (1983) 143.
- [78] Details about the calorimeter can be found in Refs. [77,79];  
more information about the tube chamber system is contained in Refs. [83,87,94];  
the ToF system is described most completely in Refs. [85,86].
- [79] M. Oreglia, Ph.D. Thesis, Stanford University (1980), SLAC Report-236 (1980);  
M. Oreglia et al. (Crystal Ball), Phys. Rev. D25 (1982) 2259.
- [80] R. Lee, Ph.D. Thesis, Stanford University (1985), SLAC Report-282 (1985).
- [81] D. Sievers, Diploma Thesis, Universität Hamburg (1985) (in German).
- [82] W. Maschmann, Diploma Thesis, Universität Hamburg (1984) (in German).
- [83] K. Wachs, Ph.D. Thesis, Universität Hamburg (1988), DESY internal report F31-88-01.
- [84] P. de Barbaro and T. Skwarnicki, Internal Crystal Ball note (Sep. 1983).
- [85] M. Kobel, Diploma Thesis, Universität Erlangen-Nürnberg (1986),  
DESY internal report F31-86-03.
- [86] D. Prindle, Ph.D. Thesis, CMU Pittsburgh, PA (1985).
- [87] K. Karch, Diploma thesis, Universität Würzburg (1986).
- [88] R.L. Ford and W.R. Nelson, SLAC Report-210 (1978).
- [89] Z. Jakubowski and M. Kobel, Nucl. Inst. Meth. A297 (1990) 60.
- [90] H. Fesefeldt, PITHA report 85/02, Aachen (1985).
- [91] Z. Jakubowski and S. Keh, Internal Crystal Ball note (April 1985);  
cf. also Ref. [135].
- [92] Z. Jakubowski, Ph.D. Thesis, INP Cracow (1990), DESY internal report F31-90-01.
- [93] Z. Jakubowski, private geometry program.
- [94] K. Wachs et al. (Crystal Ball), Z. Phys. C42 (1989) 33.
- [95] D.P. Barber et al., Phys. Lett. B135 (1984) 498.
- [96] Z. Jakubowski et al. (Crystal Ball), Z. Phys. C40 (1988) 49.
- [97] F.A. Berends, P.H. Daverfeldt and R. Kleiss, Comp. Phys. Comm. 40 (1986) 271.
- [98] J.A.M. Vermaseren, Nucl. Phys. B229 (1983) 347.
- [99] S.J. Brodsky, T. Kinoshita, and H. Terazawa, Phys. Rev. D4 (1971) 1532.
- [100] S. Jadach and Z. Wąs, Comp. Phys. Comm. 36 (1985) 191;  
The events were left to us by the friendly cooperation of Bart Janssen.

- [101] S. Lowe, Ph.D. Thesis, Stanford University (1986).
- [102] F.A. Berends, P.H. Daverfeldt and R. Kleiss, *Comp. Phys. Comm.* 40 (1986) 285.
- [103] As measured by H. Lenzen and M. Schneider (private communications).
- [104] T. Sjöstrand, *Comp. Phys. Comm.* 39 (1986) 347.
- [105] T. Sjöstrand and M. Bengtsson, *Comp. Phys. Comm.* 43 (1987) 367.
- [106] A.M. Boyarski et al., *Phys. Rev. Lett.* 34 (1975) 1357.
- [107] Ch. Berger et al. (PLUTO), *Z. Phys. C1* (1979) 343.
- [108] P. Bock et al. (DESY-HD), *Z. Phys. C6* (1980) 125.
- [109] B. Niczyporuk et al. (LENA), *Z. Phys. C15* (1982) 299.
- [110] H. Albrecht et al. (DASP), *Phys. Lett. B116* (1982) 383.
- [111] D. Andrews et al. (CLEO), *Phys. Rev. Lett.* 50 (1983) 807.
- [112] D. Besson et al. (CLEO), *Phys. Rev. D30* (1984) 1433.
- [113] T. Kaarsberg et al. (CUSB), *Contr. Paper #286 to Int. Symp. on Lepton and Photon Interactions, Hamburg* (1987).
- [114] H. Albrecht et al. (ARGUS), *Z. Phys. C35* (1987) 283.
- [115] T. Kaarsberg et al. (CUSB), *Phys. Rev. Lett.* 62 (1989) 2077.
- [116] W.-Y. Chen et al. (CLEO), *Phys. Rev. D39* (1989) 3528.
- [117] A. Onuchin et al. (MD-1), *Talk given at the DESY Seminar* (Sep. 1990).
- [118] P. Haas et al. (CLEO), *Phys. Rev. D30* (1984) 1996.
- [119] H. Albrecht et al. (ARGUS), *Z. Phys. C28* (1985) 45.
- [120] See Ref. [115].
- [121] K.R. Schubert, private communication.
- [122] A. Bizetti, J. Schütte et al. (Crystal Ball), *DESY report 91-051* (1991),  
subm. to *Phys. Lett. B*;  
J. Schütte, Ph. D. Thesis, Universität Erlangen-Nürnberg (1989),  
*DESY internal report F31-89-03* (in German);  
A. Bizetti, Ph. D. Thesis, University of Firenze, (1986) (in Italian).
- [123] R. Marshall, *Z. Phys. C43* (1989) 585.
- [124] P.B. Mackenzie and G.P. Lepage, *Proc. Conf. Perturb. QCD, Tallahassee* (1981) 176, ed. D.W. Duke, J.F. Owens.
- [125] W. Kwong, P.B. Mackenzie, R. Rosenfeld, and J.L. Rosner,  
*Phys. Rev. D37* (1988) 3210.

- [126] S.E. Csorna et al. (CLEO), *Phys. Lett.* 138B (1984) 225;  
R.D. Schamberger et al. (CUSB), *Phys. Rev. Lett.* 56 (1986) 1222;  
H. Albrecht et al. (ARGUS), *Phys. Lett.* 199B (1987) 291.
- [127] E.A. Uehling, *Ann. Rev. Nucl. Part. Sci.* 4 (1954) 315.
- [128] E.J. Kobetich and R. Katz, *Phys. Rev.* 170 (1968) 391.
- [129] R.M. Sternheimer, *Phys. Rev.* 88 (1952) 851;  
R.M. Sternheimer, *Phys. Rev.* 91 (1953) 256.
- [130] E. Fermi, *Phys. Lett.* 57 (1940) 485.
- [131] H.A. Bethe, *Ann. Phys.* 5 (1930) 325.
- [132] R.M. Sternheimer, M.J. Berger, and S.M. Seltzer,  
*Atom. Data Nucl. Data Tables* 30 (1984) 261.
- [133] R.M. Sternheimer, *Phys. Rev.* 145 (1966) 247.
- [134] R.M. Sternheimer and R.F. Peierls, *Phys. Rev.* B3 (1971) 3681.
- [135] Z. Jakubowski and M. Kobel, DESY report 89-165 (1989);  
(extended version of Ref. [89]).
- [136] F. Bloch, *Z. Phys.* 81 (1933) 363.
- [137] L.D. Landau, *J. Phys. USSR* 8 (1944) 201.
- [138] H.D. Maccabee and D.G. Papworth, *Phys. Lett.* 30A (1969) 241.
- [139] D.F. Morgan, Internal Crystal Ball note, (Aug. 1985).

# Lebenslauf

Name : Michael Kobel  
Geboren : 10. 10. 1961 in Bayreuth  
Eltern : Lilly Kobel, geb. Buch, und Herbert Kobel  
Staatsangehörigkeit : deutsch  
Familienstand : verheiratet, ein Kind

## Verlauf der Ausbildung

Okt. 1967 - Juli 1971 : Besuch der Pestalozzi-Grundschule Kulmbach  
Sept. 1971 - Juni 1980 : Besuch des MGF-Gymnasiums Kulmbach  
(Abschluß : Abitur)  
Nov. 1980 - Mai 1986 : Studium der Physik  
an der Friedrich-Alexander Universität Erlangen-Nürnberg  
(Abschluß : Diplom)  
Nov. 1982 : Diplomvorprüfung  
Aug. 1983 - Sep. 1983 : Werkstudent bei Siemens, Erlangen  
ab Okt. 1984 : Diplomarbeit bei Prof. H. Wegener  
in der Crystal Ball Kollaboration am DESY in Hamburg  
Mai 1986 : Diplomhauptprüfung  
Juni 1986 - Aug. 1986 : Forschungsaufenthalt am Stanford Linear Acc. Center, USA  
seit Juni 1986 : Wiss. Mitarbeiter am Phys. Inst. der Univ. Erlangen-Nürnberg,  
Weiter Mitarbeit am Crystal Ball Experiment

